

# Hybrid discretizations of the Boltzmann equation for the dilute gas flow regime

**Citation for published version (APA):**

Di Staso, G. (2018). *Hybrid discretizations of the Boltzmann equation for the dilute gas flow regime*. [Phd Thesis 1 (Research TU/e / Graduation TU/e), Applied Physics and Science Education]. Technische Universiteit Eindhoven.

**Document status and date:**

Published: 17/12/2018

**Document Version:**

Publisher's PDF, also known as Version of Record (includes final page, issue and volume numbers)

**Please check the document version of this publication:**

- A submitted manuscript is the version of the article upon submission and before peer-review. There can be important differences between the submitted version and the official published version of record. People interested in the research are advised to contact the author for the final version of the publication, or visit the DOI to the publisher's website.
- The final author version and the galley proof are versions of the publication after peer review.
- The final published version features the final layout of the paper including the volume, issue and page numbers.

[Link to publication](#)

**General rights**

Copyright and moral rights for the publications made accessible in the public portal are retained by the authors and/or other copyright owners and it is a condition of accessing publications that users recognise and abide by the legal requirements associated with these rights.

- Users may download and print one copy of any publication from the public portal for the purpose of private study or research.
- You may not further distribute the material or use it for any profit-making activity or commercial gain
- You may freely distribute the URL identifying the publication in the public portal.

If the publication is distributed under the terms of Article 25fa of the Dutch Copyright Act, indicated by the "Taverne" license above, please follow below link for the End User Agreement:

[www.tue.nl/taverne](http://www.tue.nl/taverne)

**Take down policy**

If you believe that this document breaches copyright please contact us at:

[openaccess@tue.nl](mailto:openaccess@tue.nl)

providing details and we will investigate your claim.

# Hybrid discretizations of the Boltzmann equation for the dilute gas flow regime

This work is part of the project 'Stick to the surface!', which is supported by the STW under project number 12817.

Eindhoven University of Technology  
Department of Applied Physics  
Research group: Turbulence and Vortex Dynamics  
PO Box 513  
5600 MB Eindhoven, The Netherlands

Copyright © 2018 by Gianluca Di Staso, Eindhoven, The Netherlands.  
Cover design by Ilse Modder  
Printed by Gildeprint, Enschede, The Netherlands

A catalogue record is available from the Eindhoven University of Technology  
Library  
ISBN: 978-90-386-4655-8  
NUR: 924

Hybrid discretizations of the Boltzmann equation for the dilute gas flow regime  
/ by Gianluca Di Staso. – Eindhoven: Technische Universiteit Eindhoven, 2018. –  
Proefschrift.

# Hybrid discretizations of the Boltzmann equation for the dilute gas flow regime

PROEFSCHRIFT

ter verkrijging van de graad van doctor aan de  
Technische Universiteit Eindhoven, op gezag van de  
rector magnificus, prof.dr.ir. F.P.T. Baaijens, voor een  
commissie aangewezen door het College voor  
Promoties in het openbaar te verdedigen  
op maandag 17 december 2018 om 16.00 uur

door

Gianluca Di Staso

geboren te Foggia, Italië



Dit proefschrift is goedgekeurd door de promotoren en de samenstelling van de promotiecommissie is als volgt:

voorzitter:	prof. dr. ir. G.M.W. Kroesen
1 <sup>e</sup> promotor:	prof. dr. H.J.H. Clercx
2 <sup>e</sup> promotor:	prof. dr. F. Toschi
leden:	prof. dr. A.L. Garcia (San José State University, USA)
	prof. dr. J.D.R. Harting (Friedrich-Alexander Universität Erlangen-Nürnberg, Germany)
	prof. dr. ir. E.H. van Brummelen
	prof. dr. ir. P.P.A.M van der Schoot

Het onderzoek of ontwerp dat in dit proefschrift wordt beschreven, is uitgevoerd in overeenstemming met de TU/e Gedragscodex Wetenschapsbeoefening.

# Contents

<b>Nomenclature</b>	<b>1</b>
<b>1 Introduction</b>	<b>3</b>
1.1 Introduction to the thesis . . . . .	3
1.2 Approaches to the modeling of fluid motion . . . . .	4
1.3 Research objectives . . . . .	10
1.4 Thesis outline . . . . .	11
<b>2 Lattice Boltzmann and Direct Simulation Monte Carlo numerical methods</b>	<b>13</b>
2.1 Analogies and dissimilarities between the DSMC and the LBM . .	13
2.2 Basics of the DSMC method . . . . .	16
2.3 Basics of the LBM method . . . . .	26
2.4 Conclusions . . . . .	44
2.A Gauss quadratures . . . . .	45
<b>3 Development and validation of the DSMC solver</b>	<b>49</b>
3.1 DSMC code: implementation details . . . . .	49
3.2 Validation test cases for the DSMC code . . . . .	54
3.2.1 Power-law velocity profile in the Knudsen layer . . . . .	54
3.2.2 Shear stress model . . . . .	59
3.2.3 Lid-driven cavity flow . . . . .	61
3.2.4 Flows with open boundary conditions . . . . .	66
3.3 Conclusions . . . . .	78
<b>4 Coupling DSMC-LBM: methodology</b>	<b>81</b>
4.1 Coupling methodology . . . . .	81
4.1.1 Mapping schemes . . . . .	84
4.1.2 DSMC2LB mapping scheme . . . . .	86
4.1.3 LB2DSMC mapping scheme . . . . .	88
4.1.4 Stability issues for the coupling schemes . . . . .	91
4.1.5 Numerical results of the coupling schemes . . . . .	92
4.1.6 Numerical results for the DSMC2LB mapping scheme . . .	95
4.1.7 Numerical results for the LB2DSMC mapping scheme . . .	97

4.2	Breakdown parameter for the hybrid model . . . . .	102
4.3	D3Q19 lattice case . . . . .	102
4.4	Effect of the temperature on the mapping schemes . . . . .	114
4.5	Conclusions . . . . .	117
4.A	Scaling factors . . . . .	118
4.B	Hermite polynomials . . . . .	119
<b>5</b>	<b>Hybrid DSMC-LBM solver for monodimensional flows</b>	<b>121</b>
5.1	Application of the coupling methodology . . . . .	121
5.2	Coupling schemes . . . . .	123
5.3	Numerical results . . . . .	126
5.4	Conclusions . . . . .	131
<b>6</b>	<b>Hybrid DSMC-LBM solver for complex flows</b>	<b>133</b>
6.1	Introduction . . . . .	133
6.2	Review of the hybrid LBM-DSMC coupling method . . . . .	135
6.3	Treatment of complex geometries and wall boundary conditions . .	140
6.4	Comparison study: LBM, DSMC and hybrid method . . . . .	145
6.5	Computational costs . . . . .	162
6.6	Conclusions . . . . .	170
6.A	Conversion of units from LB to SI and vice versa . . . . .	171
6.B	Implementation of slip boundary conditions in LBM . . . . .	172
6.C	Set-up of initial conditions to speed-up the DSMC simulation . . .	174
<b>7</b>	<b>Concluding remarks and outlook</b>	<b>177</b>
7.1	Conclusions . . . . .	177
7.2	Outlook . . . . .	180
<b>A</b>	<b>Fluctuations on hydrodynamic moments: DSMC study</b>	<b>183</b>
A.1	Relations for fluctuations at equilibrium . . . . .	183
A.2	Conclusions . . . . .	188
	<b>Bibliography</b>	<b>189</b>
	<b>List of publications</b>	<b>205</b>
	<b>Summary</b>	<b>207</b>
	<b>Acknowledgements</b>	<b>209</b>
	<b>Curriculum Vitae</b>	<b>211</b>

# Nomenclature

BE	Boltzmann Equation 3
BGK	Bhatnagar-Gross-Krook 13
CAD	Computer-Aided Design 51
CE	Chapman-Enskog 7
CLL	Cercignani-Lampis-Lord 20
DSMC	Direct Simulation Monte Carlo 3
DUGKS	Discrete Unified Gas Kinetic Scheme 61
DVM	Discrete Velocity Method 6
ESM	Equilibrium Statistical Mechanics 184
GHS	Generalized Hard Sphere 24
HOL	Higher-order lattice 84
HS	Hard Sphere 18
LBM	Lattice Boltzmann Method 3
MB	Maxwell Boltzmann 18
MCS	Move-Collide-Sample 17
MM	Moments Method 7
MPI	Message Passage Interface 51
MRT	Multi Relaxation Time 28
MSC	Move-Sample-Collide 17
MSCS	Move-Sample-Collide-Sample 17
NTC	No Time Counter 16

SRT	Single Relaxation Time	28
TMAC	Tangential Momentum Accommodation Coefficient	143
VHS	Variable Hard Sphere	24
VSS	Variable Soft Sphere	24

# 1 Introduction

## 1.1 Introduction to the thesis

Rarefied and non-equilibrium gas flows represent an open research challenge as physics, mathematical modeling as well as computer science requirements have to be taken into account simultaneously in order to provide an accurate and efficient description. In fact, the nature of these flows is such that physical phenomena which are typically not encountered when studying flows under continuum conditions emerge. The velocity slip and temperature jump at the walls, non-Fourier-like transport of heat, or the suppression of convective motions also for conditions only slightly departing from the continuum ones, are some of the most common ones. The peculiarities of rarefied gas flows require that, in order to properly capture them, specific mathematical models have to be employed. While for continuum flows, the Navier-Stokes equations represent an accurate model to study the fluid motion, in case of rarefied gas flows, a more fundamental approach should be invoked and the solution of the Boltzmann Equation (BE) should be sought. However, the mathematical complexity of the BE, and the associated computational effort required to generate a direct numerical solution of it, limits the applicability of such an approach to relatively simple flow set-ups. Therefore, alternative methods, but still stemming from the BE, have to be adopted.

Rarefied and non-equilibrium gas flows assume also an important role in the determination of the performance of several high-tech industrial processes, such as in material processing tools, and products, such as micro- and nano-electromechanical systems. In these applications, it is often possible to detect an additional feature: the gas flows are characterized by a large range of rarefaction and non-equilibrium effects, and, therefore, they possess an intrinsic multi-scale nature.

In this view, this thesis involves aspects related to the physics and modelling of flows presenting variable rarefaction conditions, and to the development of novel hybrid numerical methods, coupling the Lattice Boltzmann Method (LBM) and the Direct Simulation Monte Carlo (DSMC), to study such flows. It also involves, as a feasibility study, the application of the method to a concrete flow set-up of industrial interest, which implies several characteristic length and time scales, and complex boundary conditions. This latter application challenges commonly adopted numerical approaches.

## 1.2 Approaches to the modeling of fluid motion

In this section, we provide a brief overview about some of the mathematical models commonly used to deal with rarefied and non-equilibrium flows. In chapter 2, we will focus on the description of two methods, the LBM and the DSMC, which we will use to define the hybrid method subject of this work.

The nature of a flow in terms of rarefaction and non-equilibrium effects is generally classified according to the so-called Knudsen number,  $\text{Kn}$ . This dimensionless number is defined as the ratio between a molecular length scale, i.e. the mean free path,  $\lambda$ , and a flow-related length scale,  $L$ :

$$\text{Kn} = \frac{\lambda}{L}. \quad (1.1)$$

The mean free path  $\lambda$  represents the average distance traveled by a moving gas molecule between two successive collisions, and it is inversely proportional to the gas density. The characteristic flow length scale, instead, can be defined in two ways. Taking into account an overall dimension of the flow, e.g. the height of a channel, a single global Knudsen number,  $\text{Kn}_G$ , can be defined. Instead, if the scale  $L$  is defined according to the macroscopic flow gradients as

$$L = \frac{Q}{|dQ/d\ell|}, \quad (1.2)$$

a local Knudsen number,  $\text{Kn}_\ell$ , can be defined.

In Eq. (1.2),  $Q$  might be chosen as the gas density, velocity, temperature, or also other hydrodynamic quantities and  $\ell$  is the smallest hydrodynamic length scale. The choice of  $Q$ , then, may depend on the features of the studied flow.

Based on these definitions, it is possible to specify different flow regimes. This traditional way to classify the flows is based on the appearance of flow phenomena typical of each regime, as well as on the mathematical models used to describe such flows. In Fig. 1.1, a graphical representation of the different flow regimes, and the corresponding models used to describe them is shown. It has to be mentioned that this scheme has only a descriptive nature and does not want to represent a precise and comprehensive treatment of the subject, which, indeed, can be found elsewhere, [1–3].

It is customary, therefore, to classify, based on a phenomenological point of view, the gas flows into the hydrodynamic ( $\text{Kn} < 0.01$ ), slip ( $0.01 < \text{Kn} < 0.1$ ), transition ( $0.1 < \text{Kn} < 10$ ) and free molecular regime ( $\text{Kn} > 10$ ).

From a mathematical point of view, a very fundamental approach to the description of fluid flows would require to represent the gas as a collection of  $N$  particles in a

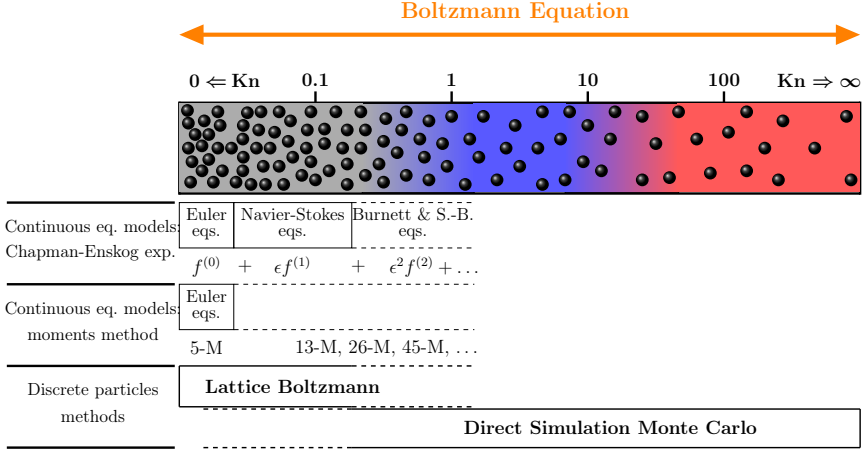


**Figure 1.1:** Schematic representation of the numerical methods, derived from the Boltzmann Equation (BE), commonly adopted to deal with flows at different levels of rarefaction. While the BE is able to span the complete  $Kn$  range, the models derived from it provide accurate and efficient flow representations in a limited range of  $Kn$ . The acronym S.-B. stands for Super-Burnett, while the summation  $f^{(0)} + \epsilon f^{(1)} + \epsilon^2 f^{(2)} + \dots$  indicates the Chapman-Enskog expansion formalism. The nomenclature  $x$ -M is typically employed to classify the different models falling under the so called Moments Method. Here,  $x$  identifies the number of hydrodynamic moments, and, correspondingly, equations, involved in the model. More details about this picture are provided in the text of section 1.2.

box of volume  $V$  at temperature  $T$  and interacting via an intermolecular potential  $\Phi(\mathbf{r})$ , where  $\mathbf{r}$  is the particle separation, and where, for simplicity, a possible velocity dependence of the potential has been dropped. If any relevant length scale of the system is much larger than the de Broglie wavelength,  $\Lambda = h/p$ , where  $h$  is the Planck constant and  $p$  is the particle momentum, the dynamics of such particles, which can be treated as point-like objects, is governed by the Newton equations of motion for the particle position,  $\mathbf{x}_i$ , and velocity,  $\boldsymbol{\xi}_i$ , for each particle  $i$  under the effects of the potential  $\Phi$  and possibly external forces, both included in the force term  $\mathbf{F}_i$ :

$$\frac{d\mathbf{x}_i}{dt} = \boldsymbol{\xi}_i, \quad (1.3)$$

$$\frac{d\boldsymbol{\xi}_i}{dt} = \frac{\mathbf{F}_i}{m}. \quad (1.4)$$

Providing proper initial and boundary conditions, these equations could be numerically integrated in time so to obtain a set of  $6N$  functions of time ( $\mathbf{x}_i(t)$ ,  $\boldsymbol{\xi}_i(t)$ ), thus producing a complete picture of the state of the system.



Such approach is the one which is at the basis of the Molecular Dynamics simulation method, [4].

However, taking into account the order of magnitude of  $N$  (which is in the order of the Avogadro number,  $\sim 10^{23}$  for standard pressure conditions), it is clear that such approach does not represent a viable possibility from a computational point of view, when one wants to simulate macroscopic scale flows. In fact, also under very rarefied conditions,  $N$  is generally a very large number.

In addition to this, even if we would be able to track the system composed of  $N$  particles over a sufficiently long time, this huge amount of information would be of little help. In fact, in the vast majority of the cases, we are interested on observables such as density, velocity and so on, which are indeed derived as statistical averages over a large number of individual molecular informations. It is therefore functional to the description of the system to shift from an individual-molecule approach to a statistical one where we are interested in the collective behavior of an ensemble of molecules.

Under the framework of such an approach, therefore, the main aim is to determine the probability to find a molecule at position  $\mathbf{x}$  with velocity  $\boldsymbol{\xi}$  at time  $t$ . Such probability, generally indicated as  $f(\mathbf{x}, \boldsymbol{\xi}, t)$ , is the central object of the kinetic theory of gases, since when, in 1872, the Austrian scientist Ludwig Boltzmann derived an equation describing the temporal evolution of  $f$  in terms of microscopic interactions, [5], the celebrated BE, which reads as:

$$\frac{\partial f}{\partial t} + \boldsymbol{\xi} \cdot \nabla_{\mathbf{x}} f + \mathbf{F} \cdot \nabla_{\boldsymbol{\xi}} f = Q. \quad (1.5)$$

In Eq. (1.5), the left-hand side represents the streaming motion of the molecules along the trajectories connected with the force field  $\mathbf{F}$  and the right-hand side takes into account the effects of two-body collisions among molecules. A complete description of the derivation of this equation, and the applied assumptions, can be found in textbooks such as [6].

Our interest here is to indicate, as done in the top part of Fig. 1.1, that the BE is a tool capable to describe a flow at any rarefaction condition as determined by the Knudsen number and as bounded by the fully continuum flow condition ( $\text{Kn} \rightarrow 0$ ) and the collisionless or free-molecular flow regime ( $\text{Kn} \rightarrow \infty$ ).

Even if the search for a solution of the BE has dramatically decreased the required computational effort with respect to the individual-molecule approach, the direct deterministic numerical simulation of the BE is still a very challenging task.

Several methods have been developed to tackle this task. Some of them are based on the Discrete Velocity Method (DVM), where the phase space  $(\mathbf{x}, \boldsymbol{\xi})$  is discretized so that the resulting equations can be solved numerically, [7–9]. Traditional DVM

prescribes that the discretized BE is explicitly solved, thus constraining the time step and the cell size to be compliant with the molecular scales. As a consequence, the DVM works well for highly rarefied gas flows, but becomes computationally very expensive for near-continuum conditions. Therefore, in order to have an efficient DVM at any Kn, the so-called asymptotic preserving (AP) schemes have been proposed, [9–11].

Besides the DVM, several other methods, directly derived from the BE, appeared. As indicated in Fig. 1.1, it is possible to distinguish between those methods, which we name "continuous equations models", based on a macroscopic theory which involves the solution of a system of coupled partial differential equations and describing the evolution of the physical system via macroscopic quantities such as density, velocity and temperature, and those methods which make use of the concept of particles, computational objects representing a large amount of real molecules, and that can be named "particle-based methods".

The continuous equation models can be further split in two main approaches: the Chapman-Enskog (CE) method, and the Moments Method (MM).

Both methods start from the definition of transport equations for the moments of the distribution function,  $f$ , see e.g. [3] for the derivation of such equations. Upon writing five of such transport equations for the conserved moments, namely the density, velocity and temperature, it is evident that such conservation laws contain eight additional quantities, i.e. the components of the stress tensor and of the heat flux vector, once an equation of state relating pressure, density and temperature has been included. This set of equations, therefore, is not closed. The difference between the two approaches is the way in which the closure issue is handled.

In particular, the CE prescribes that the system of equations is limited to the five expressing the conservation laws and finds relations between the stress and the heat flux in terms of the lower-order variables and their local space derivatives. The basic idea of the CE method, independently developed by Chapman, [12, 13], and Enskog, [14, 15], is to expand the distribution  $f$  into a series in the formal smallness parameter  $\epsilon$  as

$$f = f^{(0)} + \epsilon f^{(1)} + \epsilon^2 f^{(2)} + \epsilon^3 f^{(3)} + \dots \quad (1.6)$$

In Eq. (1.6),  $\epsilon$  plays the role of the Knudsen number (the procedure, in fact, is generally performed on the dimensional BE) and  $f^{(0)}$  is the so-called Maxwellian distribution which encompasses a local equilibrium state, a condition that microscopically corresponds to the case for which any direct/inverse collision is balanced by another inverse/direct collision. Under such state, therefore, the right hand side term of the BE is equal to zero. The terms  $f^{(i)}$  in Eq. (1.6), with  $i > 0$ , instead, represent the perturbations with respect to the state at the order  $i - 1$ .

By inserting in the BE the relation of Eq. (1.6), truncated at the desired order, it is possible to derive a closed set of equations. While the main variables are the same at any level of the expansion, the relations which link the main variables to the stress and the heat flux vary according to the order of the expansion. So, for example, truncating the series at the 0-th order, the Euler equations are recovered and the stress and the heat flux are absent.

Truncating the expansion to the first order leads to the classical well-known Navier-Stokes-Fourier laws with explicit expressions for the viscosity and heat conductivity as a function of the pressure and temperature, and where the stress and the heat flux are linear functions of the velocity and temperature gradients, respectively. It is intuitive to understand that increasing the order of the truncation, more non-equilibrium effects could be dealt with. The method has been further developed up to the second order, recovering the so-called Burnett equations, [16, 17], but only partly to third order, which yields the super-Burnett equations, [18]. These last two sets of equations, however, are not widely used for a number of reasons, including that no proper boundary conditions for the equations are known and they are unstable for transient problems, [19]. It is therefore customary to stop the truncation at the first order (thus recovering the classical Navier-Stokes-Fourier equations).

The other approach falling under the continuous equation models is the Moments Method. A comprehensive treatment of it can be found in [3]. Here, we just want to shed some light on the differences between the CE and MM approaches.

The MM prescribes to solve additional transport equations for the stress and the heat flux variables. The moment equations are obtained by firstly multiplying the BE by  $m\mathbf{c}^{(n)}$ , where  $m$  is the molecular mass and  $\mathbf{c}^{(n)}$  is the rank- $n$  tensor such that  $\mathbf{c}^{(0)} = 1$ ,  $\mathbf{c}^{(1)} = \boldsymbol{\xi} - \mathbf{u}$  (intrinsic velocity as difference between the molecular and fluid velocities),  $\mathbf{c}^{(2)} = (\boldsymbol{\xi} - \mathbf{u})(\boldsymbol{\xi} - \mathbf{u})$  and so on, and by subsequently performing an integration over the velocity space.

The structure of the moment equations so obtained is such that the equation for a given moment contains the next higher order moment as its flux and the previous lower order moment are present in the source term. Therefore, since the equation at order  $n$  contains the moments at the order  $n \pm 1$ , the moments equations are coupled and form an infinite set of equations. In addition, the production terms, originating from the collision process and which vanish only for the equations corresponding to the conserved moments, are related to the distribution function  $f$ . To have a complete set of equations, therefore, it is also needed to express the production terms in terms of the moments, [20]. This can be generally done if a relation between the moments and  $f$  is known. It is with this perspective that Grad, [21], proposed to solve the closure problem by expanding the distribution

function  $f$  into Hermite polynomials. Once the order of the expansion is chosen, the truncated distribution function can be used to compute the fluxes and the production terms as functions of the moments and, therefore, the system of the moment equations is closed. Again, in [3], a rigorous derivation can be found.

At this point, it is natural to ask which moments, and how many, one has to take into account. Indeed, there is not a conclusive answer to such question, and it is not an objective of this work to look for such answer. However, it is intuitive that taking into account more non-equilibrium effects, the number of moments should increase. As demonstrated in [3], the number of moments, and consequently of equations, cannot be chosen arbitrarily, but, for example, meaningful sets of equations involves 5, 13, 26, 45, 71, 105, 148, 201, 265, 341, 430,  $\dots$ , moments. It is interesting to notice that, in order to describe largely non-equilibrium flows, the number of moments may become so large that other methods, notoriously computationally expensive, such as DVM, may become more efficient.

Moreover, the physical meaning associated with each moment is quickly lost. In fact, we can have a direct physical intuition only for the first 13 moments (involving density, velocity, temperature, stress, heat flux). This, indeed, represents also a challenge when imposing boundary conditions.

Finally, it is possible to link the CE and MM approaches: the 5-equation system generated via the MM corresponds to Euler equations as derived from the CE method when stopped at the 0-th order. Analogously, the 13-moment system provides a description equivalent to the one provided by the Burnett equations, and the 26-moment system correspond to the super-Burnett equations.

With respect to the formulation of Grad, the MM has witnessed several advancements, which helped to extend the range of applicability of the method, such as the regularized 13 moments formulation (R13), [22], and the divergence-based closure procedure, [23].

After this brief description of the continuous equation models, we can pass to the description of the discrete particle-based methods. In Figure 1.1, we indicate as particle-based methods only those two that we will adopt in the rest of this work, i.e. the LBM, [24, 25], and the DSMC, [1, 26].

However, many more particle-based methods to simulate fluid flows have appeared in literature, such as the Smoothed Particle Hydrodynamics (SPH, [27]), Dissipative Particle Dynamics (DPD, [28]), Stochastic Rotation Dynamics (SRD, [29]) but these methods are not relevant for the type of flows of interest here.

As the description of the LBM and DSMC methods is subject of chapter 2, here we will mention only few details.

First of all, the DSMC, a mesoscopic stochastic simulation method, represent the de facto standard when dealing with rarefied and non-equilibrium gas flows. How-

ever, from a computational point of view, it becomes more and more expensive as the Knudsen number approaches 0, i.e. the flow approaches continuum conditions, due to the fact that molecular scales have to be taken into account when defining the simulation grid and the time step duration. From the other side, the LBM, which also represents a mesoscopic approach to the simulation of fluid flows, while it is particularly efficient when dealing with continuum flows, requires more and more modelling efforts as  $Kn$  increases.

These two methods, therefore, appear to be complementary as they provide their best at the two opposite limits of the  $Kn$  range. Moreover, since they share common kinetic theory roots, they can be seen as ideal candidates to construct a hybrid method taking advantages from both methods and allowing to simulate flows characterized by variable non-equilibrium conditions.

Before concluding this section, it is interesting to point out that the LBM might be interpreted as a special formulation of the DVM as proposed in [30]. Moreover, in the formal derivation of the method, presented in chapter 2, we will also make use of the same technical tool proposed by Grad to solve the closure issue for the MM: the distribution function  $f$  is expanded in a series of Hermite polynomials.

### 1.3 Research objectives

The study of rarefied and non-equilibrium gas flows still represents a challenging task due to the complexity of the required modelling and numerical tools. There are, therefore, many open questions related to this field of research. In this thesis, we address some of such questions, and, in particular, we will deal with the following ones:

- Can we understand what are the limitations for the LBM in describing flows at finite  $Kn$  as a function of the number of lattice discrete velocities?
- Can we define a hybrid method which takes advantage of the peculiarities of the LBM and DSMC methods to simulate flows characterized by a large range of non-equilibrium effects? Is it possible to construct coupling algorithms between the LBM and the DSMC able to transfer also non-equilibrium information?
- Can we implement these algorithms in an efficient way in a single code infrastructure?
- Can we take advantage of the efficiency of the developed hybrid method to open up the possibility to investigate with high accuracy the physics of realistic flows within industrial applications?

In the next chapters, we will provide answers to such questions.

## 1.4 Thesis outline

This thesis is organized as follows. In chapter 2, we introduce the basics of the LBM and DSMC methods. While we present the LBM in a rigorous way taking advantage of Grad's formulation of the single particle distribution function  $f$  as expansion in Hermite polynomials, and of the Gauss-Hermite quadrature tool to evaluate the coefficients of such expansions, we introduce the DSMC in a more practical way, underlining the criteria to be fulfilled in order to obtain an accurate numerical solution.

In chapter 3, we present the results of the validation of the DSMC code developed during the PhD project. The code is benchmarked against typical rarefied gas flow tests. Few details about the implementation of the code, which took into consideration the full compatibility with the already existing LBM code and its treatment of flows in complex domains, are also provided.

The proposed presentation of the LBM and DSMC methods in chapter 2 is also instrumental to the comprehension of the content of chapter 4, where we introduce the coupling algorithms able to transfer non-equilibrium information from the LBM to the DSMC and vice versa. The proposed recipes are tested in a Poiseuille flow set-up by using two different LBM models (the D3Q19 and the D3Q39 lattice), that are able to recover the same description level as guaranteed by the Navier-Stokes equations and the Burnett equations, respectively.

In chapter 5, we discuss the implementation of the coupling algorithm into an hybrid method based on the domain decomposition technique. While the LBM is applied to the whole flow domain, the DSMC is adopted only in those regions where non-equilibrium effects are stronger. The method is tested against the classical Couette flow problem, and the large increase in the efficiency of the hybrid method when compared to the DSMC applied to the whole flow domain is demonstrated. The proposed hybrid model is further tested in chapter 6 against a 3D flow set-up of industrial interest. Such application represents a challenge both from a modelling point of view, as a wide range of rarefaction conditions are simultaneously present in different regions of the flow, as well as from a computational point of view, as the flow requirements are such that more than 100 millions cells and, consequently, billions of particles have to be used. For each tested method, i.e. LBM, DSMC, and the hybrid LBM-DSMC, the specific strengths and weaknesses are described. In particular, the hybrid LBM-DSMC method, while reproducing with good accuracy the solution provided by the DSMC, is able to substantially reduce the computational cost to reach the final solution (more than a fourfold

reduction in wall clock time).

In the last chapter, chapter 7, we summarize our main results, underline the current limitations of the proposed hybrid method and we propose strategies and approaches to overcome such limitations.

Finally, in the appendix A, we present the results about the estimates with DSMC of the fluctuations associated to the evaluation of the macroscopic hydrodynamic variables. This is done to guarantee that in the passage of information between the LBM and the DSMC, and vice versa, also the contributions from the fluctuations are also correctly included. The results are then compared with standard equilibrium statistical mechanics theory.

## 2 Lattice Boltzmann and Direct Simulation Monte Carlo numerical methods

In this thesis, we use two numerical tools to simulate flow fields under non-continuum, non-equilibrium gas conditions: the Lattice Boltzmann Method (LBM) and the Direct Simulation Monte Carlo (DSMC) approach.

This chapter provides an introduction to these methods, which share the same common roots based on the kinetic theory of gases. Starting from a brief discussion about the analogies and differences between the methods, we describe the basic steps characterizing the specific algorithms which are implemented within the code used throughout this thesis. For the LBM we rigorously derive the connection between the order of the discretization of the BE, under the Bhatnagar-Gross-Krook (BGK) collision operator, and the accuracy at the macroscopic level of the resulting discrete Boltzmann equations. For the DSMC, instead, we follow a more practical approach, specifying the typical simulation set-up conditions associated to each step of the algorithm so to obtain an accurate numerical solution.

### 2.1 Analogies and dissimilarities between the DSMC and the LBM

In this chapter, we provide some introductory elements to describe the LBM and DSMC methods. Exhaustive treatments of the two methods can be found in [1, 24, 25].

While the DSMC method represents the standard numerical method for the simulation of rarefied gas flows, the LBM has recently emerged as a popular numerical tool for computational fluid dynamics able to provide an accurate solution to the Navier-Stokes equations. It has been successfully used in a wide range of flow applications both for single and multiphase laminar flows, [31], flow in porous media, [32], as well as turbulent flow applications, [33–35]. More recently, it has been extended also towards flows characterized by finite rarefaction and non-equilibrium effects, [36–39].



It is important here to underline that both methods share a common origin based on the kinetic theory of gases. This will prove beneficial not only for the development of the coupling algorithm, but also, for example, when treating boundary conditions. In fact, particle-surface interactions can be modeled in a similar way in the two methods and at a more fundamental level than in classical solvers for the Navier-Stokes equations.

Not rigorously speaking, both DSMC and LBM methods aim to determine the fluid motion as described by the BE. In few words, the BE is a transport equation for the probability distribution function,  $f(\mathbf{x}, \mathbf{p}, t)$ , which represents the probability that a particle occupies a given region of space,  $d^3\mathbf{x}$ , centered at the position  $\mathbf{x}$ , and a given region of momentum space,  $d^3\mathbf{p}$ , centered at the momentum  $\mathbf{p}$ , at a given instant of time  $t$ . For details about the derivation of such an equation the reader should refer to [6].

In the framework of DSMC and LBM as BE solvers, both methods are based on a splitting algorithm scheme. If we consider, just for simplicity, the force-free form of the BE:

$$\begin{aligned} \frac{\partial f(\mathbf{x}, \boldsymbol{\xi}, t)}{\partial t} + \boldsymbol{\xi} \cdot \frac{\partial f(\mathbf{x}, \boldsymbol{\xi}, t)}{\partial \mathbf{x}} &= Q, \\ f(\mathbf{x}, \boldsymbol{\xi}, 0) &= f_0(\mathbf{x}, \boldsymbol{\xi}), \end{aligned} \quad (2.1)$$

where  $\boldsymbol{\xi} = \mathbf{p}/m$  is the velocity of the particle,  $m$  is the mass of the gas molecules,  $Q$  is the term related to the collisions between particles and  $f_0(\mathbf{x}, \boldsymbol{\xi})$  represents a given initial condition, we can split the problem into two steps: a free flow step (i.e. streaming of the particles) in which we solve the collisionless BE over a time interval  $\Delta t$ :

$$\begin{aligned} \frac{\partial h_1(\mathbf{x}, \boldsymbol{\xi}, t)}{\partial t} + \boldsymbol{\xi} \cdot \frac{\partial h_1(\mathbf{x}, \boldsymbol{\xi}, t)}{\partial \mathbf{x}} &= 0, \\ h_1(\mathbf{x}, \boldsymbol{\xi}, 0) &= f_0(\mathbf{x}, \boldsymbol{\xi}), \end{aligned} \quad (2.2)$$

and a collision step during which we solve a space homogeneous BE:

$$\begin{aligned} \frac{\partial h_2(\mathbf{x}, \boldsymbol{\xi}, t)}{\partial t} &= Q, \\ h_2(\mathbf{x}, \boldsymbol{\xi}, 0) &= h_1(\mathbf{x}, \boldsymbol{\xi}, \Delta t), \end{aligned} \quad (2.3)$$

for which the initial condition  $h_2(\mathbf{x}, \boldsymbol{\xi}, 0)$  is represented by the solution of the previous free flow step,  $h_1(\mathbf{x}, \boldsymbol{\xi}, \Delta t)$ . The final solution  $h_2(\mathbf{x}, \boldsymbol{\xi}, \Delta t)$  after one time interval  $\Delta t$  represents an approximate form of the solution of the BE,  $f(\mathbf{x}, \boldsymbol{\xi}, \Delta t)$ . A graphical representation of the application of such splitting algorithm is provided

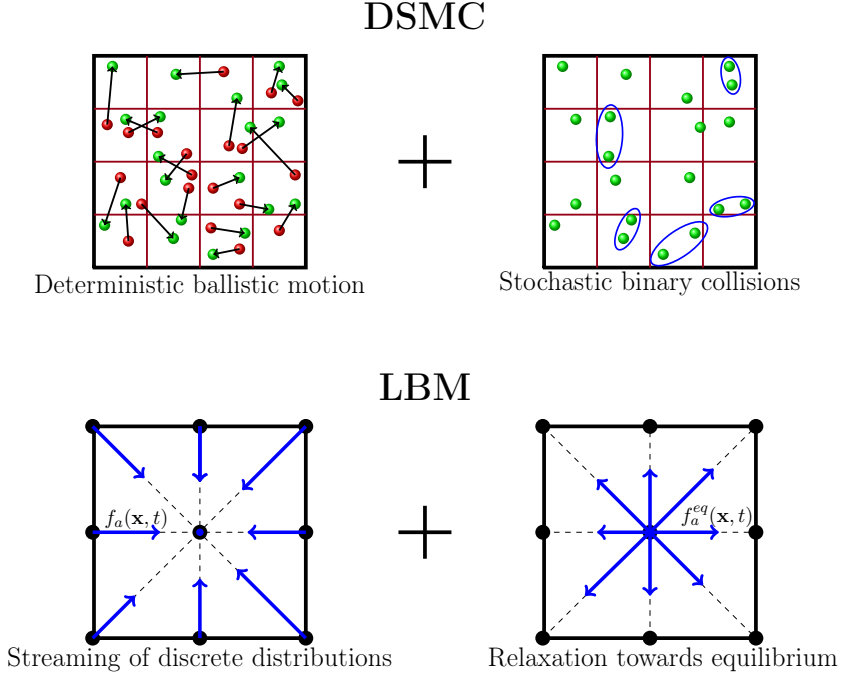


**Figure 2.1:** Graphical representation of the splitting algorithm scheme applied to DSMC and LBM: while the treatment of the streaming step is common to both methods, but only in the sense that the particles move undisturbed in the domain, the treatment of the collision step is very different. In DSMC, stochastic simulated binary collisions between particles residing in the same collisional cell are performed (see the encircled particles). In LBM, instead, the collision phase is reduced to a relaxation process towards a local equilibrium as determined by the fluid density and velocity. For the LBM, a classical two-dimensional lattice with 9 discrete speeds (commonly termed as D2Q9) is shown.

in Fig. 2.1 where the DSMC and LBM streaming and collision steps are depicted. From Fig. 2.1, it is also possible to identify some of the dissimilarities which distinguish the two methods. The main feature which clearly differentiates the LBM from the DSMC is the drastic reduction of the degrees of freedom of the velocity space. In LBM, particles at each lattice site,  $\mathbf{x}$ , can propagate during the streaming step only along a finite number of directions with assigned speed  $\xi_a$ , where the index  $a$  represents one of the possible allowed directions. In DSMC, instead, the velocity space is not constrained to any predetermined set of discrete velocities.

At this stage, a clarification about the concept of "particle" in LBM is needed, as in the following pages we will also use the terms populations or discrete distributions as synonyms of the term particle. A particle in the LBM framework represents a

given amount of real molecules which all have the same velocity and are located in the same position within the domain. This definition is basically the definition of the single particle distribution function  $f(\mathbf{x}, \boldsymbol{\xi}, t)$  as evolved within the BE. In this sense, both the LBM and DSMC particles represent the same physical and mathematical quantities. In fact, also in the DSMC method, a computational molecule represents a (very large) number of real molecules that are moving along the same direction with the same speed. Again, the difference resides in the streaming step. In LBM the particles are forced to move exclusively along prescribed directions with an assigned speed, while in the DSMC the particles are free to span the whole phase space.

The treatment of the collision step is also different in the two methods. In the LBM, it is reduced to a relaxation process whose dynamics is generally determined by a single parameter (the so-called relaxation time) incorporating all the information about the collision process. In the DSMC, instead, this process encompasses stochastic binary collisions between particles sufficiently close. More details about this step will be provided in the next sections.

## 2.2 Basics of the DSMC method

In analogy with other numerical methods, DSMC does not refer to a single method, but to a vast class of different schemes. In the in-house developed DSMC code used for the simulations of this study, we employ a classical method originally developed by Bird, [1], named No Time Counter (NTC) algorithm. This popular algorithm is one of the several schemes described in literature to determine the number of potential collision pairs during a time step. Other common schemes are, for example, the time counter, [40], the majorant collision frequency, [41], the Bernoulli trials scheme, [42]. The NTC scheme was chosen as it represents a good compromise between accuracy and efficiency. Further details about it are presented in the paragraph dealing with the collision step.

In Fig. 2.2, a typical flowchart for a DSMC simulation employing the NTC algorithm and for a steady-state flow simulation is illustrated. We briefly go through the indicated steps.

### Initialization of the simulation

During the initialization phase, the grid composed of sampling cells and collisional subcells is created. The sampling cells network provides the geometric areas and volumes to evaluate the macroscopic flow properties by sampling the microscopic properties of the computational molecules (mass, momentum, energy) according to classical kinetic theory. The collisional subcell network, instead, is used by the

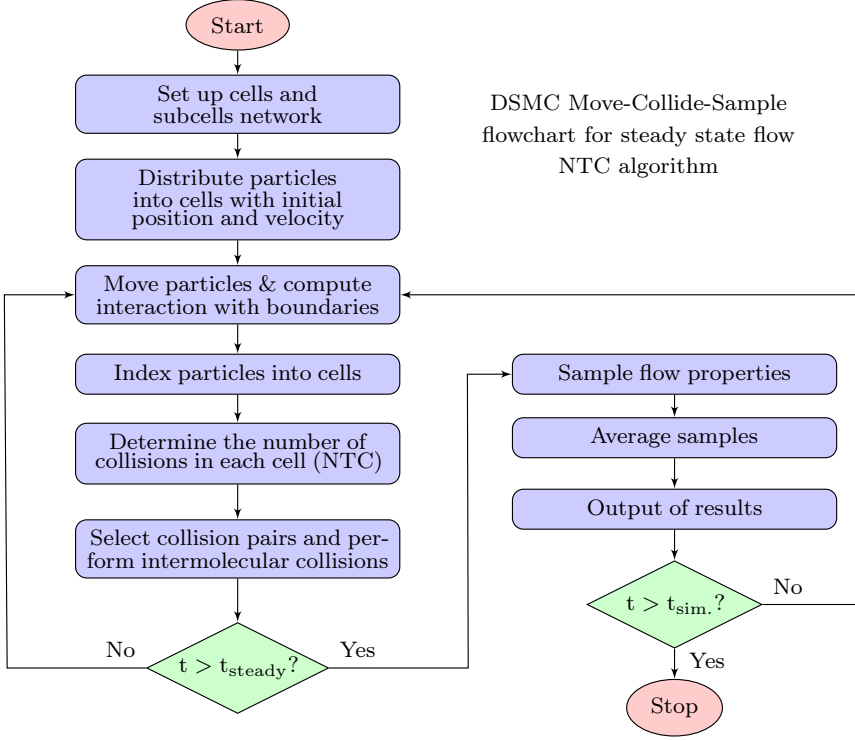


**Figure 2.2:** Typical DSMC simulation flowchart for the NTC algorithm and for steady state flow. The represented order of the operations, Move-Collide-Sample (MCS), is the classical one, but other options exist. For example, the Move-Sample-Collide (MSC), where the order of the collision and sample steps is inverted, and the Move-Sample-Collide-Sample (MSCS), where two sampling operations are performed in a single time step are two other possibilities. While the latter shows better performance in reducing the noise on the measurements of the higher order hydrodynamic moments, we still employ the MCS scheme. This, in fact, has shown to have the same accuracy for the lower order conserved moments (density, momentum, temperature) as guaranteed by the MSCS scheme, [43], while requiring less computational effort. In the graph,  $t_{steady}$  represents the estimated transient time characterizing the studied flow. Flow properties are sampled only after this phase is complete. The simulation continues until a predetermined number of time steps is performed so that the cumulated time reaches the final simulation time,  $t_{sim}$ . In case the flow does not possess a final steady state, or the transient phase before reaching the final state is of interest, the averaging over time is not performed. To reduce the statistical noise, instead, an ensemble average among independent DSMC simulations may be performed.

collision process model in the sense that only those particles located in the same subcell are allowed to interact. The distinction between cells and subcells stems mainly from a computational cost consideration. In fact, in order to correctly reproduce the transport of momentum and energy due to collisions, the collisional subcell size,  $\Delta x$ , should be at most comparable in size to the microscopic molecu-

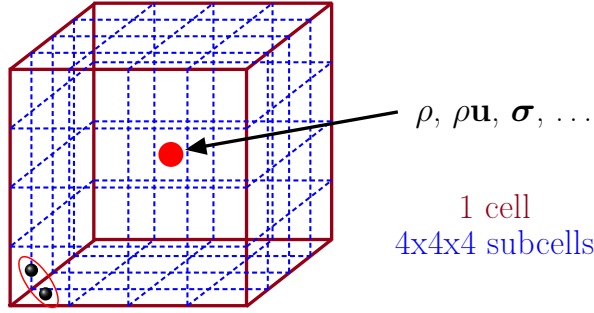


**Figure 2.3:** Schematic representation of a sampling cell comprising  $4 \times 4 \times 4$  collisional subcells. Only particles residing in the same subcell are allowed to interact. It is also a common practice to assign the values of the hydrodynamic moments, e.g. the density  $\rho$ , the momentum  $\rho \mathbf{u}$ , the shear stress  $\boldsymbol{\sigma}$ , evaluated by sampling the molecular information within a sampling cell, to the center of such cell, represented here by the red dot. This way to discretize the flow domain allows to reduce the required computational effort, but at the cost of a reduced resolution.

lar scale, i.e.  $\Delta x \sim \lambda$ , where  $\lambda$  is the molecular mean free path. One of the rules of thumb typically employed in DSMC simulations, actually, prescribes for the collisional cell that  $\Delta x \leq \lambda/3$ , [1]. However, in order to get a less computationally expensive simulation, it is customary to relax such requirement when dealing with the definition of the sampling cell network.

Fig. 2.3 shows a sketch of a typical sampling cell which comprises  $4 \times 4 \times 4$  collisional subcells. The following example further illustrates this aspect. Consider that a gas composed of Argon atoms occupies a square box of size  $L=1$  mm at a pressure  $p=10^3$  Pa and at a temperature  $T=273$  K. According to the Hard Sphere (HS) model, the mean free path is about  $\lambda=6.3 \mu\text{m}$ , and, based on the prescribed rule of thumb,  $\Delta x=2.1 \mu\text{m}$ . Hence, to fully discretize the domain, at least  $1.1 \cdot 10^8$  cells should be employed. However, if the decoupling between the collisional and sampling cells is applied, and, a  $4 \times 4 \times 4$  collisional subcell per each sampling cell is adopted,  $1.7 \cdot 10^6$  sampling cells can be used. Clearly, this option allows to reduce the computational cost at the expense of the flow field resolution which will be inevitably lower.

Once the grid has been defined according to the above consideration, the cells can be populated with the particles. This step involves to assign to each particle a random initial position within a cell and to sample the three velocity components from a probability distribution function (pdf) taking into account the local flow properties. Several possible pdfs can be used at this aim. The most commonly used is the Maxwell Boltzmann (MB) distribution,  $f(\boldsymbol{\xi}, \{\mathbf{u}, T\})$ . However, this is not the only option. As we will see in chapter 4, in the algorithm of the hybrid LBM-DSMC method, the velocity of the particles generated in the buffer layer

is sampled from a Grad distribution,  $f(\boldsymbol{\xi}, \{\mathbf{u}, T, \mathbf{P}, \mathbf{Q}\})$ , which takes into account also the information related to the local shear stress tensor,  $\mathbf{P}$ , and heat flux,  $\mathbf{Q}$ . In other hybrid methods not dealing with the LBM, instead, a Chapman-Enskog distribution truncated at first order,  $f(\boldsymbol{\xi}, \{\mathbf{u}, T, \nabla\mathbf{u}, \nabla T\})$ , where  $\nabla\mathbf{u}$  and  $\nabla T$  represent the flow velocity and temperature gradients, is generally employed when generating particles in the buffer layer at the boundary between the coupled methods, [44].

It has still to be decided how many particles will be generated. Again both numerics and physics can help in suggesting a rule of thumb. In most of the simulations, in fact, about 20 particles per sampling cell are thought to be sufficient so to reduce the risk of repeated collisions between the same particles and to reduce the noise present in the measurement of the hydrodynamic moments. Related to this last aspect, it should be emphasized that the presence of noise on the hydrodynamic moments is not an artefact of the numerical method, but it is strictly related to the stochastic nature of DSMC when dealing with the collision step and the interaction with boundaries. If the simulation aims at the mean flow properties, the noise can then be reduced through averaging (time averaging if the steady state solution is sought or ensemble averaging if the transient behavior is studied). Moreover, it has been demonstrated, [45], that the fluctuations present on the conserved hydrodynamic moments are correctly reproduced by the DSMC as they show the same behavior as predicted by the equilibrium statistical mechanics theory, [46]. In relation to this, in appendix A, we show some validation results obtained using the in-house developed DSMC code.

As already mentioned, each DSMC particle represents a large number of real molecules. But how many? Going back to the example used before to set up the grid, each sampling cell has a volume equal to about  $9.3 \cdot 10^{-18} \text{ m}^3$  and would contain  $2.5 \cdot 10^6$  real Argon atoms. It is then trivial to see that, if 20 particles per cell are used, each DSMC particle represents about  $1.25 \cdot 10^5$  real Argon atoms, and, therefore, still a very large number.

### Streaming step

At this stage, it is possible to enter inside the time loop during which the sequence of streaming and collision steps is performed. The pre- and post-streaming configurations of the particles within the domain are shown in Fig. 2.4. During the streaming phase, the particles' positions are updated according to their velocity and the imposed time step. If external forces are not present, it is possible to integrate the equation of motion via the Euler method:

$$\mathbf{x}_i(t + \Delta t) = \mathbf{x}_i(t) + \boldsymbol{\xi}_i \Delta t. \quad (2.4)$$

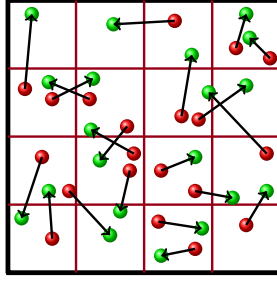


**Figure 2.4:** *Particles configuration before (red dots) and after the streaming step (green dots). Particles are free to stream along any direction with any speed.*

The duration of the imposed time step  $\Delta t$  is closely related to the space discretization  $\Delta x$ . In fact, to minimize inaccuracies in the collisional transport,  $\Delta t \sim t_{coll} = \lambda/v$ , where  $v$  is a typical microscopic velocity such as the most probable velocity:  $v = v_{mp} = (2k_B T/m)^{1/2}$ . Usually a stricter condition is applied as it is imposed that the time step is smaller than the residence time for a particle in a cell. Therefore:

$$\Delta t < t_{res} = \frac{\Delta x}{(v_{mp} + U_f)} \quad (2.5)$$

where  $U_f$  is the estimated flow velocity. The typical time step duration, then, is set as  $\Delta t = t_{res}/4$ . In this way, it is very probable that a particle will at most move only to a nearest neighbor cell during one time step, thus reducing possible errors related to an excessive collisional transport.

## Boundary interactions

During the time step, the interactions with solid boundaries are also performed. In this thesis, we will mainly apply two models, or a proper combination of them, to deal with interactions between particles and walls: the specular and the diffuse wall models. The main idea of such models is to mimic real gas-surface interactions using simplified mechanisms. In Fig. 2.5, the sketches graphically representing such models are depicted. To be noted that other more complex interactions are available in literature, such as the Cercignani-Lampis-Lord (CLL) model, [47, 48], which provides a good interaction model when thermal effects play an important role.

The first step, common to both boundary conditions, requires to evaluate the residual time step,  $\Delta t^*$ , that the particle will stream once it is re-emitted from the wall, and the position where the particle hit the wall. The knowledge of the position at which the particle-wall interaction occurs is a valuable information

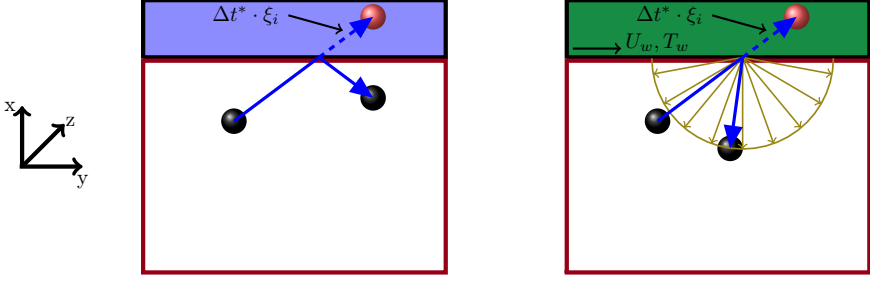


**Figure 2.5:** Representation of the gas-surface interactions for a flat wall: specular (left) and diffuse (right) models. The diffuse model assumes that, as soon as the particle hits the wall, it reaches the equilibrium with the wall conditions.  $\Delta t^*$  is the residual time step that the particle has still to stream after the interaction with the wall occurs and  $\xi_i$  is the particle velocity component along the direction normal to wall against which the interaction takes place.  $U_w$  and  $T_w$  are the velocity and temperature of the wall, respectively. The yellow semi-circle graphically represents the fact that, for the diffuse wall case, there is an equal probability of reflection in any direction. A combination of these two models is also commonly employed to better reproduce the characteristics of realistic solid surfaces.

when computing surface-based higher order moments such as the shear stress or the heat flux at the walls. The specular wall model, implicitly assuming that the surface is perfectly smooth, prescribes that, once a particle hits a wall, the velocity component normal to the wall is reverted while the other two components are unchanged. The diffuse wall model, instead, assuming a microscopically rough surface, prescribes that the post-interaction velocity components are sampled from a biased Maxwellian distribution in the frame of reference of the wall. For the sketch of Fig. 2.5, right panel, such distributions have the following form:

$$P_{\xi_x}(\xi_x) = -\frac{m}{k_B T_w} \xi_x \exp\left(-\frac{m \xi_x^2}{2k_B T_w}\right), \quad (2.6)$$

$$P_{\xi_y}(\xi_y) = \sqrt{\frac{m}{2\pi k_B T_w}} \exp\left(-\frac{m(\xi_y - U_w)^2}{2k_B T_w}\right), \quad (2.7)$$

$$P_{\xi_z}(\xi_z) = \sqrt{\frac{m}{2\pi k_B T_w}} \exp\left(-\frac{m \xi_z^2}{2k_B T_w}\right), \quad (2.8)$$

where  $T_w$  and  $U_w$  are the wall temperature and translational velocity. These relations also assume that there is an equal probability of reflection in any direction. Once the particle velocity components are re-computed according to the wall conditions, it will stream for the residual time step,  $\Delta t^*$ .

The treatment of the open boundaries (more specifically imposed pressure and mass flow rate boundary conditions) will be described in chapter 3 of this thesis.



## Sorting and indexing particles

Once the particles have completed the streaming process and the boundary conditions have been applied, they are sorted and indexed into the cell and subcell networks. This is required for two reasons:

1. The particles are sorted into the collisional subcells since the intermolecular collisions are performed only between particles in the same subcell.
2. The particles are sorted into the sampling cells since the macroscopic fields are computed evaluating the properties of particles residing in the same sampling cell

## Collision step

At this stage, collisions between particles within the same collisional subcell can be performed. Again, many different models are available in literature. All models have in common the same approach: explicit intermolecular forces are replaced with stochastic collisions. The simplest model is the so-called Hard Sphere (HS) model for which fully elastic interactions between two particles are assumed to occur. The aim of this step is to determine the post-collision velocities  $\xi_1^*$  and  $\xi_2^*$  satisfying the detailed balance of momentum and energy, see e.g. Fig. 2.6 for a graphical representation of the pre- and post-collision particle velocity. The conservation of momentum, in fact, imposes three constraints in the form:

$$m_1 \xi_1 + m_2 \xi_2 = m_1 \xi_1^* + m_2 \xi_2^* = (m_1 + m_2) \xi_{cm}, \quad (2.9)$$

while the conservation of energy imposes a further constraint:

$$m_1 \xi_1^2 + m_2 \xi_2^2 = m_1 \xi_1^{*2} + m_2 \xi_2^{*2}. \quad (2.10)$$

Moreover, the magnitude of the relative velocity should remain unchanged:

$$|\xi_r| = |\xi_1 - \xi_2| = |\xi_r^*| = |\xi_1^* - \xi_2^*|. \quad (2.11)$$

In order to fully define the post-collision relative velocity  $\xi_r^*$ , the collision solid angle has to be properly set. For the HS model, the scattering is isotropic in the center of mass frame of reference, i.e. all the directions for  $\xi_r^*$  are equally probable. Therefore, we can express  $\xi_r^*$  as:

$$\xi_r^* = |\xi_r| [(\sin \chi \cos \phi) \hat{\mathbf{x}} + (\sin \chi \sin \phi) \hat{\mathbf{y}} + \cos \chi \hat{\mathbf{z}}], \quad (2.12)$$

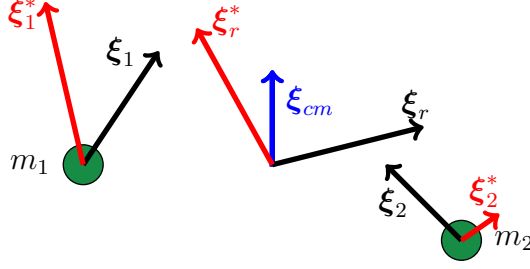


**Figure 2.6:** Sketch representing the pre-collision,  $\xi_1$ ,  $\xi_2$ , and post-collision,  $\xi_1^*$ ,  $\xi_2^*$ , particles velocities. The velocity of the center of mass,  $\xi_{cm}$ , expressed by Eq. (2.9), as well as the pre- and post-collision relative velocities,  $\xi_r$ ,  $\xi_r^*$ , which obey the constraint given by Eq. (2.11), are also indicated. According to the kinematic relations for elastic collisions and to the stochastic model employed to mimic the real intermolecular forces, it is possible to calculate the post-collision velocities employing the relations in Eqs. (2.12) and (2.13). Note that in DSMC, it is not required that the two particles touch in order to have a collisional event. To draw the sketch, two particles of equal mass have been considered.

where the azimuthal angle  $\phi$  is uniformly distributed between 0 and  $2\pi$  while the distribution for the elevation angle  $\chi$  is of the form:

$$P_\chi(\chi) d\chi = \frac{1}{2} \sin \chi d\chi.$$

Once the angles have been sampled, the post-collision velocities can be set:

$$\xi_1^* = \xi_{cm} + \left( \frac{m_2}{m_1 + m_2} \right) \xi_r^*, \quad \xi_2^* = \xi_{cm} - \left( \frac{m_1}{m_1 + m_2} \right) \xi_r^*. \quad (2.13)$$

Once the mechanics of collisions is defined according to the chosen interparticle potential, the total number of collisions to be performed among the particles residing within the same collisional cell has to be determined. To do this, as mentioned before in this section, we make use of the NTC algorithm. For such model, we pre-determine, according to the collisional subcell conditions, the number of attempted collisions as:

$$M_{cand} = \frac{1}{2} \frac{N(N-1)}{\Delta V} (\sigma_T \xi_r)_{max} \Delta t, \quad (2.14)$$

where  $\sigma_T$  is the collision cross-section ( $\sigma_T = \pi d^2$  for HS where  $d$  is the molecular diameter),  $N$  is the instantaneous number of particles in the subcell and  $\Delta V$  is the subcell volume. An attempted collision between two randomly selected partners

is then accepted with probability:

$$P(\boldsymbol{\xi}_1, \boldsymbol{\xi}_2) = \frac{\sigma_T \xi_r}{(\sigma_T \xi_r)_{max}}. \quad (2.15)$$

The denominator of Eq. (2.15) represents the maximum of the product of the relative velocity and the collision cross-section and it is a collisional subcell-based quantity continuously updated. Moreover, Eq. (2.15) also expresses the fact that pairs with larger relative velocity are more probable to collide.

It should be realized that one important consequence of such HS model is that the resulting computational gas presents macroscopic transport coefficients, such as the dynamic viscosity,  $\mu$ , which are function of the temperature as  $T^\alpha$  with  $\alpha = 1/2$ . However, experimentally, it is known that  $\alpha$  is different from  $1/2$  and generally it is close to  $3/4$ . It is possible to recover such dependency by changing the collision mechanism: if the diameter of the molecules, and therefore the collision cross-section, is expressed as an inverse power law function of the relative velocity as:

$$d = d_{ref} \left( \frac{\xi_{r,ref}}{\xi_r} \right)^\alpha \quad (2.16)$$

then, macroscopically, one recovers the following relation for the gas dynamic viscosity:

$$\mu = \mu_{ref} \left( \frac{T}{T_{ref}} \right)^\alpha \quad (2.17)$$

where  $\mu_{ref}$  is the dynamic viscosity at the reference temperature  $T_{ref}$ . It has to be noted that the value of  $\alpha$  in Eqs.(2.16) and (2.17) is the same, [1]. This modified version of the Hard Sphere model is named Variable Hard Sphere (VHS) model. As already mentioned, other models are also available such as the Variable Soft Sphere (VSS) model, the Maxwell model, the Generalized Hard Sphere (GHS) model. In [1], details on these models can be found.

### Sampling and averaging flow properties

According to the Move-Collide-Sample (MCS) scheme, after the streaming and collision steps, the flow macroscopic properties are evaluated. Such measurements are performed by statistical sampling since the DSMC always provides a fluctuating flow field. If volume-averaged measurements are employed, as done in our code, then the average moments can be evaluated as:

$$\langle \gamma(\boldsymbol{\xi}) \rangle = \frac{1}{S} \sum_{s=1}^S \frac{1}{\Delta V} \sum_{i=1}^{N(s,t)} \gamma(\boldsymbol{\xi}_i(t)), \quad (2.18)$$

where  $S$  is the number of acquired samples,  $N(t)$  is the number of particles residing in the sampling cell and  $\gamma$  is a generic microscopic property. Using the relation of Eq. (2.18), the standard hydrodynamic moments are evaluated as:

$$\rho = \langle m \rangle, \quad (2.19)$$

$$\mathbf{u} = \langle m \boldsymbol{\xi} \rangle / \rho, \quad (2.20)$$

$$T = \frac{2m}{3k\rho} \left( \frac{1}{2} \langle m \xi^2 \rangle - \frac{1}{2} \rho u^2 \right), \quad (2.21)$$

$$\sigma_{\alpha\beta} = \langle m (\boldsymbol{\xi}_\alpha - \mathbf{u}_\alpha) (\boldsymbol{\xi}_\beta - \mathbf{u}_\beta) \rangle. \quad (2.22)$$

It is now natural to ask: How many samples should be taken so to reduce the noise on the measurements of the moments to an acceptable level?

To evaluate such number, one can take into account the fact that the fluctuations present on the instantaneous value of the measured moments follow the equilibrium statistical mechanics theory (for the conserved quantities). So, for example, considering one of the flow velocity components,  $u_i$ , it is possible to evaluate a fractional error as, [45]:

$$E_{u_i} = \frac{\sigma_{u_i}}{|u_i|} = \frac{\sqrt{\langle \delta u_i^2 \rangle}}{\sqrt{S} |u_i|} \approx \frac{1}{\sqrt{SN}} \frac{1}{\text{Ma}} \quad (2.23)$$

where  $\text{Ma} = u_i / c_s$  is the Mach number and  $c_s = \sqrt{\gamma R T}$  is the speed of sound of the gas, with  $\gamma = c_p / c_v$  the specific heat ratio and  $R$  the ideal gas constant. From such relation, it is clear why the classical DSMC is computationally expensive for low-speed flows. In fact, if a 1% fractional error is desired and 20 particles per cell are used, then  $S = 500$  if  $\text{Ma} = 1$ , a value typical of aerospace applications, while  $S = 5 \cdot 10^8$  if  $\text{Ma} = 0.001$ , a value typical of microscale flows.

In addition to this consideration, one should also take into account that two successive samples should be temporally uncorrelated. This is generally done performing the sampling operation with a prescribed frequency and not at each time step. Typical frequencies might be one sampling operation every 10 time steps. The just mentioned criterion, that is achieving a prescribed level of statistical accuracy on the measurement of the flow properties, could be used to define a convergence condition to decide when to stop the simulation. The computation will continue performing the sequence of steps just described until a sufficiently large number of samples, and, therefore, a sufficiently low statistical noise on the measured quantities, is achieved.

It should be noted that, recently, in literature, several attempts to improve the convergence properties of DSMC for low speed flows have appeared. In particular,

the low-variance deviational method has been proposed in [49, 50], while the DSMC-IP (Information Preservation) has been proposed in [51]. They could represent a useful extension of the hybrid LBM-DSMC method presented in this work as the (very) low speed flows could be simulated more efficiently.

To conclude, historically, the DSMC aim was to consistently and accurately mimick the physical phenomena connected to the gas molecular transport rather than to solve an underlying mathematical model. However, as a remark which justifies the validity of the method also from a theoretical point of view, it should be mentioned that, under the conditions of a large number of particles per cell and for sufficiently small time and space discretizations, the DSMC method provides a solution which is equivalent to the one given by the Boltzmann equation, as demonstrated in [52].

## 2.3 Basics of the LBM method

While we presented in a rather phenomenological way the basics of the DSMC method implemented in our code, we now introduce the basics of the LBM in a more rigorous and mathematically consistent way. Following this approach, it is possible to systematically derive higher-order approximations to the continuum BE so that the resulting macroscopic moments equations, at each level of discretization, give rise to the Navier-Stokes hydrodynamics and to those representations beyond it, [37]. It has to be noted that the treatment which we report here is based on a series of papers, published in the last 20 years, which are at the basis of the mathematical foundations of the LBM, [37, 53, 54]. This approach to consistently derive a LBM model, in turn based on Grad's method, [21], to represent the single particle probability distribution function, and on Gauss-Hermite quadratures to evaluate the coefficients of such expansion, is not the only one. For example, the entropic LBM formulation, as proposed by Karlin and co-workers, [55–57], has recently proven its validity as an alternative approach. However, for the purpose of the hybrid LBM-DSMC, the formulation proposed here is the one which guarantees a consistent derivation of the coupling algorithms between the two methods and, therefore, it is the chosen one. Such treatment, moreover, allows to demonstrate that, despite the extreme reduction in the degrees of freedom of the microscopic velocity space, the resulting system of equations provides a correct fluid dynamic description avoiding drawbacks typical of the conventional higher-order hydrodynamic formulations.

To illustrate the derivation of the Lattice Boltzmann Equation model based on Grad's method to expand the single particle distribution function and on Gauss-Hermite quadratures to evaluate the coefficients of the expansion, we start from

the BE which is given by:

$$\frac{\partial f}{\partial t} + \boldsymbol{\xi} \cdot \nabla_{\mathbf{x}} f + \mathbf{F} \cdot \nabla_{\boldsymbol{\xi}} f = Q, \quad (2.24)$$

where  $\mathbf{F}$  is the force field and the right hand side, the so-called collision operator, represents the effect of intermolecular collisions. In Eq. (2.24), the dependency of the distribution function  $f$  from the position,  $\mathbf{x}$ , microscopic velocity,  $\boldsymbol{\xi}$ , and time,  $t$ , has been dropped for ease of notation. The expression of the collision term,  $Q$ , is a complicated integral and even introducing the Boltzmann ansatz of molecular chaos and neglecting multi-body collisions, it is still very complex to handle as it can be seen inspecting the following relation:

$$Q = \int (f' f'^1 - f f^1) g \sigma(g, \Omega) d\Omega d\boldsymbol{\xi}. \quad (2.25)$$

In Eq. (2.25),  $f'$  and  $f'^1$  represent the post-collision distribution function (for the two-body collisions) while  $f$  and  $f^1$  represent the pre-collision ones;  $g$  is the relative speed between two particles,  $\sigma$  is the collision cross-section and  $\Omega$  is the collision solid angle.

Due to the complexity of the collision term, it is therefore customary in LBM to apply the so-called BGK model, [58], which prescribes to replace such collision mechanism with a relaxation process towards a local equilibrium. In essence, because of the collisions, the BGK model assumes that the distribution function will tend to the local Maxwell-Boltzmann equilibrium distribution function given by:

$$f^{eq} = \frac{\rho}{(2\pi T)^{D/2}} \exp\left(-\frac{(\boldsymbol{\xi} - \mathbf{u})^2}{2T}\right) \quad (2.26)$$

and, therefore, the term  $f' f'^1$  in Eq. (2.25) may be replaced by  $f'^{eq} f'^{eq,1} = f^{eq} f^{eq,1}$ , where the last equality holds because of the equilibrium condition (i.e. any direct/inverse collision is balance by another inverse/direct collision). Under these assumptions, it is possible to re-write the integral in Eq. (2.25) as:

$$Q = f^{eq} \int f^{eq,1} g \sigma(g, \Omega) d\Omega d\boldsymbol{\xi} - f \int f^1 g \sigma(g, \Omega) d\Omega d\boldsymbol{\xi} \quad (2.27)$$

Finally, if the difference between the two integrals in Eq. (2.27) may be neglected, the BGK collision term becomes:

$$Q = -\frac{1}{\tau} [f - f^{eq}], \quad (2.28)$$

where  $\tau$  is the so-called relaxation time which incorporates information about the collision frequency, and it is directly used to determine the gas transport coefficients.

The classical BGK model is characterized by a single relaxation time, and, indeed, it represents the standard formulation employed in LBM. This, however, has as consequence the fact that all the gas diffusivities have the same numerical value, see e.g. [25] for a demonstration of this feature of the BGK model. To overcome such limitation, more sophisticated collision kernels, such as the Multi Relaxation Time (MRT) model appeared in literature, [59, 60]. However, since here we are interested in isothermal single phase gas flow applications, and, therefore, the only relevant diffusivity is the kinematic viscosity, we will nonetheless employ the Single Relaxation Time (SRT) BGK model. The solution of the BE, either in its original formulation, Eq. (2.24), or under the BGK approximation, where the collisional term is expressed by Eq. (2.28), allows to calculate the conventional hydrodynamic variables as:

$$\rho = mn(\mathbf{x}, t) = m \int f d\boldsymbol{\xi} = m \int f^{eq} d\boldsymbol{\xi}, \quad (2.29a)$$

$$\rho \mathbf{u}(\mathbf{x}, t) = m \int f \boldsymbol{\xi} d\boldsymbol{\xi} = m \int f^{eq} \boldsymbol{\xi} d\boldsymbol{\xi}, \quad (2.29b)$$

$$\rho e(\mathbf{x}, t) = \frac{1}{2} m \int f |\boldsymbol{\xi} - \mathbf{u}|^2 d\boldsymbol{\xi} = \frac{1}{2} m \int f^{eq} |\boldsymbol{\xi} - \mathbf{u}|^2 d\boldsymbol{\xi}, \quad (2.29c)$$

$$\mathbf{P}(\mathbf{x}, t) = m \int f \mathbf{c} \mathbf{c} d\mathbf{c}, \quad (2.29d)$$

$$\mathbf{Q}(\mathbf{x}, t) = m \int f \mathbf{c} \mathbf{c} \mathbf{c} d\mathbf{c}, \quad (2.29e)$$

where the integrals are intended to extend over  $\mathbb{R}^3$ , and  $\mathbf{c} = \boldsymbol{\xi} - \mathbf{u}$  is the intrinsic velocity. Note that the first three relations of Eqs. (2.29) involve the moments corresponding to the conservation laws of mass, momentum and energy,  $e$ , while the last two express, respectively, the momentum flux tensor, in turn connected to the shear stress tensor, and the third order momentum flux tensor, in turn connected to the heat flux vector.

### Grad's expansion method

Given the system of equations (2.24, 2.26, 2.29), we look for solutions by expanding the single particle distribution function  $f(\mathbf{x}, \boldsymbol{\xi}, t)$  in Hermite polynomials, as originally proposed by Grad in [21].

A unique feature which justifies the use of Hermite polynomials as expansion

basis is that the expansion coefficients correspond to the moments — or a proper combination of those — of the distribution up to the given degree, [21]. In terms of the dimensionless Hermite orthonormal polynomials in the velocity space  $\boldsymbol{\xi}$ , one can express the single particle distribution function as:

$$f(\mathbf{x}, \boldsymbol{\xi}, t) = \omega(\boldsymbol{\xi}) \sum_{n=0}^{\infty} \frac{1}{n!} \mathbf{a}^{(n)}(\mathbf{x}, t) \mathcal{H}^{(n)}(\boldsymbol{\xi}), \quad (2.30)$$

where  $\omega(\boldsymbol{\xi})$  is the weight function associated with the Hermite polynomials:

$$\omega(\boldsymbol{\xi}) = \frac{1}{(2\pi)^{D/2}} \exp(-\boldsymbol{\xi} \cdot \boldsymbol{\xi}/2), \quad (2.31)$$

$\mathbf{a}^{(n)}(\mathbf{x}, t)$  and  $\mathcal{H}^{(n)}(\boldsymbol{\xi})$  are the  $n$ -th rank symmetric expansion coefficients and Hermite polynomial tensors, respectively. The first Hermite polynomials are given by:

$$\begin{aligned} \mathcal{H}^{(0)}(\boldsymbol{\xi}) &= 1, \\ \mathcal{H}_i^{(1)}(\boldsymbol{\xi}) &= \xi_i, \\ \mathcal{H}_{ij}^{(2)}(\boldsymbol{\xi}) &= \xi_i \xi_j - \delta_{ij}, \\ \mathcal{H}_{ijk}^{(3)}(\boldsymbol{\xi}) &= \xi_i \xi_j \xi_k - \xi_i \delta_{jk} - \xi_j \delta_{ik} - \xi_k \delta_{ij}, \end{aligned} \quad (2.32)$$

where  $\delta_{ij}$  is the identity tensor. Additional details about the properties of Hermite polynomials are reported in Appendix 4.B.

By definition, the expansion coefficients are given by:

$$\mathbf{a}^{(n)}(\mathbf{x}, t) = \int f(\mathbf{x}, \boldsymbol{\xi}, t) \mathcal{H}^{(n)}(\boldsymbol{\xi}) d\boldsymbol{\xi}. \quad (2.33)$$

By inserting into Eq. (2.33), the expressions for the Hermite polynomials provided in Eq. (2.32), it can be seen that the coefficients correspond to the usual hydrodynamic variables:

$$\begin{aligned} \mathbf{a}^{(0)} &= \int f d\boldsymbol{\xi} = \rho, \\ \mathbf{a}^{(1)} &= \int f \boldsymbol{\xi} d\boldsymbol{\xi} = \rho \mathbf{u}, \\ \mathbf{a}^{(2)} &= \int f (\boldsymbol{\xi}^2 - \delta) d\boldsymbol{\xi} = \mathbf{P} + \rho(\mathbf{u}^2 - \delta), \\ \mathbf{a}^{(3)} &= \int f (\boldsymbol{\xi}^3 - \boldsymbol{\xi} \delta) d\boldsymbol{\xi} = \mathbf{Q} + \mathbf{u} \mathbf{a}^{(2)} - (D-1) \rho \mathbf{u}^3, \end{aligned} \quad (2.34)$$



where represents the dimensionality of the problem.

It is also possible to express the hydrodynamic variables in terms of the expansion coefficients:

$$\begin{aligned}\rho &= \mathbf{a}^{(0)}, \\ \rho \mathbf{u} &= \mathbf{a}^{(1)}, \\ \rho e &= \frac{1}{2} \left[ a_{ii}^{(2)} - \rho(u^2 - D) \right], \\ \mathbf{P} &= \mathbf{a}^{(2)} - \rho(\mathbf{u}^2 - \boldsymbol{\delta}), \\ \mathbf{Q} &= \mathbf{a}^{(3)} - \mathbf{u}\mathbf{a}^{(2)} + (D-1)\rho\mathbf{u}^3,\end{aligned}\tag{2.35}$$

where, in the relation for the energy variable,  $\rho e$ , the summation over the repeated indices is intended.

From the above considerations, it is evident that if we are able to compute the coefficients of the expansion, we essentially have a complete knowledge of the flow field at the desired level of accuracy through the knowledge of  $f(\mathbf{x}, \boldsymbol{\xi}, t)$ . Before defining a way to compute such coefficients, we can notice that due to the mutual orthonormality of Hermite polynomials, the leading moments of  $f(\mathbf{x}, \boldsymbol{\xi}, t)$  up to the  $N$ -th order are preserved by truncations of the higher-order terms in the Hermite expansion of  $f(\mathbf{x}, \boldsymbol{\xi}, t)$ . Therefore, we can approximate  $f(\mathbf{x}, \boldsymbol{\xi}, t)$  by its projection onto the subspace spanned by the first  $N$  leading Hermite polynomials without affecting the first  $N$  moments:

$$f(\mathbf{x}, \boldsymbol{\xi}, t) \approx f^N(\mathbf{x}, \boldsymbol{\xi}, t) = \omega(\boldsymbol{\xi}) \sum_{n=0}^N \frac{1}{n!} \mathbf{a}^{(n)}(\mathbf{x}, t) \mathcal{H}^{(n)}(\boldsymbol{\xi}). \tag{2.36}$$

Here, up to  $N$ -th order,  $f^N(\mathbf{x}, \boldsymbol{\xi}, t)$  has the same velocity moments as the original  $f(\mathbf{x}, \boldsymbol{\xi}, t)$ . This has as an important consequence the fact that a fluid-dynamic system can be fully constructed by using only a finite set of macroscopic variables, i.e. the hydrodynamic moments.

The next step in the construction of the LBM is to recognize that the truncated distribution function of Eq. (2.36), or, equivalently its expansion coefficients, can be completely and uniquely determined by its values at a set of discrete values of the microscopic velocity  $\boldsymbol{\xi}$ , [37].

This is valid because using the truncated series  $f^N$  into Eq. (2.33), the integrand function can be written as:

$$f^N(\mathbf{x}, \boldsymbol{\xi}, t) \mathcal{H}^{(n)}(\boldsymbol{\xi}) = \omega(\boldsymbol{\xi}) p(\mathbf{x}, \boldsymbol{\xi}, t) \tag{2.37}$$

where  $p(\mathbf{x}, \boldsymbol{\xi}, t)$  is a polynomial of degree  $\leq 2N$  in  $\boldsymbol{\xi}$ . Applying the Gauss-Hermite quadrature, the coefficients  $\mathbf{a}^{(n)}$ , in fact, can be precisely expressed as a weighted sum of the functional values of  $p(\mathbf{x}, \boldsymbol{\xi}, t)$ :

$$\mathbf{a}^{(n)} = \int \omega(\boldsymbol{\xi}) p(\mathbf{x}, \boldsymbol{\xi}, t) d\boldsymbol{\xi} = \sum_{a=1}^q w_a p(\mathbf{x}, \boldsymbol{\xi}_a, t) = \sum_{a=1}^q \frac{w_a}{\omega(\boldsymbol{\xi})} f^N(\mathbf{x}, \boldsymbol{\xi}_a, t) \mathcal{H}^{(n)}(\boldsymbol{\xi}) \quad (2.38)$$

where  $w_a$  and  $\boldsymbol{\xi}_a$ ,  $a = 1, \dots, d$  are the weights and abscissae of a Gauss-Hermite quadrature of a degree  $\geq 2N$ . The set of discrete function values  $f^N(\mathbf{x}, \boldsymbol{\xi}_a, t)$  completely determines the coefficients of the truncated distribution and, therefore, its first  $N$  moments, once the values of the weights,  $w_a$ , and the location of the quadrature abscissae,  $\boldsymbol{\xi}_a$ , are known. The same procedure followed for the non-equilibrium distribution functions,  $f(\mathbf{x}, \boldsymbol{\xi}, t)$ , can be applied to the equilibrium distribution functions,  $f^{eq}(\mathbf{x}, \boldsymbol{\xi}, t)$ . In fact, we have that:

$$f^{eq}(\mathbf{x}, \boldsymbol{\xi}, t) \approx f^{eq,N}(\mathbf{x}, \boldsymbol{\xi}, t) = \omega(\boldsymbol{\xi}) \sum_{n=0}^N \frac{1}{n!} \mathbf{a}^{(eq,n)}(\mathbf{x}, t) \mathcal{H}^{(n)}(\boldsymbol{\xi}). \quad (2.39)$$

where

$$\begin{aligned} \mathbf{a}^{(eq,0)} &= \rho, \\ \mathbf{a}^{(eq,1)} &= \rho \mathbf{u}, \\ \mathbf{a}^{(eq,2)} &= \rho [\mathbf{u}^2 + (T-1)\boldsymbol{\delta}], \\ \mathbf{a}^{(eq,3)} &= \rho [\mathbf{u}^3 + (T-1)\boldsymbol{\delta} \mathbf{u}]. \end{aligned} \quad (2.40)$$

The explicit expression of the  $f^{eq}(\mathbf{x}, \boldsymbol{\xi}, t)$  is, therefore:

$$\begin{aligned} f^{eq}(\boldsymbol{\xi}) &= \omega(\boldsymbol{\xi}) \rho \left\{ 1 + \boldsymbol{\xi} \cdot \mathbf{u} + \frac{1}{2!} [(\boldsymbol{\xi} \cdot \mathbf{u})^2 - u^2 + (T-1)(\xi^2 - D)] \right. \\ &\quad \left. + \frac{\boldsymbol{\xi} \cdot \mathbf{u}}{3!} [(\boldsymbol{\xi} \cdot \mathbf{u})^2 - 3u^2 + 3(T-1)(\xi^2 - D - 2)] + \dots \right\} \end{aligned} \quad (2.41)$$

If an isothermal system is considered, and by setting  $T = 1$ , then Eq. (2.41) reduces to

$$f^{eq}(\boldsymbol{\xi}) = \omega(\boldsymbol{\xi}) \rho \left\{ 1 + \boldsymbol{\xi} \cdot \mathbf{u} + \frac{1}{2!} [(\boldsymbol{\xi} \cdot \mathbf{u})^2 - u^2] + \frac{\boldsymbol{\xi} \cdot \mathbf{u}}{3!} [(\boldsymbol{\xi} \cdot \mathbf{u})^2 - 3u^2] + \dots \right\}. \quad (2.42)$$

Note that imposing  $T = 1$  means that we are setting a uniform homogeneous temperature in the system.

If, for example, we truncate the expansion at the order  $N = 2$ , then Eq. (2.42) further reduces to

$$f^{eq}(\boldsymbol{\xi}) = \omega(\boldsymbol{\xi})\rho \left\{ 1 + \boldsymbol{\xi} \cdot \mathbf{u} + \frac{1}{2!} [(\boldsymbol{\xi} \cdot \mathbf{u})^2 - u^2] \right\}. \quad (2.43)$$

This expression, as it will be evident in the next sections, is at the basis of the standard formulation of the equilibrium distribution functions used in LBM.

Finally, the same projection procedure onto the Hermite polynomial subspace spanned by the first  $N$  polynomials can be applied to the forcing term:

$$F(\boldsymbol{\xi}) = \omega(\boldsymbol{\xi})\rho \left\{ \mathbf{F} \cdot \boldsymbol{\xi} + (\mathbf{F} \cdot \boldsymbol{\xi})(\mathbf{u} \cdot \boldsymbol{\xi}) - \mathbf{F} \cdot \mathbf{u} + \frac{1}{2\rho} \mathbf{a}^{(2)} [(\mathbf{F} \cdot \boldsymbol{\xi})\mathcal{H}^{(2)}(\boldsymbol{\xi}) - 2\mathbf{F}\boldsymbol{\xi}] + \dots \right\}, \quad (2.44)$$

where we have introduced the following definition  $F(\boldsymbol{\xi}) \equiv -\mathbf{F} \cdot \nabla_{\boldsymbol{\xi}} f$ .

Recalling Eq. (2.38), and the definitions of the moments of the (truncated) distribution function, we have:

$$\begin{aligned} \rho &= \sum_{a=1}^q \frac{w_a f^N(\boldsymbol{\xi}_a)}{\omega(\boldsymbol{\xi}_a)}, \\ \rho \mathbf{u} &= \sum_{a=1}^q \frac{w_a f^N(\boldsymbol{\xi}_a) \boldsymbol{\xi}_a}{\omega(\boldsymbol{\xi}_a)}, \\ \mathbf{P} + \rho \mathbf{u}^2 &= \sum_{a=1}^q \frac{w_a f^N(\boldsymbol{\xi}_a) \boldsymbol{\xi}_a \boldsymbol{\xi}_a}{\omega(\boldsymbol{\xi}_a)}, \\ \rho(DT + u^2) &= \sum_{a=1}^q \frac{w_a f^N(\boldsymbol{\xi}_a) \xi_a^2}{\omega(\boldsymbol{\xi}_a)}. \end{aligned} \quad (2.45)$$

Defining  $f_a(\mathbf{x}, t) = w_a f^N(\mathbf{x}, \boldsymbol{\xi}_a, t) / \omega(\boldsymbol{\xi}_a)$ , the above relations become:

$$\begin{aligned} \rho &= \sum_{a=1}^q f_a, \\ \rho \mathbf{u} &= \sum_{a=1}^q f_a \boldsymbol{\xi}_a, \\ \mathbf{P} + \rho \mathbf{u}^2 &= \sum_{a=1}^q f_a \boldsymbol{\xi}_a \boldsymbol{\xi}_a, \\ \rho(DT + u^2) &= \sum_{a=1}^q f_a \xi_a^2, \end{aligned} \quad (2.46)$$

where  $(\mathbf{x}, t)$  has been dropped for ease of notation. Eq. (2.46) represents the usual way to evaluate the hydrodynamic moments in any LBM code.

At this point, however, we still need to write the evolution equations for the  $f_a$ . By directly evaluating the BE, Eq. (2.24), at the Gauss-Hermite abscissae,  $\xi_a$ , it is possible to obtain a BE-like relation for each of the  $f_a$ :

$$\frac{\partial f_a}{\partial t} + \xi_a \cdot \nabla_{\mathbf{x}} f_a = -\frac{1}{\tau} [f_a - f_a^{eq}] + F_a \quad (a = 1, \dots, d) \quad (2.47)$$

where, on the right-hand side, we have:

$$\begin{aligned} f_a^{eq} \equiv \frac{w_a}{\omega(\xi_a)} f^{(0)}(\xi_a) = w_a \rho \left\{ 1 + \xi_a \cdot \mathbf{u} + \frac{1}{2!} [(\xi_a \cdot \mathbf{u})^2 - u^2 + (T-1)(\xi^2 - D)] \right. \\ \left. + \frac{\xi_a \cdot \mathbf{u}}{3!} [(\xi_a \cdot \mathbf{u})^2 - 3u^2 + 3(T-1)(\xi^2 - D - 2)] + \dots \right\} \end{aligned} \quad (2.48)$$

and

$$\begin{aligned} F_a \equiv \frac{w_a}{\omega(\xi_a)} F(\xi_a) = w_a \rho \{ \mathbf{F} \cdot \xi_a + (\mathbf{F} \cdot \xi_a)(\mathbf{u} \cdot \xi_a) - \mathbf{F} \cdot \mathbf{u} \\ + \frac{1}{2\rho} \mathbf{a}^{(2)} [(\mathbf{F} \cdot \xi_a) \mathcal{H}^{(2)}(\xi_a) - 2\mathbf{F} \xi_a] + \dots \} \end{aligned} \quad (2.49)$$

If we assume an isothermal system and we truncate the series at the second order, then Eq. (2.48) assumes the form:

$$f_a^{eq} \equiv \frac{w_a}{\omega(\xi_a)} f^{eq}(\xi_a) = w_a \rho \left\{ 1 + \xi_a \cdot \mathbf{u} + \frac{1}{2!} [(\xi_a \cdot \mathbf{u})^2 - u^2] \right\} \quad (2.50)$$

Eq. (2.50) has the same form as the discrete equilibrium distribution functions if the classical derivation is used, i.e. the Taylor expansion around zero fluid velocity,  $\mathbf{u} = 0$ , up to the second order of the exponential form of the MB distribution, Eq. (2.26), see e.g. [24, 25]. In the derivation presented here, however, it is obtained following a completely different route. The result obtained with the present formulation, in fact, corresponds to a defined order of accuracy for the macroscopic moments. Moreover, approximations higher than the second-order can be systematically constructed with the present approach without a posteriori matching intended macroscopic dynamics.

In summary, Eqs.(2.46)-(2.49) form a closed set of differential equations governing the set of variables  $f_a(\mathbf{x}, t)$  in the configuration space.

### **Accuracy determination: matching Hermite and Chapman-Enskog expansions**

Closely related to the previous steps, a natural question which might arise at this point is: At what order  $N$  should the series in Eq. (2.36) be truncated?

To answer such question, it should be noted that the accuracy and range of validity in the resulting macroscopic hydrodynamic behavior are indeed strictly related to the order of truncation, and each level of truncation represents a well-defined approximation to the BGK-BE. It is intuitively clear that the level of accuracy is increased if higher-order terms in the truncated expansion are retained and if quadratures of sufficient algebraic precision are employed. However, it is important to determine an estimate about the ability of different levels of truncation to recover macroscopic physical effects associated with different level of departure from the equilibrium state.

The technical tool useful to perform such analysis is the Chapman-Enskog (CE) expansion. It can be used to infer a condition for the terms retained in the truncated Hermite basis required for describing flows at a certain level of non-equilibrium. According to the classical CE procedure, the single particle probability distribution function,  $f$ , can be expanded in powers of a smallness parameter,  $\epsilon$ , measuring the extent of the departure from equilibrium conditions, as:

$$f = f^{eq} + \epsilon f^{(1)} + \epsilon^2 f^{(2)} + \dots + \epsilon^k f^{(k)} + \dots \quad (2.51)$$

Without entering into the details of the derivation, if Eq. (2.51) is inserted into the BE, it is possible to derive recurrence relations between the coefficients  $\mathbf{a}^{(n)}(\mathbf{x}, t)$  at the different orders of truncation in both Hermite and Chapman-Enskog expansion series:

$$\mathbf{a}_{k+1}^{(n)} = -\tau \left[ \sum_{m=0}^k \partial_t^{(k)} \mathbf{a}_{k-m}^{(n)} + n \nabla \mathbf{a}_k^{(n-1)} + \nabla \cdot \mathbf{a}_k^{(n+1)} - n \mathbf{F} \mathbf{a}_k^{(n-1)} \right]. \quad (2.52)$$

The rigorous derivation of such recurrence relation is presented in [37]. In Eq. (2.52), the index  $k$  indicates the order of truncation in the Chapman-Enskog series, while the index  $n$  indicates the order of truncation in the Hermite series.

It is possible to interpret the relation in Eq. (2.52) as follows: the  $n$ -th Hermite term in  $f^{(k)}$  depends on the accuracy of the  $(n+1)$ -th terms in  $f^{(k-1)}$ , and, subsequently, the  $n$ -th hydrodynamic moment at the  $k$ -th Chapman-Enskog level is satisfied if the MB distribution is accurate up to  $(n+k)$ -th order terms in Hermite expansion. This relation clearly defines a rule that allows approximations to the BE at any level of the CE expansion to be constructed by retaining terms at a

sufficient order in the Hermite expansion and by using a Gauss-Hermite quadrature of sufficient algebraic precision.

Exploiting the relation of Eq. (2.52), it is now possible to draw a table, Table 2.1, where information about the order in the CE expansion level, Hermite series truncation and recovered macroscopic equations are collected.

To be noted that the Chapman-Enskog expansion tool is used to compile Table 2.1 only as an indication to measure the order of accuracy; the resulting kinetic equations, therefore, do not suffer from the closure problems encountered in the conventional representations. Moreover, the Navier-Stokes representation for the momentum equation is strictly recovered if  $n = 3$ . However, if the truncation of the Hermite expansion is stopped at  $n = 2$ , the introduced error is related only to a compressibility effect. If the flow velocity is small with respect to the speed of sound, therefore, the error can be safely neglected, [37].

The last two columns of Table 2.1, whose meaning will become clearer in the next paragraph, report the minimum required lattice size, in 3D, able to reproduce the intended macroscopic behavior and the relative computational cost with respect to the D3Q19 case. The almost linear scaling with the number of discrete speeds has been directly found in this investigation, see chapter 4, for the passage from 19 to 39 speeds. The data relative to the D3Q121, instead, is inferred assuming that the same almost linear scaling is valid. This table, therefore, should be read as follows: given a 39-speed lattice, the resulting macroscopic behavior guaranteed by its application will follow the Navier-Stokes level of description for the energy equation and the Burnett level of description for the momentum equation. It will be also about two times more expensive than the D3Q19. Moreover, the expansion in Hermite polynomials of the equilibrium distribution should include the terms at least of order four. Note also that here are considered only those lattices corresponding to quadratures with integer abscissae, due to the clear advantage from the algorithmic point of view that such choice guarantees, as Cartesian grids can still be adopted. One important information contained in Table 2.1, and which is clearly visible from Eq. (2.52), is that, macroscopically, the energy equation lags one level behind in terms of the Chapman-Enskog expansion with respect to the momentum equation. For example, for the D3Q39 lattice, the resulting momentum field will be compatible with a Burnett level of representation, but the energy field will be compatible only with a Navier-Stokes level of representation.

Now that a clear and rigorous relation between the order of truncation of the Hermite series expansion and the corresponding macroscopic equations is available, the question about how many equations in the form of Eq. (2.47) are required to achieve the desired accuracy has to be answered. In other words, how can we define the Gauss quadrature algebraic precision needed to be able to evaluate the

<i>k</i> -th order in CE expansion	<i>n</i> -th order in Hermite exp.	Macroscopic equation	Lattice	Comput. cost
1	3	Momentum Navier-Stokes	D3Q19	1.0
1	4	Energy Navier-Stokes	D3Q39	2.1
2	4	Momentum Burnett	D3Q39	2.1
2	5	Energy Burnett	D3Q121	6.6
3	5	Momentum Super-Burnett	D3Q121	6.6

**Table 2.1:** Comparison between the required orders of truncation for the Chapman-Enskog expansion, the Hermite series and the recovered macroscopic fluid dynamic equations. The table is compiled using the recurrence relation of Eq. (2.52). The column Lattice indicates the lattice model needed to recover the required order of truncation. In this context, the concepts of lattice and quadrature are synonyms. The column Comput. cost indicates the relative computational cost with respect to the D3Q19 case which represents the minimum lattice model needed to recover the Navier-Stokes equations representation for the fluid momentum. It is relevant to note that, given a lattice, i.e. a Gauss-Hermite quadrature, the corresponding macroscopic description as determined by the Chapman-Enskog expansion shows that the energy equation lags one level behind with respect to the momentum equation.

coefficients  $\mathbf{a}_k^{(n)}$  at the required *k*-th and *n*-th levels?

Previously, we have already underlined that to accurately evaluate the coefficients of the Hermite expansion truncated at the order *N* requires Gaussian quadratures with degree  $n \geq 2N$ . Considering Table 2.1, to reproduce an isothermal Navier-Stokes level of description requires a quadrature of a degree of precision greater than six; if, however, compressibility effects can be assumed to be negligible, then  $N=2$  and it is sufficient a quadrature of degree larger than four. The compressibility error, at macroscopic level, in fact, is in the form  $\tau \mathbf{u}^2 \nabla \cdot \mathbf{u}$ , and, therefore it is of order  $O(\text{Ma}^3)$ , [37], where Ma is the Mach number defined as the ratio between the flow speed and the gas speed of sound,  $\text{Ma}=u/c_s$ .

Examples of quadratures of this type are provided in Appendix 2.A at the end of this chapter. A typical candidate is represented by the  $E_{3,5}^{19}$  in the three-dimensional case and  $E_{2,5}^9$  in the two-dimensional case. The notation of the indicated quadratures should be read as follows: in  $E_{D,m}^q$ , *D* is the dimensionality, *m* is the algebraic precision and *q* is the number of abscissae of the quadrature. Note that the classical D3Q19 symbol indicates the same model as the  $E_{3,5}^{19}$ .

We are now ready to perform the last step in order to construct a fully consistent

LBE model. Eq. (2.47), which can be written for each abscissa  $\boldsymbol{\xi}_a$ , is a discretized (in the velocity space only) version of the full BE. We have to discretize it also in the configuration space  $(\mathbf{x}, t)$  in order to be solved numerically.

If a first-order upwind finite difference scheme is used to discretize the left-hand side of Eq. (2.47), we have:

$$\frac{\partial f_a}{\partial t} + \boldsymbol{\xi}_a \cdot \nabla f_a \cong [f_a(\mathbf{x} + \boldsymbol{\xi}_a \Delta t, t + \Delta t) - f_a(\mathbf{x}, t)] \quad (2.53)$$

and, if the usual unitary time step is chosen, then the standard form of the Lattice Boltzmann equation can be recovered:

$$f_a(\mathbf{x} + \boldsymbol{\xi}_a, t + 1) - f_a(\mathbf{x}, t) = -\frac{1}{\tau} [f_a(\mathbf{x}, t) - f_a^{eq}(\mathbf{x}, t)], \quad (2.54)$$

which is evolved on a special grid that is invariant under the transformation  $\mathbf{x} \rightarrow \mathbf{x} + \boldsymbol{\xi}_a$ , meaning that if  $\mathbf{x}$  is a node of the grid,  $\mathbf{x} + \boldsymbol{\xi}_a$  are also nodes of the grid. The quadratures of Table 2.2 in Appendix 2.A all satisfy such requirements. It should be noted that despite the formal first-order approximation of the discretization, the model achieves a second-order accuracy because of the absorption of the propagation error into an effective viscosity  $\nu = c_s^2(\tau - 1/2)$ , [61, 62]. After this final step, we are ready to implement Eq. (2.54) into a numerical code.

At this stage, we can summarize the steps performed so far: starting from the BE and introducing the expansion of the  $f(\mathbf{x}, \boldsymbol{\xi}, t)$  in a Hermite polynomials series, we were able to determine a set of discrete values of the microscopic velocity such that the system of related discrete Boltzmann equations provides a macroscopic description at the desired level of accuracy in terms of the CE expansion. Realizing that such set can be found through Gauss-Hermite quadrature, and further discretizing in time the discrete Boltzmann equations with a first-order upwind scheme, we ended up with a system of explicit lattice Boltzmann equations which can be solved on a special grid, invariant under the transformation  $\mathbf{x} \rightarrow \mathbf{x} + \boldsymbol{\xi}_a$ . In Fig. 2.7, a representation showing the meaning of the  $f_a(\mathbf{x}, t)$  as evolved in the LBM is sketched.

It is now natural to ask why the LBM should be used to simulate a fluid-dynamic system instead of other conventional methods and if it presents advantages. First of all, one should realize that with respect to other methods the non-linearities are local and the non-localities are linear. In fact, the non-local operations, i.e. the streaming step, involve only the shifting of data to adjacent nodes. Moreover, due to the special characteristics of the grid, the streaming step is an exact operation. This should be compared with other methods where the discretization scheme used to discretize the advection term, inevitably introduce approximations. All the non-



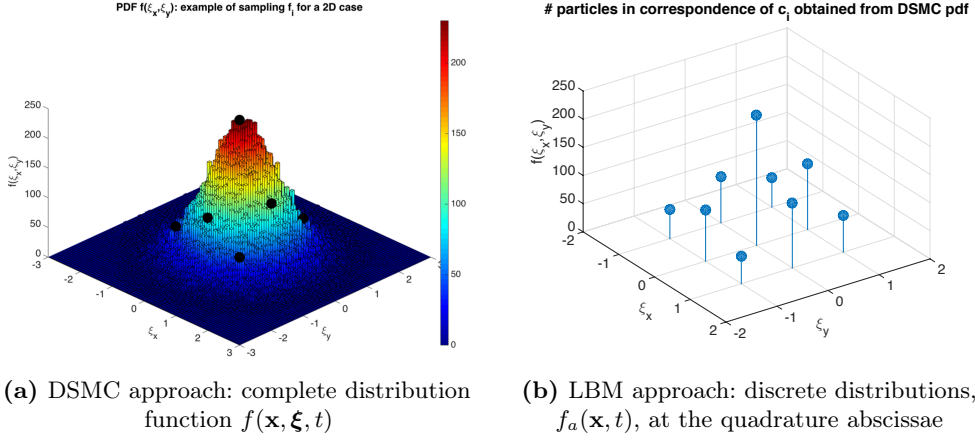


**Figure 2.7:** Representation of the discrete distribution functions,  $f_a(\mathbf{x}, t)$ , as the values of the single particle distribution function,  $f(\mathbf{x}, \boldsymbol{\xi}, t)$ , evaluated in correspondence of a set of predetermined microscopic velocities,  $\boldsymbol{\xi}_a$ . In (a), the full pdf is extracted from a DSMC simulation, and the black dots are placed in correspondence of the quadrature abscissae,  $\boldsymbol{\xi}_a$ , for a D2Q9 lattice. In (b), the full pdf has been removed and only the quantities which evolve within the nine Lattice Boltzmann equations of the kind of Eq. (2.54), i.e. the discrete distributions, are visualized. It is evident the drastic simplification in the description of the flow system. However, the derivation presented here guarantees that the knowledge of the values of the discrete distribution functions is sufficient to obtain a correct macroscopic description of the flow problem. For the D2Q9 model shown here, such description is the same as the one provided by the Navier-Stokes equations for two-dimensional flows. The data are collected in a DSMC cell located in the centerline of a Poiseuille channel flow.

linearities are also local, in fact the collision step, which requires to compute terms at least in the form  $u^2$  as present in the equilibrium distribution functions, is performed on a node-based way and no information from neighboring nodes is required.

### Lattice Boltzmann Method algorithm

After having rigorously derived the Lattice Boltzmann Equation, we provide a brief description of the steps involved in the algorithm implemented in our code. At this aim, it is helpful to follow the scheme of Fig. 2.8. It is again underlined that such scheme shows several similarities with the DSMC scheme drawn in Fig. 2.2.

**Initialization of the simulation.** During the initialization phase, the lattice constants, more specifically the weights,  $w_a$ , and the abscissae of the quadrature,  $\boldsymbol{\xi}_a$ ,

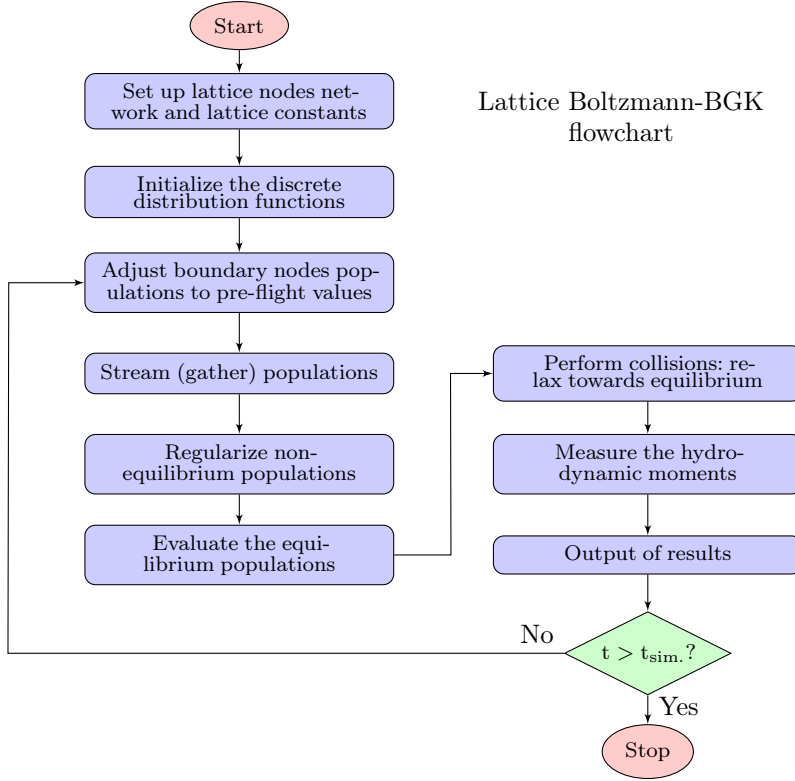


**Figure 2.8:** Typical LBM simulation flowchart. Comparing it with the DSMC flowchart, Fig. 2.2, the analogies are evident. After the initialization phase, the sequence of the steps involving the application of the boundary conditions, streaming of the populations to neighboring nodes, evaluation of the equilibrium distributions, collision and measurement of the relevant hydrodynamic quantities is performed until the final time step is reached ( $t > t_{sim.}$ ) or a convergence criterion is fulfilled. Note that with respect to the standard LBM commonly presented in literature, this flowchart includes one more step, the regularization step, which is briefly described in the next paragraphs.

more often called discrete velocities, are set according to the chosen lattice model. The grid, moreover, is also automatically defined, in the sense that the discrete distribution functions,  $f_a$ , during the streaming step, will shift from a node to a neighboring one according to the relative discrete velocity  $\xi_a$ .

**Boundary conditions: pre-flight adjustment.** Defined the initial state of the system, it is possible to enter the time loop during which the sequence of streaming and collision steps is performed.

Before performing the streaming step, we first apply the boundary conditions,

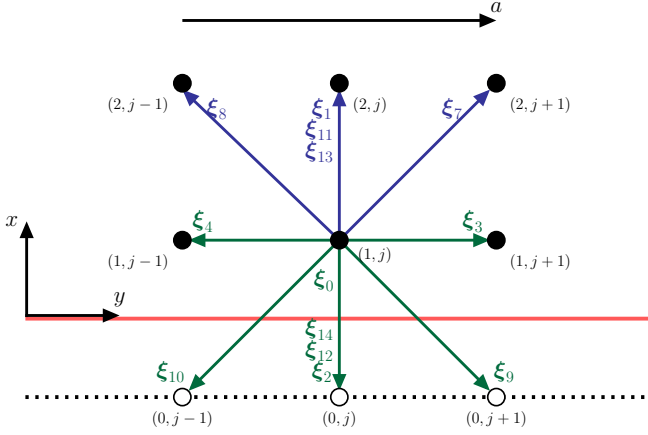


**Figure 2.9:** Lattice and boundary configuration. The solid wall is placed at  $x = 1/2$  (red line). The 2D projection onto the  $x - y$  plane of the D3Q19 lattice is shown here. From an algorithmic point of view, before the streaming step, the discrete distributions colored in blue are unknown and they are evaluated according to the specific chosen combination of specular and diffuse reflection as prescribed by the Eq. (2.55). Hollow circles represent the so-called ghost nodes (physically outside of the fluid domain) where the boundary conditions are imposed, while the filled circles represent the fluid nodes.

adjusting the values of the distribution functions according to the specific chosen boundary condition implementation.

In the same way as done for the DSMC simulations, we will mainly apply specular or diffuse wall boundary conditions, or a proper combination of those, so to be able to reproduce the experimentally found value of a Tangential Momentum Accommodation Coefficient, TMAC. The diffuse wall boundary conditions in LBM essentially mimic what is commonly done in DSMC, i.e. as soon as a population streams within a wall, it is re-emitted at the equilibrium conditions prescribed by the wall velocity and temperature, [63]. Also the treatment of the specular boundary conditions follow a similar approach as done in DSMC.

It is interesting to note that it is possible to recover the slip velocity at the wall prescribed by any slip model provided that the fraction of each boundary condition component is properly chosen. In Appendix 6.B at the end of chapter 6, we show how this can be done for a D3Q19 LBM model when Navier-Stokes equations level of description is intended to be reproduced.

In Fig. 2.9 we represent a typical condition found at a wall where we want to apply a combination of specular and diffuse boundary conditions. In this case, the unknown distributions at the fluid node  $(1, j)$ , namely  $f_1$ ,  $f_7$ ,  $f_8$ ,  $f_{11}$ , and  $f_{13}$ , can be determined according to the value of the accommodation coefficient  $\sigma$ :

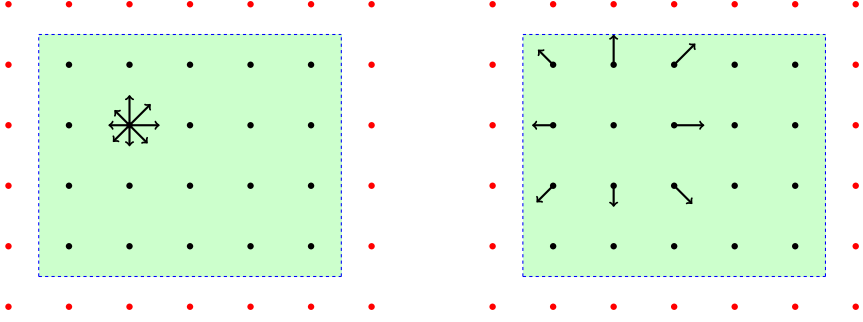


**Figure 2.10:** Streaming step visualization: scatter scheme. The discrete distributions in one grid node, whose value is represented by the length of the arrows, shift to the neighboring nodes according to the relative discrete velocity. If properly implemented, the scatter (shown here) and gather (shown in Fig. 2.1) schemes are analogous. However, the treatment of the boundary conditions, in particular the order of the operations for the streaming step and the application of the boundary conditions, is reverted in the two cases.

$$\begin{aligned}
 f_1 &= \sigma f_1^{(eq)}(\rho, \mathbf{u}_w) + (1 - \sigma) f_2^* \\
 f_7 &= \sigma f_7^{(eq)}(\rho, \mathbf{u}_w) + (1 - \sigma) f_9^* \\
 f_8 &= \sigma f_8^{(eq)}(\rho, \mathbf{u}_w) + (1 - \sigma) f_{10}^* \\
 f_{11} &= \sigma f_{11}^{(eq)}(\rho, \mathbf{u}_w) + (1 - \sigma) f_{12}^* \\
 f_{13} &= \sigma f_{13}^{(eq)}(\rho, \mathbf{u}_w) + (1 - \sigma) f_{14}^*
 \end{aligned} \tag{2.55}$$

where with  $f_a^*$  the post-collision distributions are indicated. In Eqs.(2.55), the first term at the right-hand side is the diffuse reflection contribution while the second term is related to the specular reflection.

**Streaming step.** With the populations correctly set at the boundary nodes, the streaming step is performed and each population, according to the related quadrature abscissa, shifts to a neighboring node. In Fig. 2.1, the so-called gather scheme, for which

$$f_a(\mathbf{x}, t) \leftarrow f_a(\mathbf{x} - \boldsymbol{\xi}_a, t),$$

is shown. If properly implemented, the other option, i.e. the scatter scheme, represented in Fig. 2.10, and for which

$$f_a(\mathbf{x}, t) \rightarrow f_a(\mathbf{x} + \boldsymbol{\xi}_a, t),$$

provides an equivalent result.

**Regularization step.** It can be recognized that the usual LBM algorithm, which carries out a sequence of streaming and collision steps, when viewed as a projection of the continuum BGK-BE into the (truncated at order  $N$ ) basis,  $\mathbb{H}^N$ , as described in the previous sections, introduces an error due to the fact that the non-equilibrium distributions,  $f_a$ , differently from the equilibrium distributions,  $f_a^{eq}$ , do not automatically lie entirely within the  $\mathbb{H}^N$ . The regularization procedure, firstly proposed in [38], can be applied to ensure that also the non-equilibrium part lies in the same subspace. If the post-streaming distribution is splitted as:

$$f_a = f'_a + f_a^{eq}, \quad (2.56)$$

the regularization acts to convert the  $f'_a$  to a new distribution  $\tilde{f}'_a$  which now lies entirely in  $\mathbb{H}^N$ . In few words, such process removes from the  $f_a$  all those moments that cannot be accurately evaluated by the available quadrature and which could contain numerical discrete artefacts. If we use the classical D3Q19 lattice, for all the considerations we mentioned about the algebraic degree of precision of the quadrature, the single particle distribution function can be truncated at the order  $N = 2$  and so we can expand the  $\tilde{f}'_a$  as:

$$f'_a \approx \tilde{f}'_a = w_a \sum_{n=0}^2 \frac{1}{n!} \mathbf{a}'^{(n)} \mathcal{H}^{(n)} \quad a = 0, \dots, 18 \quad (2.57)$$

where now

$$\mathbf{a}'^{(n)} = \sum_{a=0}^{18} f'_a \mathcal{H}^{(n)}(\boldsymbol{\xi}_a) \quad n = 0, \dots, 2. \quad (2.58)$$

The first two coefficients, actually, are zero due to the null contribution from the non-equilibrium distribution to the mass and momentum, which are, indeed, conserved quantities. The 2-nd coefficient, instead, is given by:

$$\mathbf{a}'^{(2)} = \sum_{a=0}^{18} f'_a \boldsymbol{\xi}_a \boldsymbol{\xi}_a. \quad (2.59)$$

Moreover, due to the orthonormality of the Hermite polynomial basis, the regularized distribution  $\tilde{f}'_a$  provide the same second-order fluxes as the original  $f'_a$ :

$$\sum_{a=0}^{18} \tilde{f}'_a \boldsymbol{\xi}_a \boldsymbol{\xi}_a = \sum_{a=0}^{18} f'_a \boldsymbol{\xi}_a \boldsymbol{\xi}_a. \quad (2.60)$$

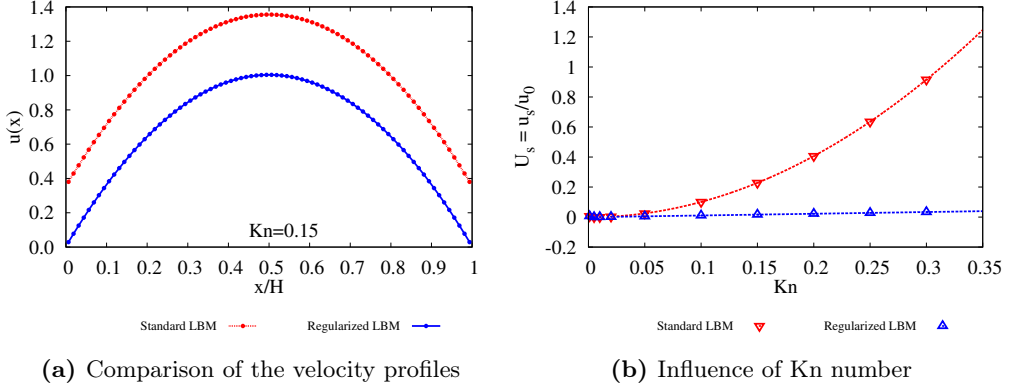


**Figure 2.11:** Example of the effectiveness of the regularization procedure in removing the excessive slip velocity. (a) Poiseuille channel flow for  $Kn=0.15$ . As the bounce-back boundary condition is imposed and, therefore, a no-slip condition is expected at the wall, it is evident the influence of the regularization (blue symbols) when compared to the standard LBM formulation (red symbols) in enforcing the prescribed velocity boundary condition. In the standard LBM, in fact, an artificial slip velocity at the walls at  $x/H=0$  and  $x/H=1$  is observed. (b) Evaluation of the slip velocity at the wall as a function of  $Kn$  for the bounce-back wall boundary condition in the case of regularized (blue symbols) and standard LBM (red symbols). A large reduction of the undesired slip velocity is achieved over a large range of  $Kn$ . The same behavior is found also for the diffuse boundary condition (not shown here).

This is an essential step to preserve the required non-equilibrium properties affecting the macroscopic flow. With the definition of Eq. (2.59), the discrete non-equilibrium distributions projected onto  $\mathbb{H}^2$  are fully specified by:

$$\tilde{f}'_a = w_a \left[ \frac{\mathcal{H}^{(2)}(\xi_a)}{2!} \sum_{b=0}^{18} f'_b \xi_b \xi_b \right]. \quad (2.61)$$

Finally, incorporating the regularization procedure into the LBM modifies the LBE in Eq. (2.54) as

$$f_a(\mathbf{x} + \xi_a, t + 1) - f_a(\mathbf{x}, t) = \left( 1 - \frac{1}{\tau} \right) \tilde{f}'_a(\mathbf{x}, t) + F_a(\mathbf{x}, t) \quad (2.62)$$

where also the body-force term should be projected onto the same basis. For  $\mathbb{H}^2$ , one has

$$F_a = w_a \rho \mathbf{F} \cdot (\xi_a + u_a \xi_a - \mathbf{u}). \quad (2.63)$$

Such procedure demonstrated to be very useful for the simulations presented in

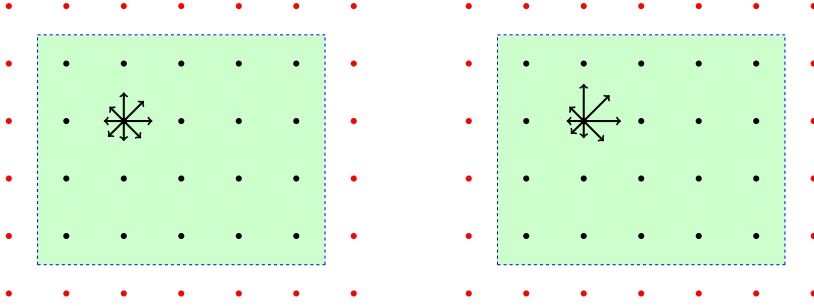


**Figure 2.12:** Collision step visualization: a re-arrangement of the populations towards a local equilibrium is performed. This operation is based on the BGK collision model as described in section 2.3 and it is a local operation, not requiring any information from the neighboring nodes.

this thesis. One of the main advantages guaranteed by the method is the reduction of the excessive slip provided by the standard LBM at the walls, see Fig. 2.11a and 2.11b. Another advantage, as will be shown in the chapter 6, is connected to the removal of discrete artifact effects due to compressibility (high Ma flow conditions).

Of course, this procedure comes at a larger computational cost, which can be quantified in about a doubling of the wall clock time to perform the same number of time steps, when compared with a standard LBE.

**Collision step and measurement of the hydrodynamic moments.** Finally, it is possible to perform the collision step, once that the equilibrium distributions have been updated according to Eq. (2.50). As already mentioned, since the BGK-BE model is employed, the interparticle collisions are replaced by a relaxation process for the non-equilibrium distributions towards a local equilibrium constructed according to the local density and velocity. In Fig. 2.12, a representation of such process is depicted. It is then possible to measure the hydrodynamic moments as shown in Eqs. (2.46). Note that for the conserved moments, it is irrelevant to measure the hydrodynamic moments before or after the collision step, but this is not the case for the non-conserved ones.

The simulation will continue to run until e.g. a pre-defined criterion on the accuracy of the solution is met or the final time step is reached.

## 2.4 Conclusions

In this chapter, we provided an introduction to the numerical methods that will be used to construct the hybrid model presented in the next chapters.

While we approached the theoretical foundations of the LBM following a rigorous mathematical treatment, in turn based on Grad's method for the definition of the single particle distribution function as a series in Hermite polynomials and on Gauss-Hermite quadratures for the evaluation of the coefficients of the series, we employed a more phenomenological way to present the DSMC.

We also showed the several analogies, as well as dissimilarities, between the two methods stemming from the common kinetic theory roots. Such common origin, in fact, plays in favor of the LBM as a promising numerical method to be coupled to the DSMC in order to make more efficient the simulation of non-equilibrium, non-continuum gas flows.

## 2.A Gauss quadratures

The mathematical tool of the Gauss quadrature is an essential ingredient to construct the Lattice Boltzmann Equation model. Few details are reported here; the complete treatment can be found in [37, 64].

Given a polynomial function  $f(\xi)$ , the Gaussian quadrature seeks to obtain the best evaluation of the integral

$$\int_a^b \omega(\xi) f(\xi) d\xi$$

choosing the optimal set of abscissae  $\xi_a$ ,  $a = 1, \dots, n$ , such that:

$$\int_a^b \omega(\xi) f(\xi) d\xi = \sum_{a=1}^n w_a f(\xi_a) \quad (2.64)$$

where  $\omega(\xi)$  is a weighting function — in the present case it is given by Eq. (2.31) — and  $w_a$  is a set of constant weights. The estimate in Eq. (2.64) has an algebraic degree of precision of degree  $m$  if an exact equality holds in that relation for any  $f(\xi)$  of degree up to  $m$ . The choice of  $\xi_a$  should maximise the precision for the given number of abscissae  $n$ . The optimal abscissae of the  $n$ -point Gaussian quadrature are the roots of the  $n$ -th corresponding orthogonal polynomial, and the weights are given by:

$$w_a = \frac{\langle P_{n-1}, P_{n-1} \rangle}{P_{n-1}(\xi_a) P'_n(\xi_a)}, \quad P'_n = dP_n/dx. \quad (2.65)$$

Eq. (2.64) has an algebraic degree of precision of  $2n-1$ . In one dimension, the Gauss-Hermite quadrature is the Gauss quadrature over the interval  $[-\infty, \infty]$



Quadrature	Abscissae $\xi_a$	Weights $w_a$
$E_{1,5}^3$	0	2/3
	$\pm\sqrt{3}$	1/6
$E_{1,9}^5$	0	8/15
	$\pm\sqrt{5-\sqrt{10}}$	$(7+2\sqrt{10})/60$
	$\pm\sqrt{5+\sqrt{10}}$	$(7-2\sqrt{10})/60$

**Table 2.2:** Numerical values of the abscissae and weights of Gauss-Hermite quadratures. The quadrature symbol  $E_{D,m}^q$  can be read as follows:  $D$  is the dimensionality of the flow problem,  $m$  and  $q$  are the algebraic degree of precision and the number of abscissae of the chosen quadrature, respectively. As already mentioned, to recover the isothermal Navier-Stokes equation,  $m$  should be larger than 4 and therefore the quadrature  $E_{1,5}^3$  is sufficient.

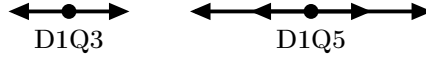


**Figure 2.13:** Graphical representation of the  $E_{1,5}^3$  (left) and  $E_{1,9}^5$  (right) quadratures. They correspond to the common monodimensional lattices named D1Q3 and D1Q5, respectively. From these quadratures, using production formulae, it is possible to determine the quadratures, and therefore the lattices, also for higher-order dimensions.

with respect to the weight function of Eq. (2.31). The corresponding polynomials are the Hermite polynomials and the abscissae of the  $n$ -point quadrature are the zeros of  $\mathcal{H}^{(n)}$ . The weights, therefore, are defined as

$$w_a = \frac{n!}{[n\mathcal{H}^{(n-1)}(\xi_a)]^2}. \quad (2.66)$$

In Table 2.2, the numerical values of the abscissae and weights of some Gauss-Hermite quadratures are reported. Actually, such quadratures correspond to the classical D1Q3 and D1Q5 lattices, graphically represented in Fig. 2.13. It should be noted that no known generalizations for higher dimensions of the Gauss quadrature theory exist. However, from one-dimensional formulae it is possible to derive, through production formulae, extensions to two- and three-dimensional cases. So, for example, using the one-dimensional formula  $E_{1,5}^3$  of Table 2.2 in two- and three-dimensions, it is possible to derive the quadratures  $E_{2,5}^9$  and  $E_{3,5}^{19}$ , see Table 2.3, which correspond to the most used lattices D2Q9 and D3Q19.

Quadrature	Lattice stencil	Algebraic precision	$N$ -th order in Hermite exp.
$E_{2,5}^9$	D2Q9	5	2
$E_{2,7}^{21}$	D2Q21	7	3
$E_{3,5}^{19}$	D3Q19	5	2
$E_{3,7}^{39}$	D3Q39	7	3

**Table 2.3:** Examples of two- and three-dimensional quadratures and related lattices. The algebraic precision and corresponding order of truncation in Hermite expansion are also reported. Combining this table with the information of Table 2.1, it is possible to determine what lattice should be employed to recover the desired level of accuracy at macroscopic level. It has to be noted that, in general, the zeros of Hermite polynomials are irrational, but the abscissae of the quadratures listed here are grid points of Cartesian coordinates. Such property is highly desirable from an implementation point of view, as it allows to maintain the classical Cartesian grid with equidistant nodes.



## 3 Development and validation of the DSMC solver

The DSMC code used in this work has been developed during the PhD project. In this chapter, we provide few implementation details, underlining the peculiar treatment of the streaming step. In fact, each step is divided into a sequence of substeps whose duration is such that a particle cannot move further than a distance equal to a cell size. This algorithmic choice, done in order to preserve a full compatibility with the LBM code for the treatment of flows in complex geometries, ensures the efficiency of the parallelization and particle-boundary interaction routines. In addition, we present the results of several validation tests typically encountered in rarefied gas flow literature. These include the study of the formation of the Knudsen layer in proximity of a solid surface, the evaluation of the shear stress for the Couette flow problem and the lid-driven cavity flow under a wide range of rarefaction conditions. Finally, the implementation of pressure and mass flow rate boundary conditions is tested for a plane channel flow.

The LBM code used during this PhD project, instead, has been adopted in the past years to study a broad range of fluid mechanics problems, including, e.g. turbulent flows, [35], multiphase and multicomponents fluid flows, [65, 66], solid particle-laden flows, [67]. For this reason, in the present work, we provide results about the validation of the LBM code only in relation to the extension of it towards flows characterized by a finite Kn number. Such results are included in the chapters 4, 5, and 6.

### 3.1 DSMC code: implementation details

In section 2.2, we presented the steps at the basis of the DSMC method.

In this section, we provide few details about the specific implementation of the DSMC code used in this work. As it will be mentioned also in chapter 6, the algorithmic choices behind the DSMC code implementation were mainly driven by the constraint that it should preserve a full compatibility with the treatment of flows in complex geometries as handled in the LBM code, especially in relation to the application of the boundary conditions. In the LBM implementation, in fact, at each node the value of a flag field specifying whether the node is a "fluid"

Substepping routine algorithm
1. $\forall$ particle $j$ , compute the substep duration $\Delta t_{adv,j} = \min_i(\text{cell\_size}_i / u_i)$
2. Evaluate the number of substeps $nsteps_j$ as $\Delta t_{DSMC} = \text{floor}\left(\frac{\Delta t_{DSMC}}{\Delta t_{adv,j}}\right) \Delta t_{adv,j} + \Delta t_{residual,j} = nsteps_j \Delta t_{adv,j} + \Delta t_{residual,j}$
3. Advance each particle $j$ by $\Delta t_{adv,j}$
4. If the particle $j$ has completed its $nsteps_j$ substeps, remove $j$ from the list of particles that still need to stream
5. If a particle $j$ interacts with a domain boundary, apply the boundary condition and go to point 1. $\Delta t_{DSMC}$ now is the left part of the initial time step
6. Once all the particles have completed the $nsteps_j$ substeps, the collision step is performed

**Table 3.1:** Steps of the substepping routine algorithm adopted in the DSMC code. For each particle  $j$ , the duration and number of substeps needed to complete a full time step is calculated based on the grid cell size and the particle velocity. In the same code routine where particles stream, the boundary conditions as well as the inter-process communication, in case a particle enters the domain assigned to another process during a substep, are applied.

or "wall" node is assigned according to the flow domain geometry. The position where the wall boundary condition is applied, then, is placed half-way between a fluid and a wall node. The same procedure has been implemented also in the DSMC code so that a cell can be assigned a wall or fluid condition in the same way as done in the LBM code.

One of the main features of the current DSMC implementation is the splitting of the streaming step into substeps sufficiently short so that a particle can move at most to the nearest-neighbor cells, thus imitating what is routinely done in a LBM code adopting a single shell lattice. In this way, two advantages are achieved: firstly, a frame layer, a single cell wide, would be sufficient to treat inter-process communication, and, secondly, only the particles residing on a fluid cell adjacent to a wall cell will be checked for eventual interactions with the walls.

Algorithmically, the substepping routine is described in Table 3.1. The advection substep time duration  $\Delta t_{adv,j}$  is evaluated, for each particle, as the minimum cell residence time based on the particle velocity components and the cell size along each coordinate direction. To each particle, therefore, a specific number of substeps,  $nsteps_j$ , to (sub-)stream before completing the full advection phase is attributed. A further measure to improve the efficiency of the algorithm is that as soon as a particle has concluded its advection phase (and eventual interactions with the

walls), it is excluded from the list of particles that will be further treated. In addition, the algorithm guarantees that the case of multiple interactions with the walls is automatically handled.

An example of application of the algorithm is shown in the series of plots of Fig. 3.1, where the particles still to be treated after each successive substep of a single time step are depicted. Initially, Fig. 3.1a, all the particles reside within the flow domain (black cloud completely covering the domain). After the first substep, (b), some particles have streamed into the wall cells (orange dots) and some others will have completed their advection phase and so disappear from the subsequent plots. The steps in Table 3.1 are repeated until all the particles streams for the required  $\Delta t_{\text{DSMC}}$ . In the last substep, Fig. 3.1i, a single particle is left (indicated by the green arrow). This will eventually stream for its remaining part of the time step,  $\Delta t_{\text{residual},j}$ .

Note that the number of represented substeps in Fig. 3.1 is generally not encountered (and should not occur) in a well-defined simulation, but it has only the scope to represent the application of the algorithm. The  $\Delta t_{\text{DSMC}}$ , in fact, is too large to produce an accurate final solution. For a properly set up simulation, instead, it is possible to find a distribution of `nsteps` as it will be presented in Fig. 6.5, where it is shown that almost all the particles will substep at most twice. The proposed implementation is generic in the sense that it can handle any geometry. Two possible strategies to define the flow geometry are currently available. The first possibility, which can be defined as the "hard-coding" option, prescribes to define a routine within the code where the scalar field relative to the fluid/wall condition associated to each cell is set according to the desired geometrical configuration. This option is used to determine the geometry in the simulations in chapters 4, 5, and 6. Other examples of such approach are shown in Fig. 3.2. The second option, instead, allows one to import geometries constructed with Computer-Aided Design (CAD) softwares. In Fig. 3.3, the process to translate a 3D CAD drawing into the scalar field needed within the DSMC code to determine the fluid/wall regions is shown.

In order to further increase the computational efficiency, the streaming step, as well as the particle interactions with the domain boundaries (walls, open boundaries, ...), the inter-process communication operations and the indexing of the particles within each cell, are performed in a single "fused" routine.

The other routines implementing the steps described in section 2.2, i.e. the collision step and the evaluation of the hydrodynamic quantities, are performed separately. Finally, the implemented DSMC code, which is fully parallelized with Message Passage Interface (MPI) on a three-dimensional Cartesian toroidal processor grid, presents good scaling parallel efficiency, as well as the capability of running very

large simulations as demonstrated in chapter 6, where the results from simulations run over thousands of cores involving hundreds of millions of cells, and, consequently, billions of particles, are reported.

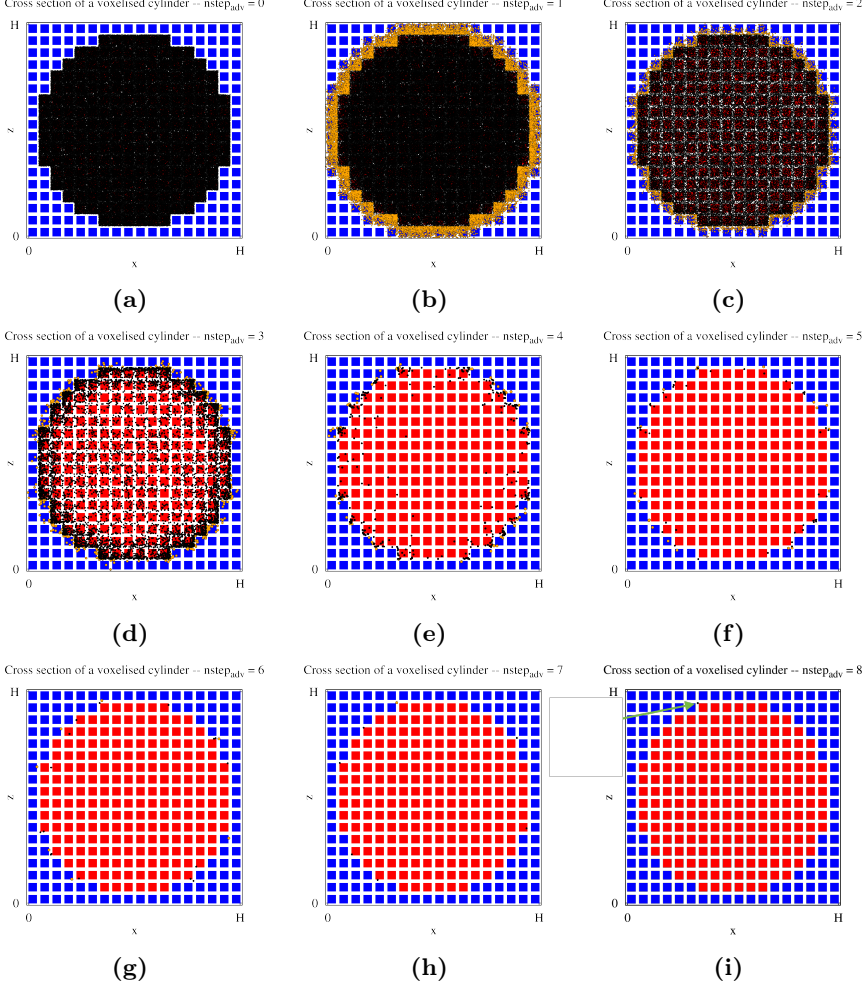


**Figure 3.1:** Sequence of the substeps needed to stream for a whole time step  $\Delta t_{DSMC}$ . The plots refer to a section of a circular geometry defined using the "hard-coding" option. The staircase nature is visible as the circle radius is discretized with only 8 cells. The red squares indicate the flow domain cells, while the blue squares indicate the wall cells. Black dots represent particles that reside, at the end of each substep, in a cell within the flow domain; orange dots represent the particles which streamed outside the flow domain, and, therefore, undergo an interaction with a boundary. As  $nsteps_j$  increases, the number of particles which need to further stream decreases until, for the case reported here, only one particle is left for  $nsteps=8$ , as shown in (i).

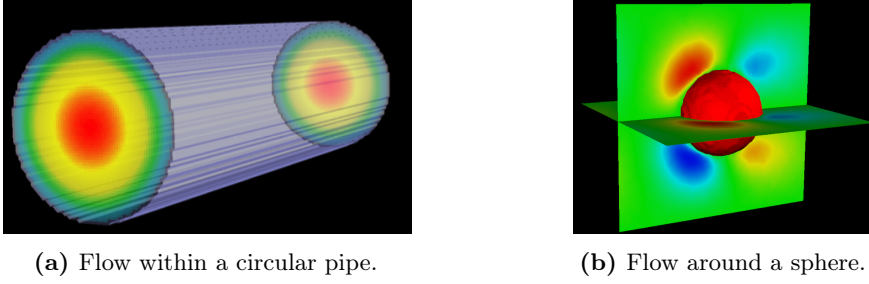


**Figure 3.2:** Examples of application of the "hard-coding" option for the definition of the flow domain into the DSMC code: (a) Fluid velocity magnitude field for a force-driven flow within a circular pipe. The simulation domain is discretized with about 2.75 million cells and 55 millions particles are used. (b) Vertical velocity component of the flow on the vertical plane passing through the center of a sphere, and horizontal component on a similar horizontal plane (red indicating positive velocity and blue negative velocity). On the fluid, a body force is applied. The domain is discretized with about 500,000 cells and it is initially populated by about 10 millions particles.

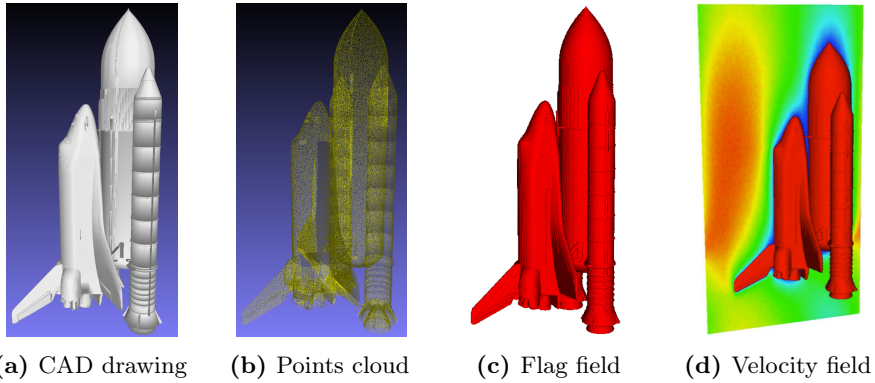


**Figure 3.3:** Sequence of the operations needed to import a generic geometry drawn in a CAD software into the DSMC code. Starting from the CAD drawing, (a), in correspondence of the geometry surfaces, a cloud of points is generated, (b). Such cloud of points is translated into the DSMC grid and at those cells within whose volume at least one point is present, the status of wall is assigned, (c). The domain is now fully defined and the simulation can start after the proper boundary conditions are imposed. In (d), for example, the velocity magnitude field, obtained imposing the values of the pressure at the upper and lower boundaries is shown. The simulation grid is composed of more than 70 millions cells and the initial number of particles is about 1.4 billions. The calculation is performed on 720 CPUs using the `broadwell` partition of the Dutch national supercomputer, *Cartesius*. Such partition is composed of 32-processors nodes with E5-2697A v4 Intel Xeon Processor (2.6 GHz clock frequency) and with 64 GB of memory. The import operation, (a)-(c), required about 15 minutes to be completed. The calculation to get the final solution, shown in (d), took about 6 hours.



## 3.2 Validation test cases for the DSMC code

In this section, the results about several tests performed in order to validate the developed DSMC code are presented. The tests cover classical problems typically encountered in rarefied gas flow literature.

### 3.2.1 Power-law velocity profile in the Knudsen layer

An important feature typical of a gas flowing over a solid surface is the formation of the so-called Knudsen layer. Within such layer, which extends to a distance in the order of one mean free path from the solid surface, molecules collide with the surface more frequently than with each other [68]. Consequently, in this region, the probability distribution function of the molecular velocities is significantly perturbed from an equilibrium state. This ultimately results in clear rarefaction phenomena: the gas at the surface shows a finite velocity relative to the surface itself, the so-called slip velocity, and it displays a non-Newtonian behavior. Such non-Newtonian behavior, however, is a flow-related property, rather than a real gas property, [69].

The Knudsen layer formation and its structure are the subject of several studies, performed with various numerical and analytical tools, [70–77]. In particular, in [78] and in [79], the results from DSMC calculations and the solution of the linearized Boltzmann equation for a shear flow past a solid wall, respectively, showed that the bulk gas velocity  $u$  parallel to the wall is accurately described by a power-law relation in the form

$$u \propto y^\alpha, \quad (3.1)$$

where  $y$  is the normal distance from the surface and  $\alpha \approx 0.8$ . The behaviour prescribed by Eq. (3.1) is found to be valid up to about one mean-free path from the surface.

Several collisional models have been adopted to verify such behaviour. For example, in [78] and in [79], the HS model is used. In [80], instead, the VSS is adopted. Here, we employ a VHS approach with the aim to verify that the power-law description in Eq. (3.1) is only weakly dependent on the employed interaction model, thus confirming that the law in Eq. (3.1) is a physical phenomenon emerging from the Boltzmann equation.

From a microscopic point of view, the VSS and VHS model share the same inverse power law behavior for the molecular diameter,  $d$ :

$$d = d_{\text{ref}} (c_{\text{r,ref}}/c_{\text{r}})^\nu \quad (3.2)$$

where  $c_r$  is the relative velocity between colliding molecules, the exponent  $\nu$  depends on the particular gas under consideration and the subscript "ref" denotes the reference values at the reference temperature. The two collision models, however, differ for the formulation of the collision deflection angle law. For both cases, such law can be defined as:

$$\chi = 2 \cos^{-1} (b/d)^{1/\beta}, \quad (3.3)$$

where  $b$  is the distance of the closest approach in the center of mass frame of reference of the undisturbed trajectories of the molecules undergoing the collision. For the VHS model,  $\beta \equiv 1$  holds, while, for the VSS model, the value of  $\beta$  lies between 1 and 2 and it is chosen so that the simulated gas has the ability to reproduce the diffusion coefficient experimentally measured for the real gas.

Going back to the macroscopic results, an important consequence of Eq. (3.1) is that there exists a velocity gradient singularity at the surface. This is consistent with the results in [72, 81], where the same feature was found when using the linearized BGK model equation.

As done in the other mentioned works using the DSMC, [78] and [79], the Knudsen layer is studied employing the Couette flow problem set up. In Fig. 3.4, the geometry used for the DSMC calculations is shown: two walls are put into motion with opposite velocity.

In order to avoid interferences between the Knudsen layers generating from each wall, the wall separation,  $H$ , should be sufficiently large in proportion to the mean

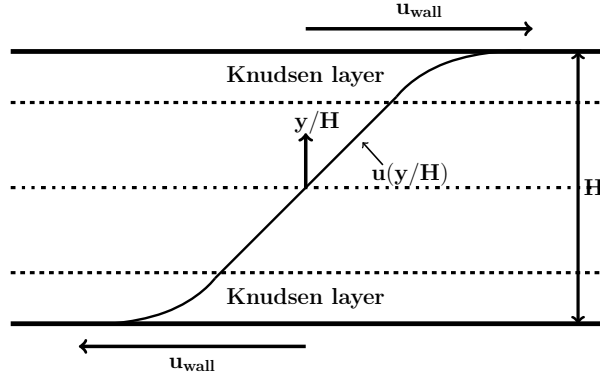


**Figure 3.4:** Geometry of the flow domain used in the DSMC simulations to study the Knudsen layer formation. The bulk flow velocity  $u$  is a function of  $y$  only. Such variable represents the displacement from the midplane where  $y=0$ . The walls are located at  $y = \pm H/2$  and they are assumed to be diffusively reflecting. Periodic boundary conditions are applied along the other directions.

Parameter	Value
number of cells	$N_{\text{cell}}=1000$
initial number particles/cell	100
initial number density	$n_0=[0.008 - 2.656]\times 10^{23} \text{ m}^{-3}$
wall velocity	$u_{\text{wall}}=30 \text{ m s}^{-1}$
wall temperature	$T_{\text{wall}}=273 \text{ K}$
wall Mach number	0.098
molecular mass	$6.63\times 10^{-26} \text{ kg}$
molecular diameter (VHS, Argon)	$4.17\times 10^{-10} \text{ m}$
Kn number	$[0.4 - 0.0125]$
total particle moves	$\sim 10^{12}$

**Table 3.2:** Summary of the parameters of the DSMC simulations for the study of the Knudsen layer formation. The number of employed cells is sufficient to obey the classical DSMC rules of thumb on grid resolution also for the most demanding case ( $\text{Kn}=0.0125$ ). It is kept constant for all the examined cases. The flow Kn is set according to the initial number density,  $n_0$ . In fact, the mean free path,  $\lambda$ , is defined, based on the VHS model as:

$$\lambda = \frac{2(5 - 2\omega)(7 - 2\omega)}{15} \left( \frac{\mu}{mn_0} \right) \left( \frac{m}{2\pi k_B T} \right)^{1/2},$$

where  $\omega=0.81$  is the VHS viscosity index for Argon,  $m$  is the Argon mass, and  $\mu$  is the viscosity coefficient, [1]. The imposed wall velocity,  $u_{\text{wall}}$ , is such that the  $\text{Ma}_{\text{wall}}=0.1$ , where  $\text{Ma}_{\text{wall}} = u_{\text{wall}}/c_s$ , with  $c_s$  the gas speed of sound. This value allows to limit the flow temperature variations due to dissipation, and, therefore, to exclude any potential thermal effect on the measured velocity profile. For any investigated Kn, the increase of temperature has been verified to be less than 1.5K.

free path, i.e. the Knudsen number ( $\text{Kn}=\lambda/H$ ) should be sufficiently small.

In Table 3.2, the simulation parameters for this study are collected. In Fig. 3.5, the velocity profiles normalized with the imposed wall velocity are plotted for several Kn. Besides the presence of a slip velocity, the non-linearity of the velocity profile while approaching from the centerline ( $y/H = 0$ ) towards the wall ( $y/H = 1$ ) is evident for any investigated Kn.

In order to let emerge the mentioned power-law behavior of the velocity profile, a transformation of coordinates is necessary. In particular, we define the new coordinates as:

$$\tilde{y} = \frac{1}{\text{Kn}} \left( \frac{1}{2} - \frac{y}{H} \right), \quad (3.4)$$

$$\tilde{u} = \frac{1}{\gamma \text{Kn}} \left( \frac{1}{2} - \frac{u}{u_{\text{wall}}} \right), \quad (3.5)$$

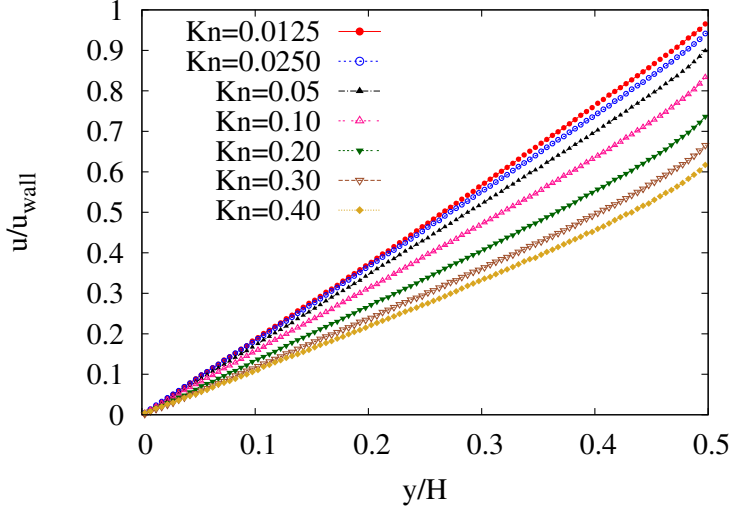


**Figure 3.5:** Gas velocity as a function of the normal distance from the midplane,  $y/H = 0$ , for the Couette flow problem of Fig. 3.4 and with  $Kn$  as parameter. Half of the domain is shown and, for clarity of visualization, only few data points are plotted. For any investigated  $Kn$ , a non-linear velocity profile is found in proximity of the wall (within the Knudsen layer) located at  $y/H=0.5$ . An increasing velocity slip is also observed while  $Kn$  increases.

where  $\gamma$  is a normalized midplane velocity gradient given as

$$\gamma = \frac{H}{u_{\text{wall}}} \left[ \frac{du}{dy} \right]_{y=0}. \quad (3.6)$$

The value of  $\gamma$  is found performing a linear regression on the velocity profile for distances larger than  $3\lambda$  from the walls. For those cases for which  $3\lambda$  is larger than  $H/2$ , the regression analysis is performed using data for which  $-H/10 \leq y \leq H/10$ . In Fig. 3.6a, the behavior of  $\tilde{u} - \tilde{u}(0)$ , where  $\tilde{u}(0)$  is the velocity at the channel midplane, versus  $\tilde{y}$  is plotted on a double logarithmic scale for  $Kn=0.20$ . It is evident that, for  $\tilde{y} < 1$ , the velocity profiles follow the proposed power-law behavior. In Fig. 3.6b, the exponents obtained for each  $Kn$  are plotted and compared with the results available in literature. In particular, the found results agree well with those obtained using DSMC and employing the VSS interaction model, [79], as well as those obtained the solution of the linearized Boltzmann equation for a hard sphere gas, [73, 82]. The error bars in Fig. 3.6b represent the 99% confidence intervals for the regression calculations. For the first  $Kn$  value, equal to 0.0125, the error bars extend from 0.60 to 1.14. It is also evident that the error decreases with

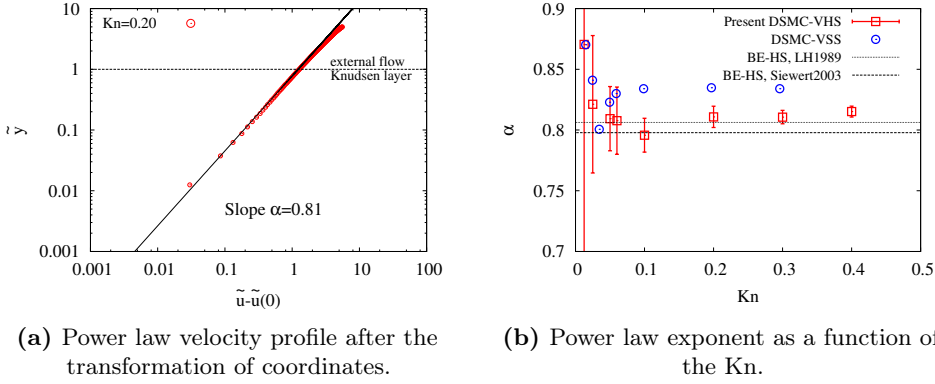


**Figure 3.6:** Knudsen layer formation: (a) Velocity profiles after the transformation of coordinates proposed in Eqs. (3.4, 3.5) and for  $Kn=0.20$ . The straight continuous line represents a power-law relation in the form of Eq. (3.1), with the slope equal to the exponent of such law ( $\alpha = 0.81$  for  $Kn=0.20$ ). The dashed horizontal line for  $\tilde{y} = 1$  represents a guide for the eye rather than a clear distinction between the inner Knudsen layer and the external flow region. (b) The values of the exponent  $\alpha$ , evaluated from the simulations performed with the present DSMC code and using the VHS collisional model (red squares), are plotted along with reference data for several  $Kn$ . A good agreement is found when comparing the results of simulations performed with another DSMC code using a VSS particle interaction model, [79] (DSMC-VSS in the caption), and with the solution of the linearized Boltzmann equation for a hard sphere gas. In [82]  $\alpha=0.806$  (in the legend indicated as BE-HS, LH1989), while in [73]  $\alpha=0.799$  (in the legend indicated as BE-HS, Siewert2003). The error bars represent the 99% confidence intervals for the regression calculation of the quantity  $\gamma$  from the fitting of Eq. (3.6). The width of the error bars for the data obtained from the present DSMC code results rapidly shrink while increasing  $Kn$  due to the larger number of data points present within the Knudsen layer. The fact that the results from the different methods show a good agreement confirms that the collisional model has a limited influence of the determination of the velocity profile within the Knudsen layer.

increasing  $Kn$ . This can be attributed to the fact that the number of cells available to fit the power-law within the Knudsen layer, given by  $KnN_{cell}$ , increases with  $Kn$ , leading to a smaller error in the regression calculations.

To conclude, the results provided by the present DSMC code show that the expected power-law behavior for the velocity profile within the Knudsen layer is accurately recovered. Moreover, by using a different molecular interaction model, VHS instead of HS or VSS, it was confirmed that the found power-law description is only weakly dependent on the chosen collisional model, thus suggesting, as stated in [79], that the power-law behavior is a physical phenomenon emerging, at least, for all monoatomic gases within the framework of the Boltzmann equation. It should also be noted that the underlined difference in the collision deflection angle law, as expressed in Eq. (3.3), has a limited influence on the viscosity cross-section

and therefore on the gas viscosity coefficient, while it has a large effect on the diffusion cross-section, i.e. on the self-diffusion coefficient, [1, 83]. This may be seen as a possible explanation of the fact that different molecular interaction models provide similar results for the investigated problem where only the viscosity coefficient plays a role.

### 3.2.2 Shear stress model

We also validated the DSMC code against literature shear stress models for rarefied gas flows. We employ a Couette flow problem set up to investigate the effects of Kn on the shear stress. A new set of simulations is performed to study this problem. In particular, we adopt a hard-sphere collisional model for the computational particles, assumed to represent an Argon gas (molecular mass  $m = 6.63 \cdot 10^{-26}$  kg and  $d_{\text{HS}} = 3.66 \cdot 10^{-10}$  m). The flow domain wall surfaces are maintained at  $T_w = 273$  K and a fully diffuse reflection is enforced for the molecule-wall interaction. The initial fluid temperature is also set at 273K, while the initial fluid density is set according to the desired Kn number and uniformly within the flow domain. The grid resolution is such that a minimum of 3 cells per mean free path is ensured. Each cell is initially populated with 30 particles. The time step is chosen to be five times smaller than the particle residence time in a cell, based on the most probable velocity at the initial temperature. The domain walls are put into motion with opposite velocity,  $u_w$ , and once the steady-state is reached, macroscopic flow variables are sampled every 10 time steps. At least  $1.0 \times 10^6$  samples are cumulated. A wide range of Kn is investigated, spanning from almost continuum flow conditions (Kn=0.0125) up to the free molecular flow regime (Kn=14.0). The imposed wall velocity,  $u_w$ , is such that the Mach number, defined as  $\text{Ma}_w = u_w/c_s$ , where  $c_s$  is the gas speed of sound at the initial temperature, is kept equal to 0.1 for any Kn. As mentioned in the previous paragraph, this is done to guarantee an isothermal condition, and, as a consequence, any temperature effect on the gas dynamic viscosity related to the particular chosen molecular interaction model can be excluded. Even in the most extreme case, in fact, the fluid temperature increase with respect to the initial temperature, is less than 1.5K. As underlined in [85], the shear stress for the Couette flow is characterized by two asymptotic behaviors for the limit cases of the continuum flow condition and the free molecular flow regime. According to the classical constitutive law for the Navier-Stokes equations, the shear stress is proportional to the velocity gradient and it is given by:

$$\tau_{xy,\text{cont}} = \mu \frac{du}{dy} = -\mu \frac{2u_w}{H}. \quad (3.7)$$

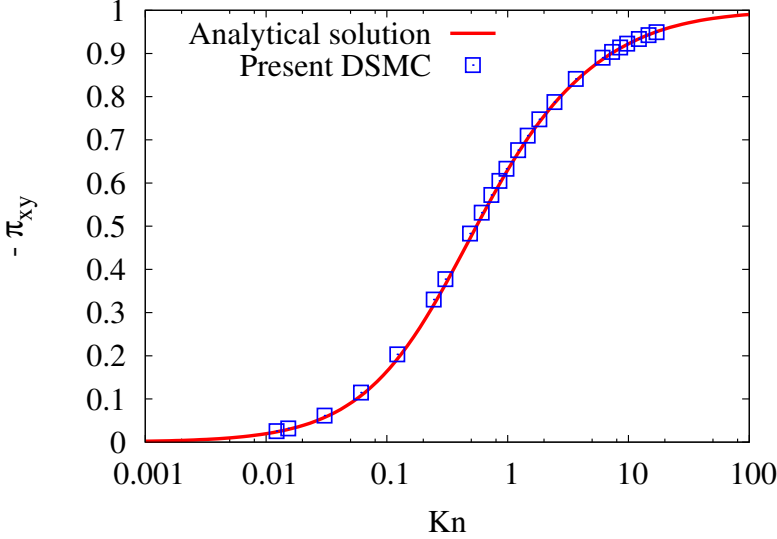


**Figure 3.7:** Variation of the normalized shear stress as a function of  $Kn$  for the Couette flow simulations (blue symbols) compared with the analytical relation, Eq. (3.9), obtained in [84] from the solution of the linear Boltzmann equation and using a hard-sphere interaction model. A very good agreement (maximum deviation about 1% for the DSMC data with respect to the analytical solution) is found over the whole investigated  $Kn$  range.

In Eq. (3.7),  $\mu$  is the dynamic viscosity and  $H$  is the channel height.

At the other extreme, in the free molecular flow regime, the shear stress is given as, [86]:

$$\tau_{xy,\infty} = -\rho u_w \sqrt{\frac{2RT_w}{\pi}}, \quad (3.8)$$

where  $\rho$  is the fluid density, and  $R$  is the specific gas constant.

In order to match the two extremes in a single model, which can then be used also for engineering applications, several relations appeared in literature. Both empirical relations, see e.g. [85] and [87], as well as analytical solutions are available. In particular, in this section we compare the results provided by the present DSMC code with the analytical solution provided in [84] and expressed as:

$$\pi_{xy} = -\frac{aKn^2 + bKn}{aKn^2 + cKn + d}, \quad (3.9)$$

where  $\pi_{xy}$  is the shear stress normalized with the free molecular shear stress, given by Eq. (3.8). In Eq. (3.9), the coefficients  $a$ ,  $b$ ,  $c$ , and  $d$  depend on the inter-particle

collision model, and, for the case of hard-sphere particles, they are given by:

$$a = 1.3056, \quad b = 2\pi, \quad c = 7.5939, \quad d = \pi. \quad (3.10)$$

In Fig. 3.7, the results from the DSMC simulations are plotted together with the analytical solution provided by Eq. (3.9). A very good agreement is found over the whole range of the investigated Kn numbers as the maximum deviation from the reference solution, in fact, is at most 1%.

### 3.2.3 Lid-driven cavity flow

The cavity flow problem is a common benchmark test for the validation of continuum flow numerical solver, [88, 89], but it can also serve as a validation test for the present DSMC code. In fact, the effects of rarefaction on the flow properties have been investigated by means of a variety of numerical tools.

In [90], the problem is treated by adopting a Discrete Velocity Method (DVM) to solve the linearized Bhatnagar-Gross-Krook kinetic equation in order over a wide range of rarefaction conditions.

In [91], instead, the so-called Discrete Unified Gas Kinetic Scheme (DUGKS), a finite volume scheme for the solution of the Boltzmann equation with the BGK collision model, characterized by a flexible mesh adaptation for the particle velocity space, is employed. A good agreement for the velocity field with the reference DSMC solution, [92], is found.

A finite difference scheme to compute the solution of the regularized 13 moment equations (R13), as proposed in [93, 94], is adopted in [95]. The results found show a reasonable accuracy with the DSMC data for the temperature field also for a flow in the transition flow regime ( $\text{Kn} \approx 0.4$ ).

Despite the variety of the employed approaches, the DSMC solution, however, is generally used as the benchmark one. In this paragraph, therefore, we adopt the DSMC results from [92, 96] as the reference for the validation of the present code. For all the simulations whose results are reported here, the gas is assumed to consist of monoatomic molecules corresponding to that of Argon with mass  $m = 6.63 \times 10^{-26}$  kg. The variable hard sphere collision model is used, setting a reference particle diameter equal to  $d = 4.17 \times 10^{-10}$  m.

In order to ensure the accuracy of the computed flow variables, the DSMC guidelines on space and time discretization have been followed. In Fig. 3.8, the geometry configuration of the square cavity, of size  $L$ , is shown. Fully diffusive reflection is imposed at the cavity walls. The top lid moves with a fixed tangential velocity  $U_w$  in the positive  $x$ -direction while the other walls are stationary. The wall temperature and the initial gas temperature are set to  $T_w = T_0 = 273$  K.



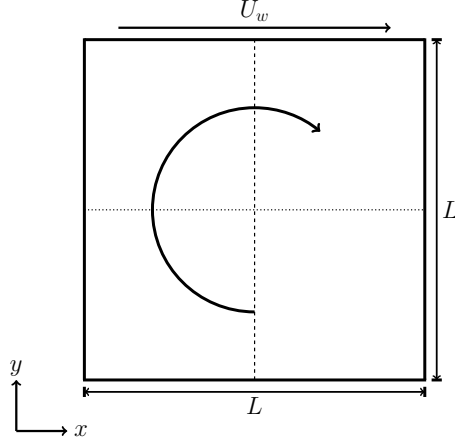


**Figure 3.8:** Geometry of the flow domain used in the DSMC simulations to study the cavity flow problem. The top wall is moving with a positive velocity along the  $x$ -direction,  $U_w$ . The dashed vertical line is placed at  $x/L = 0.5$ , while the dotted horizontal line is located at  $y/L = 0.5$ . A large scale vortex occupying the whole domain (represented by the circular arrow) is expected to develop.

A wall Mach number, based on the lid velocity and the speed of sound evaluated at the wall temperature, can be defined as:

$$\text{Ma}_w = \frac{U_w}{\sqrt{\gamma R T_w}}, \quad (3.11)$$

where  $\gamma$  and  $R$  are the specific heat and gas constant for Argon, respectively. The rarefaction conditions are adjusted by varying  $\text{Kn}$ , defined as

$$\text{Kn} = \frac{\lambda_0}{L}. \quad (3.12)$$

The desired  $\text{Kn}$  value is achieved by changing the mean free path  $\lambda_0$  which, in turn, is set by properly fixing the initial gas density  $\rho_0$  according to the typical relation for VHS particles, [1]:

$$\lambda_0 = \frac{2(5 - 2\omega)(7 - \omega)}{15} \frac{\mu_0}{\rho_0} \left( \frac{m}{2\pi k_B T_0} \right)^{1/2}, \quad (3.13)$$

where  $\mu_0$  represents the reference dynamic viscosity at the initial temperature  $T_0$ . To validate the present DSMC code, the impact of the lid velocity and  $\text{Kn}$  on the flow behavior are investigated.

### Influence of the lid velocity

At first, the influence of the lid velocity is verified. The flow velocity components,  $u$  and  $v$ , in the  $x$ - and  $y$ -directions, normalized with the wall velocity as

$$U = \frac{u}{U_w}, \quad V = \frac{v}{U_w} \quad (3.14)$$

are shown in Figs. 3.9a, 3.9b and 3.9c, 3.9d for  $Ma_w=0.16$  and  $Ma_w=0.65$ , respectively. In both cases,  $Kn=1.0$ . With the considered value of  $Kn$ , the two Mach numbers provide values of the Reynolds number, calculated on the basis of the lid velocity as:

$$Re = \frac{\rho_0 U_w L}{\mu_0}, \quad (3.15)$$

equal to about 0.3 and 1.2. The velocity profiles  $U(y/L)$  and  $V(x/L)$  are plotted along the centerline axis drawn in Fig. 3.8 as the dashed vertical line ( $x/L = 0.5$ ) and the dotted horizontal line ( $y/L = 0.5$ ), respectively. A very good agreement is found between the present DSMC code results and the reference DSMC data, [92], for both the velocity components profiles and for both the values of the wall Mach number.

For illustration purposes, the velocity vectors overlaid on the velocity magnitude field, in turn normalized with the lid velocity, are shown in Fig. 3.10. In Fig. 3.11, finally, the velocity profiles obtained from the simulations at the two investigated Mach numbers are compared in the same graph. The  $U$  profile is characterized by a velocity slip at the upper and lower walls. Moreover, it is interesting to verify that this profile is largely unaffected by the significant change in the lid velocity. A more evident effect caused by the larger lid velocity, instead, is visible on the  $V$  velocity component. Increasing the lid velocity reduces the symmetrical behavior about the vertical line crossing the cavity center as it is also typically found for the continuum case when  $Re > 0$ .

### Influence of the Knudsen number

After having analyzed the impact of the lid velocity on the flow field, the effects on the flow properties induced by rarefaction are studied. In particular, keeping constant the wall Mach number  $Ma_w=0.16$ , six simulations characterized by  $Kn$  ranging from the slip regime ( $Kn=0.1$ ) through the free molecular regime ( $Kn=8$ ), are performed. In Figs. 3.12a and 3.12b, the  $U$  and  $V$  velocity profiles, measured along the horizontal and vertical axis passing through the center of the cavity, are plotted for the different tested  $Kn$ . As expected, the slip at the wall, for both  $U$  and  $V$ , increases while increasing  $Kn$ . More in details, for the  $U$  profiles, this

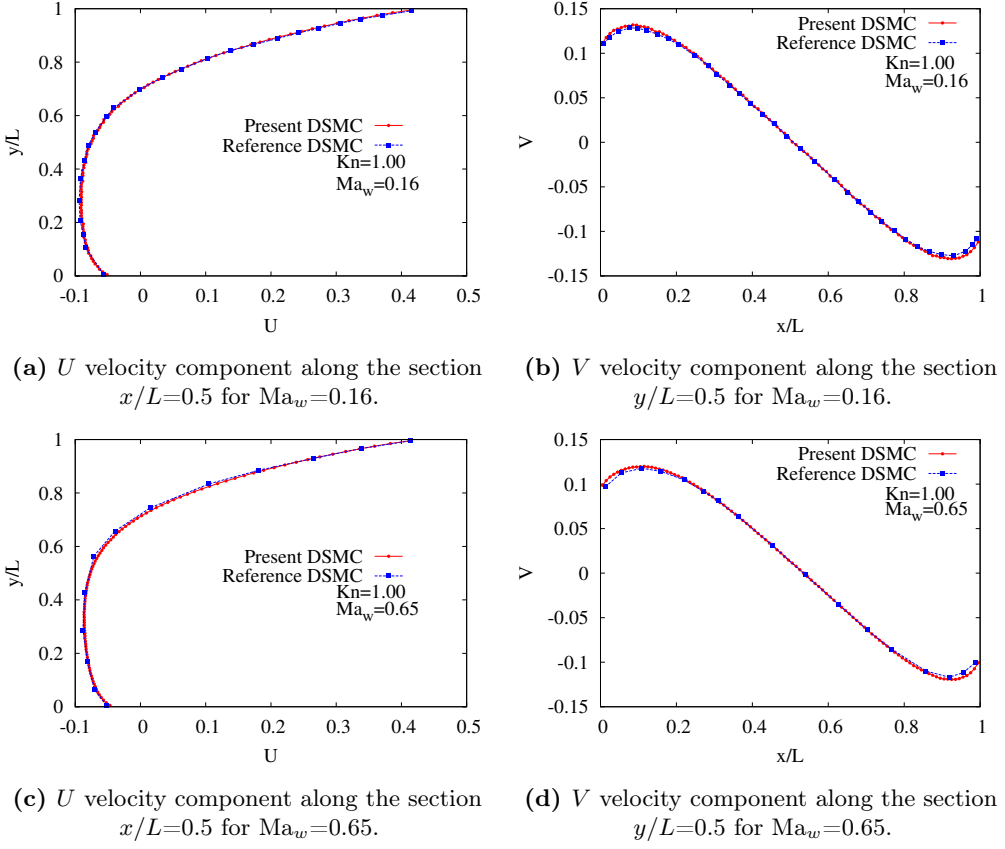


**Figure 3.9:** Lid-driven cavity flow:  $U$  and  $V$  velocity components plotted along the sections at  $x/L=0.5$ , (a), (c), and at  $y/L=0.5$ , (b), (d), for the two investigated  $Ma_w$ . The initial gas density, set homogeneously within the flow domain, is such that  $Kn=1.0$ . A very good agreement with the reference DSMC data, [92], is obtained. At the top wall ( $y/L=1$ ), a large slip velocity due to the rarefaction conditions is measured, ( $U \cong 0.415$  vs  $U=1.0$  at continuum flow conditions). A large slip is also present at  $x/L=0, 1$  for the  $V$  velocity component.

rarefaction effect is particularly evident at the wall located at  $y/L = 1$ . In fact, already for  $Kn=0.1$ , the fluid velocity is about 35% smaller than the imposed lid velocity. Also for  $y/L = 0$ , the fluid velocity  $U$  shows a non-zero value for all the investigated  $Kn$  numbers. For the  $V$  velocity profiles, it is also clear that the slip velocity at the walls for both  $x/L = 0$  and  $x/L = 1$  increases while increasing  $Kn$ . To conclude this section, the cavity flow has been used as a validation test for the present DSMC code. The impact of the rarefaction conditions and of the lid velocity have been investigated finding a very good agreement with the reference

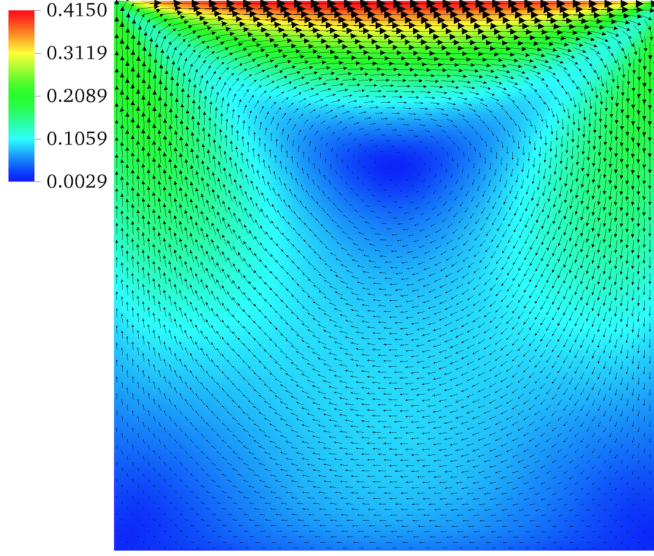


**Figure 3.10:** Lid-driven cavity flow: velocity vectors plotted on top of the velocity magnitude field, and normalized with the lid velocity, for the  $Ma_w=0.16$  and  $Kn=1.0$  case. A vortex occupying the whole flow domain develops. The maximum flow velocity, found in proximity of the top moving wall, is only 0.415 times the imposed wall velocity. Such large velocity slip is the typical result of the substantial rarefaction conditions present for the performed test.

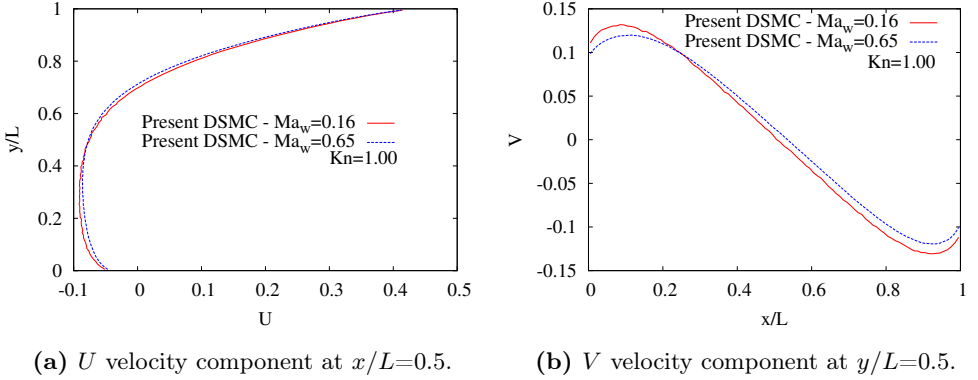


**Figure 3.11:** Lid-driven cavity flow: comparison of the  $U$  and  $V$  velocity components for the two investigated  $Ma_w$  at  $Kn=1.0$ . While the influence of  $Ma_w$  is rather limited for the  $U$  component, in fact the same slip velocity at the walls at  $y/L=0$  and  $y/L=1$  is measured, a larger effect is visible on the  $V$  component.

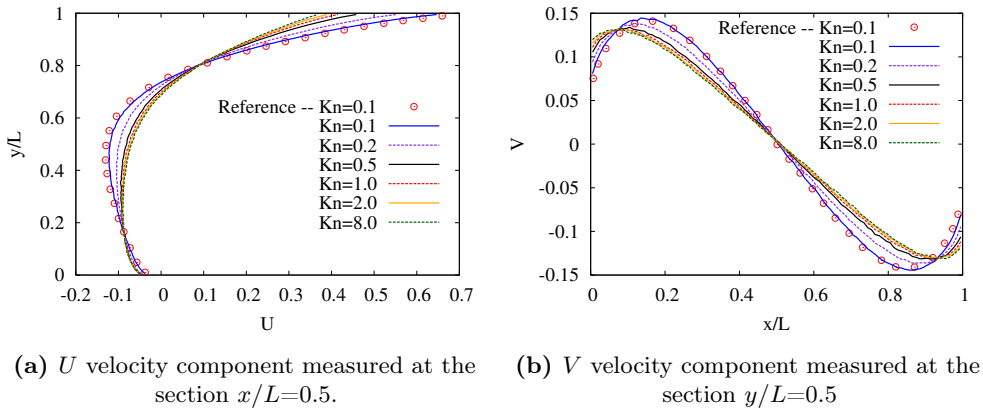


**Figure 3.12:** Lid-driven cavity flow: the influence of the rarefaction conditions is measured. (a)  $U$  velocity profile at  $x/L=0.5$ ; (b)  $V$  velocity profile at  $y/L=0.5$ . All the simulations are performed with  $Ma_w=0.16$ . For readability, the comparison with the reference data from [92] is shown only for  $Kn=0.1$ . A good agreement is found for the present DSMC code. A similar level of accuracy is reached also for the profiles at the other investigated  $Kn$  numbers. The main effect of rarefaction conditions is to increase the slip velocity.

data from [92].

### 3.2.4 Flows with open boundary conditions

The implementation of open boundary conditions in a particle-based method, namely the imposition of a desired pressure or mass flow rate at the inlet/outlet sections of the flow domain, faces difficulties related to the fact that macroscopic flow variables have to be imposed by properly setting the number and the microscopic properties of the sampled particles, such as their velocity and internal energy. In this work, moreover, we are mainly interested in the simulation of subsonic flows within microchannels and this poses further challenges in the proper definition of the inlet/outlet boundary conditions with respect to the classical boundary conditions employed in the DSMC method, which are suitable when simulating external high speed flows. In this last case, in fact, one is free to specify all the macroscopic flow properties, defining the so-called stream boundary condition. Particles, in fact, are simply removed when they cross inlet or outlet boundaries and a given number of particles are injected into the cells at the inlet and the outlet, according to a Maxwellian distribution, provided that the macroscopic velocity, temperature and number density at those locations are known. Eventually, in the case of vacuum conditions, particles are just removed as soon as they cross the inlet or outlet

boundaries.

In contrast, at the inlet section of a subsonic flow, information on one of the macroscopic flow variables has to come from the interior part of the flow domain. At the outlet section, then, only one of the macroscopic flow properties can be specified, while all the other needed flow properties must be obtained from inside the flow domain.

Two types of inlet boundary conditions for subsonic flows have been proposed in literature: one in which the pressure and temperature of the incoming flow are prescribed (pressure boundary condition) and one in which the mass flow rate and temperature are specified (mass flow rate boundary condition). For each of these two types, several implementations are available.

As underlined in [97], in all pressure boundary condition treatments, information about the streamwise velocity is obtained from within the flow domain. This macroscopic velocity, then, represents the mean velocity of the sampled particles. The streamwise velocity can be accessed in a variety of ways: instantaneous calculation of the average velocity of the particles crossing the inlet boundary, [98–100]; use of the continuum characteristic line method to compute the streamwise velocity at the location of the inlet boundary, [101]; 0-th order extrapolation of the streamwise velocity, [51, 102, 103]. This last approach is also the method implemented in the present work.

We provide now few details about the implementation of this kind of inlet pressure boundary condition. The following discussion assumes that the problem is defined so that the inlet/outlet surfaces are normal to the  $x$ -component of the mean flow velocity vector but the implementation can be easily extended to arbitrarily oriented boundary surfaces by considering the component of the inflow vector that is normal to the boundary face.

The instantaneous, streamwise velocity in each cell  $j$  along the inlet boundary,  $U_{in,j}$ , is obtained by calculating the average of the streamwise velocity component of each individual particle,  $u_{p,j}$ :

$$U_{in,j} = U_j = \frac{1}{N_{p,j}} \sum_{p=1}^{N_{p,j}} u_{p,j}. \quad (3.16)$$

In Eq. (3.16),  $N_{p,j}$  is the number of particles in the cell  $j$ . Since we are interested in obtaining steady-state solutions, the instantaneous values are averaged over time.

The inlet number density,  $n_{in}$  is determined, using the ideal gas equation of state,

from the imposed pressure,  $p_{in}$ , and the temperature,  $T_{in}$ , as:

$$n_{in} = \frac{p_{in}}{k_B T_{in}}, \quad (3.17)$$

where  $k_B$  is the Boltzmann constant.

The values of  $U_{in,j}$ ,  $n_{in}$  and  $T_{in}$  are then used to calculate the number of particles to be injected in each cell  $j$ , see e.g. [102]:

$$N_{in,j} = \frac{n_{in} C_m M}{2\sqrt{\pi}} \Delta t A_{\text{face}}, \quad (3.18)$$

where

$$M = \exp\left(-\frac{U_{in,j}^2}{C_m^2}\right) \pm \sqrt{\pi} \frac{U_{in,j}}{C_m} \left[1 \pm \operatorname{erf}\left(\frac{U_{in,j}}{C_m}\right)\right], \quad (3.19)$$

$$C_m = \sqrt{2k_B T/m}, \quad (3.20)$$

with  $C_m$  the most probable molecular speed,  $\Delta t$  the simulation time step,  $A_{\text{face}}$  the area of the cell face that lies on the inlet boundary. The particle velocity  $C = (u_p, v_p, w_p)$  is then sampled from a Maxwellian distribution in the form

$$f_{in}(C) = \frac{2u_p}{\pi C_m^4 M} \exp\left(-\frac{1}{C_m^2} \left[(u_p \mp U_{in,j})^2 + v_p^2 + w_p^2\right]\right). \quad (3.21)$$

The plus sign in the Eqs. (3.19) and (3.21) is for the upstream case (particles flowing into the domain through the inlet boundary), and the minus sign is for the downstream case (particles flowing into the domain through the outlet boundary). For what concerns the mass flow rate boundary condition, two approaches are available. The first method, reported in [99], prescribes that the average density in the cells along the inlet boundary is obtained by weighting the sampled density in each cell by the height of the cell. The average density is then used at the inlet, along with the assumption of constant velocity magnitude across the inlet and the specified total mass flow rate, to compute the inflow velocity.

In the second approach, reported in [97] and implemented also in this work, the assumption of a uniform velocity magnitude across the inlet surface is replaced with a uniform mass flux,  $\dot{m}/A$ , across the inlet surface, where  $\dot{m}$  and  $A$  are the desired mass flow rate and total area of the inlet boundary, respectively. The mean streamwise inlet velocity at each cell face is calculated from Eq. (3.16) and the inlet number density at each cell face is given by:

$$n_{in,j} = \frac{\dot{m}}{U_{in,j} A} \frac{N_A}{\mathcal{M}}, \quad (3.22)$$

where  $N_A$  is the Avogadro number and  $\mathcal{M}$  is the gas molecular weight. The values of  $n_{in,j}$  and  $U_{in,j}$  are used to calculate the number of the sampled particles at each cell face by using Eq. (3.18) and the velocity components of each of those particles using Eqs. (3.19) and (3.21).

As underlined in [97], during the transient phase of the simulation, it is possible that the velocity provided by Eq. (3.16) becomes negative, meaning that the direction of the average flow velocity at the inlet is pointing out of the domain. When this occurs, the inlet velocity is not updated and the value from the previous time step is used also at the current time step.

With respect to the last issue, in the present implementation we impose a stricter condition. In fact, to avoid that, in the case  $U_{in,j}$  is close to zero, a large number of particles is generated in a single time step, a minimum allowable streamwise inlet velocity,  $V_{init}$ , is initially set in the simulation.

Fig. 3.13 shows the probability distribution function of the injected number of particles per cell,  $N_{in,j}$ , at each time step. The data for three different  $V_{init}$  are shown. It is clear that the closer the  $V_{init}$  to zero, the more probable that a large number of particles is generated at each time step, this representing an issue from the computational point of view. Ideally, the closer the  $V_{init}$  to the value of the streamwise flow velocity provided by the final solution, the better for the solution to efficiently reach the final solution.

Several approaches have been proposed in literature also for the subsonic outlet boundary conditions in order to allow a constant pressure to be specified. They all share the same idea that the particles entering the domain are modeled as having come from an equilibrium reservoir at the specified pressure. The other properties, required to fully characterize the reservoir, are the density and the flow velocity components and they can be obtained from the domain interior. The different approaches vary according to the way in which such required flow properties are calculated at the outlet. A possible method involves a combination of the estimates of the average velocity of the particles crossing the outlet boundary, [99]. Another method considers the 0-th order extrapolation of the macroscopic properties in the first cell along the outlet to the boundary surface, [51], and finally the possibility to use the continuum characteristic line method to compute the macroscopic properties at the outlet boundary, [98, 100–102]. This last approach is also the one implemented in this work. The use of the theory of characteristics implicitly assumes that the flow is locally inviscid and adiabatic. Following the formulation in [104], the macroscopic flow variables can be obtained at each cell  $j$  at the outlet



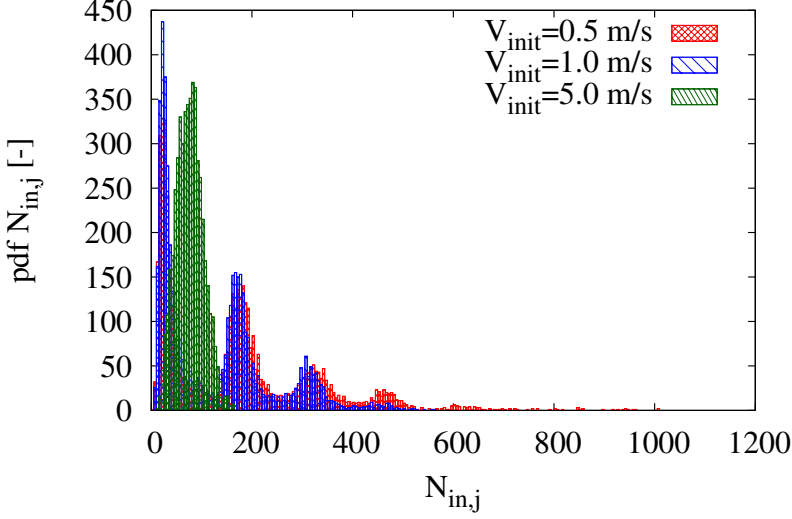


**Figure 3.13:** Mass flow rate boundary conditions: probability distribution function of the number of particles injected at each time step per cell. The initial threshold velocity,  $V_{init}$ , is used as parameter. For  $V_{init}=0.5$  m/s, up to 1000 particles per time step per cell are injected. This extreme number is sensibly reduced when the threshold velocity is increased to 5 m/s when, at most, about 180 particles are injected. The average number of particles expected to be injected is 100 and it is based on the prescribed mass flow rate. The bin width is equal to 5 particles.

as:

$$(\rho_o)_j = \rho_j + \frac{p_o - p_j}{(c_{s,j})^2}, \quad (3.23)$$

$$(U_o)_j = U_j + \frac{p_o - p_j}{\rho_j c_{s,j}}, \quad (3.24)$$

$$(V_o)_j = V_j, \quad (3.25)$$

$$(T_o)_j = \frac{p_o}{(\rho_o)_j R}, \quad (3.26)$$

$$(n_o)_j = \frac{(\rho_o)_j}{m}, \quad (3.27)$$

where  $V$  is the flow velocity component normal to the outlet surface and  $c_s$  is the speed of sound. From these values, using Eqs. (3.18-3.21), the properties of the particles entering through the outlet boundary can be determined. A full treatment to derive the relations of Eqs. (3.23-3.27) can be found in [104, 105].

Finally, few additional considerations on the number of sampled particles for both the inlet and outlet boundary conditions are needed. As underlined in chapter 6, instead of injecting a number of particles as determined by the value provided by Eq. (3.18), we inject a number of particles determined by sampling a Poisson distribution with the mean given by Eq. (3.18). This, indeed, is more consistent with the physics of the system as, from equilibrium statistical mechanics, [46], we expect that the number of particles leaving a reservoir at equilibrium conditions during a fixed time interval, to be Poisson-distributed. Moreover, it has been shown in [106] that this procedure eliminates possible non-physical non-equilibrium effects originated from correlations of momentum and density fluctuations when injecting a number of particles as obtained from Eq. (3.18). In the remaining part of this section, we present the results of the validation of the just described inlet/outlet boundary conditions for the case of a 2D plane channel flow. Firstly, we investigate the case of the pressure boundary condition, and, then, the case of the mass flow rate boundary condition. Results obtained from the present DSMC code are compared with those obtained from other DSMC codes and with analytical relations when these are available. Finally, few remarks about compressibility and rarefaction effects on the pressure distribution within the channel flow are drawn.

### Pressure boundary condition

The first test aims to validate the implementation of the pressure boundary conditions. The simulation set-up is described in Table 3.3 and it prescribes the flow of a gas composed of  $O_2$  molecules within a microchannel at slip flow conditions. The domain geometry is shown in Fig. 3.14. As reported in Table 3.3, while the cell size along the direction transversal to the flow, which is the direction of greatest gradients in the flow properties, is based on the requirements for an accurate DSMC simulation, the cell size along the main flow direction is greatly enlarged, considering the small ratio of the gradient length scale along the flow and transversal to the flow directions. In Fig. 3.15, the results obtained with the present DSMC code are compared with the DSMC data from [51] and with the analytical results provided in [107]. The analytical relation is obtained from the solution of the Navier-Stokes equations supplemented with first-order slip boundary conditions. For the pressure distribution along the flow direction  $x$ , one has:

$$\frac{p}{p_o} \left( \frac{x}{L} \right) = \sqrt{\left( 6Kn_o \frac{2-\sigma}{\sigma} + \frac{p_i}{p_o} \right)^2 - \frac{x}{L} \left( \left( \frac{p_i}{p_o} \right)^2 - 1 + 12Kn_o \frac{2-\sigma}{\sigma} \left( \frac{p_i}{p_o} - 1 \right) \right)} + 6Kn_o \frac{2-\sigma}{\sigma}, \quad (3.28)$$

Parameter	Value
Gas	O <sub>2</sub>
Channel length, $L$ , $\mu\text{m}$	15.0
Channel h, $H$ , $\mu\text{m}$	0.53
Inlet pressure, Pa	$2.5 \times 10^5$
Outlet pressure, Pa	$1.0 \times 10^5$
Time step, s	$1.0 \times 10^{-11}$
$T_{\text{wall}}$ , K	300
$T_{\text{in}}$ , K	300
Number of cells	$80 \times 50$
Number of particles per cell	100
Viscosity index, $\omega$	0.77
VHS diameter, m	$4.07 \times 10^{-10}$
VHS reference temperature, K	273
Wall accommodation coefficient, $\sigma$	1

**Table 3.3:** Pressure boundary conditions validation: summary of the parameters of the DSMC microchannel simulations. The flow domain is discretized with 80 and 50 cells along the axial and transversal directions, respectively. The microchannel aspect ratio, defined as the ratio between the length and height of the channel,  $AR=L/H$ , is equal to  $AR=28.3$ , and so sufficiently large to allow a fair comparison with the analytical results derived in [107]. The gas is composed of O<sub>2</sub> molecules and the VHS interparticle collision model is adopted. Each cell is initially populated with 100 particles and the initial pressure field is fixed at the average value between the inlet and the outlet pressure values.

where the pedices  $i$  and  $o$  indicate quantities at the inlet and outlet conditions, respectively.

A very good agreement is found with the numerical DSMC results from [51]. We underline that the pressure profile within the channel is not linear. We will come

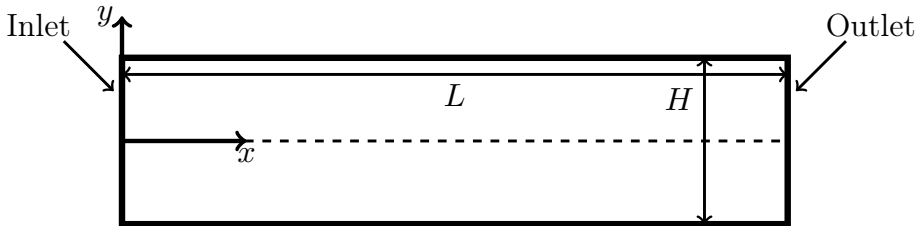


**Figure 3.14:** Microchannel geometry. The dimensions in SI units, as well as the pressure values at the inlet and outlet sections, are reported in Table 3.3.

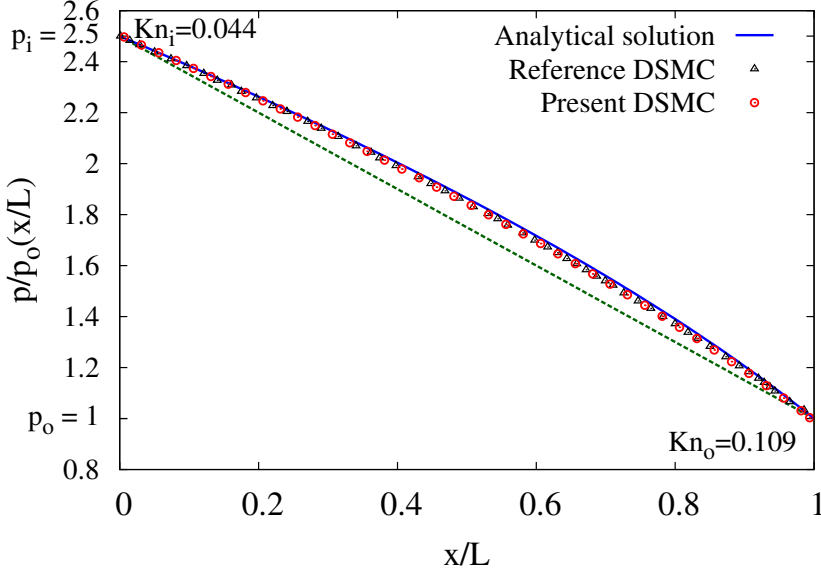


**Figure 3.15:** Validation for the pressure boundary conditions: comparison among the numerical data provided by the present DSMC code (red circles), the reference DSMC, [51], (black triangles) and the analytical relation for the pressure distribution, Eq. (3.28) (blue line). The simulation settings are reported in Table 3.3. From the inlet and outlet imposed pressure, and from the height of the channel, the inlet and outlet  $Kn$  reported in the plot can be calculated. The dashed green line represents the linear pressure distribution between the imposed pressures. The actual profile deviates from the linear one. Later, we will show that this is due only to a compressibility effect.

back later on this point trying to clarify that this effect is not a rarefaction effect, but, rather, a compressibility one. A small deviation from the analytical pressure distribution is found. This can be attributed to the fact that the local  $Kn$  while approaching the outlet section becomes larger, going beyond the range of validity (slip flow regime) for the analytical results. In Fig. 3.16, the distribution of the axial velocity at the channel centerline as obtained from the present DSMC is compared with the DSMC results in [51] and in [97], as well as with the analytical solution provided in [107], and reported here:

$$U\left(\frac{x}{L}\right) = \frac{1}{2\mu} \frac{dp}{dx} \left( -H^2 Kn \frac{2-\sigma}{\sigma} - \frac{H^2}{4} \right). \quad (3.29)$$

In Fig. 3.29,  $dp/dx$  is the pressure gradient evaluated from Eq. (3.28). Also in this case, a good agreement with the reference data is found and, as previously

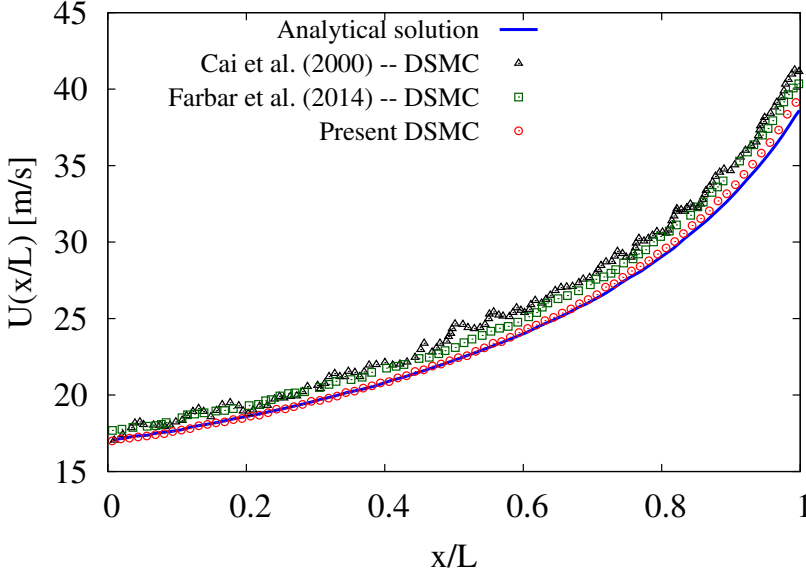


**Figure 3.16:** Validation for the pressure boundary conditions: comparison among the numerical data provided by the present DSMC code (red circles) as well as from [51] (indicated as Cai et al. (2000) in the legend, black triangles) and from [97] (indicated as Farbar et al. (2014) in the legend, green squares) and the analytical results for the axial velocity at the channel centerline, Eq. (3.29), blue line. The simulation set-up conditions are reported in Table 3.3. A close agreement with the analytical results is found for the present DSMC data. A clear deviation starts to appear while approaching the outlet section at  $x/L = 1$  as the Kn goes beyond the slip flow regime limit. Note also that the present DSMC data appear to be much less noisy than those from the other two references, [51] and [97].

detected for the pressure distribution, the present DSMC data and the analytical solution start to diverge while getting closer to the outlet section at  $x/L = 1$ . This, again, can be explained invoking the increasing Kn.

In Fig. 3.17, the pressure and axial velocity contours within the microchannel are visualized.

### Mass flow rate boundary condition

We now consider the case of the mass flow rate boundary condition. The same simulation set-up used for the pressure boundary condition is employed here, apart from the inlet condition where, instead of a fixed pressure value, we impose a given mass flow rate. For validation purpose, this value is chosen to be equal to the one

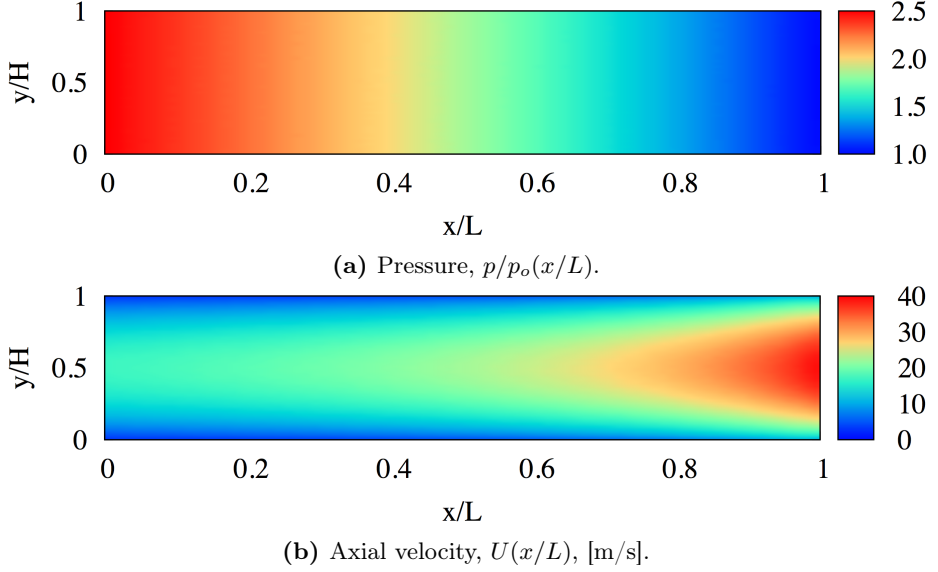


**Figure 3.17:** (a) Contours of the pressure  $p/p_o(x/L)$ , and (b) of the axial velocity  $U(x/L)$  in the microchannel for the simulation settings reported in Table 3.3 and applying the pressure boundary conditions at the inlet and outlet. At any given section  $x/L=\text{const.}$ , the pressure distribution is constant over the channel height.

we calculate from the pressure boundary condition simulation as

$$\dot{m} = \int_0^H \rho U(y) dy. \quad (3.30)$$

The value obtained from the DSMC simulation when pressure boundary conditions are applied is equal to  $2.18 \times 10^{-5}$  kg/s and it is very close to the value of  $2.17 \times 10^{-5}$  kg/s, obtained from the analytical relation:

$$\dot{m} = \frac{H^3 w p_o^2}{24 \mu L R T_{in}} \left( \left( \frac{p_i}{p_o} \right)^2 - 1 + 12 \frac{2 - \sigma}{\sigma} \text{Kn}_o \left( \frac{p_i}{p_o} - 1 \right) \right), \quad (3.31)$$

derived in [107] and where  $w$  is the channel depth.

In Fig. 3.18a, the pressure distributions obtained from the simulations using the two boundary conditions are plotted. A very good agreement between the two is found, meaning that the mass flow rate boundary condition provides the expected results. Finally, in Fig. 3.18b, the centerline axial velocity is plotted, again finding a good agreement with the DSMC data from [97] and the analytical solution,

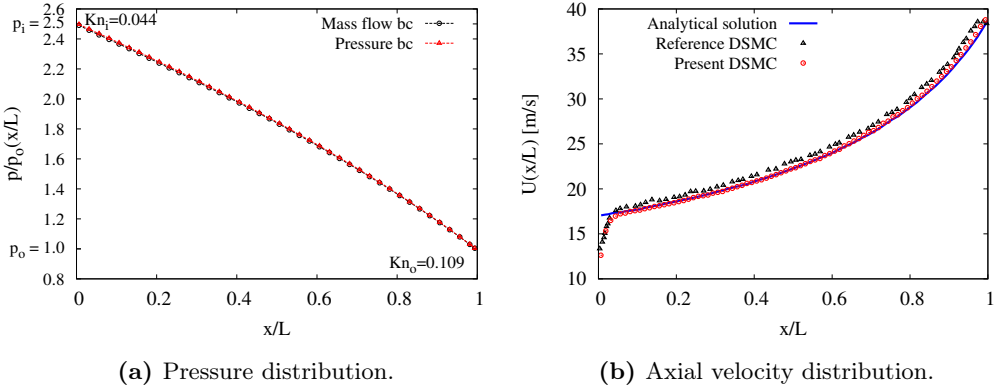


**Figure 3.18:** Validation for the mass flow rate boundary conditions: (a) comparison among the pressure distributions obtained imposing the pressure (red triangles) and the mass flow rate (black circles) boundary condition, respectively. The imposed inflow mass flow rate is computed as the value obtained from the pressure boundary condition simulation using Eq. (3.30). Since a very good agreement between the two curves is found, the validity of the implementation of the mass flow rate boundary condition is confirmed. (b) Axial velocity distribution at the channel centerline for the mass flow rate boundary condition as obtained from the present DSMC (red circles) and from the reference DSMC data (black triangles), [97]. A clear entrance effect is visible. The analytical profile plotted here is the one obtained when imposing the pressure boundary condition, Eq. (3.29), and, therefore, it does not show the entrance effect. With respect to the reference data, [97], the results of the present DSMC are closer to the analytical solution.

excluding the entrance area. For  $x/L \lesssim 0.05$ , in fact, a clear entrance effect is visible. This is present because of a uniform mass flux,  $\dot{m}/A$ , across the inlet surface, is imposed.

### Compressibility and rarefaction effects

Finally, we examine the influence of rarefaction and compressibility on the pressure distribution along the microchannel centerline. As already mentioned, the pressure shows a non-linear variation. This evidence is sometimes erroneously attributed to the influence of the gas rarefied conditions, see e.g. [108]. In fact, the non-linearity is solely a compressibility effect as underlined by the analytical solution provided in [107]. This can be also proven numerically by performing DSMC simulations at several pressure ratios while keeping fixed the Kn at the inlet and outlet conditions, and varying the rarefaction conditions while keeping constant the pressure ratio. In Fig. 3.19a, the pressure profiles obtained from the DSMC simulations characterized by different values of the pressure ratio are collected. It is evident that the smaller the pressure ratio, and therefore the compressibility effects, the closer the

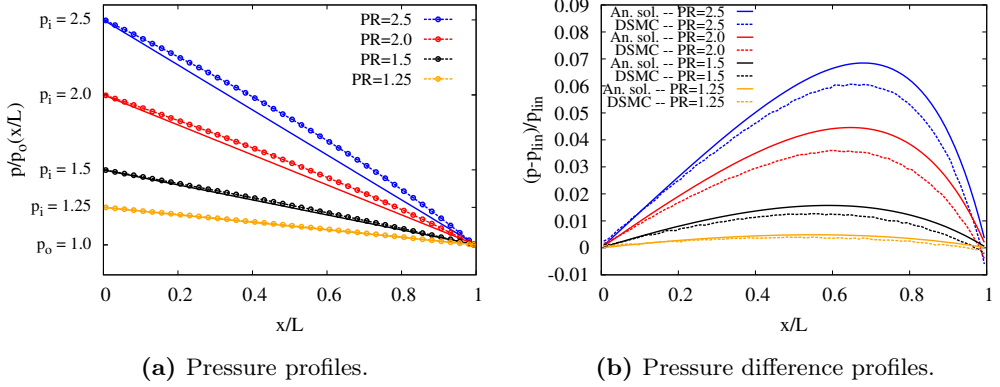


**Figure 3.19:** Effect of the pressure ratio (PR) on the linearity of the pressure profile for the microchannel flow: (a) DSMC pressure distribution along the microchannel with the pressure ratio (PR) as parameter while keeping constant the Kn ( $Kn_i=0.044$  and  $Kn_o=0.109$  at the inlet and outlet sections, respectively). The smaller the pressure ratio, the closer the distribution to a linear profile, the proper one for an incompressible gas flow. (b) Difference between the actual pressure profile and the linear one, then further normalized with the linear distribution, while keeping constant the Kn and changing the pressure ratio (PR). The continuous lines represent the analytical relation of Eq. (3.28) and the dashed lines represent the DSMC data. It is clear that the compressibility effects act in the sense of increasing the non-linearity of the pressure profile.

pressure distribution to a linear profile. This is also confirmed by inspecting the plots of Fig. 3.19b, where the difference between the actual profile and the linear one, then normalized with the linear profile, is plotted for each pressure ratio. The smaller the pressure ratio, the smaller the quantity plotted in Fig. 3.19b, meaning that the non-linearity of the pressure profile decreases. It has to be noted that in a standard DSMC simulation, the computational gas follows the ideal gas law, and, therefore, the only way to vary the compressibility is to limit the pressure differences within the flow. The effects induced by the rarefaction conditions are also evaluated. In particular, looking at the plot of Fig. 3.20, it is clear that the larger the Kn, the closer the pressure profile to the linear one. Therefore, it is confirmed that the non-linearity of the pressure profile can be attributed to the gas compressibility. Concluding this section, we have validated the implementation of open boundary conditions in the present DSMC code. In particular, the pressure boundary condition, for which the pressure at the inlet is prescribed, and the mass flow rate boundary condition, for which the mass flow rate at the inlet is imposed, have been tested against analytical results for the slip flow regime and other reference DSMC data finding a good agreement.



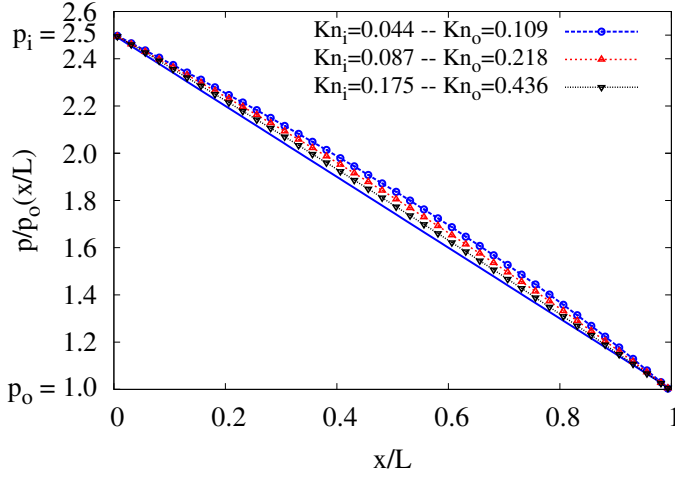


**Figure 3.20:** Influence of the rarefaction conditions on the linearity of the pressure profile for the microchannel flow. While the pressure ratio is kept constant, the indicated values of the  $Kn$  at the inlet and outlet conditions,  $Kn_i$  and  $Kn_o$ , are obtained by adjusting the height of the microchannel. The main result is that the larger the  $Kn$ , the more linear the pressure distribution.

### 3.3 Conclusions

Concluding this chapter, we firstly provided few details about the implementation of the algorithm adopted in the DSMC code developed during the PhD project. We underlined that the peculiar treatment of the streaming step phase, which allows the particles to move at each substep not further than a distance equal to the cell size, thus mimicking the LBM approach, ensures the efficiency of the parallelization routine and of the particle-wall interactions.

We then focused on the validation of the DSMC code against classical problems encountered in rarefied gas flow literature. In particular, the tests covered the formation of the Knudsen layer within the flow field in proximity of a moving wall. The main result is that the present DSMC code is able to reproduce the typical power-law velocity profile within such layer.

We also tested the capability of the DSMC code to accurately evaluate the shear stress field for a Couette flow problem. The obtained results show a very good agreement with the reference analytical relation over a wide range of rarefaction conditions spanning from the near-continuum to the free molecular flow regime. The lid-driven cavity flow was also considered as a good validation test benchmark. A good agreement with the results provided by another DSMC code were found

while varying the rarefaction conditions and the compressibility effects induced by the cavity lid motion.

Finally, the implementation of the pressure and mass flow rate boundary conditions, needed to simulate the flow subject of the study in chapter 6, is tested against analytical and other DSMC codes results for a plane channel flow. A very good agreement is found for both the velocity and the pressure distributions with respect to the reference data. The influence of the compressibility of the gas and of the rarefaction conditions on the non-linearity of the pressure profile is also clarified.



## 4 Coupling DSMC-LBM: methodology

In this chapter, we present the methodology at the basis of the coupling between the Direct Simulation Monte Carlo and the Lattice Boltzmann Method. We derive the two-way mapping algorithms to exchange information between the two methods showing that a proper truncation of the expansion in Hermite polynomials of the single particle distribution function, in turn strictly related to the employed LBM model, allows to transfer also non-equilibrium contributions. We then validate the proposed approaches for two different LBM quadratures, namely the D3Q19 and the D3Q39, underlining that the latter is able to reproduce the results from DSMC for a Poiseuille flow up to  $Kn=0.25$  with good accuracy. Finally, we evaluate the influence of the inclusion of the DSMC fluctuations on the measurement of the hydrodynamic moments as well as the effect of different temperature levels on the coupling algorithms.

### 4.1 Coupling methodology

We present the formulation of a kinetic mapping scheme between the Direct Simulation Monte Carlo and the Lattice Boltzmann Method which is at the basis of the hybrid model used to couple the two methods in view of efficiently and accurately simulate isothermal flows characterized by variable rarefaction effects. Owing to the kinetic nature of the LBM, the procedure we propose ensures to accurately couple DSMC and LBM at a larger  $Kn$  number than usually done in traditional hybrid DSMC-Navier-Stokes equation models. We show the main steps of the mapping algorithm and illustrate details of the implementation. Good agreement is found between the moments of the single particle distribution function as obtained from the mapping scheme and from independent LBM or DSMC simulations at the grid nodes where the coupling is imposed.

---

The content of the sections 4.1-4.2 of this chapter has been adopted from G. Di Staso, H.J.H. Clercx, S. Succi, and F. Toschi. "DSMC-LBM mapping scheme for rarefied and non-rarefied gas flows," *J. Comput. Sci.*, vol. 17, pp. 357-369, 2016, [109]. The content of the remaining sections 4.3-4.4, instead, covers validation tests propedeutical to further extend the range of applicability of the present hybrid model towards transient and non-isothermal flow problems.

Research in gas flows characterized by a large range of scales and by disparate levels of non-equilibrium effects poses a challenge to statistical physics modelling and rises interest in industry for simulating flows in micro-, nano-electromechanical systems and in material processing tools [110–112]. The extent of the departure of a flow from the equilibrium state is traditionally measured in terms of the Knudsen number:

$$\text{Kn} = \frac{\lambda}{\ell} \approx \frac{\lambda}{Q} \left| \frac{dQ}{d\ell} \right|, \quad (4.1)$$

where  $\lambda$  is the gas mean free path,  $\ell$  is the smallest hydrodynamic characteristic scale and  $Q$  is a fluid dynamic quantity of interest such as the gas pressure, velocity, temperature [113]. According to the Knudsen number, the gas flows can be classified into the hydrodynamic ( $\text{Kn} < 0.01$ ), slip ( $0.01 < \text{Kn} < 0.1$ ), transition ( $0.1 < \text{Kn} < 10$ ) and free molecular regime ( $\text{Kn} > 10$ ). The kinetic description of gases based on the Boltzmann equation, valid at any Kn, allows to cover flow conditions from the very rarefied to the hydrodynamic limit [6]. The two limits, rarefied and continuum, have traditionally been studied numerically by approximating the Boltzmann equation via the Direct Simulation Monte Carlo (DSMC) [1] or by solving the Navier-Stokes equations which can be derived from truncation at first order of the Chapman-Enskog procedure [83]. While the DSMC method is particularly suited to rarefied gas flow (transitional regime), its computational costs make it unpractical to study hydrodynamic flows [111]. Conversely, the continuum description of the flow provided by solving the Navier-Stokes equations and applying the no-slip boundary condition is not accurate whenever  $\text{Kn} > 0.01$  [44]. Corrections to the boundary conditions of Navier-Stokes equations such as to reproduce the velocity slip and temperature jump at the gas-surface interface in case of slip flow regime are often not accurate and may also predict incorrect qualitative behavior of the flow [114, 115]. Moreover, the derivation of extended hydrodynamic equations employing higher-order Chapman-Enskog approximations (Burnett and super-Burnett equations) have shown limited success [44]. Alternatively, macroscopic transport equations can be originated from moments expansion methods such as the Grad's method [3, 21]. However, difficulties in imposing boundary conditions for those moments without a clear physical meaning, as well complexity in the resulting systems of equations, prevent the application of the method for the simulation of flows of industrial interest.

It is therefore evident that whenever the flow presents a large range of Kn, due to the current computational and modelling limitations of the available methods, a multiscale hybrid model has to be used.

When dealing with multiscale models, domain decomposition techniques represent the most natural way to handle the problem. Within this approach, the domain

is decomposed according to a continuum breakdown parameter between regions where continuum-level macroscopic equations (either Euler or Navier-Stokes equations) are valid and regions where substantial non-equilibrium effects are present and kinetic methods, typically DSMC, are needed (see Refs. [44, 116–122]). Then a special treatment is imposed to couple the flow fields in the areas of overlap between the different regions, e.g. [123–125].

For completeness, the domain decomposition technique is not the only method adopted in the literature as alternative approaches are proposed. For example in [126], the Boltzmann equation is solved for a short period of time to obtain the rate of change of the average flow variables which are then used to update the continuum-level velocity field. In [127], instead, macroscopic equations are modified so to include effects due to kinetic contributions which take into account perturbations from the equilibrium state of the velocity distribution.

The approach that we introduce here follows the domain decomposition technique as commonly done in models proposed in literature but with the difference that the flow at the continuum level and at moderate rarefied conditions is simulated with the Lattice Boltzmann Method (LBM).

Moreover, since it has been largely demonstrated that LBM, due to its intrinsic kinetic nature, is an accurate and efficient numerical solver not only for flows at Navier-Stokes description level but also for flows at finite Kn number (see Refs. [36, 38, 39, 128–137]), the present model has the advantage, over the other hybrid methods which use traditional Navier-Stokes solvers, that the need for using the computationally expensive DSMC solver can be postponed to larger values of Kn. This is equivalent to say that the size of the domain where DSMC solver is still needed can be significantly reduced, thus improving the overall computational efficiency of the simulation.

In this work we principally focus on the most delicate aspect of any hybrid coupling model, i.e. the two-way extraction and transfer of information at the interface between the two numerical methods. The mapping schemes we developed, in fact, allow to pass from DSMC to LBM domains and vice versa correctly transferring also the non-equilibrium information. The amount of non-equilibrium information that can be passed is then essentially determined by the LB model and in particular by the chosen set of discrete velocities and the isotropy conditions the set is able to fulfill.

Simulations performed to validate the mapping scheme show that an accurate transfer of information is achievable for flows up to  $\text{Kn}=0.25$  for a 39-points Gauss-Hermite quadrature with sixth-order isotropy (D3Q39), under the assumption that the flow is isothermal, i.e. no external heat source is present, and viscous dissipation or other thermal effects are negligible.

#### 4.1.1 Mapping schemes

Both the LBM and DSMC methods aim to determine the fluid motion as described by the Boltzmann equation. As discussed in chapter 2, the main feature which clearly distinguishes the LBM from the DSMC is the reduction of the degrees of freedom of the velocity space. In fact in the LBM, particles at each lattice site  $\mathbf{x}$  can only propagate along a finite number of directions with an assigned speed  $\xi_a$ , while in DSMC the velocity space is not constrained to a set of discrete velocities. Before introducing the mapping scheme between the DSMC and LBM, we note that in order to quantitatively reproduce DSMC solutions for finite-Kn number flows, the LB model needs three basic ingredients:

1. kinetic boundary conditions, [63, 137–141];
2. higher-order lattice (HOL), [37, 38];
3. regularization procedure, [38, 142].

Few words on the two lattices used in this work are in order. The conventional D3Q19 LB model, satisfying isotropy conditions up to the fourth order, is able to describe the flow up to the Navier-Stokes level of description. In order for LB to accurately simulate rarefied gas flows, it is essential that the set of discrete velocities satisfies higher order isotropy conditions. In this work we shall take a step further, beyond the standard D3Q19 model, requiring that the lattice satisfies isotropy conditions up to the sixth order. A lattice able to fulfil this requirement, and still maintaining the Cartesian coordinate implementation is the D3Q39 model as described in [37]. In Table 4.1 the D3Q39 lattice discrete velocities  $\xi_a$  and weights  $w_a$  are collected. For comparison, the same is done also for the D3Q19 model. The main idea at the basis of the mapping scheme is that the single particle distribution function  $f(\mathbf{x}, \xi, t)$  can be expanded in terms of the dimensionless Hermite orthonormal polynomials,  $\mathcal{H}(\xi)$ , in the velocity space  $\xi$  as [3, 21, 37]:

$$f(\mathbf{x}, \xi, t) = \omega(\xi) \sum_{n=0}^{\infty} \frac{1}{n!} \mathbf{a}^{(n)}(\mathbf{x}, t) \mathcal{H}^{(n)}(\xi), \quad (4.2)$$

where  $\omega(\xi)$  is the weight function associated with the Hermite polynomials, and  $\mathbf{a}^{(n)}$  are the  $n$ -th rank tensors representing the dimensionless expansion coefficients defined as:

$$\mathbf{a}^{(n)} = \int f(\mathbf{x}, \xi, t) \mathcal{H}^{(n)}(\xi) d\xi. \quad (4.3)$$

The first coefficients of the series, due to the definition of the Hermite polynomials (see Appendix 4.B for the definition of Hermite polynomials), can be identified

LB model	$\xi_a$	$w_a$	$a$
D3Q19	(0, 0, 0)	1/3	0
	( $\pm 1$ , 0, 0)	1/18	1 - 2
	(0, $\pm 1$ , 0)	1/18	3 - 4
	(0, 0, $\pm 1$ )	1/18	5 - 6
	( $\pm 1$ , $\pm 1$ , 0)	1/36	7 - 10
	( $\pm 1$ , 0, $\pm 1$ )	1/36	11 - 14
	(0, $\pm 1$ , $\pm 1$ )	1/36	15 - 18
D3Q39	(0, 0, 0)	1/12	0
	( $\pm 1$ , 0, 0)	1/12	1 - 2
	(0, $\pm 1$ , 0)	1/12	3 - 4
	(0, 0, $\pm 1$ )	1/12	5 - 6
	( $\pm 1$ , $\pm 1$ , $\pm 1$ )	1/27	7 - 14
	( $\pm 2$ , 0, 0)	2/135	15 - 16
	(0, $\pm 2$ , 0)	2/135	17 - 18
	(0, 0, $\pm 2$ )	2/135	19 - 20
	( $\pm 2$ , $\pm 2$ , 0)	1/432	21 - 24
	( $\pm 2$ , 0, $\pm 2$ )	1/432	25 - 28
	(0, $\pm 2$ , $\pm 2$ )	1/432	29 - 32
	( $\pm 3$ , 0, 0)	1/1620	33 - 34
	(0, $\pm 3$ , 0)	1/1620	35 - 36
	(0, 0, $\pm 3$ )	1/1620	37 - 38

**Table 4.1:** Sets of discrete velocities and weights for the D3Q19 model (lattice speed of sound,  $c_s^2 = 1/3$ ) and the D3Q39 model ( $c_s^2 = 2/3$ ). While the D3Q19 model features a so-called single-shell lattice, meaning that in the streaming step only the first nearest neighbors nodes are involved, the D3Q39 model presents a three-shell lattice. From an algorithmic and implementation point of view, the D3Q39 model requires to adapt the routines for the application of the boundary conditions, as well as the routines related to the code parallelization. The collision step, instead, being a local operation, does not require any adaptation.

as the hydrodynamic moments (or a combination of those) of the distribution  $f(\mathbf{x}, \xi, t)$ :

$$\mathbf{a}^{(0)} = \int f(\mathbf{x}, \xi, t) \mathcal{H}^{(0)}(\xi) d\xi = \int f(\mathbf{x}, \xi, t) d\xi = \rho, \quad (4.4)$$

$$\mathbf{a}^{(1)} = \int f(\mathbf{x}, \xi, t) \mathcal{H}^{(1)}(\xi) d\xi = \int f(\mathbf{x}, \xi, t) \xi d\xi = \rho \mathbf{u} \quad (4.5)$$

$$\mathbf{a}^{(2)} = \int f(\mathbf{x}, \xi, t) \mathcal{H}^{(2)}(\xi) d\xi = \int f(\mathbf{x}, \xi, t) (\xi \xi - c_s^2 \delta) d\xi = \mathbf{P} + \rho (\mathbf{u} \mathbf{u} - c_s^2 \delta) \quad (4.6)$$



$$\mathbf{a}^{(3)} = \int f(\mathbf{x}, \boldsymbol{\xi}, t) \mathcal{H}^{(3)}(\boldsymbol{\xi}) d\boldsymbol{\xi} = \int f(\mathbf{x}, \boldsymbol{\xi}, t) (\boldsymbol{\xi} \boldsymbol{\xi} \boldsymbol{\xi} - c_s^2 \boldsymbol{\xi} \boldsymbol{\delta}) d\boldsymbol{\xi} = \mathbf{Q} + \mathbf{u} \mathbf{a}^{(2)} - (D-1) \rho \mathbf{u} \mathbf{u} \mathbf{u} \quad (4.7)$$

and analogously for the higher-order coefficients. In Eqs. (4.6) and (4.7),  $\boldsymbol{\delta}$  represents the identity tensor while  $\mathbf{P}$  and  $\mathbf{Q}$  represent the full second and third order moments which have the usual appearance if the intrinsic velocity,  $\mathbf{c} = \boldsymbol{\xi} - \mathbf{u}(\mathbf{x}, t)$ , is used:

$$\mathbf{P} = m \int f \mathbf{c} \mathbf{c} d\mathbf{c} \quad (4.8)$$

$$\mathbf{Q} = m \int f \mathbf{c} \mathbf{c} \mathbf{c} d\mathbf{c} \quad (4.9)$$

Due to the orthonormality of the Hermite polynomials,

$$f(\mathbf{x}, \boldsymbol{\xi}, t) \approx f^N(\mathbf{x}, \boldsymbol{\xi}, t) = \omega(\boldsymbol{\xi}) \sum_{n=0}^N \frac{1}{n!} \mathbf{a}^{(n)}(\mathbf{x}, t) \mathcal{H}^{(n)}(\boldsymbol{\xi}) \quad (4.10)$$

and  $f^N(\mathbf{x}, \boldsymbol{\xi}, t)$  has the same leading  $N$  velocity moments as the complete  $f(\mathbf{x}, \boldsymbol{\xi}, t)$ . It is possible now to describe the two mapping procedures:

- the DSMC2LB (or projection) step that allows to project the DSMC hydrodynamic variables (fine level of description) onto the LBM discrete distributions (coarse level of description);
- the LB2DSMC (or reconstruction) step that allows to reconstruct from the LBM discrete distributions (coarse level), the continuous, truncated, distribution function (fine level) from which the velocities of the DSMC particles can be sampled via an acceptance/rejection method.

It has to be noted that the following procedures can be extended to any suitable LB stencil whose discrete speeds are actually abscissae of a Gauss-Hermite quadrature.

#### 4.1.2 DSMC2LB mapping scheme

Firstly, we present the DSMC2LB projection step. As a remark, the main characteristic of this coupling step is that, instead of directly using information from DSMC particles, namely their velocities, we chose to adopt a different approach which uses the DSMC hydrodynamic moments, and Grad's formalism, to determine the discrete non-equilibrium distribution functions to be advanced in time by the LB solver. In this way, not only the coupling step is fully consistent with the LB Grad's formalism, but it has also the advantage to reduce possible stability issues related to the large fluctuations inherent to the DSMC representation. More

considerations on stability issues are given in section 4.1.4. In correspondence with the DSMC cells/LBM nodes where the coupling occurs, the cumulative averages of the DSMC hydrodynamic variables, properly scaled (see Appendix 4.A on how to perform such scaling), are used to compute the coefficients  $\mathbf{a}_{\text{DSMC}}^{(n)}$  of the truncated distribution  $f_{\text{DSMC}}^N(\mathbf{x}, \boldsymbol{\xi}, t)$  in Eq. (4.10).

We now take advantage of the fact that the distribution  $f_{\text{DSMC}}^N(\mathbf{x}, \boldsymbol{\xi}, t)$  can be completely and uniquely determined by its values at a set of discrete velocities and, if the Gauss-Hermite quadrature is used, then the coefficients  $\mathbf{a}_{\text{DSMC}}^{(n)}$  can be expressed as:

$$\begin{aligned} \mathbf{a}_{\text{DSMC}}^{(n)} &= \int f_{\text{DSMC}}^N(\mathbf{x}, \boldsymbol{\xi}, t) \mathcal{H}^{(n)}(\boldsymbol{\xi}) d\boldsymbol{\xi} = \\ &\sum_{a=0}^{d-1} \frac{w_a}{\omega(\boldsymbol{\xi}_a)} f_{\text{DSMC}}^N(\mathbf{x}, \boldsymbol{\xi}_a, t) \mathcal{H}^{(n)}(\boldsymbol{\xi}_a), \end{aligned} \quad (4.11)$$

where  $w_a$  and  $\boldsymbol{\xi}_a$  are the weights and abscissae of a Gauss-Hermite quadrature of algebraic precision of degree  $\geq 2N$ , and  $d$  is the total number of discrete velocities of the quadrature. The definitions of the first hydrodynamic moments in the LBM are:

$$\begin{aligned} \rho &= \sum_a f_a, \quad \rho \mathbf{u} = \sum_a f_a \boldsymbol{\xi}_a \\ \mathbf{P} &= \sum_a f_a \boldsymbol{\xi}_a \boldsymbol{\xi}_a - \rho \mathbf{u} \mathbf{u}, \quad \mathbf{Q} = \sum_a f_a \boldsymbol{\xi}_a \boldsymbol{\xi}_a \boldsymbol{\xi}_a - \rho \mathbf{u} \mathbf{u} \mathbf{u} \end{aligned} \quad (4.12)$$

and similarly for higher-order moments.

Comparing Eq. (4.11) with Eq. (4.12) and recalling the definitions of the Hermite polynomials  $\mathcal{H}^{(n)}$  and that the coefficients  $\mathbf{a}^{(n)}$  are the velocity moments of the  $f^N(\mathbf{x}, \boldsymbol{\xi}, t)$ , or a proper combination of those, it is immediate to see that the discrete distributions are the scaled values of the continuous distribution function evaluated at the Gauss-Hermite quadrature abscissae  $\boldsymbol{\xi}_a$ :

$$f_{\text{DSMC2LB},a}(\mathbf{x}, t) = \frac{w_a f_{\text{DSMC}}^N(\mathbf{x}, \boldsymbol{\xi}_a, t)}{\omega(\boldsymbol{\xi}_a)}. \quad (4.13)$$

In essence, once the  $f_{\text{DSMC}}^N(\mathbf{x}, \boldsymbol{\xi}, t)$  is built from the DSMC hydrodynamic moments according to Eq. (4.10) and evaluated at the quadrature abscissae,  $f_{\text{DSMC}}^N(\mathbf{x}, \boldsymbol{\xi}_a, t)$ , the discrete (non-equilibrium) distributions to be supplemented to the LBM solver at the coupling nodes can be computed from Eq. (4.13).

### 4.1.3 LB2DSMC mapping scheme

The inverse reconstruction step (LB2DSMC) requires that, at the LBM lattice nodes/DSMC cells where the coupling occurs, the velocities of the DSMC particles are sampled from a continuous distribution function.

At those lattice sites, the LBM discrete non-equilibrium functions  $f_{\text{LB},a}$ , are used to compute the coefficients of the expansion in Eq. (4.10):

$$\mathbf{a}_{\text{LB}}^{(n)} = \sum_{a=0}^{d-1} f_{\text{LB},a}(\mathbf{x}, t) \mathcal{H}^{(n)}(\boldsymbol{\xi}_a) \quad (4.14)$$

These allow to build the continuous truncated distribution  $f_{\text{LB}}^N(\mathbf{x}, \boldsymbol{\xi}, t)$ . To generate the velocities of the DSMC particles, the distribution should be sampled.

Several algorithms can be employed to this aim. We chose to adopt an acceptance/rejection algorithm similar to the one presented in [125]. However, while in [125] a Chapman-Enskog distribution was sampled, in the present case a Grad's distribution has to be sampled but, nonetheless, most of the steps presented there can be used here.

The Grad's velocity distribution, truncated up to order  $N$ , can be written as

$$g^N(\mathbf{x}, \boldsymbol{\xi}, t) = g^{(0)}(\boldsymbol{\xi}) G(\mathbf{x}, \boldsymbol{\xi}, t) \quad (4.15)$$

where  $g^{(0)}(\boldsymbol{\xi})$  is the weight function associated with the Hermite polynomials

$$g^{(0)}(\boldsymbol{\xi}) = \omega(\boldsymbol{\xi}) = \frac{1}{(2\pi)^{D/2}} \exp\left(-\frac{\boldsymbol{\xi}^2}{2}\right) \quad (4.16)$$

with  $D$  being the dimensionality of the flow problem. Eq. (4.16) represents also a global Maxwell-Boltzmann distribution at thermodynamic equilibrium (here we set a constant temperature  $T = 1$  as we are interested in isothermal flows).

At thermodynamic equilibrium  $G(\mathbf{x}, \boldsymbol{\xi}, t) = 1$ , while away from that condition, it can be expressed as:

$$G(\mathbf{x}, \boldsymbol{\xi}, t) = 1 + \frac{1}{2!} \mathbf{a}_{\text{LB}}^{(2)} \mathcal{H}^{(2)}(\boldsymbol{\xi}) + \frac{1}{3!} \mathbf{a}_{\text{LB}}^{(3)} \mathcal{H}^{(3)}(\boldsymbol{\xi}) + \cdots + \frac{1}{N!} \mathbf{a}_{\text{LB}}^{(N)} \mathcal{H}^{(N)}(\boldsymbol{\xi}) \quad (4.17)$$

The steps followed in the generation of the velocities of DSMC particles are outlined in Table 4.2. Some comments on those steps. The acceptance/rejection method needs to define an envelope function  $\gamma(\boldsymbol{\xi})$  such that  $\gamma(\boldsymbol{\xi}) \geq g(\boldsymbol{\xi})$  for any  $\boldsymbol{\xi}$ . In step 3, an amplitude parameter  $C$  is set. In this way it is guaranteed that the function  $\gamma(\boldsymbol{\xi}) = Cg^{(0)}(\boldsymbol{\xi})$  envelops most of the Grad's distribution function below it. The larger this parameter, the less probable is the chance that  $G(\mathbf{x}, \boldsymbol{\xi}, t)$

---



---

**Sampling acceptance/rejection algorithm for the Grad's distribution LB2DSMC**


---

1. Compute the coefficients

$$a_{\text{LB},ij}^{(2)} = \sum_a f_{\text{LB},a}(\xi_{a,i}\xi_{a,j} - \delta_{ij}) \quad (4.18)$$

and similarly for the higher-order ones

2. Find

$$M \equiv \max \left( \left| a_{\text{LB},ij}^{(2)} \right|, \left| a_{\text{LB},ijk}^{(3)} \right|, \dots, \left| a_{\text{LB},ijk\dots}^{(N)} \right| \right) \quad (4.19)$$

3. Set the parameter

$$C = 1 + 30M \quad (4.20)$$

---

 4. Sample a try particle velocity  $\boldsymbol{\xi}_{\text{try}}$  from the Maxwell-Boltzmann distribution  $g^{(0)}(\boldsymbol{\xi})$  using e.g. the Box-Müller transformation method

---

 5. Accept the  $\boldsymbol{\xi}_{\text{try}}$  if  $C\mathcal{R} \leq G(\mathbf{x}, \boldsymbol{\xi}_{\text{try}}, t)$  with  $\mathcal{R}$  a uniform deviate in the interval  $[0, 1)$  otherwise reject it and go back to step 4

---

 6. Generate the DSMC particle velocity as

$$\mathbf{v}_{j,\text{LB2DSMC}} = \left( \frac{2k_B T_{\text{DSMC}}}{m_{\text{DSMC}}} \right)^{1/2} \boldsymbol{\xi}_{\text{try}} + \mathbf{u}_{\text{LB}} \quad (4.21)$$


---



---

**Table 4.2:** Steps of the sampling acceptance/rejection algorithm for the LB2DSMC reconstruction mapping scheme used to generate the velocities of DSMC particles from LBM data. For the D3Q19 case, the order of the coefficients of Eqs. (4.18) and (4.19), stops at the second one, while for the D3Q39 case, the terms up to the third one are retained.

is larger than the envelop function, but at the same time, the smaller the efficiency of the sampling method since the efficiency is equal to  $1/C$ . In step 6, the particle velocity is generated as the sum of the thermal velocity and of the local fluid velocity. In Eq. (4.21), the thermal velocity is determined according to the temperature value and to the molecular mass of the gas as set in the DSMC simulation. Apart from the velocity, also the number of the DSMC particles,  $N_{\text{LB2DSMC}}$ , must be set in order to guarantee conservation of mass at the coupling sites so that the density from LBM and DSMC, appropriately scaled, match with each other.

In Figure 4.1, the schematic showing the main steps involved in both the mapping schemes is drawn.

It is interesting to try to identify sources of inaccuracy in the proposed mapping scheme. In the reconstruction and projection steps, in fact, some information is inevitably lost. In particular, in the LB2DSMC reconstruction step, the truncated distribution,  $f_{\text{LB}}^N(\mathbf{x}, \boldsymbol{\xi}, t)$ , is derived from the discrete distributions,  $f_{\text{LB},a}(\mathbf{x}, t)$ . This truncated distribution is such that only the first  $N$  moments are the same as those of the non-truncated continuous distribution  $f(\mathbf{x}, \boldsymbol{\xi}, t)$ , with the value of  $N$  essentially depending on the particular quadrature used. The moments of order higher than  $N$ , in fact, will not be the same as those of the original continuous distribution. This, in turn, reflects in the fact that the DSMC particles will be given a velocity which is sampled from a distribution which accurately recovers up to the first  $N$  moments. If, then, the sampling process were perfectly able to sample the velocity distribution  $f_{\text{LB}}^N(\mathbf{x}, \boldsymbol{\xi}, t)$ , then also the moments computed from the velocities of the particles would be perfectly reproduced in the limit of an infinite number of independent samples. However, since only a finite number of samples can be obtained, measurements of moments will be affected by statistical noise which will be also present in the discrete distribution functions  $f_{\text{DSMC2LB},a}(\mathbf{x}, t)$ . Analogously, in the DSMC2LB projection step, the loss of information derives from the fact that only the first  $N$  moments are used to evaluate the truncated discrete distributions  $f_{\text{DSMC2LB},a}(\mathbf{x}, t)$ , while, in principle, the DSMC solution possesses information on all the moments up to  $N \rightarrow \infty$ . The truncation, again, is performed according to the algebraic degree of accuracy of the particular LB quadrature. To be more precise, this does not imply that moments of order larger than  $N$  cannot be evaluated but it means that they are not accurately computed. If the so found discrete distributions were used to build a continuous distribution from which to sample the velocities of the DSMC particles, then the source of inaccuracy would be mainly related to the acceptance/rejection algorithm and in particular on the choice of parameter  $C$  in Eq. (4.20) which determines the extension of the envelope function  $\gamma(\boldsymbol{\xi})$ .

A further remark on the coupling steps is warranted. While the DSMC method has direct access to the temperature field, in order for the LB to accurately simulate also thermal effects, different approaches can be followed. Among those, three main strategies can be envisaged: the double distribution function approach where, besides the usual distribution function for the velocity field, a second distribution function is used for the temperature or internal energy field and standard lattices are used, [143]; the multispeed approach where lattices possessing higher isotropy conditions are used, [144]; the mixed method where the velocity field is studied with the usual LB model while the energy equation is solved by different numer-

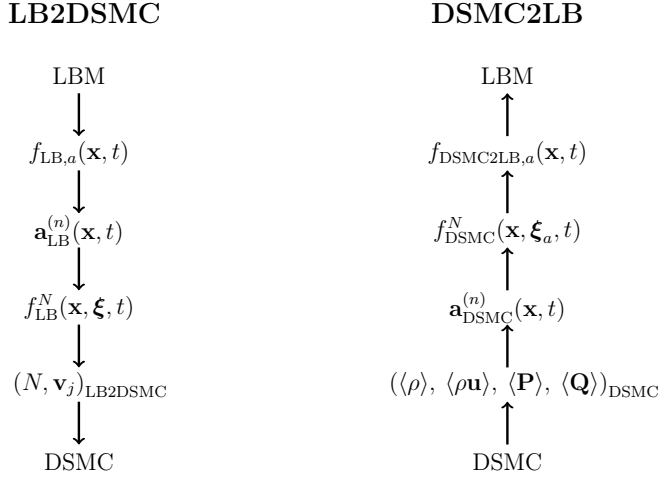


**Figure 4.1:** Schematic showing the main steps of the top-down LB2DSMC reconstruction (left) and bottom-up DSMC2LB projection (right) mapping schemes as described in sections 4.1.2 and 4.1.3. The symbol  $\langle \rangle$  represents the cumulative average measurements over time of the hydrodynamic moments from the DSMC solver. On the left scheme,  $N$  is the number of particles sampled in a cell where the coupling occurs. To each particle,  $j \leq N$ , a velocity  $\mathbf{v}_j$ , sampled as described in Table 4.2, is assigned. On the right scheme, for the D3Q19 case, only the terms up to  $\langle \mathbf{P} \rangle$ , i.e. the momentum flux tensor, are included. For the D3Q39 case, instead, also the term  $\langle \mathbf{Q} \rangle$ , i.e. the third order momentum flux tensor, is included, allowing to evaluate the expansion coefficients up to  $\mathbf{a}_{DSMC}^{(3)}(\mathbf{x}, t)$ .

ical method, usually finite-difference or finite-volume methods, [145]. Within the present multiscale scenario, the most natural among the three aforementioned schemes is the multispeed one, as it derives from the Hermite expansion approach. The extension to non-isothermal flows of the present coupling schemes, however, will be subject of future works.

#### 4.1.4 Stability issues for the coupling schemes

When dealing with the DSMC2LB coupling step, concerns about stability issues arise. Those are essentially related to the fact that fluctuations on the DSMC hydrodynamic variables may harm positivity of the LB equilibrium distribution functions. For the particular flows discussed in this paper, as we are interested in the stationary state, we choose the cumulative DSMC moments to build the single particle distribution function of Eq. (4.10). This choice, combined with the fact that the studied flow is at low Mach number, practically, staves off the aforementioned risks. For flows where the transient flow is of interest, or for which a stationary state does not exist, the instantaneous DSMC moments should be used

in Eq. (4.10). Also in this more demanding case, positivity of the LB equilibrium distribution functions can be guaranteed if a sufficiently large number of particles is employed. Fluctuations on hydrodynamic variables can be estimated by applying equilibrium statistical mechanics consideration, see [45]. For example, referring to fluctuations of the fluid velocity components within a cell, it is possible to see that the distribution of fluid velocity components realizations follows a normal distribution with standard deviation given by:

$$\sigma = \sqrt{\frac{k_B \langle T \rangle}{m \langle N \rangle}} \quad (4.22)$$

where  $k_B$  is the Boltzmann constant,  $m$  is the gas molecular mass,  $\langle T \rangle$  and  $\langle N \rangle$  are the mean local temperature and number of particles, respectively. For the settings of the simulations reported in next sections, it is easy to see that the instantaneous fluid velocity is such that  $\text{Ma} < 0.3$  for 99.7 % of the possible realizations ( $3\sigma$  rule is applied). Moreover, from Eq. (4.22), it is also evident the role of the number of DSMC particles in decreasing the intensity of the fluctuations. As a consequence, to guarantee the positivity of equilibrium distributions, a slightly larger number of DSMC particles than what would be strictly necessary for the method to provide accurate results may be needed.

### 4.1.5 Numerical results of the coupling schemes

#### Comparison between DSMC and LBM

To understand and determine the extent of the overlap region where both DSMC and LBM provide comparable accuracy in simulating rarefied gas flows, we performed independent force-driven plane Poiseuille flow simulations with two parallel plates at  $x = 0$  and  $x = H$  and compared results obtained from D3Q19 and D3Q39 LB models with DSMC data. Even if the flow is strictly monodimensional, we used three-dimensional solvers since our final aim is to be able to simulate more complex flows. This choice reflects in the fact that double periodic boundary conditions are imposed along the  $y$ - and  $z$ - directions.

Tests are performed at different Kn number, based on channel height, while keeping constant the Ma number, based on the flow centerline velocity,  $u_{max}$ :  $\text{Ma} = u_{max}/c_s = 0.1$ . The Ma number is set to a value able to guarantee that the lattice equilibria in LBM, expressed as a second-order (D3Q19) or a third-order (D3Q39) expansion in Ma number of the local Maxwellian, are positive defined, but it is still sufficiently high to prevent DSMC simulations from becoming impractically computationally expensive.

Moreover, as a result, this allows to treat the flow as isothermal. From DSMC simulations, in fact, the temperature increase is never found to exceed 0.5K, which is fairly negligible as compared to the reference temperature 273K.

In the BGK-LBM simulations, we set the flow Kn number imposing the relaxation time  $\tau$  according to the relation [146, 147]:

$$\tau = \sqrt{\frac{\pi}{8}} \frac{c}{c_s} \text{KnH} + 0.5 \quad (4.23)$$

where  $c/c_s$  is equal to  $\sqrt{3}$  for the D3Q19 model and to  $\sqrt{3/2}$  for the D3Q39 model, and H is the number of lattice sites along the channel height. Once Kn and H are set,  $\tau$  is also set. For both D3Q19 and D3Q39 models, kinetic boundary conditions and regularization procedure are applied.

In the DSMC simulations, we set the Kn number imposing the height of the channel, H, and the mean free path  $\lambda$ . To set  $\lambda$ , a proper number density  $n$  and a collision model should be defined. In the case of Hard Sphere (HS) model, the relation between  $\lambda$  and  $n$  (at equilibrium) is given by [1]:

$$\lambda = \frac{1}{\sqrt{2}\pi d_{\text{ref}}^2 n} \quad (4.24)$$

where  $d_{\text{ref}}$  is a reference molecular diameter. The determination of  $\lambda$  from Eq. (4.24) and estimates on the molecular speed allows to define the space and time discretizations.

Once the number of cells along the channel height is determined from DSMC parameters, an equal number of lattice sites is imposed in the LBM simulation so that the cells centers in DSMC and the LBM lattice sites overlap.

In Figure 4.2, the velocity profiles along the direction of the forcing, obtained from the LB models and DSMC, normalized with the centerline velocity, are shown for Kn=0.15. The velocity profiles are normalized with the applied forcing ( $\rho g$ ) and then the DSMC velocity profile is used as a reference for the LB velocity profiles. This is done to acknowledge the different speed of sound in the two lattices.

In the DSMC an Argon-like gas has been simulated and the grid resolution, kept the same for all performed tests, is based on the requirements of a DSMC simulation at Kn=0.05. In all the DSMC simulations, 100 computational molecules are initially placed in each cell of the domain.

LB solution has been considered as converged to the final solution once the fol-



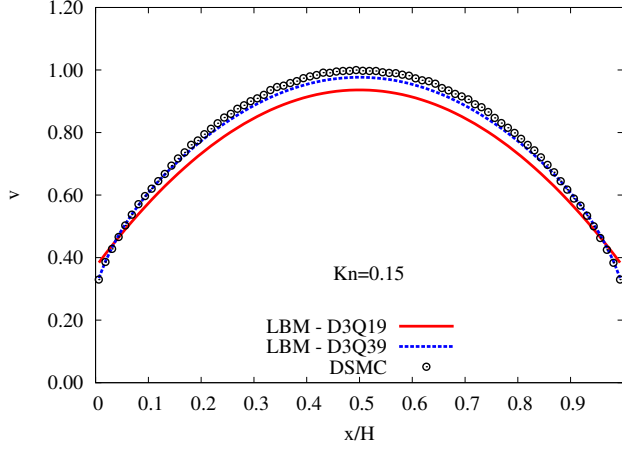


**Figure 4.2:** Velocity profiles of the planar force-driven Poiseuille flow for  $Kn=0.15$ . The LBM results with both the D3Q19 and D3Q39 models are compared with the DSMC solution. For the LB models, the regularization procedure is applied. Fully diffuse reflection is imposed at the walls,  $x/H = 0$  and  $x/H = 1$ . The profiles are normalized with respect to the centerline velocity provided by the DSMC results. The D3Q39 model is able to reproduce the DSMC data more accurately than the D3Q19 model. This can be justified considering that the truncation of the expansion includes terms up to the third ones for the D3Q39, while for the D3Q19 only those up to the second order are included. Note that for readability, the error bars on the DSMC data are not reported, but they are in the order of about 1% of the centerline velocity.

lowing criterion is fulfilled:

$$\sum_i \frac{|\mathbf{u}(\mathbf{x}_i, t) - \mathbf{u}(\mathbf{x}_i, t-1)|}{|\mathbf{u}(\mathbf{x}_i, t)|} < 10^{-6}. \quad (4.25)$$

In Eq. (4.25),  $\mathbf{u}(\mathbf{x}_i, t)$  represents the fluid velocity at the lattice nodes at time  $t$ . For DSMC, instead, a 1% fractional error on fluid velocity components is set as the requirement to assume the solution as converged. Plots similar to the one of Figure 4.2, have been drawn also for other  $Kn$  numbers but they are not reported here. It is more informative, in fact, to inspect the relative errors between DSMC and LBM data as done in Figure 4.3. The relative error is defined as:

$$\Delta v = \frac{v_{LBM} - v_{DSMC}}{v_{LBM}} \quad (4.26)$$

and it is shown for simulations at  $Kn=0.10-0.25$ .

In the plots of Figure 4.3, moreover, the boundaries of the Knudsen layer (black

dashed vertical lines) are also drawn. The Knudsen layer is a region in proximity of a solid wall which extends within the flow domain up to a distance of the order of one mean free path. Inside this region non-equilibrium effects of the flow are stronger [68, 79].

The D3Q19 model, recovering only up to the Navier-Stokes equations level of description, shows to depart from the DSMC solution also within the bulk of the flow and the error increases as the Kn number increases. The D3Q39 model, instead, is able to reproduce the DSMC data to a much better degree of accuracy. However, already at  $Kn=0.25$ , it is possible to notice some deviations especially within the Knudsen layer as the maximum relative error is about equal to 7.5%. This behavior can be explained taking into account that non-equilibrium effects at an order higher than the third may start to play a role.

With this statement, we do not imply that LBM is able to reliably simulate rarefied gas flows only for  $Kn \leq 0.25$ , but that with the current LB model we found reasonable agreement with DSMC data up to that Kn number. With larger Gauss-Hermite quadratures, in fact, being able to go beyond the third-order in Hermite polynomials expansion guaranteed by the D3Q39, further non-equilibrium effects should be correctly captured. However, we decided not to go further because the next quadrature possessing a high enough algebraic precision to allow an accurate fourth-order in Hermite polynomials expansion involves 121 discrete speeds [148].

#### 4.1.6 Numerical results for the DSMC2LB mapping scheme

Having concluded that the LBM D3Q39 model provides, for the problem at hand, a reasonable accurate solution for  $Kn \leq 0.25$ , we analyze results related to the mapping scheme step that allows to project the DSMC hydrodynamic variables onto the LBM discrete distribution functions for the D3Q39 lattice (DSMC2LB projection step).

To be noted that the unit conversion as delineated in Appendix 4.A to pass from SI units, proper of the DSMC method, to the lattice units, proper of the LB method, is applied during the simulations. To validate the procedure outlined in section 4.1.2, we ran two sets of independent DSMC and LBM simulations under the same force-driven plane Poiseuille flow with Ma based on the centerline velocity equal to 0.1 and for several Kn numbers. We verified the accordance between the discrete distributions functions as computed from the LBM,  $f_{LB,a}$ , and as obtained from the DSMC2LB projection scheme,  $f_{DSMC2LB,a}$ , applying Eq. (4.13). In Figure 4.4, a sketch showing the procedure to compare the  $f_{LB,a}$  with the  $f_{DSMC2LB,a}$  is depicted. Data refers to the first fluid node/cell in proximity to the wall located in proximity of the wall at  $x = H$ . In Figure 4.5 the ratio  $f_{DSMC2LB,a}/f_{LB,a}$  is plotted for all discrete speeds  $a = 0, \dots, d-1$  and for  $Kn=0.15$  and  $Kn=0.25$ . The larger

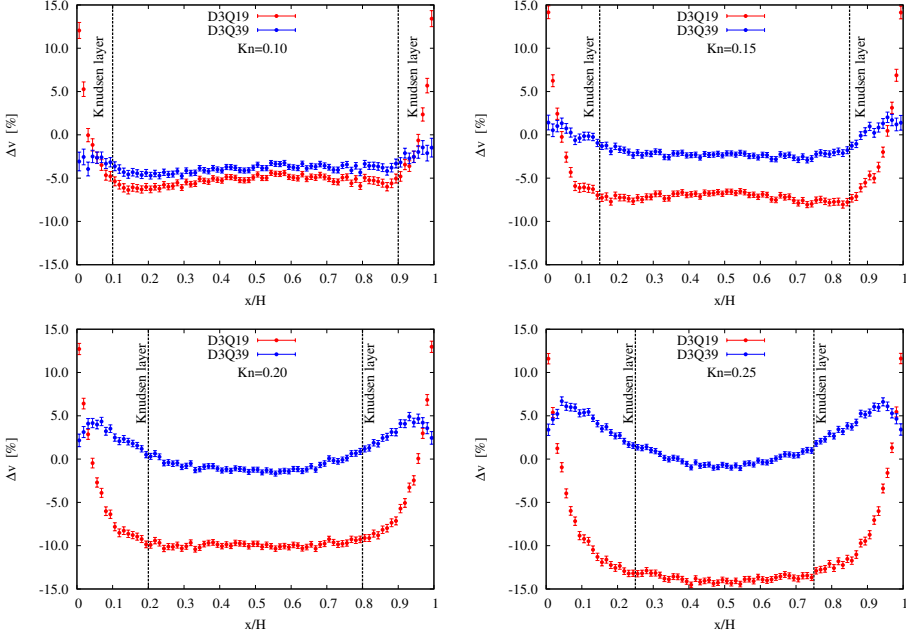


**Figure 4.3:** Relative error between LBM results and DSMC data, according to Eq. (4.26) for  $Kn=0.10 - 0.25$ . The dashed vertical lines represent the boundaries of the Knudsen layer, assumed to extend over one mean free path from the walls. The largest deviations of the LBM data with respect to DSMC occur, for both the investigated lattices, within the Knudsen layer. The error bars present in the plots are due to the statistical noise present in the reference data from the DSMC simulations. Such error bars are calculated as one standard deviation for the distribution of the instantaneous flow velocity after  $S=3600$  samples are cumulated. The error bars are at most in the order of 1% with respect to the centerline flow velocity.

errors that can be detected are about equal to 2% ( $f_{\text{DSMC2LB},36}/f_{\text{LB},36} \approx 1.02$ ) and to 5% ( $f_{\text{DSMC2LB},36}/f_{\text{LB},36} \approx 1.05$ ) for the simulations at  $Kn=0.15$  and  $0.25$ , respectively. Most of the other ratios are such that the error is below 1%.

The error bars present in the plots derive from the fact that we use the DSMC hydrodynamic moments to build the truncated distributions  $f_{\text{DSMC}}^N(\mathbf{x}, \boldsymbol{\xi}_a, t)$  and those are inherently characterized by statistical noise.

We also note that the larger error bars are present for the discrete speeds with larger module. This may be attributed to the fact that the magnitude of the discrete distribution function,  $f_a$ , is smaller the larger the module of the corresponding discrete speed,  $\boldsymbol{\xi}_a$ , while the statistical noise does not depend on the particular discrete speed.

It is difficult, however, to understand if the projection mapping scheme is providing

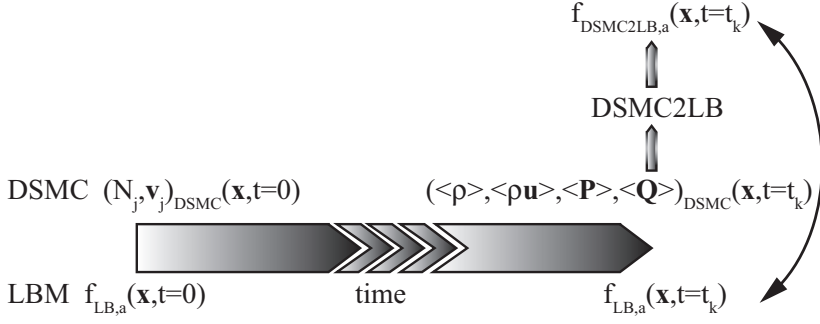


**Figure 4.4:** Schematic representing the procedure used to compare the discrete populations built from the DSMC hydrodynamic moments following the projection DSMC2LB algorithm,  $f_{\text{DSMC2LB},a}(\mathbf{x}, t = t_k)$ , with the discrete populations obtained from an independent LBM simulation,  $f_{\text{LB},a}(\mathbf{x}, t = t_k)$ , under the same flow conditions, namely  $\text{Kn}$  and  $\text{Ma}$ , at time  $t = t_k$ .

accurate results only from the comparison of the discrete distributions,  $f_a$ . So it is more informative to compute the hydrodynamic moments from  $f_{\text{LB},a}$  and from  $f_{\text{DSMC2LB},a}$ . The first few moments are reported in Table 4.3. It can be seen that a good matching is found always within the error bars.

Concluding, the projection mapping scheme is able to pass from the DSMC hydrodynamic quantities to the LBM discrete distributions preserving a reasonable level of accuracy.

<b>Kn=0.15</b>	$\rho$ [l.u.]	$\rho u_y$ [l.u.]	$P_{xy} + \rho u_x u_y$ [l.u.]
LBM	1.0	0.0282	-0.0151
DSMC2LB	$1.002 \pm 0.007$	$0.0277 \pm 0.0042$	$-0.0146 \pm 0.0027$
<b>Kn=0.25</b>	$\rho$ [l.u.]	$\rho u_y$ [l.u.]	$P_{xy} + \rho u_x u_y$ [l.u.]
LBM	1.0	0.0352	-0.0180
DSMC2LB	$0.999 \pm 0.007$	$0.0340 \pm 0.0042$	$-0.0167 \pm 0.0024$

**Table 4.3:** Comparison between the first few moments as computed from  $f_{\text{DSMC2LB},a}$  obtained from the projection mapping scheme and from the LBM simulations,  $f_{\text{LB},a}$ , by using the definitions in Eq. (4.12). The same data shown in Fig. 4.5 are used here. The moments, expressed in lattice units, and evaluated from the  $f_{\text{DSMC2LB},a}$  discrete distributions, reproduce within the error bars the moments found by using the  $f_{\text{LB},a}$  discrete distributions.

#### 4.1.7 Numerical results for the LB2DSMC mapping scheme

We now move on to analyse the results related to the mapping scheme that allows to reconstruct from the LBM discrete distributions,  $f_{\text{LB},a}$ , the continuous truncated

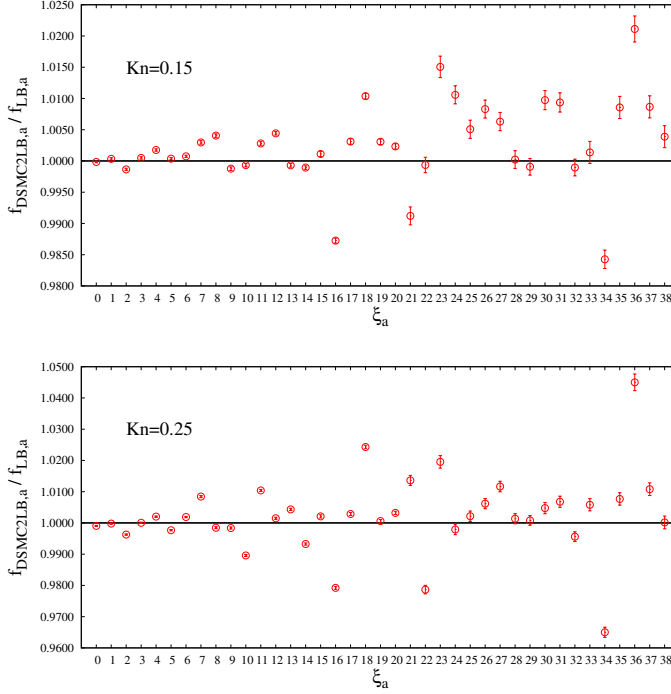


**Figure 4.5:** Ratio  $f_{\text{DSMC2LB},a} / f_{\text{LB},a}$  where  $f_{\text{DSMC2LB},a}$  are computed from Eq. (4.13) for plane Poiseuille flow at  $\text{Kn}=0.15$  (top) and at  $\text{Kn}=0.25$  (bottom) for a grid node located in proximity of the channel wall. The largest differences (ratio different from 1.0) are present for the populations with the largest indices. This can be explained considering that those populations are the ones involved in the evaluation of the higher order coefficients, as expressed in Eqs. (4.11-4.12). Note also that the symbols are not placed symmetrically with respect to the axis  $f_{\text{DSMC2LB},a} / f_{\text{LB},a} = 1$  because the node where data are collected is the one in proximity of the wall. The error bars are evaluated as one standard deviation for the distributions of each  $f_{\text{DSMC2LB},a}$  population after  $S=3600$  samples are collected.

distribution function from which, in turn, the velocities of the DSMC particles can be sampled (LB2DSMC reconstruction step).

The unit conversion as delineated in Appendix 4.A to pass from lattice units, proper of the LB method, to the SI units, proper of the DSMC method, is applied during simulations. As done for the previous step, to validate the procedure outlined in section 4.1.3, we ran two independent set of DSMC and LBM simulations under the same force-driven plane Poiseuille flow with  $\text{Ma}=0.1$  and for several  $\text{Kn}$  numbers. As shown in Figure 4.6, we compared the velocity distribution functions as obtained from the DSMC simulation collecting the velocities,  $\mathbf{v}_{j,\text{DSMC}}$ , of the particles

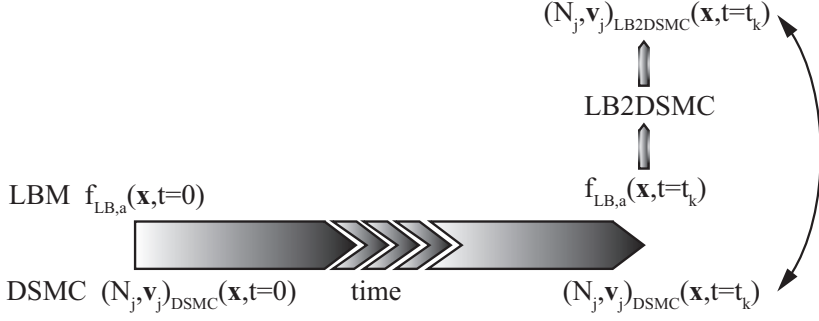


**Figure 4.6:** Schematic representing the procedure used to compare the distribution function of the velocity component,  $v_{j,DSMC}$ , obtained from a DSMC simulation with the distribution function of the velocity of the particles,  $v_{j,LB2DSMC}$ , obtained from the reconstruction mapping algorithm LB2DSMC, under the same flow conditions, namely  $Kn$  and  $Ma$ , at time  $t = t_k$ .

residing at the cell close to the domain wall, and as obtained from the velocities of the particles sampled from the velocity distribution function built as in Eq. (4.15) using the algorithm outlined in Table 4.2,  $\mathbf{v}_{j,LB2DSMC}$ . In Figure 4.7, in particular, the distributions for the velocity component along the direction of the forcing,  $v_y$ , are compared for  $Kn=0.15$  and  $Kn=0.25$ , respectively. The mean and the standard deviation for the two cases are collected in Table 4.4. The velocities of the particles are collected for both cases after a steady-state condition has been reached. The deviations between the means, about 4% for the case at  $Kn=0.15$  and about 5% for the case at  $Kn=0.25$ , are in line with the deviations that are present in Figure

<b>Kn=0.15</b>	$\langle v_y \rangle$ m/s	$\sigma_{v_y}$ m/s
DSMC	10.1	238.6
LB2DSMC	10.5	239.3
<b>Kn=0.25</b>	$\langle v_y \rangle$ m/s	$\sigma_{v_y}$ m/s
DSMC	12.8	238.8
LB2DSMC	13.4	239.6

**Table 4.4:** Comparison of the means and standard deviations of the distributions of Figures 4.7, expressed in DSMC units. Data, obtained collecting 3600 samples, refer to a node close to the domain wall and for the D3Q39 model. For each sample, 100 particles are generated. The comparison for both the statistics show a good agreement between the two datasets (DSMC, LB2DSMC). Note that, as mentioned at the point 6. of the Table 4.2, when sampling the particle velocity from the reconstructed distribution, thermal noise is added. For the simulations reported here,  $T=273K$ , and, therefore, the theoretical standard deviation, equal to  $\sigma = \sqrt{k_B T/m} = 238.4$  [m/s] for Argon, is well reproduced for both the datasets.

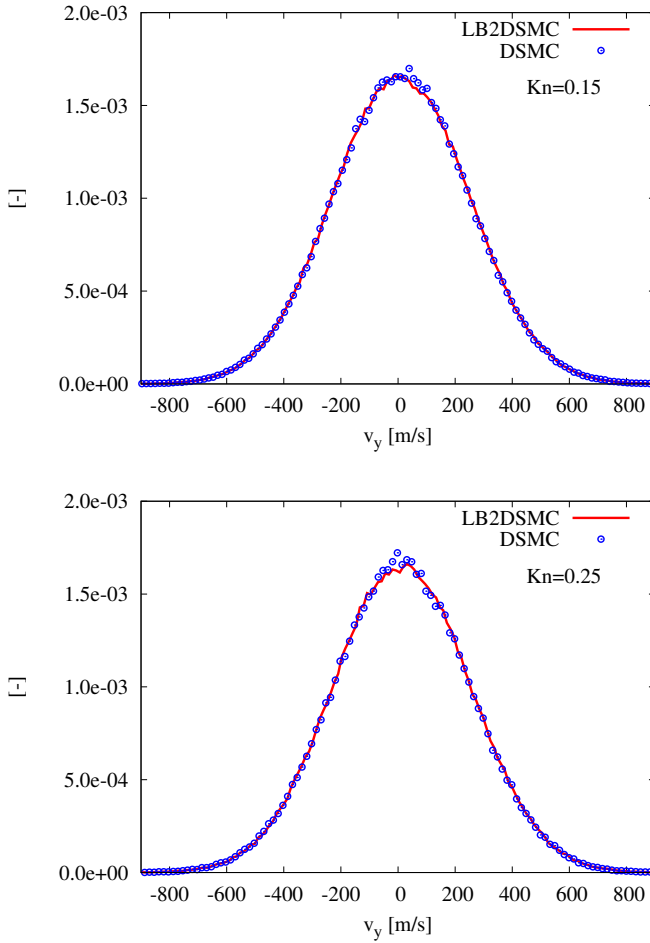


**Figure 4.7:** Distribution functions for the y-component,  $v_y$ , of the velocity of the particles, expressed in DSMC units, as obtained from the DSMC simulation and from the reconstruction mapping scheme using the algorithm LB2DSMC outlined in Table 4.2 for  $Kn=0.15$  (top) and  $Kn=0.25$  (bottom). Data refer to a cell close to the domain wall. In both cases, a good accordance is found allowing to accurately reproduce not only the expected mean (the flow velocity), but also the standard deviation, in turn linked to the flow temperature, as further demonstrated in Table 4.4.

4.3. The standard deviations of the two distributions differ for about 0.3% for both the cases. Related to this, it has to be recalled that the temperature of Eq. (4.21) is the reference temperature imposed in the DSMC simulation. The magnitudes of these standard deviations are compatible with the reference temperature ( $T=273$

K) and the molecular mass ( $m = 6.63 \cdot 10^{-26}$  kg) for the gas used in the DSMC simulation.

It is important, however, that also the distributions of the realizations of the fluid velocity as obtained from DSMC and from the reconstruction mapping scheme match with each other. These are evaluated calculating the fluid velocities as the instantaneous average velocity from all the particles velocities residing in the chosen cell (for the DSMC data, samples are taken once every 50 time steps so that they are uncorrelated). Also in this case, data are collected once the flow has reached a steady-state condition.

In Figure 4.8, the fluid velocity distributions are plotted for the case  $Kn=0.15$ . Both the mean and standard deviations of the distributions obtained from the two methods are in good agreement, demonstrating that the LB2DSMC reconstruction step correctly maps the discrete LB distribution functions into the velocities of the DSMC particles.

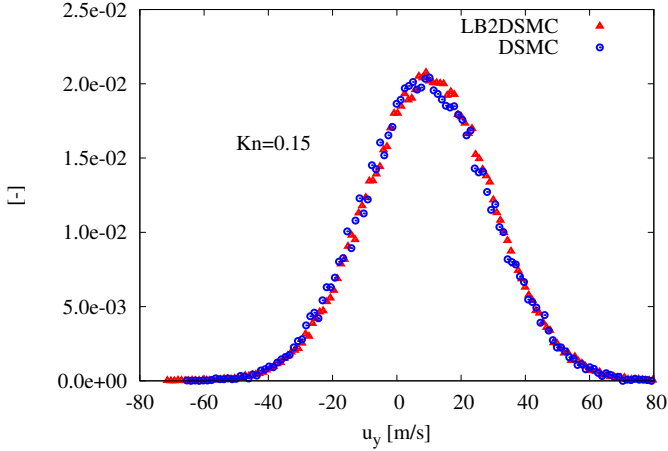


**Figure 4.8:** Flow velocity distribution functions for the y-component,  $u_y$ , expressed in DSMC units, as obtained from the DSMC simulation and from the reconstruction mapping scheme using the algorithm LB2DSMC outlined in Table 4.2 for  $Kn=0.15$ , for a cell close to the wall. As obtained for the microscopic velocity distributions, see Fig. 4.7, also the distribution of the flow velocity realizations, generated by collecting the instantaneous average flow velocity from the velocity of the particles residing in the cell, show a good agreement between the two cases.



## 4.2 Breakdown parameter for the hybrid model

The determination of the location where the coupling between the two methods is performed should be based on the identification of a breakdown parameter able to detect when the local non-equilibrium effects can no longer be accommodated within the given LB scheme. In the literature related to existing hybrid models, several definitions of the breakdown parameter are offered. The vast majority of these is based on the evaluation of the local density gradient, see e.g. [117]. This choice is justified by the fact that those hybrid models are generally applied to compressible flows problems. Such type of parameter, however, is not suitable for the LB method as, in its usual formulation, which is also adopted in this work, LB is a solver for weakly compressible flows. It is therefore needed to determine a different way to measure departure from the Navier-Stokes level of description (or Burnett, or even Super-Burnett level of description, if higher-order lattices are used).

While on a practical ground, it appears appropriate to place the interface between the two methods at least one mean free path away from the walls, a more rigorous approach might be based on the evaluation and comparison, between the LB and DSMC, of the coefficients of the Grad's expansion related to higher order moments, namely from the 2<sup>nd</sup> order on, since these are no longer associated with microscopic invariants.

The implementation of such switching criteria, that should also take into due account the presence of fluctuations in the DSMC hydrodynamic moments, and which requires additional verification, will be subject of future work.

## 4.3 D3Q19 lattice case

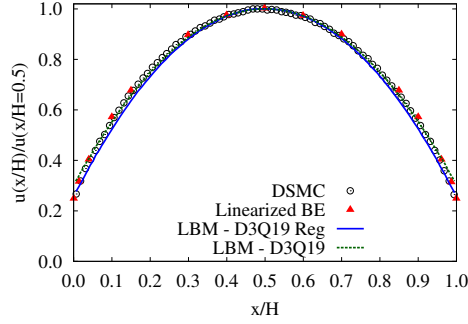
While in the previous sections we mainly investigated the performance of the coupling schemes when using a D3Q39 lattice, in the remaining part of the chapter we focus on the application of the coupling scheme when a D3Q19 lattice is adopted. This lattice, in fact, is the most employed one in literature, and it will be also adopted in the chapters 5 and 6 to validate the hybrid model. The main aim of this section, therefore, is to understand up to which rarefaction conditions we can safely apply the coupling recipes for the D3Q19 lattice.

As already discussed, the main difference between the D3Q39 and D3Q19 lattices is that the distribution function, as expressed in the series of Eq. (4.10), is truncated at the second order when adopting the D3Q19 lattice, while also the third order contributions are included in the D3Q39 case. So, for the D3Q19 case, the isothermal Navier-Stokes equations are recovered.

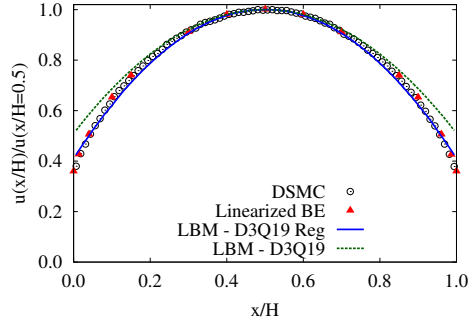
Since we will consider a (force-driven) Poiseuille flow for all the performed tests on the coupling schemes, we first compare the velocity profiles obtained by both the regularized and standard LBM formulations, with the DSMC solution and the reference data provided in [149] for several flow Kn numbers. Diffuse boundary conditions are applied at the walls and the initial temperature is 273K. In Figs. 4.9a-4.9c, the results of such comparison are shown. It should be noticed that the velocity profiles obtained by each method are normalized with the centerline velocity provided by that method. This is different from what has been done for the plots in Fig. 4.2, where the velocity profiles are normalized with the centerline velocity obtained from the DSMC simulation. In the present comparison, in fact, we aim at verifying the accordance of the velocity shape profiles with the reference data rather than the mass flow rate, as done in the comparison of Fig. 4.2. Observing the plots of Fig. 4.9, the very good accordance of the DSMC results with the data from the reference [149], obtained from the direct simulation of the linearized Boltzmann equation, is evident for any investigated Kn. For the simulations with the LBM, instead, a different behavior is observed when adopting the regularized or the standard formulation. In fact, while for the smallest investigated Kn ( $\text{Kn}=0.10$ ), the two formulations provide similar results and both are in a reasonable accordance with the reference data, increasing the flow Kn number let emerge the differences between the two LB models, where the regularized one shows a much closer agreement to the references than the standard model. In particular, the (excessive) slip velocity at the walls is drastically reduced when adopting the regularization procedure.

We are now ready to apply the previously described coupling schemes using the D3Q19 lattice for the force-driven Poiseuille flow case. At first, we report the results relative to the DSMC to LBM projection step (DSMC2LB step described in the section 4.1.2), verifying the accordance between the discrete distribution functions as computed from the LBM,  $f_{\text{LB},a}$ , and as obtained from the DSMC2LB projection scheme,  $f_{\text{DSMC2LB},a}$ , applying Eq. (4.13) where  $N = 2$ . Similarly to what is shown in Fig. 4.5, the ratios  $f_{\text{DSMC2LB},a}/f_{\text{LB},a}$  for  $a = 0, \dots, 18$  are reported in Fig. 4.10. The data refer to a node located in proximity of the channel centerline and a comparison is made between the results obtained by adopting a standard LB model and a regularized LB. In the case of perfect agreement, then  $f_{\text{DSMC2LB},a}/f_{\text{LB},a} = 1$ .

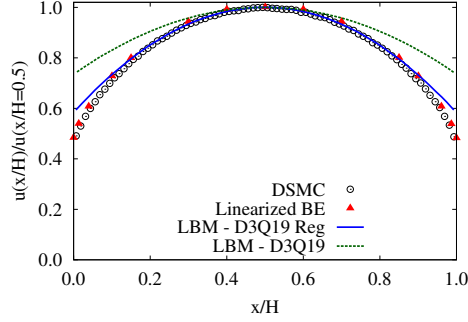
The application of the regularization procedure sensibly reduces the difference between the projected distributions,  $f_{\text{DSMC2LB},a}$ , and the distributions from the LBM,  $f_{\text{LB},a}$ , also when increasing the Kn number. In fact, while for the standard LB model the error can be as high as the 8%, for the regularized LB model such error is always below 0.6% also for  $\text{Kn}=0.25$ , as shown in the plot of Fig. 4.10d.



(a)  $Kn=0.10$ .



(b)  $Kn=0.20$ .



(c)  $Kn=0.40$

**Figure 4.9:** Comparison among the velocity profiles for a force-driven Poiseuille flow at three different  $Kn$  (a)  $Kn=0.10$ , (b)  $Kn=0.20$ , (c)  $Kn=0.40$ , obtained via four numerical methods: the standard D3Q19 LBM (green dashed line), the regularized D3Q19 LBM (blue line), the DSMC method (black circles) and the direct simulation of the linearized Boltzmann equation, based on a finite difference method (red triangles, data from [149]). Both the DSMC and the method used in [149] employ a hard-sphere collision model. Diffuse reflection boundary conditions are applied at the walls at  $x/H=0$  and  $x/H=1$ . The profiles are normalized with the centerline velocity. The DSMC data generated with our code well reproduce the reference data from [149]. For the LBM data, instead, the influence of the regularization procedure in reducing the excessive slip at the walls is clearly visible.

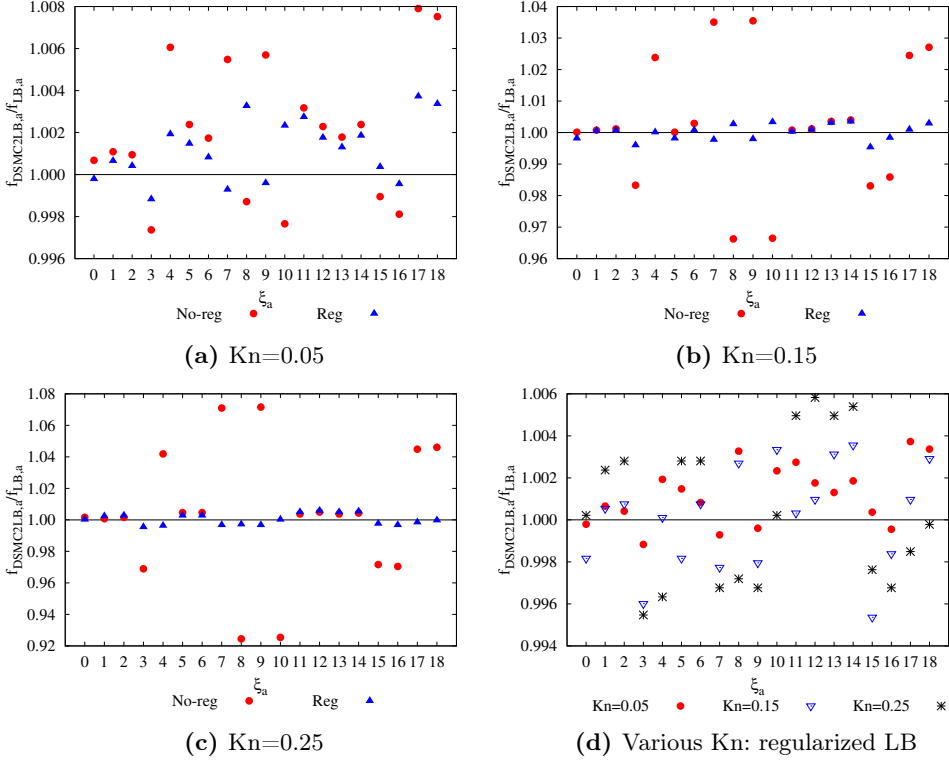


**Figure 4.10:** Ratio  $f_{\text{DSMC2LB},a}/f_{\text{LB},a}$  for the D3Q19 lattice at the centerline node for a force-driven Poiseuille flow as obtained from a standard (red dots) and a regularized (blue triangles) LB formulation at (a)  $\text{Kn}=0.05$ , (b)  $\text{Kn}=0.15$ , (c)  $\text{Kn}=0.25$ . Note the very different  $y$ -scales when passing from  $\text{Kn}=0.05$  to  $\text{Kn}=0.25$ . In (d), the data obtained from the regularized LB for the investigated  $\text{Kn}$  are collected in a single plot. A small error, below 0.6%, is found in correspondence of any discrete distribution,  $\xi_a$ . The set of speeds for the employed lattice is reported in Table 4.1.

It should be noted, however, that due to the flow set-up and to the fact that the data refer to a node in proximity of the centerline, the contributions on the discrete distributions due to the moment of order  $N = 2$ , i.e. the momentum flux tensor, are absent (besides the pressure contribution).

In order to verify also such effects, we repeated the same measurements for a node in proximity of the wall. Due to the flow set-up, in fact, this node is the one where the shear stress assumes the maximum value, and, therefore, it represents the most challenging node to test the coupling schemes.

In Fig. 4.11a, we compare the ratios  $f_{\text{DSMC2LB},a}/f_{\text{LB},a}$  for the centerline node

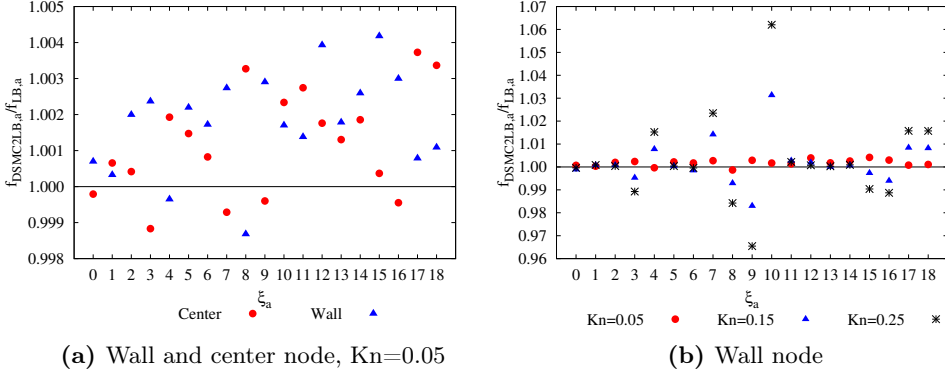


**Figure 4.11:** (a) Comparison between the ratios  $f_{\text{DSMC}2\text{LB},a}/f_{\text{LB},a}$  for  $\text{Kn}=0.05$  at a centerline (red dots) and a wall node (blue triangles). Since the flow is in the slip regime, the ratios are always very close to 1 and only small differences are visible between the two nodes. (b) The ratios  $f_{\text{DSMC}2\text{LB},a}/f_{\text{LB},a}$  evaluated at the wall node are plotted for the three investigated flow  $\text{Kn}$ . The larger the  $\text{Kn}$ , the larger the errors present in the ratios relative to the discrete distributions contributing to the evaluation of the shear stress. Note that only the data obtained from the regularized LB formulation are shown here. For  $\text{Kn}=0.15$ , an error as large as 3% on the populations contributing the most to the evaluation of the shear stress ( $f_9$  and  $f_{10}$ ) is present.

and for the wall node when  $\text{Kn}=0.05$ . As expected, since the flow is in the slip regime, the data from the two nodes are close to each other and the error is below 0.5% for any discrete distribution. In Fig. 4.11b, we also checked the influence of the  $\text{Kn}$  number. When increasing  $\text{Kn}$ , in fact, the errors increase sensibly and discrepancies up to 6% are found for the discrete distributions contributing to the calculation of the shear stress tensor terms which, for the construction of the flow set-up, has only one non-zero component. This behavior can be explained taking into account the reasons outlined in section 4.1.1: as the D3Q19 lattice can recover only up to the Navier-Stokes level, it cannot provide an accurate description of rarefied flow conditions as those encountered for the largest  $\text{Kn}$  number values investigated here. In such cases, indeed, a lattice fulfilling a larger set of isotropy conditions, e.g. the D3Q39 lattice used in the above sections, is needed.

In the analysis presented so far, we exclusively dealt with the case of steady-state flow conditions. This allowed us to determine the single particle distribution function given by Eq. (4.10), and then the discrete distributions to be supplemented to the LBM solver,  $f_{\text{DSMC}2\text{LB},a}$ , making use of the DSMC moments averaged over time. This, evidently, permits to decrease the statistical noise of the final solution. However, as underlined in the section 4.1.4, in the case in which the transient flow is of interest, or when a stationary state does not exist, the instantaneous DSMC

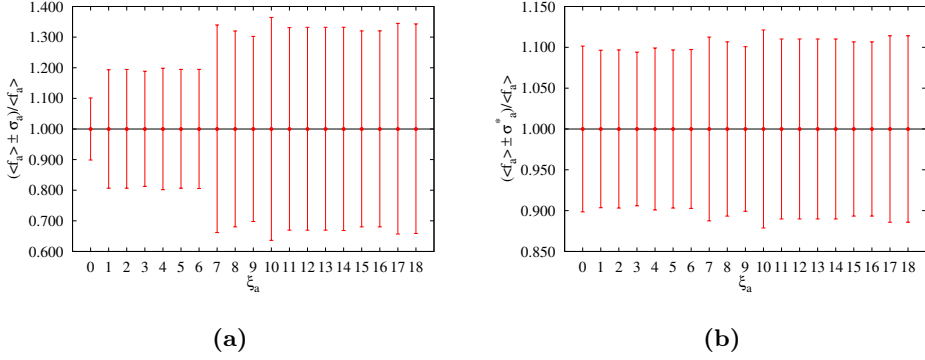


**Figure 4.12:** Influence of the inclusion of the DSMC fluctuations on the LBM discrete distributions: (a) Evaluation of the ratio of Eq. (4.27); (b) Evaluation of the ratio of Eq. (4.27) with  $\sigma_a$  normalized as in Eq. (4.29). Data refer to a force-driven Poiseuille flow for a node in proximity of the wall. The flow conditions are such that  $\text{Kn}=0.10$  and  $\text{Ma}=0.10$  (based on the centerline velocity). The standard deviations shown here are calculated using  $S=3600$  independent samples. The three levels in the standard deviations shown in (a) can be linked to the number of DSMC moments needed to evaluate the discrete distributions  $f_{\text{DSMC2LB},a}$ , as shown later in Table 4.5.

moments should be employed in Eq. (4.10).

We can now pass to investigate the effects of the fluctuations present in the measured DSMC moments in the evaluation of the discrete distributions.

In Fig. 4.12a, the following quantity is plotted:

$$\frac{\langle f_a \rangle \pm \sigma_a}{\langle f_a \rangle}, \quad (4.27)$$

where  $\langle f_a \rangle$  represents the mean value of the population  $a$  obtained through the instantaneous DSMC moments, via the relation  $\langle f_{\text{DSMC2LB},a}(\rho, \rho \mathbf{u}, \mathbf{P}) \rangle$ , and  $\sigma_a$  represents the standard deviation calculated as:

$$\sigma_a = \sqrt{\frac{1}{S-1} \sum_{i=1}^S (f_{a_i} - \langle f_a \rangle)^2}. \quad (4.28)$$

In Eq. (4.28), the  $f_{a_i}$  are the discrete distributions  $a$  evaluated from the instantaneous DSMC moments for the sample  $i$  and the summation is extended over the total number of the collected samples  $S$ , which amounts to 3600.

It is interesting to note that 3 different levels of the magnitude of the standard deviation  $\sigma_a$  are present. In particular, they appear to depend on the magnitude of the discrete velocity  $\xi_a$ . This behavior can be better understood inspecting Fig.

$f_a$	$c_{a,x}$	$c_{a,y}$	$c_{a,z}$	DSMC moments
0	0	0	0	$\rho$
1	1	0	0	$\rho, \rho u, P_{xx}$
2	-1	0	0	$\rho, \rho u, P_{xx}$
3	0	1	0	$\rho, \rho v, P_{yy}$
4	0	-1	0	$\rho, \rho v, P_{yy}$
5	0	0	1	$\rho, \rho w, P_{zz}$
6	0	0	-1	$\rho, \rho w, P_{zz}$
7	1	1	0	$\rho, \rho u, \rho v, P_{xx}, P_{xy}, P_{yy}$
8	1	-1	0	$\rho, \rho u, \rho v, P_{xx}, P_{xy}, P_{yy}$
9	-1	1	0	$\rho, \rho u, \rho v, P_{xx}, P_{xy}, P_{yy}$
10	-1	-1	0	$\rho, \rho u, \rho v, P_{xx}, P_{xy}, P_{yy}$
11	1	0	1	$\rho, \rho u, \rho w, P_{xx}, P_{xz}, P_{zz}$
12	-1	0	1	$\rho, \rho u, \rho w, P_{xx}, P_{xz}, P_{zz}$
13	1	0	-1	$\rho, \rho u, \rho w, P_{xx}, P_{xz}, P_{zz}$
14	-1	0	-1	$\rho, \rho u, \rho w, P_{xx}, P_{xz}, P_{zz}$
15	0	1	1	$\rho, \rho v, \rho w, P_{yy}, P_{yz}, P_{zz}$
16	0	1	-1	$\rho, \rho v, \rho w, P_{yy}, P_{yz}, P_{zz}$
17	0	-1	1	$\rho, \rho v, \rho w, P_{yy}, P_{yz}, P_{zz}$
18	0	-1	-1	$\rho, \rho v, \rho w, P_{yy}, P_{yz}, P_{zz}$

**Table 4.5:** List of the DSMC hydrodynamic moments involved in the evaluation of each discrete distribution  $f_a$  for an expansion in Hermite polynomials up to the  $2^{nd}$  order and for the D3Q19 lattice. For the discrete distribution corresponding to the quadrature abscissa equal to zero, only the density plays a role. For the discrete distributions corresponding to the quadrature abscissae aligned along the grid axis,  $a=1, \dots, 6$ , also the flow momentum and the terms on the diagonal of the momentum flux tensor, in turn connected to the pressure, are needed. Finally, for the evaluation of all the other discrete distributions also the shear stress terms are included.

4.12b where the standard deviation is now rescaled as

$$\sigma_a^* = \frac{\sigma_a}{1 + |\xi_a|^2}. \quad (4.29)$$

Upon such rescaling, the standard deviations  $\sigma_a^*$  show to have the same magnitude. The reason behind the presence of larger standard deviations for the discrete distributions,  $f_a$ , associated to the discrete velocity  $\xi_a$  with larger module can be explained taking into account that to calculate the values of the  $f_a$  according to the Grad's expansion in Hermite polynomials, see Eqs. (4.10, 4.11, 4.13), a larger number of DSMC hydrodynamic moments is involved. In the Table 4.5, for each

discrete distribution,  $f_a$ , the needed DSMC moments are listed. In particular, for the distribution  $f_0$ , for which the related discrete velocity has magnitude equal to 0, just the density  $\rho$  determines the value of  $f_0$  and therefore only fluctuations on  $\rho$  will affect the fluctuation on  $f_0$ . For the discrete distributions  $f_a$  with  $1 \leq a \leq 6$ , which correspond to the discrete velocities with magnitude equal to 1, also the momentum  $\rho \mathbf{u}$  and the  $P_{ii}$  terms of the momentum flux tensor are required. Then also the fluctuations on those moments will reflect on larger fluctuations on the corresponding  $f_a$ . Similarly, for the discrete distributions  $f_a$  with  $7 \leq a \leq 18$ , which correspond to the discrete velocities with magnitude  $\sqrt{2}$ , also the out-of-diagonal terms  $P_{ij}$  of the momentum flux tensor are involved. This said, the main objective of such analysis is to try to understand if potential stability issues related to the use of the instantaneous values of the DSMC hydrodynamic moments in the DSMC2LB step of the hybrid model may arise. Such issue is essentially related to the condition that the discrete distributions must be positive. Inspecting Fig. 4.12a, it is possible to see that for the discrete distribution  $f_0$ , the fluctuations are such that the instantaneous realizations of  $f_0$  could become negative with a probability of 1 over  $10^{23}$  samples (equivalent to  $10\sigma$ , assuming a normal distribution for the  $f_0$ ). Similarly, for the discrete distributions  $f_1, \dots, f_6$ , the probability that the instantaneous realization of the discrete distribution becomes negative is equal to 1 over  $1.7 \cdot 10^6$  (equivalent to  $5\sigma$ ). Finally, for the discrete distributions  $f_7, \dots, f_{18}$  such probability is equal to 1 over about 370 samples (equivalent to  $3\sigma$ ). From these considerations, therefore, it cannot be excluded the case of negative valued discrete distributions. However, it has to be noted that a single occurrence of a negative instantaneous realization of a discrete distribution does not immediately reflect into a stability issue as it was verified in the present simulation where, indeed, negative values for the discrete distributions  $f_7, \dots, f_{18}$  were measured, but this did not lead to any numerical instability phenomenon. The stability, in fact, may be harmed if the flow conditions are such that the discrete distributions constantly assume negative values. This situation may occur if the flow Mach number is sufficiently high, being the Mach number smaller than 0.3 a typical rule-of-thumb in order to avoid such occurrence.

While it is important to verify that the discrete distributions remain positive, it is rather difficult to understand if the projection mapping scheme DSMC2LB is providing accurate and physics-consistent results. At this aim, in fact, in analogy to what done in section 4.1.6, it seems to be more informative to compute the (instantaneous) values of the Grad's expansion coefficients, i.e. of the hydrodynamic moments or a combination of those, calculated from the discrete distributions  $f_{\text{DSMC2LB},a}$ , in turn evaluated via the instantaneous DSMC hydrodynamic mo-



ments as described by the following scheme:

$$\rho_{\text{DSMC}}, \mathbf{u}_{\text{DSMC}}, \mathbf{P}_{\text{DSMC}} \implies f_{\text{DSMC2LB},a} \implies a_{\text{DSMC2LB}}^{(0)}, \mathbf{a}_{\text{DSMC2LB}}^{(1)}, \mathbf{a}_{\text{DSMC2LB}}^{(2)}.$$

In Fig. 4.13, the probability distribution functions (pdf) of (some of) the expansion coefficients of the Grad's distribution up to the second order are plotted. All the data are expressed in lattice units and refer to the same simulation of Fig. 4.12. If the projection mapping scheme is sufficiently accurate, then the pdfs of the expansion coefficients should provide physics-consistent results. In particular, in Fig. 4.13a, the pdf of the  $0^{\text{th}}$  order coefficient,  $a^{(0)}$ , is shown. Note that  $a^{(0)} = \rho$  and, since the fluctuations in the density are linked to the fluctuations in the number of DSMC particles in a cell, which is a (positive) integer number, this pdf is defined only for discrete values of  $\rho$ . Moreover, since the number of particles in a cell is Poisson random variable, then also the  $a^{(0)}$  pdf follows a Poisson distribution. The indicated average value of the density  $\langle a^{(0)} \rangle = \langle \rho \rangle = 1.0002$  is very close to the expected value ( $a^{(0)} = \rho = 1.0$  when the density from DSMC is converted in lattice units), and, analogously, the standard deviation of the pdf follows the prediction from equilibrium statistical mechanics, [45, 46]:

$$\sigma_\rho = \sigma_{a^{(0)}} \sim \frac{\rho}{\sqrt{N}}. \quad (4.30)$$

In fact, given that  $N = 150$  particles are present on average in a cell (this is the number of particles initially populating each cell of the domain), and the density is equal to 1.0, then the expected standard deviation of the density pdf amounts to  $8.165 \cdot 10^{-2}$ , which is very close to the measured one, as indicated in Fig. 4.13a ( $\sigma_{a^{(0)}} = 8.16 \cdot 10^{-2}$ ).

In Fig. 4.13b, the pdf of the  $y$ -component of the  $1^{\text{st}}$  order coefficient,  $a_y^{(1)}$ , which is the component aligned with the forcing on the fluid, is shown. By definition,  $a_y^{(1)} = \rho v$  and therefore the drawn pdf corresponds to the one for the  $y$ -component of the fluid momentum. The indicated average value,  $\langle a_y^{(1)} \rangle = \langle \rho v \rangle = 0.0152$ , is very close to the expected value obtained from the DSMC,  $\rho v = 0.0155$ , once it is converted in lattice units. Note that similar pdfs can be obtained also for the other two components of the fluid momentum. For example, for the  $x$ -component  $\langle \rho u \rangle = -1.7 \cdot 10^{-4}$ , which is two orders of magnitude smaller than the  $y$ -component and very close to the theoretical value of 0, as there is no forcing on the fluid along this direction.

In Figs. 4.13c-4.13d, the pdfs of the  $xx$ - and  $xy$ -component of the  $2^{\text{nd}}$  order coefficient,  $a_{xx}^{(2)}$  and  $a_{xy}^{(2)}$ , are plotted. Due to the flow conditions, these coefficients

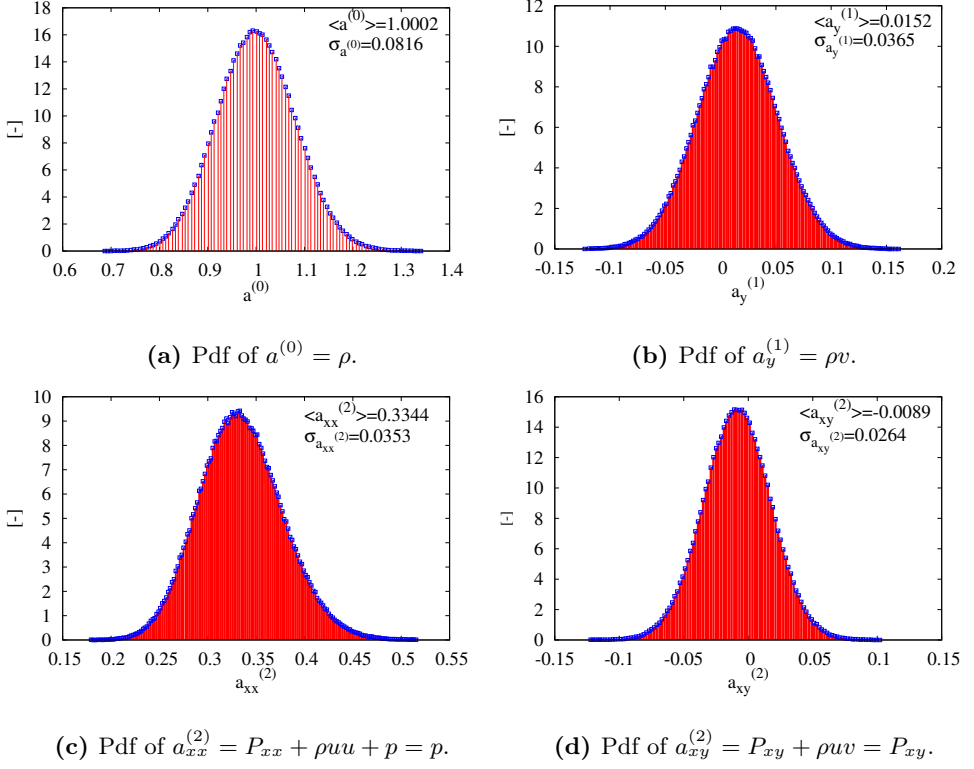


**Figure 4.13:** Evaluation of the probability distribution functions of the coefficients of the Grad's expansion as obtained from the discrete distributions,  $f_{\text{DSMC2LB},a}$ , when the instantaneous DSMC moments are used: (a)  $a^{(0)} = \rho = \sum f_{\text{DSMC2LB},a}$ , (b)  $a_y^{(1)} = \rho v = \sum f_{\text{DSMC2LB},a} c_{a,y}$ , (c)  $a_{xx}^{(2)} = p = \sum f_{\text{DSMC2LB},a} c_{a,x} c_{a,x}$ , (d)  $a_{xy}^{(2)} = P_{xy} = \sum f_{\text{DSMC2LB},a} c_{a,x} c_{a,y}$ . Data refer to a force-driven Poiseuille flow for a node in proximity of the wall and they are expressed in lattice units. The flow conditions are such that  $Kn=0.10$  and  $Ma=0.10$  (based on the centerline velocity and oriented along the  $y$ -direction with the walls normal to the  $x$ -direction). For all the shown cases, a good agreement is found between the expected values of the means, as imposed by the flow, and of the standard deviations of the distributions, as dictated by equilibrium statistical mechanics considerations.

are related to the hydrodynamic variables as follows:

$$\begin{aligned} a_{xx}^{(2)} &= P_{xx} + \rho u u + p = p, \\ a_{xy}^{(2)} &= P_{xy} + \rho u v = P_{xy}. \end{aligned} \quad (4.31)$$

The first equality in Eq. (4.31) is valid because  $u = 0$  (the forcing is along the  $y$ -axis). Similarly, the second equality in Eq. (4.31) holds because  $u = 0$ . For the

pdf of  $a_{xx}^{(2)}$ , plotted in Fig. 4.13c, the average value is given by  $\langle a_{xx}^{(2)} \rangle = p = 0.3344$ , which, indeed, is very close to the value of the pressure provided by the DSMC ( $p = 0.3340$  in lattice units), and, in addition, provided by the ideal gas equation of state proper of the LBM,  $p = \rho c_s^2 = 0.3333$ . Also in this case, equilibrium statistical mechanics considerations can help in order to evaluate the correctness of the measured standard deviation of the pdf for the pressure. In particular, one has [45, 46]:

$$\sigma_p = \sigma_{a_{xx}^{(2)}} \sim \sqrt{\frac{\gamma}{N}} p. \quad (4.32)$$

Considering that Argon is the simulated gas ( $\gamma = 1.67$ ), then  $\sigma_p = 3.528 \cdot 10^{-2}$ , which is in very close agreement with the measured value indicated in Fig. 4.13c,  $\sigma_{a_{xx}^{(2)}} = 3.530 \cdot 10^{-2}$ . Similar pdfs can be drawn for the other  $ii$  components of the second order coefficient  $\mathbf{a}^{(2)}$ .

Finally, in Fig. 4.13d, the pdf of the  $xy$ -component of the  $2^{nd}$  order coefficient,  $a_{xy}^{(2)}$ , is plotted. The indicated measured average value  $\langle a_{xy}^{(2)} \rangle = P_{xy} = -0.0089$  is indeed close to the value obtained from DSMC ( $P_{xy} = -0.0086$  in lattice units). Also the measured standard deviation of the distribution is in close agreement with the analytical prediction provided in [45]. In fact:

$$\sigma_{P_{xy}} = \sigma_{a_{xy}^{(2)}} \sim \frac{p}{\sqrt{N}}, \quad (4.33)$$

and, for the problem at hand, Eq. (4.33) gives the value of  $2.73 \cdot 10^{-2}$ , which can be compared with the measured value of  $2.64 \cdot 10^{-2}$ .

For all the other out-of-diagonal components of the  $2^{nd}$  order coefficient,  $a_{ij}^{(2)}$ , the average values are very close to zero while the measured standard deviations are close to the prediction provided by Eq. (4.33), as expected.

After having treated in depth the DSMC2LB mapping scheme, we can now investigate the results provided by the LBM to DSMC reconstruction step (LB2DSMC step described in the section 4.1.7) when the D3Q19 lattice is used. In particular, as done for the D3Q39 case, we will investigate if the imposed reconstruction step is accurate enough to reproduce the natural molecular velocity distribution function that an independent DSMC simulation would generate under the same flow conditions. To investigate this issue, we focus on the comparison between the molecular velocity pdf obtained via the sampling procedure of the Grad's distribution given by the Eq. (4.10) and the molecular velocity pdf generated by collecting the molecular velocities as obtained by the DSMC. It has to be noted that these two distributions are, in principle, different. In fact, in the framework of the Grad's distribution, while the pdf of the sampled molecular velocities is

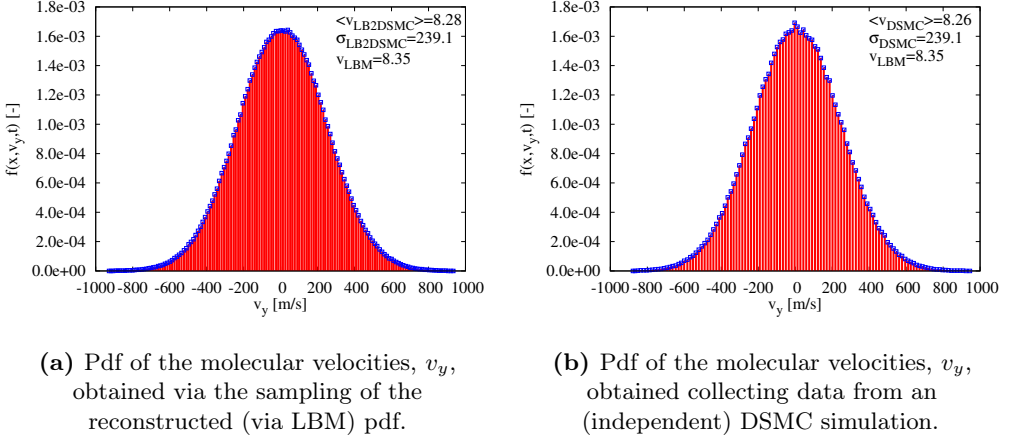


**Figure 4.14:** Comparison between the molecular velocity probability distribution functions as obtained via the reconstruction step, (a), and from a DSMC simulation, (b), for a force-driven Poiseuille flow with  $Kn=0.10$  and  $Ma=0.10$  (based on the centerline velocity). The average molecular velocity as well as the value of the standard deviation (providing an indication of the thermal velocity) are well reproduced for the sampled pdf of the molecular velocities. The flow velocity provided by the LBM is also shown for reference. In fact, the values indicated as  $\langle v_{LB2DSMC} \rangle$  and  $v_{LBM}$  show a good accordance. Here,  $\langle v_{LB2DSMC} \rangle$  represents the flow velocity calculated as average over the particles velocity sampled from  $f(\mathbf{x}, v_y, t)$  reconstructed via the LBM populations, and  $v_{LBM}$  is the flow velocity as calculated by an independent LBM simulation. The data refer to a node/cell in proximity of the wall and the velocities are expressed in SI units. On average, 150 particles are present in the cell and, in total, about  $5.4 \cdot 10^5$  samples are collected.

reconstructed using only the terms up to the second order, the pdf from the pure DSMC molecular velocities contains information from all the orders up to  $N \rightarrow \infty$ . It is intuitive to understand, therefore, that the further the flow is from the out-of-equilibrium conditions accurately described by the Navier-Stokes equations, the largest the difference between the two distributions.

In Fig. 4.14, the two molecular velocity pdfs obtained in the just mentioned ways are compared. The data refer to a force-driven Poiseuille flow with  $Kn=0.10$  and  $Ma=0.10$  (based on the centerline velocity) and for the molecular velocities of particles residing in a node/cell in proximity of the wall, once the steady-state final solution has been reached. In particular, the Fig. 4.14a shows the pdf of the molecular velocities along the forcing direction, sampled from the reconstructed pdf obtained from Eq. (4.10) once the coefficients of the series are evaluated from the (D3Q19) LBM discrete distributions. The Fig. 4.14b, instead, shows the pdf of the molecular velocities collected from a DSMC simulation under the same flow conditions.

The indicated results show that the mean value of the sampled pdf, i.e. the flow velocity, is very close to the value expected from the LBM. Similarly, the value of the standard deviation of the sampled pdf is close to the expected value. In fact, the thermal velocity is given by:

$$\sigma = \sqrt{\frac{k_B T}{m}}, \quad (4.34)$$

which for the imposed initial temperature ( $T=273$  K) and for the simulated gas (Argon,  $m=6.63 \cdot 10^{-26}$  kg) is equal to 238.4 m/s. Therefore, a less than 0.3% mismatch is found for the sampled pdf, as well as for the natural DSMC pdf. This latter difference can be attributed to the finiteness of the number of collected samples.

Finally, it has to be noted that the shown pdfs are normalized such that

$$\int_{-\infty}^{\infty} f(\mathbf{x}, v_y, t) dv_y = 1. \quad (4.35)$$

Moreover, the sampling process prescribes that the molecular velocities can be sampled only in the interval  $\langle v_y \rangle - 4\sigma \leq v_y \leq \langle v_y \rangle + 4\sigma$ . In terms of a normal distribution, this means that about 0.06% of all the possible molecular velocities cannot be generated. However, as demonstrated by the reported results, this has a very small, if not negligible, influence on the sampled molecular pdf.

Similar pdfs can be plotted also for the molecular velocities along the  $x$ - and  $z$ -directions and an analogous very good agreement for both the average value and the standard deviation is found when comparing the sampled and the natural DSMC pdf.

## 4.4 Effect of the temperature on the mapping schemes

As already mentioned in the previous discussion, the present implementation of the hybrid method is limited to flows where the thermal effects are negligible. Such limitation is essentially linked to the LBM side of the model. In fact, when adopting the Grad's formalism and the Gauss-Hermite quadrature technique, the molecular velocity,  $\xi$ , or, more precisely, the abscissae of the quadrature,  $\xi_a$ , are measured in units of a characteristic velocity,  $c_s = \sqrt{RT}$ , which, indeed, is the speed of sound of the gas within the lattice. Allowing for the flow temperature to change, and therefore also for the speed of sound to change, would reflect into a series of complications, such as that the node points of the computational grid would not be anymore equidistant, thus introducing algorithmic complexity for

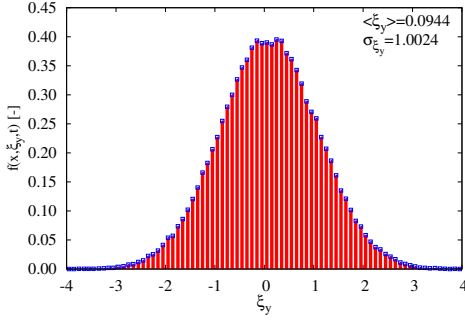
the LBM implementation. As discussed in section 4.1.3, several approaches can be followed to overcome this difficulty and the extension of the present hybrid method to include the treatment of the thermal effects will certainly allow to enlarge the possible areas of application of the hybrid model.

In this section, we will investigate if varying the initial temperature of the gas, but still keeping it uniform within the flow domain, i.e. the flow is isothermal, leads to any difference in the accuracy of the proposed mapping schemes. Should the coupling scheme be unaffected by the different imposed "energy" levels, i.e. the initial temperature, then it would mean that the coupling schemes are indeed able to respect the mentioned peculiarity of the Grad's formalism in conjunction with the Gauss-Hermite formalism.

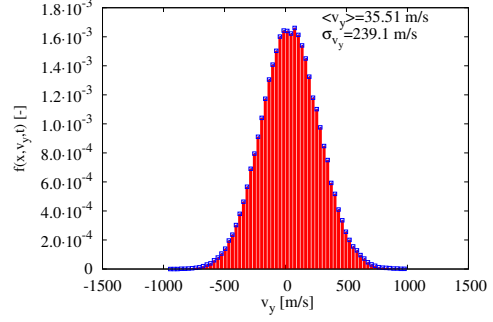
In particular, we tested three different temperatures:  $T=273$  K,  $T=323$  K and  $T=373$  K for both the DSMC2LB and the LB2DSMC mapping schemes in the case of a force-driven Poiseuille flow for which  $\text{Kn}=0.05$  and  $\text{Ma}=0.10$  (based on the centerline flow velocity). The employed lattice is the D3Q19. We adopted such low flow Kn number to be sure that the chosen D3Q19 model is capable to handle the flow non-equilibrium effects without introducing any error.

In Fig. 4.15, the results relative to the LB2DSMC step are shown. In the left column, the pdfs obtained by collecting the molecular velocities along the forcing direction,  $\xi_y$ , sampled from the truncated pdf of Eq. (4.10) according to the scheme in Table 4.2 are shown for the three tested temperatures and reported in lattice units. The choice to use this kind of units is done to demonstrate the most interesting feature: the three pdfs are essentially the same as indicated by the close agreement for the measured mean value and the standard deviation for the three temperatures. This feature would not be visible in case of a different choice of the units of the molecular velocities. This, indeed, is confirmed by the pdfs drawn in the right column of Fig. 4.15 where the molecular velocity is now expressed in terms of SI units. It has to be noted that, as expected, the standard deviation becomes larger as the temperature increases, see Eq. (4.34), but also that the mean value increases due to the fact that the simulations are characterized by the same Ma number.

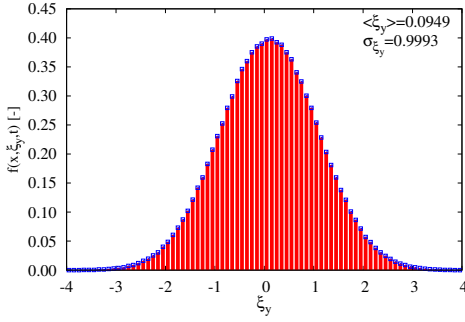
Finally, we investigate the influence of the temperature for the DSMC2LB mapping scheme. The same flow set-up employed for the tests of the LB2DSMC step are used here. In Fig. 4.16, the ratio between the discrete distribution functions as obtained from the DSMC2LB projection scheme,  $f_{\text{DSMC2LB},a}$ , and as calculated from the LBM,  $f_{\text{LB},a}$ , are compared for the three mentioned temperatures. A very good agreement is found when passing from  $T=273$  K to  $T=323$  K and finally to  $T=373$  K. This further confirm the fact that the fluid temperature is irrelevant from an accuracy point of view as long as the flow is isothermal.



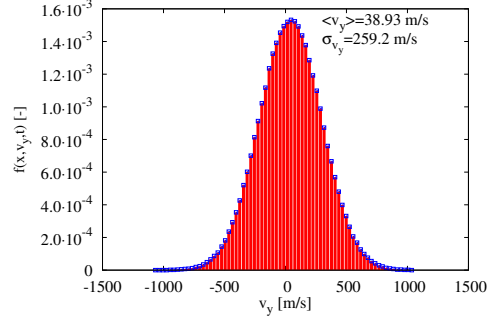
(a) Reconstructed molecular velocity pdf from LBM for  $T=273$  K (lattice units)



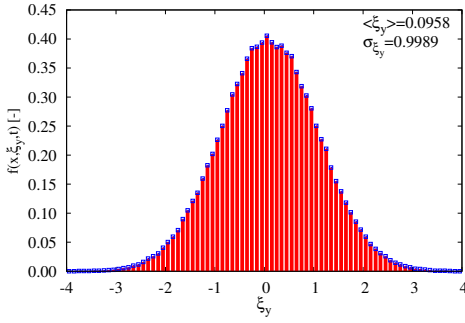
(b) Reconstructed molecular velocity pdf from LBM for  $T=273$  K (SI units)



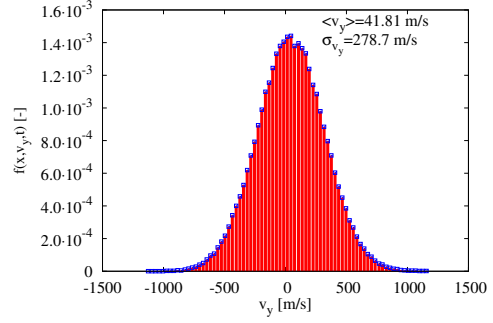
(c) Reconstructed molecular velocity pdf from LBM for  $T=323$  K (lattice units)



(d) Reconstructed molecular velocity pdf from LBM for  $T=323$  K (SI units)



(e) Reconstructed molecular velocity pdf from LBM for  $T=373$  K (lattice units)



(f) Reconstructed molecular velocity pdf from LBM for  $T=373$  K (SI units)

**Figure 4.15:** Comparison between the molecular velocity probability distribution functions as obtained via the reconstruction LB2DSMC step and expressed in lattice units (left column) and in SI units (right column). The data refer to a node/cell at the centerline of the flow channel and for  $\text{Kn}=0.05$  and  $\text{Ma}=0.10$ . The plots in (a)-(b) refer to  $T=273$  K, in (c)-(d) to  $T=323$  K, in (e)-(f) to  $T=373$  K. The indicated standard deviations,  $\sigma_{v_y}$ , are in close agreement with the expected values, calculated from Eq. (4.34). In fact, for  $T=273$  K, 239.1 m/s (measured) vs 238.4 m/s (expected); for  $T=323$  K, 259.2 m/s vs 259.3 m/s; for  $T=373$  K, 278.7 m/s vs 278.6 m/s.

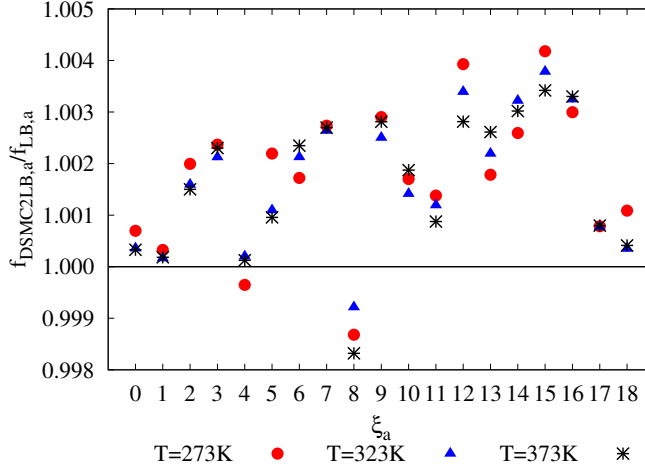


**Figure 4.16:** Ratio between the discrete distributions as evaluated from the DSMC2LB step,  $f_{\text{DSMC2LB},a}$ , and as obtained from the LBM,  $f_{\text{LB},a}$ , when the temperature of the simulated gas for the DSMC simulation is equal to 273 K (red circles), 323 K (blue triangles), 373 K (black asterisks). The same accuracy is found regardless of the tested temperature. The data are from simulations characterized by the same flow conditions indicated in the caption of the Fig. 4.15.

## 4.5 Conclusions

We developed a kinetic mapping scheme based on Grad's moments method and Gauss-Hermite quadrature in view of coupling the DSMC and LBM models to simulate isothermal flows with non-uniform rarefaction effects. The main steps of the mapping algorithm between DSMC and LBM in order to allow an accurate passage between the two methods domains were discussed. To extend the range of applicability of LBM beyond the Navier-Stokes equation level, and thus postponing the passage to the DSMC solver, the need for adopting a high-order lattice (D3Q39) and a regularization procedure for the LBM is demonstrated by finding a good agreement between the DSMC and LBM velocity profile for plane Poiseuille flow up to  $\text{Kn}=0.25$ . As a proof of concept of the hybrid method, a simpler version of the mapping scheme which enforces the passage through local equilibrium states has been performed for the simulation of a plane Poiseuille flow at  $\text{Kn}=0.05$ . We have also estimated that the adoption of the hybrid scheme significantly increases computational efficiency with respect to a DSMC simulation performed over the whole domain by a factor equal to 1.7 for the flow conditions shown in the test case. We have also applied the same coupling recipes validated for the D3Q39 quadrature to the D3Q19 lattice, finding that the regularization procedure is of



fundamental importance in order to extend the coupling applicability to the slip flow regime. We have also evaluated the effects of the inclusions of the natural fluctuations present in the DSMC moments on the coupling method finding that, for the flow speeds typically encountered in well-defined LBM simulations, such inclusion does not reflect in potentially critical stability issues.

Finally, changing the fluid initial temperature for the DSMC simulation does not imply any degradation in the precision of the coupling methodology as long as the temperature is constant throughout the domain.

## 4.A Scaling factors

To be able to apply the proposed methods also in engineering contexts and with experiments, we decided to employ in the DSMC simulations dimensional variables with SI units. This implies that, prior to any transfer of information between LB and DSMC, a proper conversion from lattice units to SI units, or vice versa according to the fact that the DSMC2LB or LB2DSMC mapping scheme is involved, has to be performed.

The basic elementary conversion scales are introduced here:

- *Length scale*

Since in LB we assume the lattice spacing  $\Delta x$  as the space unit and since we impose that the centers of the DSMC cells overlap with the LB sites, then the length scale is set as:

$$L_0 = \Delta x_{\text{DSMC}} \quad [\text{m}], \quad (4.36)$$

where  $\Delta x_{\text{DSMC}}$  is the linear distance between the centers of two adjacent DSMC cells. Note that this implies that, at least in the buffer layer, the DSMC cells are cubic;

- *Time scale*

Similarly, the time unit within the LB simulation is the elementary lattice time-step. The physical value can be defined through the speed of sound within the lattice,  $c_s$ , and of the gas in the DSMC simulation,  $a$ , as

$$T_0 = \frac{c_s}{a} \Delta x_{\text{DSMC}} \quad [\text{s}]. \quad (4.37)$$

- *Mass scale*

As the mass within the DSMC cells/LB nodes where coupling occurs must be conserved, and assuming the lattice particles are given a unit mass, then

the mass scale can be defined as follows:

$$M_0 = \frac{F_{N,\text{DSMC}} N_{\text{DSMC}} m}{\sum_a f_{\text{LB},a}} \quad [\text{kg}], \quad (4.38)$$

where  $F_{N,\text{DSMC}}$  is the number of real molecules represented by one DSMC particle,  $N_{\text{DSMC}}$  is the number of DSMC particles in a cell, and  $m$  is the gas molecular mass.

From these three scaling factors, it is possible to derive all the other physical conversion scales.

## 4.B Hermite polynomials

The  $n$ -th order Hermite polynomial is defined according to Rodrigues' formula, [64], as:

$$\mathcal{H}^{(n)}(\boldsymbol{\xi}) = \frac{(-1)^n}{\omega(\boldsymbol{\xi})} \nabla^n \omega(\boldsymbol{\xi}) \quad (4.39)$$

which is a rank- $n$  tensor and a polynomial of degree  $n$  in  $\boldsymbol{\xi}$ . In Eq. (4.39)  $\omega(\boldsymbol{\xi})$  is the weight function associated with the Hermite polynomials in  $D$ -dimensional Cartesian coordinate  $\boldsymbol{\xi}$ :

$$\omega(\boldsymbol{\xi}) = \frac{1}{(2\pi)^{D/2}} \exp\left(-\frac{\boldsymbol{\xi}^2}{2}\right). \quad (4.40)$$

The first Hermite polynomials, therefore, read as:

$$\mathcal{H}^{(0)}(\boldsymbol{\xi}) = 1, \quad (4.41)$$

$$\mathcal{H}_i^{(1)}(\boldsymbol{\xi}) = \xi_i, \quad (4.42)$$

$$\mathcal{H}_{ij}^{(2)}(\boldsymbol{\xi}) = \xi_i \xi_j - \delta_{ij}, \quad (4.43)$$

$$\mathcal{H}_{ijk}^{(3)}(\boldsymbol{\xi}) = \xi_i \xi_j \xi_k - \xi_i \delta_{jk} - \xi_j \delta_{ik} - \xi_k \delta_{ij}. \quad (4.44)$$

The Hermite polynomials form a set of orthonormal basis of the Hilbert space of the functions of  $\boldsymbol{\xi}$  with the inner product  $\langle f, g \rangle = \int \omega f g d\boldsymbol{\xi}$ .

Moreover, any function which is square-integrable can be expanded in terms of the Hermite polynomials.



# 5 Hybrid DSMC-LBM solver for monodimensional flows

In this chapter, we present the application of the coupling methodology presented in chapter 4 to a Couette flow.

Hybrid particle-continuum computational frameworks permit the simulation of gas flows by locally adjusting the resolution to the degree of non-equilibrium displayed by the flow in different regions of space and time. In this chapter, we present a new scheme that couples the Direct Simulation Monte Carlo with the Lattice Boltzmann method in the limit of isothermal flows. The former handles strong non-equilibrium effects, as they typically occur in the vicinity of solid boundaries, while the latter is in charge of the bulk flow, where non-equilibrium can be dealt with perturbatively, i.e. according to Navier-Stokes hydrodynamics. The proposed concurrent multiscale method is applied to the dilute gas Couette flow, showing major computational gains when compared to the full DSMC scenarios. In addition, it is shown that the coupling with LB in the bulk flow can speed up the DSMC treatment of the Knudsen layer with respect to the full DSMC case. In other words, LB acts as a DSMC accelerator.

## 5.1 Application of the coupling methodology

The need for the development of fast and accurate numerical methods to simulate gas flows characterized by a broad range of time and space scales represents a general challenge to statistical physics modelling. Moreover, despite the success demonstrated by computer simulations at the microscopic level, the computational requirements of the microscopic numerical methods, such as Molecular Dynamics (liquids) and direct simulation Monte Carlo (DSMC; gases), are still prohibitive for many practical applications where macroscopic scale flow problems are of interest. It is therefore evident that, for such kind of problems, where to properly simulate large scale flows it is essential to provide an accurate microscopic description, a multiscale approach, consisting of the use of different models for each relevant

---

The content of this chapter has been adopted from G. Di Staso, H.J.H. Clercx, S. Succi, and F. Toschi, "Lattice Boltzmann accelerated direct simulation Monte Carlo for dilute gas flow simulations," *Phil. Trans. R. Soc. A*, vol. 374, p. 201602256, 2016, [150].

scale, is needed. In order to link large scales to local microscopic properties, a variety of scale bridging techniques have been developed, which can be broadly classified as either sequential or concurrent. In the former class of methods, the continuum treatment conveys all microscopic details into appropriate constitutive relations or laws [120, 126, 127, 151], and systems are then simulated separately at the different levels of resolution. In the latter class, which is the one relevant to the present work, systems are analyzed in a single simulation at different levels of space and time resolution. Within this approach, which has been implemented to investigate a vast spectrum of physics problems, including hard matter [152–154], soft matter and molecular fluids [155–158], as well as dilute and dense fluid flow problems [44, 117, 119, 159–161] and fluctuating hydrodynamics [162, 163], a small region of the domain is analyzed at a finer scale level whereas the remaining part is treated on a coarser and computationally less demanding level; a hand-shaking region and appropriate exchange of information schemes, then, enable the coupling and communication across the different parts.

When investigating multiscale dilute gas flow problems, the most common approach is to adopt a solver of the continuum Navier-Stokes equations, [44] or Euler equations [117] for the part of the domain where the flow exhibits a small deviation from equilibrium, and rely on kinetic methods, typically the DSMC, wherever substantial non-equilibrium effects are present. While this coupling has led to a number of interesting results, it is plausible to expect that the replacement of the Navier-Stokes equations with a lattice kinetic solver, such as lattice Boltzmann (LB), may prove convenient in several respects. In particular, as well documented in [164], the kinetic nature of LB is reflected in a complete disentangling between non-locality and non-linearity, i.e. kinetic transport along molecular trajectories (free-streaming) is linear, as opposed to non-linear hydrodynamic advection along fluid material lines. Moreover, diffusion emerges from relaxation to local equilibria, with no requirement for second order spatial derivatives. Both features may offer significant advantages in practical implementations, especially in connection with solid boundaries. In this work we depart from the models proposed in literature as the flow at the continuum level is simulated with the efficient LB method in the BGK single relaxation time formulation, [58]. Although both DSMC and LB bear strong links to the Boltzmann kinetic equation, they show major differences in purpose and mathematical structure. Indeed, while DSMC is poised to solve the actual Boltzmann equation by retaining microscopic realism, the LB was initially devised to retain only the symmetry/conservation constraints required to reproduce the hydrodynamic equations in the low-Knudsen-number hydrodynamic limit. Thus, LB could be regarded as a Navier-Stokes solver in kinetic vests. It is only recently that higher-order versions of the LB method have been developed,

which prove capable of capturing (some) non-equilibrium effects beyond the hydrodynamic picture [37, 144, 165], but such higher-order versions are not relevant to this work. The main feature which distinguishes the LB from the DSMC is the coarse graining operated at the level of the microscopic velocity space, as the degrees of freedom of the velocity space itself are largely reduced. In fact, while, in LB, probability distributions at each lattice site  $\mathbf{x}$  are allowed to propagate only along a finite set of directions with an assigned speed  $\xi_a$ , in DSMC particles are grid-free.

## 5.2 Coupling schemes

The most important steps of any hybrid model are the definition of accurate protocols to exchange information between the different solvers at the overlapping region and the decomposition of the computational domain into the particle, continuum and overlap domains. For what concerns the first issue, as LB involves the solution of kinetic equations for the single particle distribution function evaluated at a set of discrete microscopic velocities,  $f_a(\mathbf{x}, t)$ , and not directly the hydrodynamic moments or their fluxes as in classical Navier-Stokes equations solvers, we developed specific mapping schemes that allow information to be passed from the DSMC to the LB domains and vice versa, correctly transferring also non-equilibrium information. In chapter 4, the implementation details are extensively presented. Here, for completeness, we briefly recall the most important features.

The basic idea of the mapping schemes is founded on Grad's moments method [21] and on Gauss-Hermite quadratures [64]. According to Grad's formalism, the single-particle distribution function  $f(\mathbf{x}, \boldsymbol{\xi}, t)$  can be expressed as a series in the dimensionless Hermite orthonormal polynomials,  $\mathcal{H}(\boldsymbol{\xi})$ , in the velocity space  $\boldsymbol{\xi}$  as:

$$f(\mathbf{x}, \boldsymbol{\xi}, t) \approx f^N(\mathbf{x}, \boldsymbol{\xi}, t) = \omega(\boldsymbol{\xi}) \sum_{n=0}^N \frac{1}{n!} \mathbf{a}^{(n)}(\mathbf{x}, t) \mathcal{H}^{(n)}(\boldsymbol{\xi}), \quad (5.1)$$

where  $\omega(\boldsymbol{\xi})$  is the weight function associated with the Hermite polynomials and  $\mathbf{a}^{(n)}$  are the rank- $n$  expansion coefficients tensors, which, in turn, can be identified as the hydrodynamic moments (or a combination of those), e.g.  $\mathbf{a}^{(0)} = \rho$ ,  $\mathbf{a}^{(1)} = \rho \mathbf{u}$ ,  $\mathbf{a}^{(2)} = \mathbf{P} + \rho(\mathbf{u}\mathbf{u} - c_s^2 \boldsymbol{\delta})$ , where  $\rho$  is the fluid density,  $\mathbf{u}$  is the fluid velocity,  $\mathbf{P}$  is the momentum flux tensor,  $c_s$  is the speed of sound, and  $\boldsymbol{\delta}$  is the identity tensor. In Eq. (5.1), we took advantage of the orthonormality of the Hermite polynomials to truncate the series at the order  $N$ : the complete and the truncated distributions have the same leading  $N$  velocity moments, [37].

Starting from this common ground, the two mapping schemes can be established (see also Fig. 5.1, left panel, for a schematic representation of the schemes). In

particular, the projection step (DSMC2LB) allows one to project the DSMC hydrodynamic moments (fine level of description) onto the LBM discrete distributions (coarse level of description). In correspondence of the overlapping region, where both descriptions are accessible, the coefficients  $\mathbf{a}^{(n)}$  in Eq. (5.1) are computed using the DSMC moments. In fact, because the distribution  $f^N(\mathbf{x}, \boldsymbol{\xi}, t)$  is completely and uniquely determined by its values at a set of discrete velocities, one has:

$$\mathbf{a}^{(n)} = \sum_{a=0}^{q-1} \frac{w_a}{\omega(\boldsymbol{\xi}_a)} f^N(\mathbf{x}, \boldsymbol{\xi}_a, t) \mathcal{H}^{(n)}(\boldsymbol{\xi}_a), \quad (5.2)$$

where  $w_a$  and  $\boldsymbol{\xi}_a$  are the weights and abscissae of a Gauss quadrature of algebraic precision of degree  $\geq 2N$  and  $q$  is the total number of discrete velocities. From inspection of Eq. (5.2) and taking into account the classical procedure in which moments are computed in LBM, we immediately see that the non-equilibrium discrete distributions to be supplemented to the LBM at the coupling nodes are the scaled values of the continuous distribution function evaluated at the quadrature abscissae,

$$f_a(\mathbf{x}, t) = \frac{w_a f^N(\mathbf{x}, \boldsymbol{\xi}_a, t)}{\omega(\boldsymbol{\xi}_a)}. \quad (5.3)$$

It is now possible to define the order  $N$  at which the distribution in Eq. (5.1) is truncated, as this is directly related to the algebraic precision of the quadrature. As in this work we present results for the D3Q19 lattice only, we set  $N=2$ , because the proposed quadrature is able to correctly compute the distribution moments up to the momentum flux tensor,  $\mathbf{P}$ . It can be shown, [166, 167] that the resulting solution generated by the LBM is at an isothermal Navier-Stokes level of description.

The inverse reconstruction step (LB2DSMC) allows one to reconstruct from the LBM discrete distributions (coarse level), the continuous, truncated distribution function (fine level) from which, in turn, the velocities of the DSMC particles can be sampled. At the coupling nodes, the LBM non-equilibrium populations  $f_a(\mathbf{x}, t)$  are used to determine the coefficients of the expansion in Eq. (5.1):

$$\mathbf{a}^{(n)} = \sum_{a=0}^{q-1} f_a(\mathbf{x}, t) \mathcal{H}^{(n)}(\boldsymbol{\xi}_a) \quad (5.4)$$

(cfr. Eqs. (5.2) and (5.3)). From the knowledge of the coefficients, the truncated distribution  $f^N(\mathbf{x}, \boldsymbol{\xi}, t)$  is also known. An acceptance/rejection algorithm is then used to generate the velocities of the particles, which, eventually, will evolve according to the DSMC rules. It should be noted that the zeroth- and first-order coefficients in Eq. (5.4) are routinely available in the LBM implementation, because they are used to evaluate the equilibrium distribution functions. In this work, therefore, as only the second-order coefficient terms have to be computed on

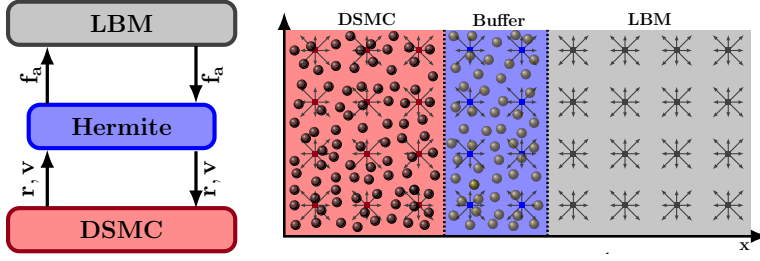


**Figure 5.1:** (Left). Schematic showing the passages from DSMC to LBM, and vice versa, through Hermite formalism. (Right). Pictorial representation of the hybrid simulation domain. On the right the pure LBM region (gray area), and on the left the high resolution region (DSMC, red area) where the DSMC2LB step is performed; in the middle, the buffer region (reservoir of particles, blue area) where the LB2DSMC step is performed via the generation of particles. The black dots represent the DSMC particles, whereas the gold dots represent the particles sampled from the distribution of Eq. (5.1). Note that the LBM extends over the whole domain and a two-level grid is therefore adopted.

purpose, the computational overhead for this coupling step turns out to be very limited.

The domain decomposition is strictly related to the information exchange strategy implemented at the interface between the different methods. In the proposed scheme, to enforce a stronger coupling between the two methods, we extend the LBM to cover the whole simulation domain, whereas the DSMC is confined only within some regions of the domain. In this way, a two-level grid is obtained (Fig. 5.1, right panel). A few basic subroutines define the implementation of the hybrid simulation adopting the illustrated projection and reconstruction steps. During the time integration of the LBM equations, the discrete distributions  $f_a(\mathbf{x}, t)$  are advanced on a coarse time level increment,  $\Delta t_{\text{LBM}}$ , over the whole domain, including the part that lays underneath the DSMC region. Then the DSMC domain is integrated, and it is advanced to the new time on the LBM level through a sequence of fine level time steps,  $\Delta t_{\text{DSMC}}$ . The ratio between the two time steps, depending on the LBM lattice spacing and the DSMC particle characteristic collision time, defines the number of sub-cycles the DSMC should run for each LBM time step. The LBM solution information in proximity of the fine level grid is passed to the DSMC via the imposition of proper boundary conditions on the particle simulation domain. At the beginning of each DSMC integration step, in fact, particles are generated within the buffer region by sampling the Grad's distribution built according to the reconstruction step. The particles, in both the DSMC and the buffer regions, are allowed to stream for one fine level time step. If a particle from the DSMC region crosses the interface, that particle will contribute to the fluxes



of mass and momentum for the LBM discrete distributions corresponding to the node where the crossing occurred so that the populations will be corrected as:

$$f_a(\mathbf{x}, m\Delta t_{\text{LBM}}) = f_a^*(\mathbf{x}, m\Delta t_{\text{LBM}}) + \sum_{i=1}^R \Delta f_a(\mathbf{x}, i\Delta t_{\text{DSMC}}) \quad (5.5)$$

where  $f_a^*$  are the populations before the application of the correction,  $R$  is the ratio between the LBM and DSMC time step durations, and the correction contribution,  $\sum_i \Delta f_a$ , can be evaluated from Eq. (5.1) for  $n \geq 1$  (only the fluxes are exchanged). After the moving of the particles, those still in the buffer region, or that moved into it, are discarded and collisions among the remaining particles are performed. Finally, the DSMC solution in the fine level region is transferred to the LBM in the overlap region (red area in Fig. 5.1, right panel) using the outlined projection step, overwriting the LBM discrete distributions for the lattice nodes in this area with the discrete distributions obtained from DSMC. A new integration of the LBM equations can then be performed.

### 5.3 Numerical results

To test the proposed hybrid method, we consider the steady isothermal Couette flow problem. The flow is driven by the walls, located at  $x/H = 0$  and  $x/H = 1$  moving with a velocity  $u_{\text{wall}}$  such that  $\text{Ma}_{\text{wall}}=0.1$ , where  $H$  is the channel height. The isothermal condition is guaranteed by the negligible viscous dissipation generated by the moving walls. The DSMC particles are treated as argon-like hard spheres (diameter  $d_{\text{ref}} = 3.66 \cdot 10^{-10}$  m; mass  $m = 6.63 \cdot 10^{-26}$  kg). The reference temperature  $T_{\text{ref}}$  and the speed of sound,  $c_s$ , are 273 K and 308 m/s, respectively. The reference density is set so that  $\text{Kn}=0.10$ , based on the channel height equal to 1 mm. At the reference density, 100 particles are initially placed in each DSMC cell, which, in turn, is of length  $0.1\lambda_0$ ,  $\lambda_0$  being the mean free path. As shown in Fig. 5.2, the flow domain is decomposed in such a way that DSMC extends over a region in proximity of the walls, where stronger non-equilibrium effects are expected to occur, equal to  $\alpha$  and the pure LBM domain extends over the remaining part of the domain. For the results of the simulations of this work, each buffer region occupy a width equal to the length of a DSMC cell. To enforce on the LBM domain the flow  $\text{Kn}$  number, we set the relaxation time  $\tau$  according to the relation  $\tau = \sqrt{\pi/8} c/c_s N_H + 0.5$ , [146, 147], where  $c/c_s = \sqrt{3}$  for the D3Q19 lattice and  $N_H$  is the number of nodes along the channel height. DSMC and LBM grids are then set, so that the centers of DSMC cells and the LBM nodes, in the overlap regions, are located at the same positions  $\mathbf{x}$ . In order for the LBM to accurately simulate such flow, it is fundamental to implement proper

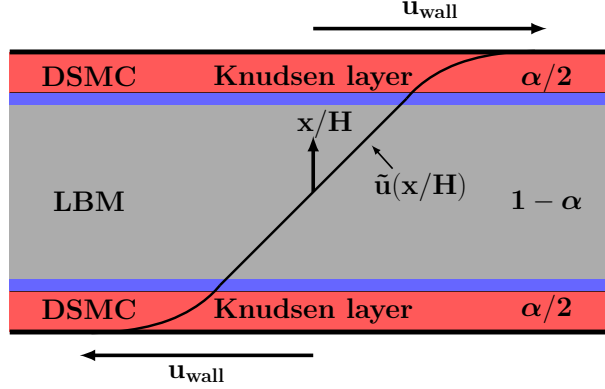


**Figure 5.2:** Sketch of the Couette flow problem. Colours identify the different simulation regions: DSMC (red area) extends over the fraction  $\alpha$  of the total domain; the pure LBM region (gray area) extends over the remaining  $1 - \alpha$  part of the total domain. The buffer region (blue area) is also shown. The sketch of the velocity profile is also reproduced: within the Knudsen layer, due to non-equilibrium effects, a nonlinear behaviour is expected, as shown in section 3.2.

wall boundary conditions, namely diffuse reflection of populations impinging into the walls, [63], and the regularization procedure, [38, 142], which, projecting the non-equilibrium discrete distributions onto the same Hermite polynomials basis used to project the equilibrium populations, allows to get rid of the moments not sufficiently supported by the lattice. Based on the test conditions investigated here, five fine level time integration steps for the DSMC are performed between two consecutive coarse level time integration steps for the LBM.

Taking into account the characteristics of the tested flow, a few additional considerations about the fluxes exchanges at the DSMC-LBM interface as prescribed by Eq. (5.5) are due. One disadvantage of imposing the fluxes across the coupling interface, instead of the related densities, resides in the fact that fluxes show larger statistical noise, [45]. As a means to increase the signal-to-noise ratio of the fluxes exchanged at the DSMC-LBM interface, besides from using the cumulative averages over time, justified by the steady-state nature of the investigated flow, we choose to evaluate them by averaging over the cell volumes, instead of measuring across the interface surface, see [44] and [168]. Moreover, it has to be noted that, for the tested case, there is no net mass flux across the interface. Nonetheless, we also impose and test the mass flux conservation constraint across the DSMC-LBM interface. We also avoid to implement fitting of the mean moments profiles so to faster damp out fluctuations, as done in [120] and [151], since such practice cannot be easily extended to complex flows.

The proposed flow problem is at  $\text{Kn}=0.10$ . While the rarefaction effects for the

tested conditions can be treated within the bulk of the flow by implementing appropriate boundary conditions for the coarse level solver, non-continuum effects produced by the flow gradients in proximity of the walls cannot be captured by the classical D3Q19 model, so a microscopic description is needed. The flow considered here, therefore, appears appropriate to validate the proposed hybrid model, as a separation of scales is naturally present. In the bulk of the flow, in fact, the hydrodynamic variables vary substantially over the macroscopic scale, in turn dictated by the domain geometry; close to the walls, especially within the Knudsen layer, those changes take place at a length-scale much closer to the molecular one. In the literature, several analytical solutions for such uniform shear stress flow have been proposed for both the case of Maxwell molecules, based on the moment-hierarchy method, [169, 170], and for the BGK collision term formulation, [171, 172]. In particular, for the latter case, which is of interest here, it was found that, within the bulk of the flow, for distances greater than at least a mean free path from either wall, a normal solution, i.e. a solution constructed by the Chapman-Enskog method, exists, at Navier-Stokes order, for a Kn based on channel height smaller than about 0.2. From a mathematical point of view, and within the Grad's formalism, this is equivalent to saying that, whereas the bulk flow can be accurately described by a single-particle distribution function truncated at the order  $N = 2$ , the flow at the wall requires that the distribution should include terms above the second-order ones. However, a clear connection between the rarefaction and non-equilibrium conditions and the order at which the series in Eq. (5.1) should be truncated is still missing, [3]. From all these considerations, it appears reasonable that the DSMC domain should cover at least one mean free path from the walls, i.e.  $\alpha/2 \geq \lambda_0$ .

Fig. 5.3, left panel, shows the velocity profiles,  $\tilde{u}(x/H)$ , averaged over time and normalized with respect to the wall velocity, as obtained by a full DSMC simulation and by a hybrid simulation when the DSMC region extends over a mean free path away from both walls ( $\alpha = 0.2$ ) and the buffer region is  $0.1\lambda_0$  wide. A good agreement between the two profiles is found as can be seen from the inset of Fig. 5.3, left panel, where the relative error, defined as:

$$\Delta\tilde{u}(x/H) = \frac{\tilde{u}_{\text{DSMC}}(x/H) - \tilde{u}(x/H)}{\tilde{u}_{\text{DSMC}}(x/H)} \quad (5.6)$$

is plotted. The largest error, in fact, is below 2%, whereas, in the case of a full LBM simulation (orange dots in the inset of Fig. 5.3, left panel), a 5% error is found to occur within the Knudsen layer. This result is obtained strictly maintaining mass conservation within the system. In Fig. 5.3, right panel, in fact, the instantaneous number of particles present in the DSMC region is compared with the averaged one which, in turn, deviates from the initial one by less than 0.05%. More importantly,

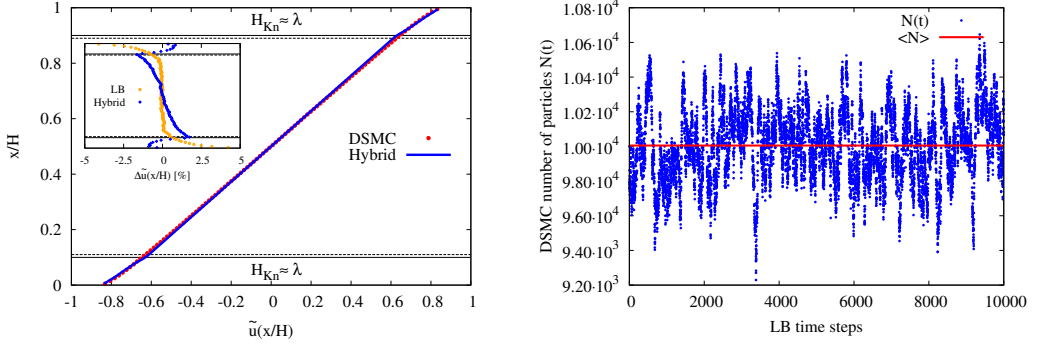


**Figure 5.3:** (Left). Comparison of the velocity profiles averaged over time and normalized with the wall velocity,  $u_{\text{wall}}$ , from a hybrid simulation ( $\alpha = 0.2$ , blue line) and a full DSMC simulation (red dots). In the inset, the relative errors as defined in Eq. (5.6) for a hybrid and a full LBM simulation are shown. (Right). Instantaneous number of particles within the DSMC region versus time step: mass conservation, on average, is strictly obeyed. The average  $\langle N \rangle$  deviates from the initial number of particles less than 0.05%.

we also measured the speed-up provided by the hybrid scheme versus full DSMC ( $\alpha = 1$ ) as a function of the parameter  $\alpha$ .

In Fig. 5.4, such speed-up is compared with the speed-up one would obtain by just summing up the computational times required for the DSMC to run over the  $\alpha$  fraction of the domain and for LBM over the whole domain. The computational times are recorded when the solution reaches a global error, for both the velocity and shear stress profiles,  $\tilde{\sigma}_{xy}(x/H)$ , below 3% with respect to a reference full DSMC simulations. The global error for the velocity is defined as:

$$\sum_{i=1}^{N_H} \frac{|\tilde{u}(x_i/H) - \tilde{u}_{\text{ref}}(x_i/H)|}{|\tilde{u}_{\text{ref}}(x_i/H)|} \cdot \frac{1}{N_H} \leq 3\%, \quad (5.7)$$

and analogously for the shear stress. The reference DSMC simulation has cumulated enough statistics to confine the difference between the maximum and the minimum values of the shear stress below 0.02%. The recorded times are then averaged over several realizations of the tested flow. It is possible to see that a substantial speed-up is achieved by applying the hybrid method. More interestingly, the required computational time,  $t_{\text{Hybrid}}$ , is smaller than what would be just the sum of the times required for DSMC to run over the  $\alpha$  fraction of the domain and for LBM over the whole domain,  $t_{\text{LBM+DSMC}}$ . In particular, for  $\alpha = 0.2$ , more than a sixfold reduction with respect to a full DSMC simulation is achieved. It has also to be noted that the computational overhead, due to the fact the LBM extends over the whole domain and not just over  $(1 - \alpha)$ , is very limited. For the

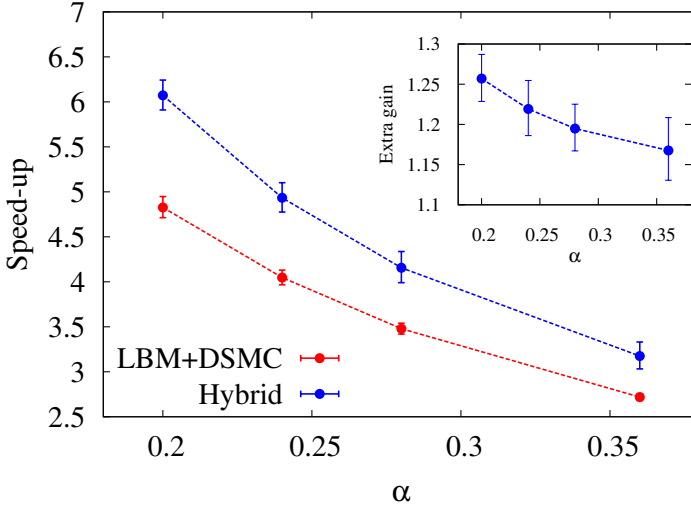


**Figure 5.4:** Speed-up as a function of the parameter  $\alpha$  comparing the computational times required to fulfill the convergence criteria of Eq. (5.7) for the hybrid method. The error bars represent one standard deviation for the computational time of 100 simulations. Blue symbols denote the speed-up obtained by the hybrid method with respect to the full DSMC simulation, whereas red symbols denote the speed-up obtained by simply summing the times required for DSMC to evolve over the  $\alpha$  part of the domain and LBM over the entire domain. In the inset, the found extra-gain is also shown. At  $\alpha = 0.2$ , a 25% extra speed-up is achieved by the hybrid method.

tested conditions, in fact, a full LBM simulation is about 80 times faster than a full DSMC simulation, performed over the whole domain. The measured extra-speed up, defined as  $t_{\text{LBM+DSMC}}/t_{\text{Hybrid}}$ , was found to be 25% for  $\alpha = 0.2$  and 16% for  $\alpha = 0.36$ . Such computational extra gain may qualitatively be explained by considering that the LB information processed in the bulk provides a higher quality, less noisy, input to the DSMC in the Knudsen layer than bulk DSMC alone. Thus, LB serves as a sort of DSMC-accelerator. Finally, a clarification about the flow domain decomposition technique and its range of applicability is due. This type of hybrid approach is a suitable choice to analyze multiscale problems if the flow features a bulk region for which a constitutive model is known to be accurate, but it may become not an efficient nor an accurate method if such a condition is not fulfilled. This would be the case, for example, of the Couette flow at a larger Kn number than the one presented here. For such condition, it is known that rarefaction effects spread also across the bulk of the flow and the classical Navier-Stokes equations can no longer accurately reproduce the flow properties found in the

bulk. To overcome this limitation, however, the kinetic roots of the LBM may help. In fact, whereas LBM was specifically designed to solve the Navier-Stokes equations, [166, 167], in the last decade various groups have begun to explore the possibility to extend the LB methodologies towards non-equilibrium flows beyond Navier-Stokes hydrodynamics by adopting higher-order lattices, [37, 144, 165], or introducing further modelling so to mimic effects of free particle streaming, [36]. This is also equivalent to say that, if a higher-order lattice is adopted, the size of the domain where the DSMC solver is still needed can be significantly reduced, thus further improving the overall computational efficiency of the simulation. In this view, it should be pointed out that the coupling strategy proposed here can be directly applied to any suitable lattice, provided that the discrete speeds are abscissae of a Gauss-Hermite quadrature.

A remark on the range of application of the proposed hybrid method is in order. While the DSMC can correctly predict thermal effects, the LB model employed here is not able to reproduce such effects, thus limiting the current implementation to isothermal flows. To overcome such limitation, essentially stemming from the lack of sufficient isotropy of the lattice, different strategies may be envisaged. In particular, three main approaches have appeared in literature to extend the LB method to thermal flows: the mixed approach, where the velocity field is solved using a usual LB model and the energy, or temperature, equation is solved by adopting a different numerical method such as finite difference or finite volume method [145]; the double distribution function approach, where a second lattice is adopted for the energy field [143]; and the multispeed approach, where a single lattice fulfilling higher-order isotropy conditions is used [144]. The most natural choice among the proposed methods is the multispeed scheme as it shares with the present hybrid model the common Hermite expansion approach.

## 5.4 Conclusions

In conclusion, a novel multiscale hybrid scheme for dilute gas flow simulations relying on the DSMC accuracy for the regions of the flow where a microscopic scale description is needed and on the efficiency of the LBM for the parts of the flow where hydrodynamic properties evolve over macroscopic scales has been proposed. The method, which is based on Grad's formalism and Gauss-Hermite quadratures, enables the flux exchange across the LBM-DSMC interface, conserving both mass and momentum. We applied the hybrid formulation to the steady Couette flow and we found that, alongside a good agreement with a full DSMC solution, up to a sixfold reduction of the computational time cost can be achieved. The application of such model could also open the way to study macroscopic flows characterized

by the presence of local regions where non-equilibrium effects are strong, and, therefore, the method is not restricted to classical micro-mechanical systems. This, indeed, will be the main topic of the chapter 6.

## 6 Hybrid DSMC-LBM solver for complex flows

In this chapter we extend the applicability of the coupling methodology presented in chapter 4 and then applied to the case of a monodimensional flow in chapter 5 to a complex three-dimensional flow.

We present the results of a comparative study performed with three numerical methods applied to a flow in a complex geometry characterized by compressibility and large rarefaction effects. The employed methods, all based on the kinetic theory of gases, are the Lattice Boltzmann Method in a regularized formulation, the Direct Simulation Monte Carlo approach and the hybrid method coupling the LBM and the DSMC presented in chapters 4, 5, in this chapter extended to the case of simulations involving many particles and complex geometries. Owing to the common kinetic nature shared by the employed methods and to their implementation in a single code infrastructure, a detailed comparison of the results can be performed on a quantitative ground. The numerical results permit to determine, for the studied flow problem, the range of applicability in terms of a geometry-based Knudsen number for the present LBM formulation. The need to employ the hybrid method is justified by the very large computational cost of the DSMC simulation. Finally, good scalability properties of the parallel algorithms, as well as the large computational cost reduction guaranteed by the hybrid method, while providing an accurate solution, are demonstrated.

### 6.1 Introduction

The solution to the standard Navier-Stokes equations accurately reproduces the real flow behavior under continuum flow conditions and for cases where non-equilibrium effects can be dealt with perturbatively with respect to the equilibrium state. Whenever such assumptions are not met anymore, i.e. typically when the

---

The content of this chapter has been adopted from G. Di Staso, S. Srivastava, E. Arlemark, H.J.H. Clercx, and F. Toschi, "Hybrid lattice Boltzmann-direct simulation Monte Carlo approach for flows in three-dimensional geometries," *Comput. & Fluids*, vol. 172, p. 492–509, 2018, [173].



molecular-level spatial scales (molecular mean free path,  $\lambda$ ) are comparable to the macroscopic ones (domain geometry or hydrodynamic characteristic length scale,  $L$ ), the Navier-Stokes equations fail to provide a reliable description. The definition of the Knudsen number as  $\text{Kn} = \lambda/L$  leads to the usual classification into hydrodynamic ( $\text{Kn} < 0.01$ ), slip ( $0.01 < \text{Kn} < 0.1$ ), transitional ( $0.1 < \text{Kn} < 10$ ) and free molecular regime ( $\text{Kn} > 10$ ). While the Navier-Stokes equations, eventually supplemented with adequate slip boundary conditions, can be applied up to the slip flow regime, [114, 115], for conditions in the transitional flow regime, the flow description needs to be based directly on a more fundamental ground, the Boltzmann equation, [6]. Among the several numerical techniques applied to approximate the Boltzmann equation in the rarefied regime, the Direct Simulation Monte Carlo method, [1], has demonstrated to be the most successful and adaptable to a wide range of applications. However, due to its particle-based nature and explicitness of the interparticle collision process, the computational cost becomes prohibitively large for the near-continuum regime.

It has to be mentioned that other numerical methods have been proposed to simulate flows in the transitional regime, such as those based on extended hydrodynamic equations using higher-order Chapman-Enskog approximations, [174], or those originated from moments expansion methods such as the Grad's method, [3, 21]. However, difficulties in imposing boundary conditions as well as the complexity of the resulting systems of equations hindered their application to the simulation of flows of industrial interest. In addition to these modelling considerations, in a non-negligible amount of industrial applications, such as micro- and nano-electromechanical systems or material processing tools, it is not possible to clearly and a priori determine that the flow is entirely within the continuum limit, but a range of non-equilibrium/rarefaction conditions are encountered. The approach to simulate a gas flow showing these characteristics using the DSMC, therefore, faces a very large computational burden. Under such circumstances, because of the current computational and modelling limitations, a hybrid method coupling continuum and rarefied flow solvers has to be employed.

The DSMC method has been already coupled to classical Navier-Stokes and Euler equations solvers in the past, [44, 116, 119]. The main drawback of such coupling schemes, however, resides in the separation of both temporal and spatial scales evolved in the two methods, especially when large non-equilibrium effects are present. The approach to use LBM as the solver for the continuum part goes in the direction to reduce such separation, in fact, due to its kinetic theory roots, shared with the DSMC, the coupling between the two methods can be performed at the microscopic scales relevant for the single particle velocity distribution function instead of the macroscopic field scales, as done in the previous models. In this

view, the LBM has already shown to be able to capture some phenomena typical of rarefied gas flows, [36, 165].

In chapter 4, we presented the coupling schemes that allow the two-way extraction and transfer of information at the interface between the LBM and the DSMC, and, in chapter 5, we applied them to a monodimensional flow case using a domain decomposition technique. In this work, we extend it to the case of complex three-dimensional geometries involving a large number of computational particles and we validate the hybrid LBM-DSMC model, both in terms of accuracy and computational cost, for an industrial application where DSMC method is reliable but time consuming and the continuum methods are fast but less accurate or even inaccurate.

The rest of the chapter is organized as follows: In section 6.2, the analogies between the LBM and DSMC methods and the coupling algorithm are reviewed. section 6.3 describes additional details with respect to those given in chapter 3, about the treatment of complex geometries in DSMC and hybrid methods. In section 6.4, we present the investigated flow problem and the results obtained individually by each method are compared in terms of mean field hydrodynamic quantities. Finally, in section 6.5, the computational cost associated to each method is analyzed.

## 6.2 Review of the hybrid LBM-DSMC coupling method

For a comprehensive treatment of the DSMC and LBM methods, the reader should refer to the reference books from Bird and Succi, respectively, [1, 24]. Here, we will briefly delineate the analogies, and differences, characterizing the two methods which are relevant for the hybrid method formulation. Both methods propose to determine the fluid motion as described by the Boltzmann equation by making use of a splitting algorithm approach: a free-flight phase, in which particles move undisturbed and unaware of the other particles, is followed by a phase during which the microscopic state changes according to the prescribed collision mechanisms typical of each method. Although the two phases both occur in the LBM and DSMC, they are enforced in very different ways. In fact, for the streaming phase, the main feature which clearly distinguishes the LBM from the DSMC is the drastic reduction of the velocity space degrees of freedom: while in DSMC particles are free to stream with any possible velocity, in LBM they are forced to propagate only along a finite set of directions with a pre-determined speed. Even more evident, it is the dissimilarity for the collision phase: in DSMC it involves stochastic binary collisions between close enough particles, in LBM, under the BGK approximation, which is used in the present work, [58], it is reduced to a relaxation process towards a local equilibrium. It can be easily understood that

the assumptions made in the LBM allow to boost numerical efficiency, but they also suggest a qualitative explanation why the LBM in its classical and minimal formulation cannot go beyond a Navier-Stokes level of representation, [166, 167]. The formalization proposed by Shan and coworkers, [37], which describes the LBM according to the Hermite expansion representation of the velocity distribution function and Gauss-Hermite quadratures for the selection of the set of discrete velocities, is fundamental for the formulation of the hybrid model. A further necessary step to treat large non-equilibrium effects, i.e. the regularization procedure, firstly proposed in [38], is also included in the present implementations of the LBM and hybrid methods. The main idea behind this technique is to ensure that the non-equilibrium part of the discrete distributions lies entirely within the same Hermite polynomial basis over which the equilibrium distributions are projected. Conceptually, such process removes from the non-equilibrium discrete distributions all those moments that cannot be accurately evaluated by the available quadrature and which could contain numerical discrete artefacts. The advantage of the application of the regularization procedure in increasing the stability properties of the LBM when simulating high-Reynolds number flows has been recently demonstrated in [142, 175]. In this chapter, we will rather exploit the properties of the regularization in overcoming existing defects in conventional LB models when simulating flows characterized by finite (weak) compressibility and rarefaction effects. In particular, as we will employ a D3Q19 lattice, the regularized LBM model will incorporate up to the second-order hydrodynamic moments, and, therefore, it can be adopted only in the limit of isothermal flows and when compressibility effects are not strong. Several approaches have been proposed in order to extend the applicability of the LBM towards high-Ma number flows. Amongst the most promising ones seems the implementation described in [176], as it provides very good comparisons with references also in the case of large supersonic flows. The main features of such scheme are the adoption of the entropic LB formulation, [56], and the construction of the local discrete equilibrium distribution functions maintaining the exponential form of the Maxwell-Boltzmann equilibrium distribution, rather than the typical polynomial form. Another interesting feature of such approach is that the streaming phase and the locality of the collisional process operations are kept unmodified. The inclusion of such implementation will be subject of future work.

As already mentioned in chapters 1 and 3, the implementation of the DSMC method adopted in this study features a standard no time counter (NTC) algorithm, [1], for the evaluation of the number of the attempted collision events that will occur between two computational particles residing at each time step in the same collisional cell. In the present DSMC implementation, however, the treat-

ment of complex geometries and of the wall boundary conditions is not standard in the sense that it has been developed so to mimick the same approach which is adopted in the LBM implementation. More details about this aspect will be provided in section 6.3.

The full treatment and validation of the hybrid LBM-DSMC model can be found in chapters 4 and 5. Here, for completeness and self-consistency of the chapter, only few details are provided. The model consists of two main features: the mapping procedures needed to transfer the information about the local flow properties from LBM to DSMC and vice versa, and the implementation of the coupling algorithm based on the flow domain decomposition method. In Fig. 6.1, a flowchart representing the hybrid model algorithm is shown. The step for the LB2DSMC transfer of information requires that at the lattice nodes/DSMC cells where the coupling occurs, the velocities of the DSMC particles are sampled from a continuous distribution function, see Fig. 6.1 (node a.). Taking advantage of the Hermite formalism, the coefficients  $\mathbf{a}_{\text{LB}}^{(n)}$  of the expanded (in Hermite polynomials) velocity distribution function can be computed via the discrete non-equilibrium  $f_{\text{LB},a}(\mathbf{x}, t)$  as:

$$\mathbf{a}_{\text{LB}}^{(n)}(\mathbf{x}, t) = \sum_{a=0}^{d-1} f_{\text{LB},a}(\mathbf{x}, t) \mathcal{H}^{(n)}(\boldsymbol{\xi}_a), \quad (6.1)$$

where  $\mathcal{H}^{(n)}(\boldsymbol{\xi})$  is the Hermite polynomial of order  $n$  and  $d$  represents the number of discrete velocities  $\boldsymbol{\xi}_a$  of the employed lattice. Since the knowledge of the coefficient is tantamount to know the distribution itself, the DSMC particles velocities can be sampled via an acceptance/rejection algorithm from the velocity distribution function reconstructed using the coefficients expressed by Eq. (6.1), which assumes the following form:

$$f(\mathbf{x}, \boldsymbol{\xi}, t) = \omega(\boldsymbol{\xi}) \sum_{n=0}^{\infty} \frac{1}{n!} \mathbf{a}_{\text{LB}}^{(n)}(\mathbf{x}, t) \mathcal{H}^{(n)}(\boldsymbol{\xi}). \quad (6.2)$$

The coupling scheme for the DSMC2LB communication, see node 5. of the flowchart in Fig. 6.1 prescribes, at the end of the DSMC subcycling, to project the cumulative averages of the DSMC hydrodynamic variables onto the LB discrete distributions taking advantage of the fact that the coefficients of the velocity distribution functions expanded in Hermite polynomials can be evaluated from the knowledge of the hydrodynamic variables themselves. The expansion coefficients, in fact, are given by

$$\mathbf{a}^{(n)} = \int f(\mathbf{x}, \boldsymbol{\xi}, t) \mathcal{H}^{(n)}(\boldsymbol{\xi}) d\boldsymbol{\xi}, \quad (6.3)$$

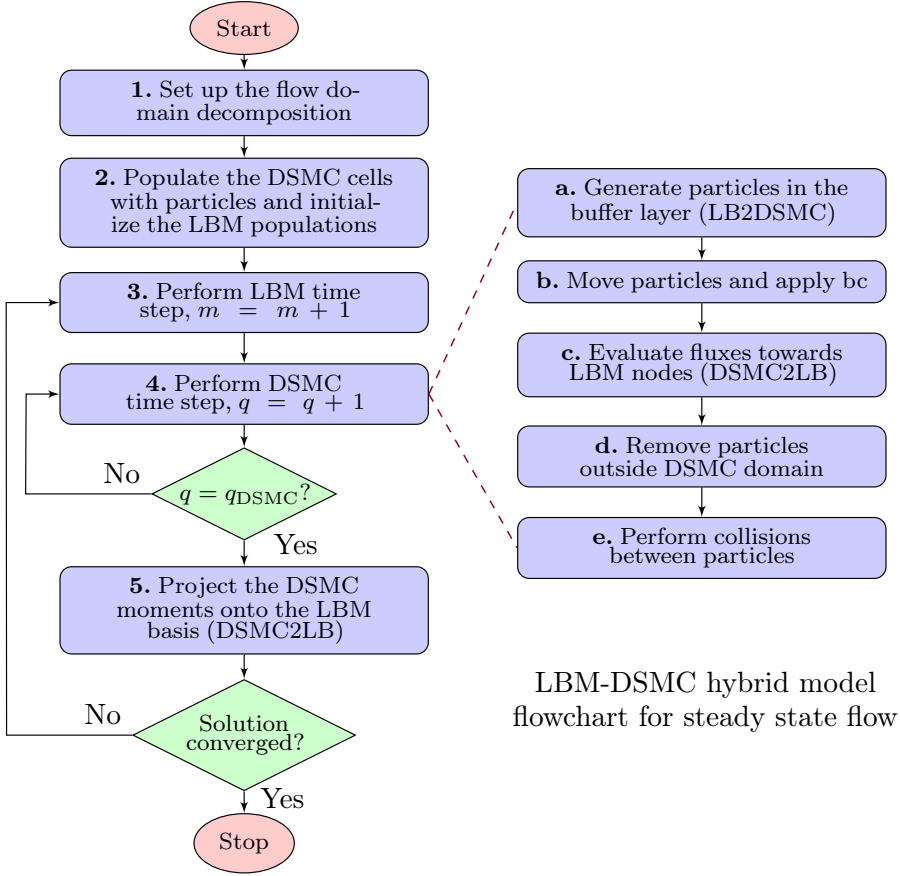


**Figure 6.1:** Flowchart for the hybrid LBM-DSMC model for steady state flows. For each LBM time step,  $m$ , (node 3.) the DSMC sub-cycles for a number of DSMC time steps equal to  $q_{\text{DSMC}}$ . During each substep, both the LB2DSMC and the DSMC2LB passage of information are applied, see nodes a. and c. After the DSMC subcycle is completed, the hydrodynamic moments, as cumulated during the DSMC subcycle, are projected onto the LBM distributions, see node 5. The computation continues until the solution convergence criterion is met. Note that the DSMC2LB step features two different phases: node 5., the projection of the DSMC hydrodynamic moments onto the LBM basis (described in chapter 4), and, (node c.), the evaluation of the fluxes of density and momentum associated to the DSMC particles crossing the interface between the LBM and the DSMC (described in chapter 5).

which, for the first coefficients, specializes to

$$\begin{aligned}
 \mathbf{a}_{\text{DSMC}}^{(0)} &= \rho_{\text{DSMC}}, \\
 \mathbf{a}_{\text{DSMC}}^{(1)} &= (\rho \mathbf{u})_{\text{DSMC}}, \\
 \mathbf{a}_{\text{DSMC}}^{(2)} &= [\mathbf{P} + \rho (\mathbf{u} \mathbf{u} - c_s^2 \delta)]_{\text{DSMC}},
 \end{aligned} \tag{6.4}$$

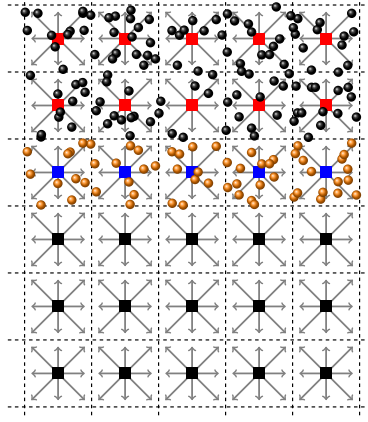


**Figure 6.2:** Schematic showing a typical domain decomposition. The LBM grid extends over the whole domain, while the DSMC is solved only in a restricted area (red squares represent the centers of the DSMC cells, filled with black particles). In this area, the DSMC hydrodynamic moments are projected onto the LBM lattice. The buffer layer (blue squares) acts as a boundary condition for the DSMC area as the orange particles are sampled from a velocity distribution reconstructed from the information provided by the LBM, i.e. the coefficients of Eq. (6.1).

where  $\rho$ ,  $\rho\mathbf{u}$ ,  $\mathbf{P}$ ,  $c_s$  and  $\delta$  are the density, the momentum, the momentum flux tensor, the speed of sound and the identity tensor, respectively. Once the velocity distribution function constructed from the coefficients of Eq. (6.4) is known, it can be evaluated in correspondence of the lattice discrete velocities  $\xi_a$  and finally supplemented to the LBM solver at the coupling nodes as:

$$f_{\text{DSMC} \rightarrow \text{LBM},a}(\mathbf{x}, t) = \frac{w_a f_{\text{DSMC}}(\mathbf{x}, \xi_a, t)}{\omega(\xi_a)}, \quad (6.5)$$

where  $w_a$  are the lattice weights and  $\omega(\xi)$  is the weight function associated with Hermite polynomials.

It should be emphasized that the order  $n$  in Eq. (6.1) and Eq. (6.3) is strictly related to the lattice employed and, in particular, to the algebraic precision of the corresponding Gauss quadrature. For the present case  $n = 2$  since we will adopt a D3Q19 lattice. Moreover, in Eq. (6.4) the following assumption is made,  $p = \rho c_s^2$ , so to mimic the LBM ideal gas equation of state.

Finally, the hybrid method prescribes the determination of the domain decomposition, i.e. the allocation of a part of the domain to be solved by the DSMC. In Fig. 6.2, a pictorial representation of the domain decomposition is shown. In the proposed scheme, the LBM extends over the complete simulation domain, while the DSMC regions are confined only in those parts of the domain where non-

equilibrium effects are stronger, so that a two-level grid is obtained. As shown in the scheme of Fig. 6.1, after the LBM discrete distributions  $f_a(\mathbf{x}, t)$  are integrated on a coarse time level increment over the whole domain,  $\Delta t_{\text{LBM}}$ , including the part below the DSMC area, the DSMC part is advanced to the new time at the LBM level through a sequence of fine level time steps,  $\Delta t_{\text{DSMC}}$ . At the beginning of each DSMC time step, particles are generated within the buffer layer, located at the interface between the DSMC and the LBM, by sampling the reconstructed and truncated velocity distribution function, Eq. (6.2), obtained from the coefficients of Eq. (6.1). The particles within the DSMC domain, and the buffer layer, stream for one  $\Delta t_{\text{DSMC}}$  and proper boundary conditions are applied to the particles trajectories, see node b. of Fig. 6.1. As soon as a particle crosses the interface between the DSMC and the LBM areas, it will contribute to the mass and momentum fluxes for the LBM populations corresponding to the node where the crossing occurred so that a correction to those populations is applied in the form:

$$f_a(\mathbf{x}, m\Delta t_{\text{LBM}}) = f_a^*(\mathbf{x}, m\Delta t_{\text{LBM}}) + \sum_{q=1}^{q_{\text{DSMC}}} \Delta f_a(\mathbf{x}, q\Delta t_{\text{DSMC}}), \quad (6.6)$$

where  $f_a^*$  are the uncorrected populations at the LBM time step  $m$ , and the correction contribution  $\Delta f_a$  at each DSMC time substep,  $q$ , can be evaluated as:

$$\Delta f_a(\mathbf{x}, q\Delta t_{\text{DSMC}}) = w_a \sum_{n=1}^2 \frac{1}{n!} \mathbf{a}_{\text{DSMC}}^{(n)}(\mathbf{x}, q\Delta t_{\text{DSMC}}) \mathcal{H}^{(n)}(\boldsymbol{\xi}_a). \quad (6.7)$$

In Fig. 6.3, a schematic representation of the steps involved in the correction phase is depicted.

After the streaming phase, the particles outside the DSMC domain are removed and collisions among the remaining particles are performed, see nodes d. and e. of the flowchart of Fig. 6.1. At the end of the DSMC subcycle, the DSMC solution is projected at the LBM level in the overlap region. Afterwards, a new LBM time step is performed until the convergence criterion, or the prescribed final time step, is reached.

## 6.3 Treatment of complex geometries and wall boundary conditions

Several approaches may be pursued in LBM and DSMC to treat complex geometries and the related boundary conditions, each having advantages and drawbacks

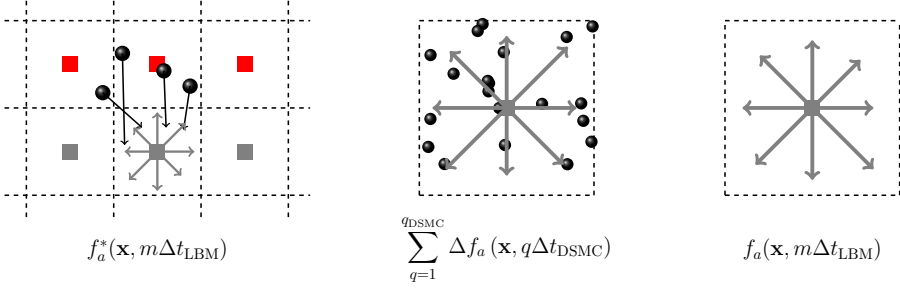


**Figure 6.3:** Steps involved in the correction of the LBM populations due to the fluxes of mass and momentum originated from particles crossing the interface between the DSMC and LBM areas. At each DSMC time substep  $q$ , (left figure), particles may cross the interface between the DSMC and the LBM, and the related fluxes of mass and momentum are stored during the whole DSMC subcycle composed of  $q_{\text{DSMC}}$  DSMC time substeps (center figure). At the end of the subcycle, the LBM populations are corrected to take into account the stored information via Eqs. (6.6) and (6.7) (right figure).

from computational and accuracy points of view.

For the LBM, the standard Cartesian grid implementation prescribes to represent the solid object walls with a staircase approximation so that they are assumed to be placed in correspondence of the midpoints of boundary links between solid and fluid nodes. An improvement of this approach is represented by interpolated boundary conditions, [177], which has the aim to reduce boundary location dependency from the relaxation time and then from the fluid viscosity. The immersed boundary method has been also introduced, [178], especially in conjunction with moving objects, for which a Cartesian grid is used and external forces localized at the object surfaces have to be imposed to satisfy the intended boundary conditions. This last approach is also used in DSMC, see e.g. [179], but, instead of the evaluation of the fictitious forces, it requires to recompute the effective volumes of the cells cut by the geometry surfaces, to achieve the correct molecular collision frequencies. Another approach commonly employed in DSMC, and similar to what is done in LBM, is the staircase representation of the geometry for which the object walls coincide with the surfaces of the Cartesian grid cells, [1, 180]. Finally, non-Cartesian body-fitted meshes can be localized in proximity of the object so to better approximate its shape, [181].

Given such a variety of options, the choice of the method to handle complex geometries is motivated by the fulfilment of some criteria, keeping in mind that the final aim is to simulate flows adopting the already developed hybrid method. The first criterion is related to the full compatibility of the implementations for the LBM and DSMC. This automatically rules out the possibility to adopt a body-fitted mesh since the LBM, in the present formulation, adopts a Cartesian grid.



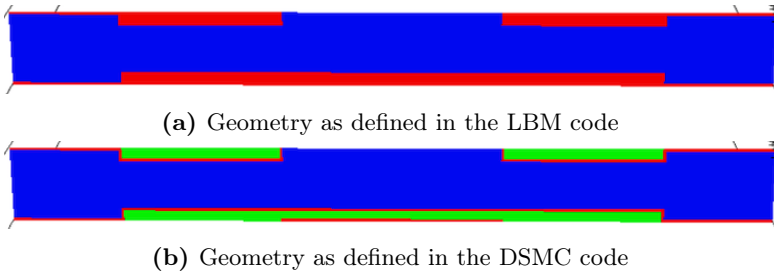


**Figure 6.4:** Comparison between the geometry as obtained in the LBM (a) and DSMC (b) codes; as it can be clearly seen, the walls, present at the interface between the red and blue areas, are localized exactly in the same position. The only difference, not relevant for the determination of the wall location, is that in the DSMC code the cells which are not fluid cell nor wall cells, but are needed to fill in the remaining part of the simulation box, are defined as empty cells, since particles cannot enter those cells (green area).

The immersed boundary method has also to be excluded due to the fact that, for the LBM, the method has been essentially used in conjunction to the enforcement of a no-slip boundary condition at the geometry walls, while in the rarefied regime we deal with flows showing a finite slip velocity at the surface.

Also the interpolated boundary conditions approach has to be dropped because, depending on the order of interpolation, more than one grid spacing is required. For the staircase representation, instead, only one node is required to impose the intended wall boundary condition. Moreover, under this last approach, the possibility to include a slip velocity in the LBM solution has been already demonstrated and it can be considered well established, [137, 143]. These considerations drove the implementation to handle complex geometries in LBM, DSMC and the hybrid method adopting the staircase implementation.

Under this approach, the definition, from an algorithmic point of view, of a geometry both in DSMC and LBM corresponds to the proper definition of a scalar field which attributes the status of fluid or wall to a cell/node, as described in chapter 3. In Fig. 6.4a-6.4b a representation of the geometry which will be used in the simulations of section 6.4 as obtained in the LBM and DSMC code is shown. The location of the position where the wall boundary conditions are imposed, placed at the interface between fluid and wall cells/nodes, is the same in the two cases.

The domain, in LBM, DSMC, as well as in the hybrid model, is currently statically decomposed into Cartesian blocks and each block is simulated by a process, with inter-process communication performed via the Message Passage Information (MPI). In the LBM implementation, when using a D3Q19 lattice, a single layer of

frame nodes surrounding each block is sufficient to perform the streaming phase across the contiguous processes.

We apply to the DSMC code a similar implementation in the sense that particles are transferred to contiguous processes only once they land in a frame cell. In order to do this, however, it is needed to guarantee that a particle streams at most one cell away. This is possible if one complete time step is divided into  $k$  substeps so that during each substep the particle trajectory along each coordinate axis direction is not larger than the cell size along that direction.

In Fig. 6.5, the distribution of the number of substeps for a time step, set according to the DSMC rules-of-thumbs, is evaluated for the conditions of the simulations of section 6.4. Almost all the particles at the conclusion of the time step still reside in the same cell ( $k=0$ ) or, at most, have moved to the next neighbor cell,  $k=1$ . Only a limited number of particles — less than 1.5% — will have to stream for a larger number of substeps ( $k>1$ ). Therefore, in practice, the computational overhead due to the fact that more than one cycle over a (small) fraction of the particles is needed to complete the streaming phase is limited. Such overhead can be more than compensated by the possibility to use only one frame of ghost cells to handle the inter-process communication. In addition, the substepping feature allows to verify if an interaction between a particle and a surface occurred, and eventually apply the particle-surface boundary conditions, only to the particles residing within the fluid cells adjacent to the walls. Additional details about the implementation of the algorithm, in particular of the streaming step phase, were provided in the section 3.1.

The definition of the interactions between a gas molecule and a surface, needed to determine the related momentum and energy transfer, and therefore to realize proper boundary conditions, is very complicated as it requires the complete knowledge of the scattering kernel, including the molecular structure of the surfaces. Such level of detail, though, is not accessible to the DSMC nor to the LBM. However, from a macroscopic mean field point of view, it is sufficient to know some average parameters, i.e. the so-called accommodation coefficients in order to characterize gas-wall interactions. In particular, as in this work we deal with flows which can be assumed isothermal, we are interested only in the Tangential Momentum Accommodation Coefficient (TMAC), defined as:

$$\sigma_v = \frac{\tau_i - \tau_r}{\tau_i - \tau_w}, \quad (6.8)$$

where  $\tau_i$ ,  $\tau_r$  and  $\tau_w$  are the tangential momentum of incoming particles, reflected particles and of the wall, respectively. Two classical limits, specular and fully diffuse wall boundary conditions can be recovered. For the specular case, the tangential

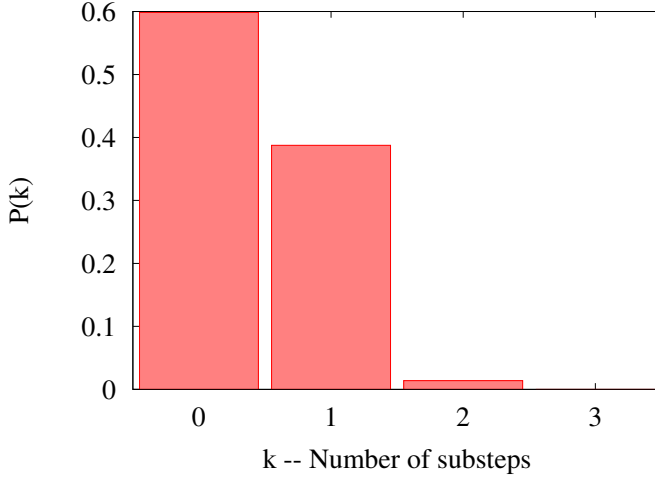


**Figure 6.5:** Distribution of the number of substeps,  $k$ , for the time step,  $\Delta t_{\text{DSMC}}$ , used for the simulations presented in section 6.4. For most of the particles, at the end of the time step, they will stream to the next neighbor cell ( $k \leq 1$ ). Only about 1.5% of particles will stream further ( $k \geq 2$ ). A similar distribution should be found for any other geometry and flow conditions, as it is dictated by the requirements to obtain a well resolved simulation.

velocity of the particles reflected from the wall is unchanged so that  $\tau_i = \tau_r$  and, therefore,  $\sigma_v = 0$ . For the fully diffuse case, instead, the particles are reflected from the wall with, on average, a velocity equal to the wall tangential velocity, so that  $\tau_r = \tau_w$ , and, therefore,  $\sigma_v = 1$ .

Due to the common kinetic theory roots, we can include in the DSMC and the LBM the just described treatment of the gas-surface interaction in a similar way. In particular, for the DSMC a particle will be reflected from a wall diffusively with probability  $\sigma_v$  or specularly with probability  $(1 - \sigma_v)$ . Analogously, for the LBM we apply a combination of diffuse and specular boundary conditions as:

$$f_i = \sigma f_i^{\text{eq}} + (1 - \sigma) f_{-i}^*, \quad (6.9)$$

where  $f_i^{\text{eq}}$  is the discrete equilibrium distribution function and  $f_{-i}^*$  is the post-collision distribution function corresponding to the population with discrete velocity specular with respect to the wall.

The value of  $\sigma$  in Eq. (6.9), however, is not, in general, the same as  $\sigma_v$  in Eq. (6.8), if the intended macroscopic slip velocity is the one provided by a slip model such as the well-known Cercignani's second-order model, [182]. In the Appendix 6.B to this chapter, a full treatment of the method to correct for this difference and therefore to correctly reproduce the slip velocity with the LBM is provided.

## 6.4 Comparison study: LBM, DSMC and hybrid method

In this section the results obtained from the simulations performed with the regularized LBM, the DSMC and the hybrid LBM-DSMC method, applied to a flow test case characterized by large rarefaction and moderate compressibility effects, are compared. In Fig. 6.6, the top view and a vertical section of the flow domain geometry are drawn. The geometry basically consists of two circular parallel disks with radius equal to  $R_2$  separated by the distance  $H$ . The gas flow inlet is realized in the upper disk through a circular duct whose radius is equal to  $R_1$ . The outlet is placed at a minimum distance of  $L/2$  from the centerline of the inlet section. If the inlet radius  $R_1$  is taken as reference, then  $R_2/R_1 = 15$ ,  $L/R_1 = 40$ , and  $H/R_1 = 0.6$ . The flowing gas is hydrogen and a large pressure difference across the flow domain is present, reflecting into a large variation of the rarefaction conditions. In fact, using the height  $H$  between the disks as the characteristic length scale and using the variable hard sphere (VHS) model to compute the gas mean free path,  $\lambda$ , one has  $\text{Kn}_{in} \cong 0.07$  and  $\text{Kn}_{out} \cong 1.6$ , so ranging from an almost continuum condition to the transitional flow regime.

For the gas-surface combination of the present test case, a TMAC equal to 0.83 was found experimentally. Finally, the numerical results obtained from the three numerical methods (LBM, DSMC and the hybrid method, all fully three-dimensional) are compared with a reference solution obtained from an axisymmetric DSMC simulation performed with the *dsmcFoam* code, [181], and with experimental data. The pressure levels found in the device are obtained via capacitance manometers. Uncertainty on the measurements is estimated to be in the order of 2%.

### LBM results

Before presenting the results of the LBM simulation, it has to be clarified that while in the DSMC the collision frequency is automatically adjusted according to the local conditions, this is not the case for the LBM. In fact, if the relaxation time  $\tau$  is kept fixed also when the fluid density changes, then the collision frequency would also be constant throughout the domain. This microscopic mismatch has as a consequence that, macroscopically, the dynamic viscosity of the gas,  $\mu$ , is a function of the local conditions. More specifically, it is a function of the pressure:

$$\mu = \rho\nu = \rho c_s^2 \left( \tau - \frac{1}{2} \right) = p \left( \tau - \frac{1}{2} \right), \quad (6.10)$$

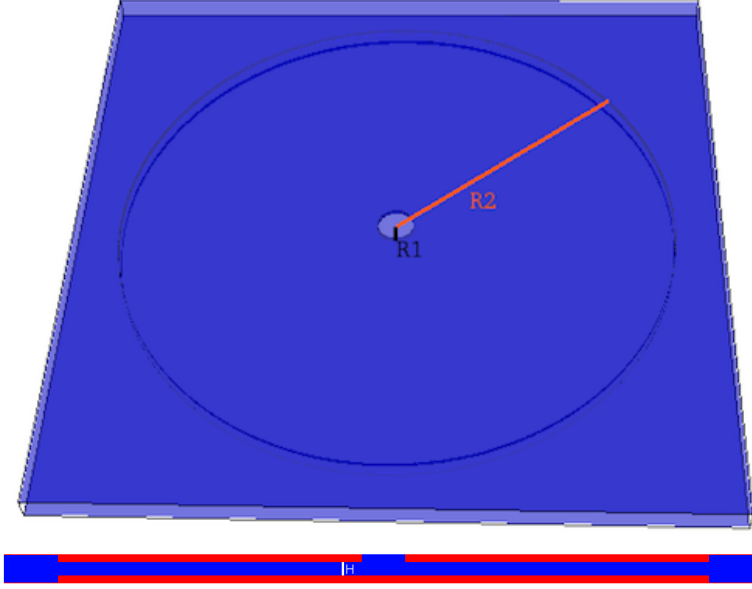


**Figure 6.6:** Simulated geometry: top and side views. The flow inlet is realized through a circular duct while the outlet is located at the lateral outer surfaces of the simulation box. Both sketches are taken from the LBM simulation: red areas represent the wall nodes, while the blue areas represent the fluid nodes. At the interface between the two areas, the wall boundary condition is applied.  $R1$  identifies the radius of the circular flow inlet;  $R2$  is the radius of the two parallel disks realizing the channel through which the gas flows. At  $R2$ , a large expansion is present. The geometrical dimensions of the device are such that a very large scale simulation is necessary. Moreover, the flow conditions impose the presence of a large range of non-equilibrium and rarefaction effects ranging from an almost continuum condition at the inlet ( $Kn_{in} \cong 0.07$ ) to a transitional one at the outlet ( $Kn_{out} \cong 1.6$ ).

which contradicts one result of the Chapman-Enskog theory, [83], i.e. the fluid transport coefficients, including the dynamic viscosity, are a function of the temperature only. To be able to respect this requirement, i.e. keeping constant the dynamic viscosity throughout the domain, as the flow is assumed isothermal, the relaxation time  $\tau$  must be a function of the local density as:

$$\tau(\mathbf{x}) = \frac{1}{2} + \frac{\rho(\mathbf{x}_0)}{\rho(\mathbf{x})} \left( \tau(\mathbf{x}_0) - \frac{1}{2} \right), \quad (6.11)$$

where  $\mathbf{x}_0$  is a reference position at which the reference relaxation time  $\tau(\mathbf{x}_0)$  is defined. Finally, setting the relaxation time is tantamount to define the mean free

path,  $\lambda(\mathbf{x}_0)$ . For VHS particles, [1]:

$$\lambda(\mathbf{x}_0) = \frac{2(5-2\omega)(7-\omega)}{15} \nu(\mathbf{x}_0) \left( \frac{m}{2\pi k_B T} \right)^{1/2}, \quad (6.12)$$

which, in the LBM, becomes:

$$\lambda(\mathbf{x}_0) = \frac{2(5-2\omega)(7-\omega)}{15} c_s \left( \tau(\mathbf{x}_0) - \frac{1}{2} \right) \left( \frac{1}{2\pi} \right)^{1/2}. \quad (6.13)$$

In Eq. (6.13)  $\omega$  is the viscosity index equal to 0.67 for hydrogen, [1]. The reference conditions are those relative to the outlet section.

Besides the slip flow boundary conditions applied at the walls as expressed in Eq. (6.9), at the inlet and outlet sections, we impose that the non-equilibrium discrete distributions are set equal to the equilibrium distributions evaluated at the local conditions:

$$f = f^{\text{eq}}(\rho, \mathbf{u}). \quad (6.14)$$

Sensitivity analysis has been performed in order to determine the simulation grid resolution able to provide an accurate solution. The analysis is based on the fact that a sufficient resolution should be guaranteed for the flow within the channel between the two disks. 24 nodes along the channel height were found to guarantee a sufficient accuracy, see also Fig. 6.31 where it is shown that a good agreement with Cercignani's second order slip model is found for  $\sigma = 1$ . Once this discretization is established, then also the discretization for all the other relevant geometrical features are automatically set since in the LBM the grid nodes are equispaced. In total, the test geometry is discretized with a  $1600 \times 52 \times 1600$  grid. This discretization will be also used for the DSMC and hybrid method full scale simulations.

In order to compare the LBM simulation results with the reference DSMC simulation results, we analyse three main mean field hydrodynamic quantities: the velocity magnitude and pressure profiles taken at half-height of the channel between the two disks,  $y = H/2$ , and the pressure profile taken at the floor of the flow domain,  $y = 0$ . In this last case, experimental data are also available. It has also to be noted that while the reference DSMC data are taken from an axisymmetric simulation, the LBM, as well as our DSMC and hybrid method simulations, employs a cubical box and, therefore, the outflow section is not equidistant from the radial position,  $r = R_2$ . To reduce this difference, which can potentially lead to mismatches, we perform an average over the angular positions with a  $1^\circ$  angular discretization. Even if it is expected that the outflow boundary condition has a small influence on the flow within the disk, as at least 200 nodes are present between the radial position  $r = R_2$  and the outflow section, we nonetheless applied

the procedure described above.

The simulation is stopped, and data are analysed, once the steady-state condition is established, i.e. the following criterion is met:

$$\sum_i^N \frac{|\mathbf{u}(\mathbf{x}_i, t) - \mathbf{u}(\mathbf{x}_i, t - 1)|}{|\mathbf{u}(\mathbf{x}_i, t - 1)|} \cdot \frac{1}{N} < 10^{-6}, \quad (6.15)$$

where the sum extends over the grid nodes  $i$ .

In Fig. 6.7, the flow velocity magnitude at the central section,  $y = H/2$ , obtained with the LBM when using  $\sigma_v = 1$  and the experimentally found value  $\sigma_v = 0.83$  are compared with the reference DSMC axisymmetric simulation (for which, indeed,  $\sigma_v = 0.83$  is enforced). A close agreement is found for the LBM simulation up to about  $\text{Kn} = \lambda/H = 0.1$ . For radial positions at which  $\text{Kn} > 0.1$ , the profiles start to diverge and a smaller velocity magnitude for the LBM is found. The large value found in correspondence of the radial position  $r = R_1$  is very well reproduced. If we define an error as

$$\frac{|\mathbf{u}_{\text{dsmcFoam}} - \mathbf{u}_{\text{LBM}}|}{|\mathbf{u}_{\text{dsmcFoam}}|}, \quad (6.16)$$

then the maximum error, for radial positions such that  $\text{Kn} < 0.1$ , is localized in proximity of  $r = 0$ . The influence of the application of the correct accommodation coefficient in reducing the error is evident. However, up to a 30% error is found in proximity of  $r = R_2$ . This mismatch can be largely attributed to the fact that the D3Q19 lattice is used, and it cannot well reproduce large non-equilibrium effects especially present in proximity of the walls. For comparison purpose with classical Navier-Stokes equations solvers, we performed a simulation of the same flow set-up using a commercial CFD solver (*Star-CCM+*) where a second-order slip boundary condition is applied at the walls. The obtained velocity magnitude profile is also reported in Fig. 6.7. It is clear that the two peaks in correspondence of the sections at  $r = R_1$  and  $r = R_2$  are recovered. However, an appreciable gap is present and the CFD solver provides smaller velocity values throughout the domain.

In Fig. 6.8 and 6.9, the pressure profiles obtained at  $y = H/2$  (centerline section) and  $y = 0$  (floor section) are compared with the reference simulation data. For this last profile, the available experimental data are also plotted. For the  $y = H/2$  profile, the LBM profile follows closely the reference one and for the radial position at which  $\text{Kn} = 0.1$  the error, defined analogously to Eq. (6.16), is about 5%. As found for the velocity magnitude, while the radial position gets further from the inlet the error increases, and the pressure level is always higher. For the pressure profile at the floor, a good accordance is found for the LBM with respect to the experimental data also for positions much further than the one at which  $\text{Kn} = 0.1$ .

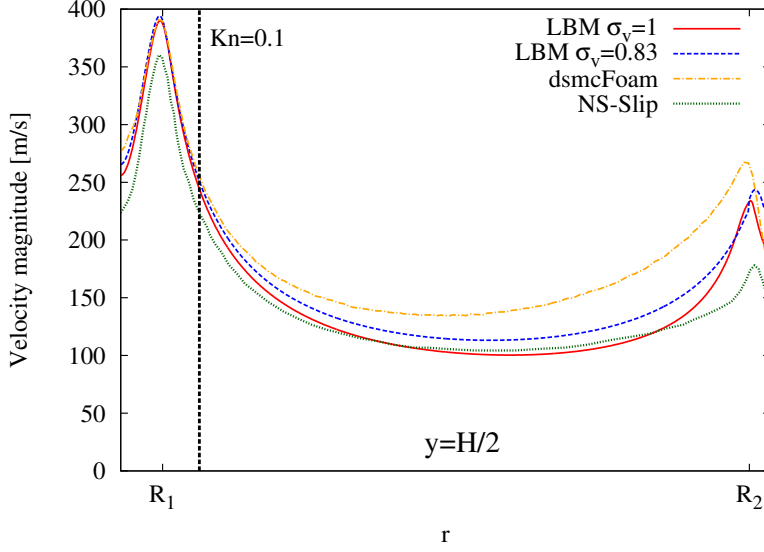


**Figure 6.7:** Velocity magnitude profile measured at  $y = H/2$  along the radial direction,  $r$ , within the flow domain. The results obtained with the regularized LBM for  $\sigma_v = 1$  (red continuous line) and  $\sigma_v = 0.83$  (blue dashed lined) are compared with the reference DSMC data (orange dash-dotted line) obtained using dsmcFoam. The radial position at which  $Kn = \lambda/H = 0.1$  is reached is also shown. Larger velocities are obtained when applying the partial slip wall boundary condition, as expected. Up to a 30% error with respect to the reference DSMC data is measured in the area of the disk in proximity of  $r = R_2$  for the LBM with  $\sigma_v = 0.83$ . Note that the LBM velocity magnitude data have been converted into SI units as explained in Appendix 6.A. Also the data from the commercial CFD solver (StarCCM+, named NS-Slip in the legend, green dashed line) are reported and lower velocity values, with respect to our LBM and reference DSMC data, are found throughout the domain.

However, for radial positions at mid-way between the inlet and the position  $r = R_2$ , the error in comparison with the experimental data becomes relevant. Finally, it is important to underline that the LBM results are taken from a simulation where the regularization has been applied. We show in Appendix 6.B the importance of this procedure in reducing the artefacts related to the rarefaction effects (excessive slip velocity at the walls). Now, we show that the regularization is beneficial also in reducing artefacts due to non-negligible compressibility effects. In Figs. 6.10a-6.10b, the flow velocity magnitude field in a region in proximity of the inlet is shown. The suppression of the discrete artefacts, due to the limited number of the speeds of the employed lattice, and related to the expansion of the gas in correspondence to the inlet edge is evident. This result is even clearer when comparing, as done



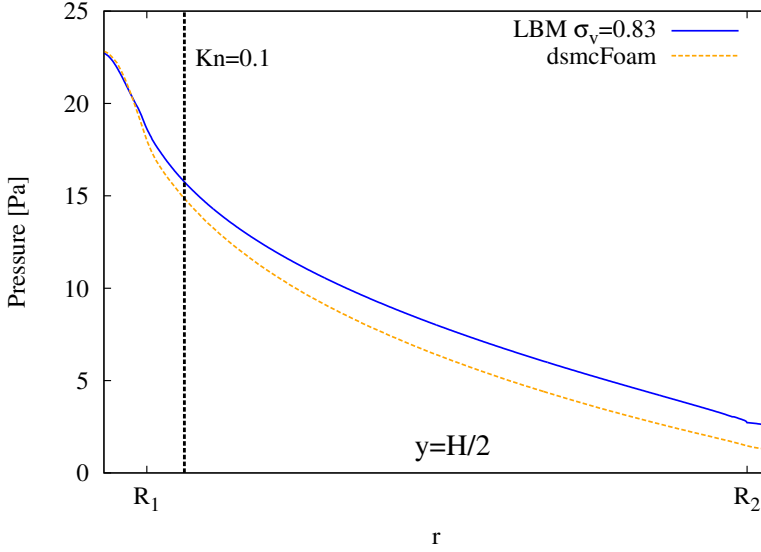


**Figure 6.8:** Static pressure profiles measured at  $y = H/2$  along the radial direction,  $r$ . The error in the LBM data with respect to the DSMC data, at the location where  $Kn=0.10$ , is less than 5%, but it increases with the radial distance. Note that the LBM data have been converted to SI units so to be easily compared with DSMC results. Also note that, even if the error looks, at first sight, limited, nonetheless it causes a large difference in the velocity profile.

in Figs. 6.11a-6.11b, the field of a local Knudsen number defined as:

$$Kn_{l,v} = \lambda \left| \frac{\nabla |\mathbf{u}|}{c_s} \right|, \quad (6.17)$$

which, indeed, makes use of the spatial derivatives of the velocity magnitude and, therefore, it is particularly sensitive to discontinuities in that field. Note also that this parameter will be used to provide a guideline for the determination of the flow domain decomposition when applying the hybrid method.

## DSMC results

A very important aspect of large DSMC simulations, moreover characterized by a large variation of the pressure level, as in the present test case, is to properly set up the initial conditions so to limit the duration of the transient phase, but still preserving an accurate simulation.

In Appendix 6.C, we treat in more details how we defined the initial pressure field within the flow domain in order to reduce the simulation computational cost.

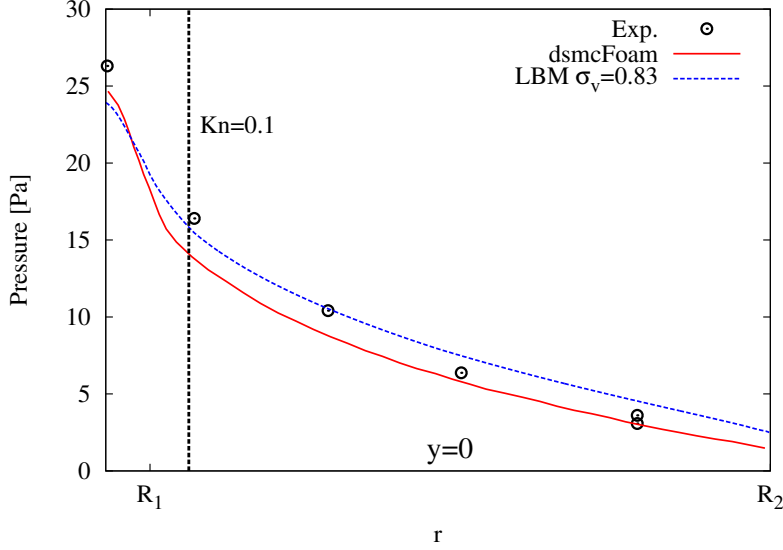


**Figure 6.9:** Comparison of the static pressure profiles measured at the floor of the device,  $y = 0$ , among the LBM, reference DSMC and experimental results. The LBM results show a good agreement with experimental data in the area close to the inlet.

Here, we only assert that we chose to initialize the simulation with an exponential pressure profile. This option is chosen so to have a starting configuration closer to the final expected one. In Fig. 6.12, in fact, the initial exponential profile (blue dash-dotted line) is compared with the final pressure profile (orange dotted line) as well as two other possible initial choices. As the initial number of particles is proportional to the integral along the radial coordinate of the mentioned curves, it can easily be envisaged the advantage to start with the pressure field set according to the exponential profile. Another aspect to be considered is the total number of particles evolved in such a large simulation. According to the rules-of-thumb of the method, in order to reproduce the correct physical collisional frequency, to avoid the possibility of repeated collisions for the same couple of particles and to reduce the number of samples to obtain a given statistical uncertainty on the measurement of the hydrodynamic moments, 20 particles per cell should be present. If we set for the cells in proximity of the outflow, where the pressure is about 1 Pa, the requirement to have 20 particles, then, for the cells in proximity of the inflow, where the pressure is about 25 Pa, on average, 500 particles per cell will be present, forcing the total number of particles to be in the order of ten billions, making the simulation extremely expensive from a computational point of view. Therefore we relax this requirement, setting the number of particles at the outflow

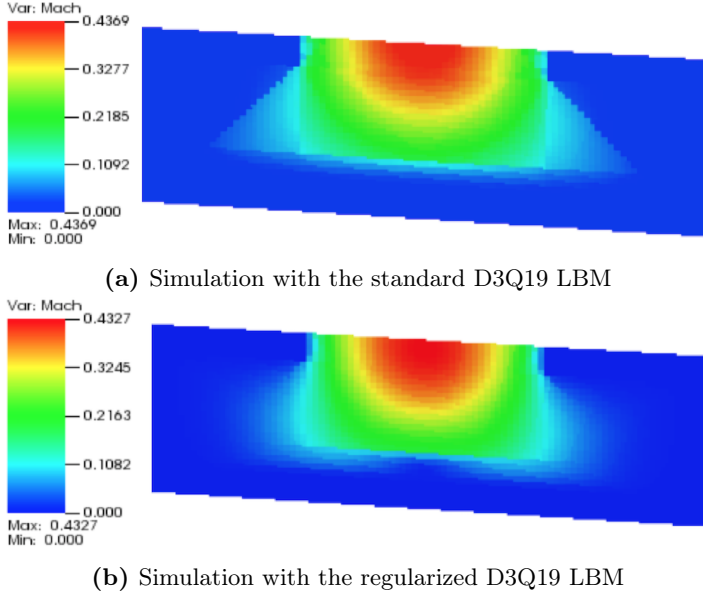


**Figure 6.10:** Comparison between the Mach number field in a section of the flow field within the geometry shown in Fig. 6.6: detail of the inlet region. In (a), the field as generated by using a standard D3Q19 LBM model, and in (b) by using a regularized LBM model are respectively shown. The reduction of the discrete effects related to the expansion of the gas at high-Ma number in proximity of the inlet section, caused by the finiteness of the lattice set of speeds, and manifested by a discontinuous Mach flow field at the outer edge of the jet originated from the inlet, is evident. Note that these snapshots are taken at an early stage of the simulation when the flow field is still developing. It is during such phase, in fact, that the application of the regularization procedure may also help in improving the stability of the method.

cells to eight. Clearly, this will impact the solution: in fact a larger number of samples will be needed to reach the required statistical uncertainty (about 60% more time steps, but the total number of particles will be reduced by a factor 2.5). For what concerns the repeated collisions issue, we can assume that it is not very compelling as in the outflow region the Kn number is very large and therefore the number of collisions is rather small.

The fully resolved DSMC simulation grid has the same discretization used for the LBM simulation, i.e. it comprises  $1600 \times 52 \times 1600$  cells and, in total, more than 133 millions of cells. The initial number of particles is  $N_{\text{particles}} \approx 2.6 \times 10^9$ . Note that the proposed discretization fully respects the common prescriptions to have the cell size smaller than the collisional mean free path also for the conditions present at the inlet, where the largest values of the pressure are found.

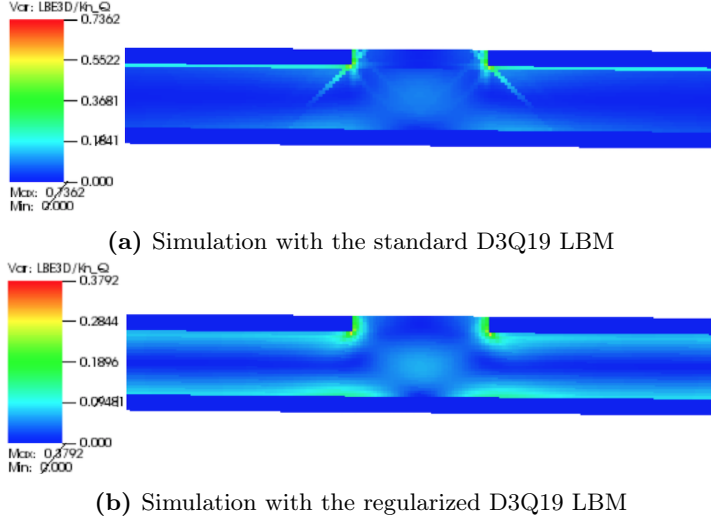


**Figure 6.11:** Comparison between the fields of the local Knudsen number,  $Kn_{l,v}$ , defined in Eq. (6.17) in a section of the flow field within the geometry shown in Fig. 6.6: detail of the inlet region. In (a), the field as generated by using a standard D3Q19 LBM model, and in (b) by using a regularized LBM model are shown. Compared to Fig. 6.10, the effectiveness of the regularization in reducing artefacts related to the high-Ma number flow is even more evident. The velocity gradient magnitude, in fact, due to a discontinuous velocity field present when the regularization is not applied, is very large at the outer edge of the jet originated from the inlet section. The maximum value of the  $Kn_{l,v}$  when not using the regularization ( $Kn_{l,v} \cong 0.74$ ) is about twice the value found when applying the regularization ( $Kn_{l,v} \cong 0.38$ ). This parameter will be also used to define a guideline to determine the domain decomposition for the hybrid method, and therefore its accurate evaluation is particularly important. As visible in (b), when the regularization is applied, the largest values of  $Kn_{l,v}$  are found in proximity of the walls.

The simulation convergence criterion is set differently with respect to the LBM case. In fact, the DSMC simulation is stopped after having cumulated enough statistics so to reach 1% fractional error on the smallest velocity magnitude ( $\sim 150$  m/s occurring at a section half-way between  $r = R_1$  and  $r = R_2$ ). Using equilibrium statistical mechanics considerations, [45], it is possible to estimate a fractional error for a velocity component as:

$$E_{u_i} = \frac{\sigma_{u_i}}{|u_i|} = \frac{\sqrt{\langle \delta u_i^2 \rangle}}{\sqrt{S}|u_i|} \approx \frac{1}{\sqrt{SN}} \frac{1}{Ma}, \quad (6.18)$$

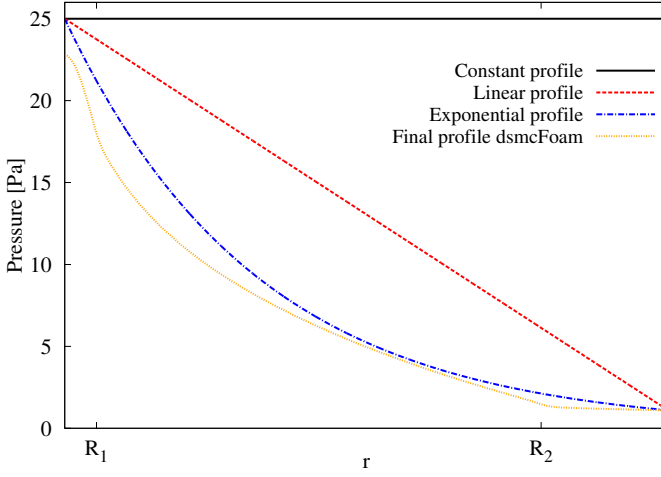


**Figure 6.12:** Visualization of the three possible initial pressure profiles imposed within the flow domain. The total number of particles for each initial configuration is proportional to the area below the curves and it directly reflects in the required computational cost associated with the transient phase before reaching the steady state condition. Note that the case of constant profile but at a pressure equal to zero, which corresponds to an initially empty domain, has been ruled out due to computational reasons: as soon as the number of particles increases, expensive memory allocation operations should be performed.

where  $N$  is the average number of particles,  $S$  is the number of required samples and  $\text{Ma}=u_i/c_s$  is the Mach number. Using Eq. (6.18) with the above mentioned conditions, it can be seen that at least 40,000 samples are needed. Since a sample is taken every 5 time steps, at least 200,000 time steps should be completed. To this number, the time steps needed to extinguish the initial transient phase have also to be added. The duration of such phase is determined based on the evaluation of an advective scale for the particles to move within the flow domain from the inlet to the outlet:

$$t_{adv} \sim \frac{\frac{L}{2}}{v_{mp}},$$

where  $v_{mp}$  is a characteristic microscopic velocity (the most probable value for a Maxwell-Boltzmann distribution). From this relation, it is possible to consider the transient phase completed after 80,000 time steps. Therefore, at least 280,000 time steps are needed to fulfill the criterion of Eq. (6.18).

In Fig. 6.13, the flow velocity magnitude profile evaluated at the centerline,  $y = H/2$ , and obtained with the in-house DSMC code is compared with the reference simulation data. As done for the LBM results, the profile is obtained averaging

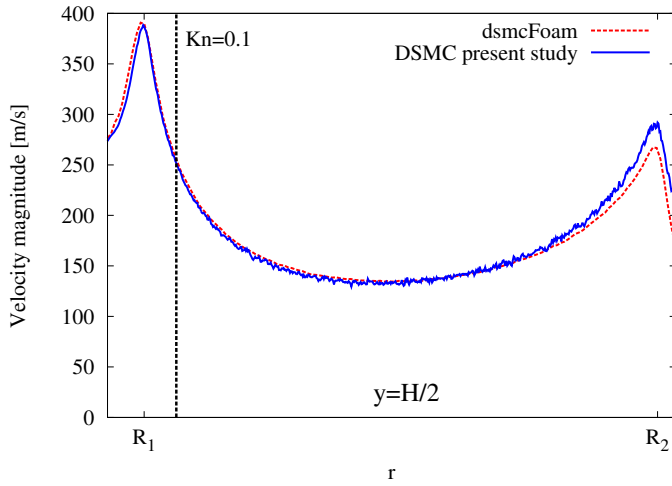


**Figure 6.13:** Velocity magnitude profile measured at  $y = H/2$ . A very good agreement between the reference (red dashed line, named *dsmcFoam*) and the in-house DSMC simulation data (blue continuous line, named *DSMC present study*) is found up to  $r$  close to  $R_2$ . At this radial position the error, defined in a way similar as in Eq. (6.16), is about 8%.

over the angular positions. A very good agreement is found between the current and the reference axisymmetric DSMC simulations also in correspondence of the stagnation area at  $r = 0$ . The largest error, similarly defined as for the LBM data, is found in proximity of the second peak at  $r = R_2$  and it is equal to about 8%.

In Fig. 6.14, the pressure profile is compared with the reference DSMC solution for the centerline section  $y = H/2$ . The behavior is well reproduced, including the change of concavity occurring at  $r = R_1$ , but the pressure is slightly shifted towards higher values. The same occurs when comparing the pressure profile for a section at  $y = 0$ . In this case, however, a closer agreement to the experimental data with respect to the reference solution is found, at least in the central part of the domain. For the stagnation area,  $r = 0$ , a difference of about 1 Pa, corresponding to about 4% error, is found when comparing with the experiments.

Finally, in Fig. 6.16, a visualization of the pressure field at the section  $y = H/2$  is shown, from where it is possible to see that the cubic simulation domain has little influence on the flow. This is also confirmed in Fig. 6.17, where the difference between the pressure along the directions  $a$  and  $b$  of Fig. 6.16, normalized with the pressure profile averaged over the angular positions, (see blue continuous line in Fig. 6.14), is shown. At most, a pressure difference equal to 1.2% is measured for  $r = R_2$ .

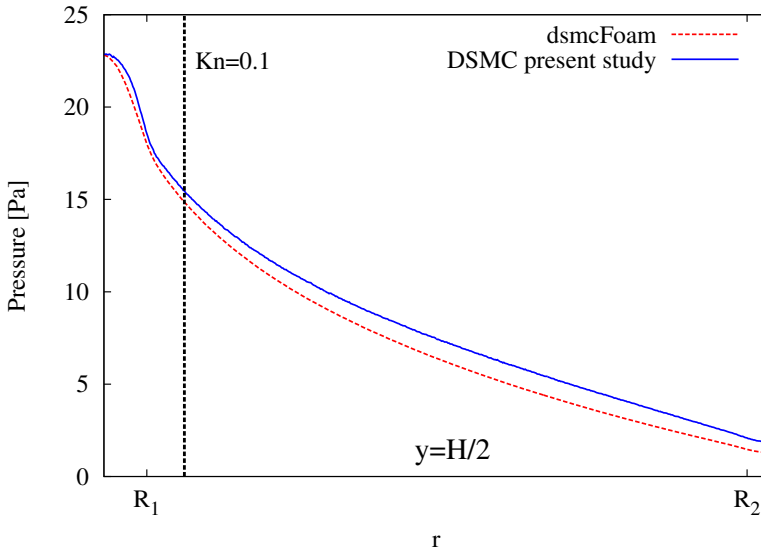


**Figure 6.14:** Comparison of the static pressure profiles measured at  $y = H/2$  for the in-house developed code (DSMC present study) and the reference axisymmetric one (dsmcFoam). While the shape is well reproduced, slightly larger values are found.

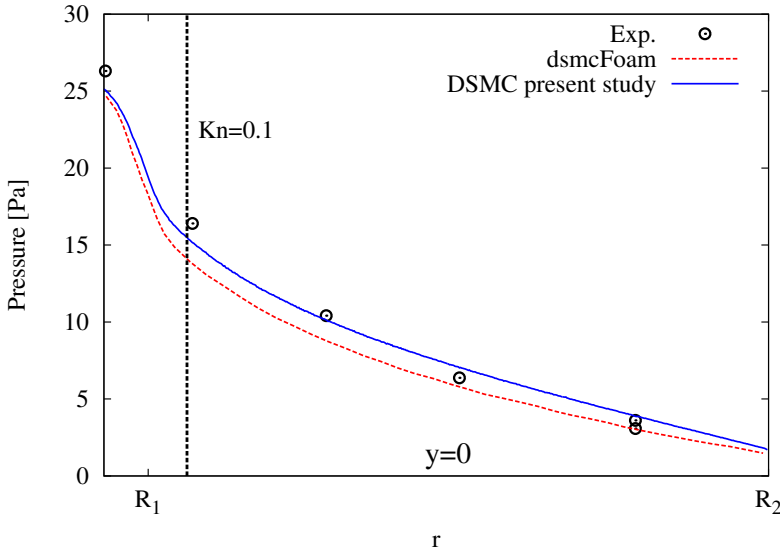


**Figure 6.15:** Comparison of the static pressure profiles measured at the floor of the device,  $y = 0$ , for the in-house developed code (DSMC present study) and the reference axisymmetric one (dsmcFoam). Available experimental data are also included and a closer agreement is found for the in-house DSMC results.

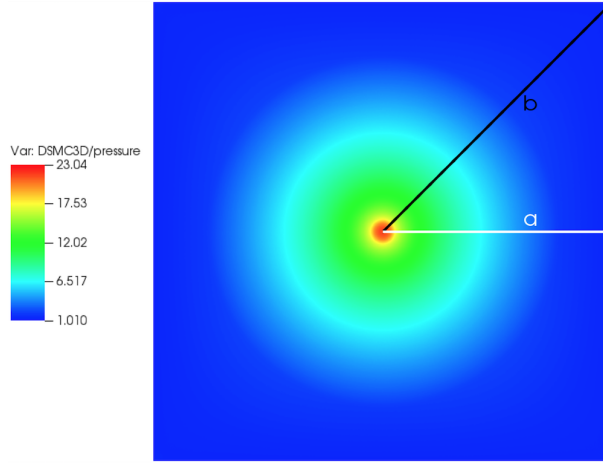


**Figure 6.16:** Visualization of the pressure field for the section at  $y = H/2$  for the present DSMC study. The fact that the simulation domain is a cubic box does not appear to affect the flow within the disk. The directions  $a$  and  $b$ , which will be used to quantitatively measure such effect, are also shown.

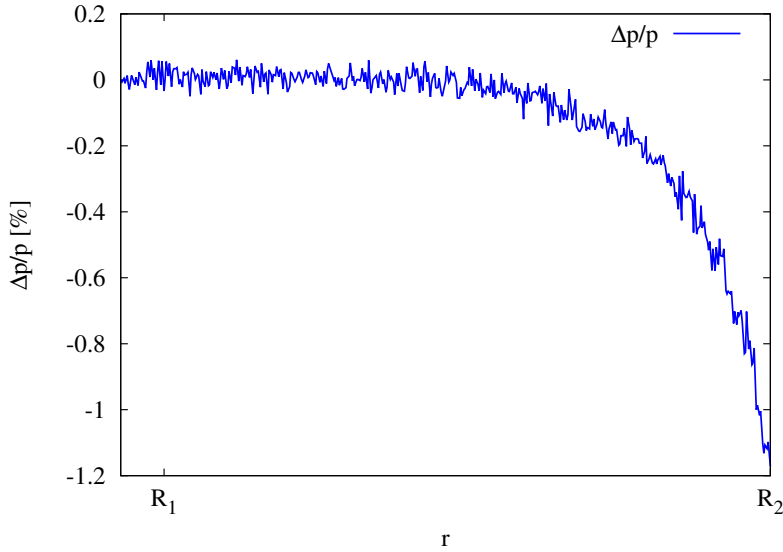


**Figure 6.17:** Pressure difference between the measurements along the directions  $a$  and  $b$  of Fig. 6.16, normalized with respect to the pressure averaged over the angular positions for  $y = H/2$ . For  $r = R_2$ , the maximum difference ( $\sim 1\%$ ) is found. The plot confirms the small influence of the cubic domain on the flow field. Even smaller discrepancies may be found further enlarging the expansion volume for  $r > R_2$ . Noise on the measurements is still noticeable because of the finiteness of the number of statistical samples.



## Hybrid LBM-DSMC method results

In order to apply the hybrid method to this test case, the last step to be specified is the definition of the decomposition of the domain and the related allocation to each method of the different parts of the flow domain. At this aim, the location at which the coupling between the LBM and DSMC methods occurs is based on the simultaneous fulfilment of two criteria: the geometry based Knudsen number,  $\text{Kn}$ , is larger than 0.1 and the local Knudsen number,  $\text{Kn}_{l,v}$ , as expressed in Eq. (6.17), is also larger than 0.1. While the first criterion is based on the already demonstrated capability of the LBM to accurately simulate the flow field up to the mentioned level of rarefaction, the second one may seem arbitrary as it should be based on a clear and precise metric to define the breakdown of the Navier-Stokes equations level of representation. However, this last aspect is still subject of study and a universal criterion has not been found yet, but it seems to be a function of the particular flow problem under investigation. It has to be noted, moreover, that in literature several breakdown parameters are presented and most of them are based on the evaluation of the local density gradient, see e.g. [117]. This approach, which is suitable for hybrid models applied to compressible flow problems, it seems to be not appropriate for the LBM, as, in its usual formulation, it is a solver for weakly compressible flows.

To verify this statement, we compare two possible definitions of the local Knudsen number: the one given in Eq. (6.17) and the following one:

$$\text{Kn}_{l,\rho} = \lambda \left| \frac{\nabla \rho}{\rho} \right|. \quad (6.19)$$

While the definition given in Eq. (6.17) considers the scale over which the velocity magnitude field encounters relevant variations as the proper hydrodynamic scale, in Eq. (6.19) such scale is determined according to the variation of the density field. In Fig. 6.18a and 6.18b, we plot the distributions of the  $\text{Kn}_{l,v}$  and  $\text{Kn}_{l,\rho}$  at two radial positions,  $r = R_1$  and  $r = (3/4)L$ , respectively.

It is evident that large variations of both the local Knudsen numbers occur for  $r = R_1$ . However, since at this section the global Knudsen number, based on the domain height is equal to 0.07, we assume that the flow can be accurately described by using a Navier-Stokes level of representation, and, therefore, LBM is in charge to solve the flow in this section. Moving downstream, instead, the behaviour of the two local Knudsen numbers is sensibly different. In fact, at  $r = (3/4)L$ , where the global Knudsen number is equal to 0.4, the  $\text{Kn}_{l,\rho}$  profile is essentially constant throughout the domain height, while the profile of  $\text{Kn}_{l,v}$  is able to capture the non-equilibrium effects associated with the wall presence. The superiority of  $\text{Kn}_{l,v}$

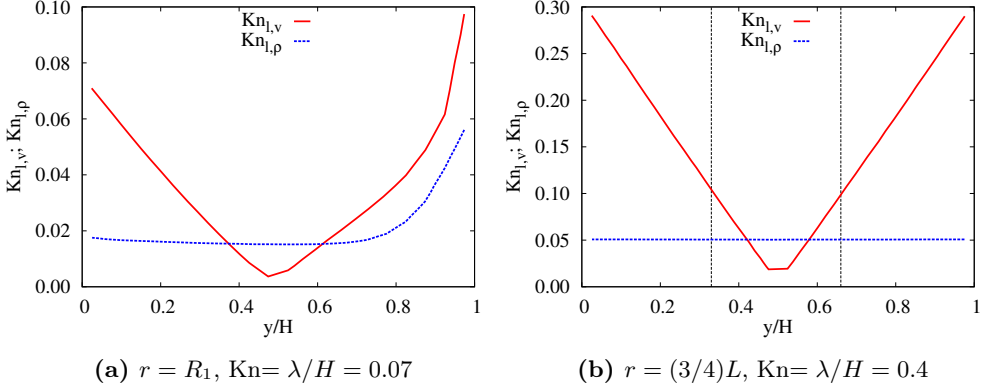


**Figure 6.18:** Profiles of the local Knudsen number defined according to Eq. (6.17),  $\text{Kn}_{l,v}$  (red continuous line) and to Eq. (6.19),  $\text{Kn}_{l,\rho}$  (blue dashed line) evaluated at two radial positions: (a)  $r = R_1$ ; (b)  $r = (3/4)L$ . At  $r = R_1$ , the global  $\text{Kn}$  based on the domain height, is lower than 0.1, and, therefore, the flow is solved by the LBM only. At  $r = (3/4)L$ , instead,  $\text{Kn} = 0.4$  and the DSMC solver is adopted when  $\text{Kn}_{l,v} \geq 0.1$ . The vertical dashed lines are placed in correspondence of the nodes where  $\text{Kn}_{l,v} = 0.1$ . It is clear that the definition based on the density variations is not a suitable one for the present flow set-up. In fact,  $\text{Kn}_{l,\rho}$  is nearly constant throughout the domain height, thus not detecting the non-equilibrium effects due to the wall presence.

over  $\text{Kn}_{l,\rho}$  in detecting the non-equilibrium effects, therefore, is clear.

The threshold of  $\text{Kn}_{l,v} = 0.1$ , as already mentioned, is somewhat arbitrary. However, it is based on the balance between accuracy and computational efficiency and on the results of low resolution simulations of the same flow set-up. It is evident, in fact, that a larger value of the threshold, allowing a smaller area to be solved by the DSMC, would provide a more efficient calculation, but at the expense of the solution accuracy. On the contrary, a smaller value of the threshold, while guaranteeing a more accurate solution, would require larger computational resources.

Finally, it should be noted that also other definitions of the local Knudsen number have been investigated in [183]. In particular, the criterion there proposed is based on the difference between the hydrodynamic near-equilibrium fluxes and the actual values of the stress and heat flux as evaluated from the molecular solver.

The evaluation of such local Knudsen numbers and the comparison with the definitions of Eqs. (6.17) and (6.19), will be subject of future work.

The application of the two criteria cited above, i.e. the geometry based Knudsen number larger than 0.1 and the local Knudsen number based on the velocity magnitude gradient larger than 0.1, allows to define a domain decomposition where the DSMC is essentially limited to the regions close to the walls. In Fig. 6.11b and 6.18b, it was already evident that  $\text{Kn}_{l,v}$  shows the largest values in proximity

of the walls. This finding can be further understood qualitatively comparing the velocity profiles at the radial position  $r = (3/4)L$  obtained from the LBM and DSMC simulations as done in Figs. 6.19a-6.19b. It is evident that the LBM has a velocity profile with lower velocities in proximity of the walls with respect to the DSMC solution. Applying such criteria to the same grid used for the LBM and DSMC simulations ( $1600 \times 52 \times 1600$ ), the number of cells within the DSMC domain is about 19 millions, while the LBM extends over 92 millions of nodes, meaning that the fraction of the number of DSMC cells over the number of LBM nodes is  $\alpha \cong 0.2$ .

Finally the buffer layer between the pure LBM and DSMC domains is only 1 cell wide. As it was already understood in chapter 4, one cell is sufficient to accurately generate the DSMC particles from the LBM fields. This is essentially due to the fact that the time step duration is chosen based on physics arguments such that only very few particles can move further than two cells away and therefore, according to the proposed algorithm, only very few particles could reach the DSMC area starting from a buffer layer cell placed further than one cell away from the DSMC area. The total number of buffer layer cells is about 2.5 millions.

In order to have a fair comparison, in terms of computational cost, with the DSMC simulation, the initialization of the fields of the hybrid simulation is done in a way similar to the one used in the DSMC simulation: the initial pressure profile is an exponential function of the radial coordinate. This will also induce an exponential variation with the radial coordinate of the number of particles in the cells occupied by the DSMC method so that the initial number of DSMC particles is about 500 millions. As done in the LBM simulations, we will stop the hybrid method simulation when the following convergence criterion is fulfilled:

$$\sum_i^N \frac{|\mathbf{u}(\mathbf{x}_i, t) - \mathbf{u}(\mathbf{x}_i, t - 1)|}{|\mathbf{u}(\mathbf{x}_i, t)|} \cdot \frac{1}{N} < 10^{-6}, \quad (6.20)$$

where the sum extends over the whole grid nodes  $i$ .

The effects of the fluctuations proper of the DSMC method, in fact, are largely reduced when using the hybrid method, and so it is possible to use a criterion as that of Eq. (6.20).

As done for the LBM and the DSMC simulations, we will evaluate the accuracy of the final hybrid solution comparing it with the reference solution provided by the DSMC axisymmetric code.

In particular, in Fig. 6.20, the flow velocity magnitude measured at  $y = H/2$  is shown. As usual, the plotted profile is an average over the angular positions. It can be seen that the profile is very close to the reference one throughout the domain.

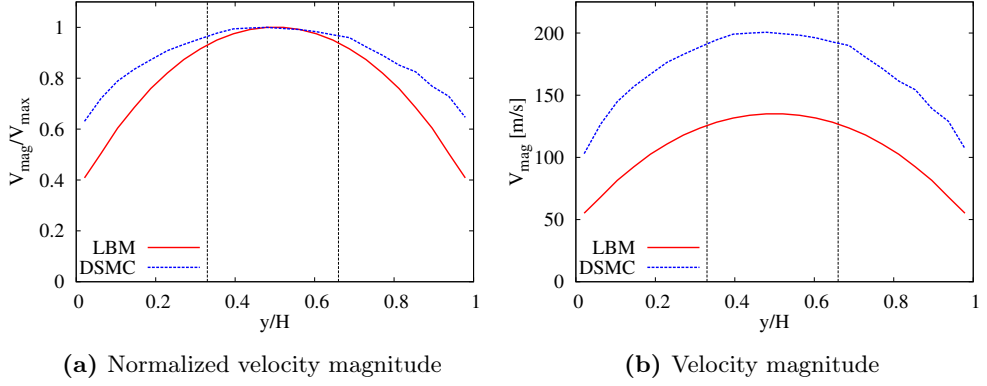


**Figure 6.19:** Velocity profiles along the disk channel height measured at a radial position  $r = (3/4)L$ . On the left, the velocities normalized with the maximum velocity, obtained from the in-house DSMC and LBM simulations. LBM velocity profile shows smaller values in proximity of the walls. On the right, the non-normalized profiles are shown. The vertical dashed lines represent the location at which the coupling should occur according to the defined criteria on  $Kn$  and  $Kn_{l,v}$ .

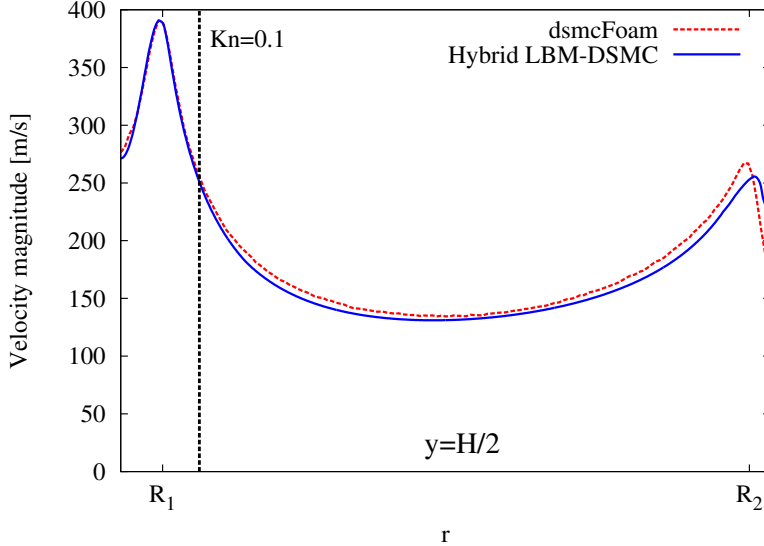


**Figure 6.20:** Velocity magnitude profile measured at  $y = H/2$ . A very good agreement between the reference DSMC results (dsmcFoam, red dashed line) and the hybrid simulation (Hybrid LBM-DSMC, blue line) is found. The largest error occurs, as for the LBM and the in-house DSMC, in proximity of the expansion part of the domain localized at  $r = R_2$ .

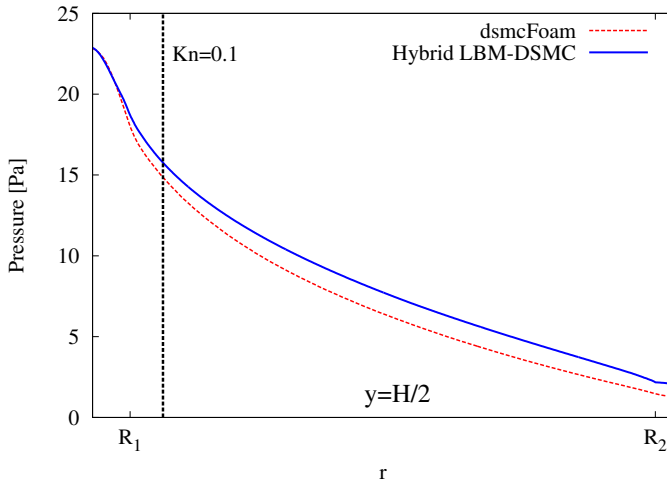


**Figure 6.21:** Comparison between the static pressure profiles measured at  $y = H/2$  obtained by the reference DSMC axisymmetric code (red dashed curve) and the hybrid model code (blue continuous curve). Slightly larger values for the static pressure are found with the hybrid method.

The largest error occurs, as in the LBM and DSMC simulations, in correspondence of the radial coordinate  $r = R_2$ . The hybrid model, therefore, is able to provide a solution with an accuracy comparable to the one provided by the in-house DSMC code. This is also confirmed when comparing the pressure profiles at  $y = H/2$  and  $y = 0$  as done in Fig. 6.21 and 6.22. For this last case, the hybrid model is able to reproduce the experimental data in a large part of the domain in a closer way than the reference DSMC can provide. In Fig. 6.23a and 6.23b, the pressure field obtained from the hybrid method simulation in a vertical section is shown. The smooth passage from one method to the other is visibly guaranteed.

Finally, in the series of Figs. 6.24-6.26, the results obtained from the different numerical methods are collected in the same plots. The main result is that the hybrid method is able to provide a solution which has an accuracy comparable to the one provided by the in-house DSMC implementation over large part of the flow domain.

In the next section, the computational cost associated with each method and their parallel performance are discussed.

## 6.5 Computational costs

When dealing with hybrid continuum-DSMC methods — but the same reasoning can be applied to any hybrid method coupling a fast, but not accurate enough

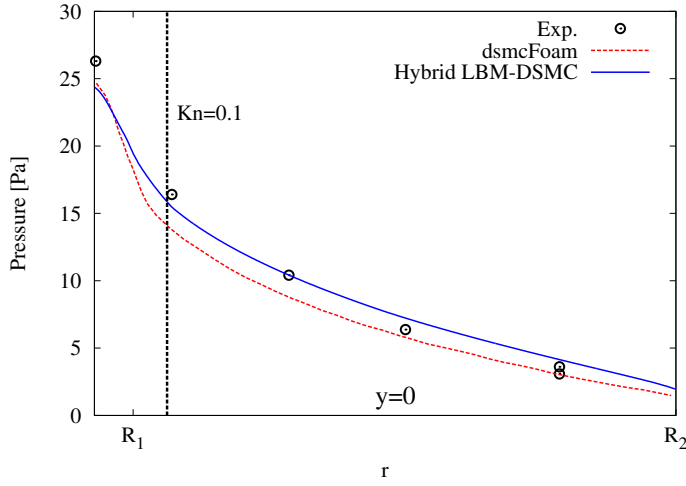


**Figure 6.22:** Comparison between the static pressure profiles measured at the device floor,  $y = 0$ , as obtained by the reference DSMC axisymmetric code (red dashed curve) and the hybrid model code (blue continuous curve). For the hybrid method, a good agreement with the experimental data is found.

numerical scheme with a more computationally expensive, but accurate method — aside the requirement that the hybrid method provides a solution with an accuracy comparable to the DSMC solution, we also require it is sensibly less computationally demanding than the DSMC itself, when this last method is applied to the whole simulation domain. Actually, any hybrid method owes its existence only because of this last feature. In this section, we will analyze the computational costs associated to each of the three employed numerical methods as well as their parallel efficiency.

As a remark, all the following considerations are architecture-dependent. Therefore, all the simulations whose results have been reported in this chapter were run on the **broadwell** partition of the Dutch national supercomputer, Cartesius. This partition has 32-processors nodes with E5-2697A v4 Intel Xeon Processor (2.6 GHz clock frequency) and with 64 GB of memory. Inter-node communication is guaranteed by a Mellanox ConnectX-3 InfiniBand adapter providing  $4 \times$  FDR resulting in 56 GBit/s bandwidth. Note also that different architectures may provide different results.

## LBM computational cost

We start our consideration from the LBM case. As already mentioned, the LBM has proved itself, due to its intrinsic nature, to be a very efficient fluid-dynamic

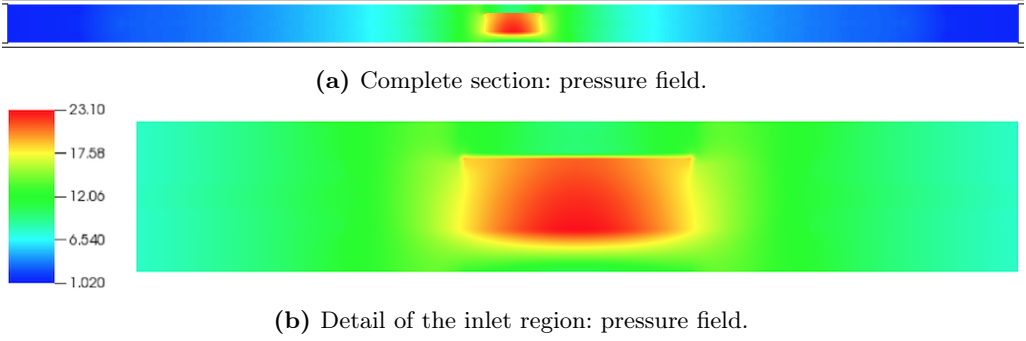


**Figure 6.23:** Pressure field in a section at  $x = L/2$  and close to the inlet obtained with the hybrid method. It is not possible to clearly identify the areas where DSMC or only LBM is applied, meaning that the solution is smooth when passing from one method domain to the other.

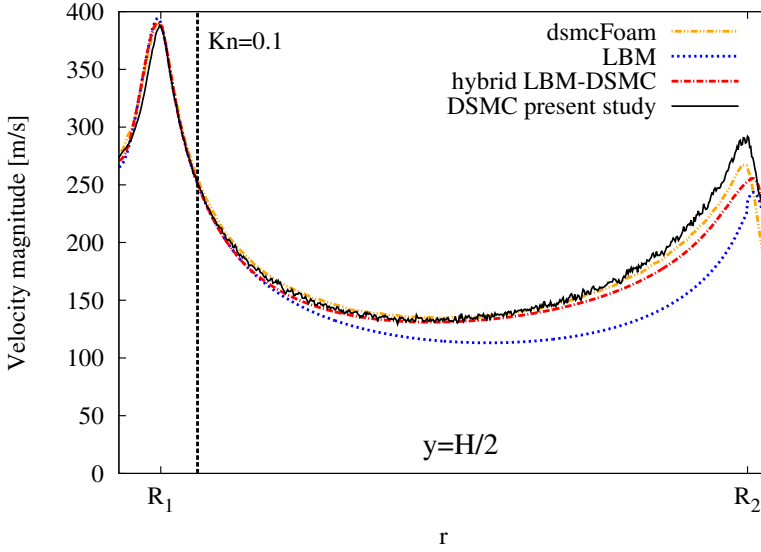


**Figure 6.24:** Comparison among the velocity magnitude profiles provided by the three different numerical methods employed in this study and the reference DSMC data (dsmcFoam) for  $y = H/2$ . The three solutions are close to the reference one (orange dot-dot-dashed line) when  $Kn \leq 0.1$ . After this section, the LBM solution (blue dashed line) starts to largely diverge, while the in-house DSMC code (black continuous line) and the hybrid LBM-DSMC method (red dot-dashed line) are closely reproducing the reference solution.

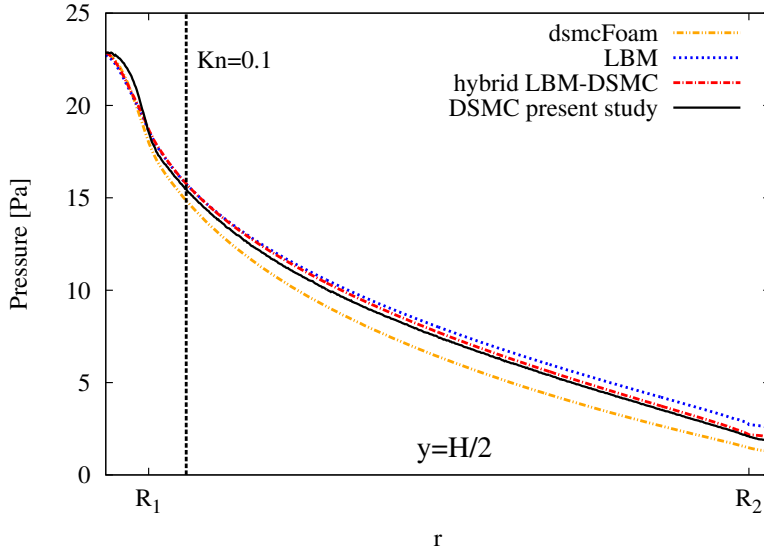


**Figure 6.25:** Comparison among the static pressure profiles provided by the three different numerical methods employed in this study for a section at  $y = H/2$ . All the methods provide larger values of the pressure with respect to the reference one (dsmcFoam); however, the hybrid method show a pressure profile very close to the in-house DSMC code.

solver. Moreover, the same reasons allow to obtain a very good parallel scaling performance. In Fig. 6.27, the scaling properties of the code used to simulate the flow within the studied geometry are shown.

As the simulation is very large, in fact more than 133 millions nodes defined the grid, we ran it on 256 processors and, therefore, a total of 8 **broadwell** nodes was needed. With such resources, the simulation took about 10 hours to fulfil the convergence criterion defined in Eq. (6.15).

## DSMC computational cost

The DSMC method is, in general, a very expensive method due to its particle-based and Monte Carlo nature. Moreover, this also leads to difficulties in reaching very good parallel scaling performances, as a large amount of inter-processor communications may be required. Since the present DSMC code has been newly developed, we performed several tests to verify the parallel scaling efficiency of the algorithm. Such verification includes two tests: one to verify the strong scaling efficiency of the DSMC code and one to assess the influence of the number of particles per cell. In Fig. 6.28, the results of the strong scaling parallel efficiency test are plotted for two different configurations: the blue triangles refer to the data obtained for



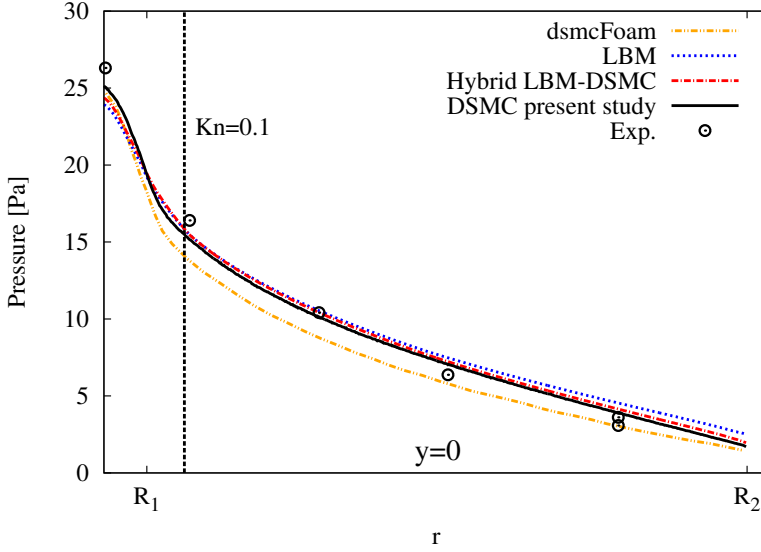


**Figure 6.26:** Comparison of the numerical solutions with the experimentally determined pressure measured at the floor of the flow domain,  $y = 0$ . The in-house DSMC, as well as the hybrid method show a closer agreement to the experimental data with respect to the reference DSMC (*dsmcFoam*).

the flow configuration of section 6.4 (called 3D complex flow in the legend); the red circles refer to the data obtained from a simple three-dimensional box in equilibrium conditions at  $T=300$  K and with Ar as gas (called 3D box). In both cases, a good scaling performance is achieved. The larger value of the scaling exponent found for the 3D complex flow case ( $\sim 0.9$ ) with respect to the 3D box case ( $\sim 0.8$ ) can be explained considering that the 3D complex flow case is much more computational intensive than the 3D box case and, therefore, the inter-processor communication costs can be more easily compensated. In Fig. 6.29, instead, we plotted the results for the test about the influence of the number of particles per cell for a smaller two-dimensional flow setup which confirmed a good scaling efficiency. Adopting such configuration allowed to span a large range of parameters using a small amount of computational time on the Cartesius supercomputer. Finally, about the computational cost, to run the DSMC simulation over the studied geometry required much larger resources than the LBM one. In fact we ran the same grid resolution on 1600 processors and, therefore, a total of 50 nodes was needed. With such resources, the simulation took about 120 hours to fulfil the defined convergence criterion of 1% fractional statistical error on the velocity magnitude measurements. We can therefore say that the DSMC simulation required about

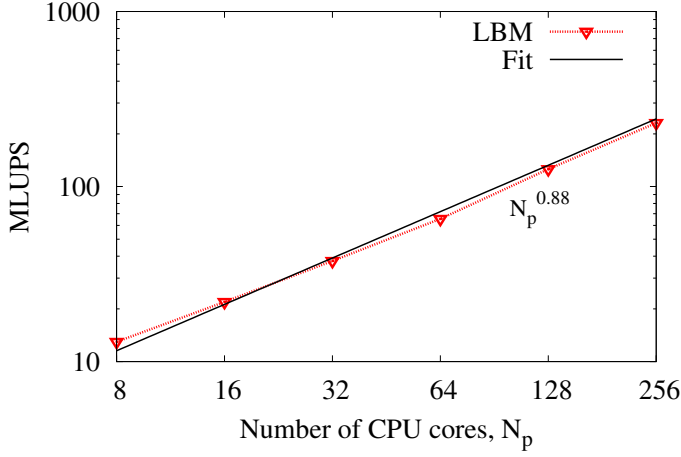


**Figure 6.27:** Strong scaling parallel efficiency for the LBM code. The parallelization efficiency is measured in terms of MLUPS (Million Lattice Updates per Second) and, besides the code implementation per se, it depends also on the domain size and physics features involved in the test. The data refer to simulations under the same flow and domain configuration presented in section 6.4. The scaling exponent with the number of CPU cores is 0.88.

75 times more resources than the LBM simulation:  $1600 N_p \times 120 h / (256 N_p \times 10 h) \cong 75$ . A similar ratio was also found for the test reported in chapter 4. This is also the reason why only up to  $N_p=256$  cores were used to draw the plots of Fig. 6.27 (LBM data), while, for the DSMC code, the scaling performance is tested up to few thousands core, Fig. 6.28.

### Hybrid method computational cost

The computational cost of the hybrid LBM-DSMC method is largely dependant on the flow domain decomposition and in particular on the fraction of the domain occupied by the DSMC method. In chapter 4, we found that a very large speed-up was guaranteed by the application of the hybrid method. In fact, for the particular flow setup there investigated, which was characterized by  $\alpha = 0.2$ , i.e. the DSMC occupied 20% of the total number of grid cells, we found a 6-fold speed-up, even larger than the expected value of 4.8 based on the simple addition of the time spent by DSMC and LBM to evolve 0.2 and 0.8 part of the total domain, respectively. The hybrid simulation of the present geometry, for which  $\alpha \cong 0.2$ , was run with the same number of processors as the DSMC simulation: 1600 processors. In order to fulfil the convergence criterion in Eq. (6.20), it took about 29 hours. This number essentially tells that it was possible to achieve a  $\sim 4.15$  factor in the reduction

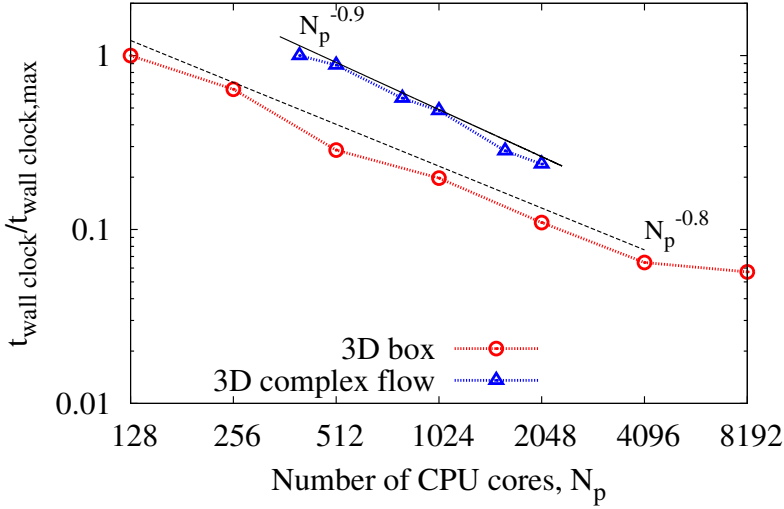


**Figure 6.28:** Strong scaling parallel efficiency for the in-house DSMC code: wall clock time per time step as a function of the number of CPU cores. The data refer to two different set-ups. The first data-set (red circles, named 3D box in the legend) refer to a three-dimensional box in equilibrium conditions at  $T=300$  K and with Ar as gas, composed of more than 16.7 millions of cells ( $256^3$  resolution) and more than 335 millions of particles (20 particle per cell). The second data-set refer to the configuration of section 6.4 (blue triangles, called 3D complex flow). The data are normalized with respect to the  $N_p=128$  case for the 3D box and for  $N_p=400$  for the 3D complex flow case. For the 3D box case, the scaling exponent is 0.8 and it is maintained up to 4096 cores. For 8192 cores, the performance degrades sensibly because of the limited number of particles evolved in a single core. For such case, the run time is dominated by inter-processor communication. For the 3D complex case, instead, the scaling exponent is 0.9 and it is constantly maintained over the whole range of the investigated number of CPU cores.

of the computational time with respect to the full DSMC simulation. Even if it was not possible to replicate the very good results of chapter 4, it is still a quite remarkable achievement.

Several reasons may be put forward to explain the non-perfect scaling of the reduction of the computational cost, but the most probable one is essentially related to the domain decomposition imposed by the hybrid algorithm. i.e. to a load balance issue. In fact, due to the proposed domain decomposition, a certain amount of processors may not be involved at all in the code routines related to the hybrid method, in the sense that they fully reside within the area where only DSMC or LBM is used. This means that those processors will just wait the other processors performing the operations related to the hybrid algorithm. This clearly introduces an overhead which may result in a loss of efficiency. In the case of

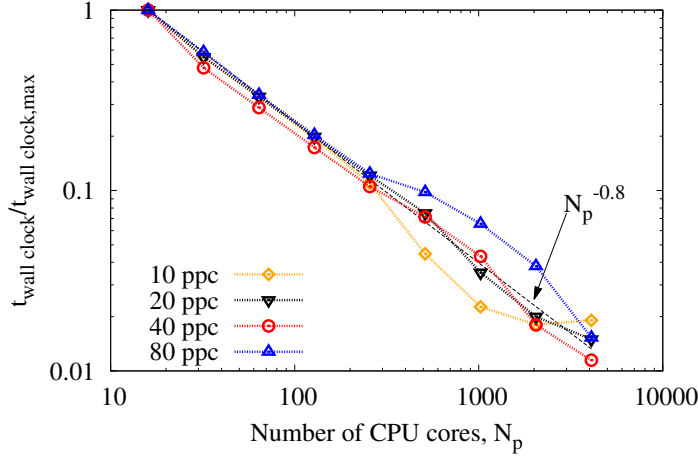


**Figure 6.29:** Strong scaling parallel efficiency for the in-house DSMC code: influence of the number of particles per cell (ppc in the legend) on the wall clock time per time step as a function of the number of CPU cores. Data refer to a two-dimensional force-driven channel flow with Ar as flowing gas ( $Kn=0.1$ ) and with a  $1024 \times 512$  grid resolution. Data are normalized with respect to the  $N_p=16$  case. 5.2 millions of particles are evolved. The same scaling exponent found in the 3D box case and shown in Fig. 6.28, is achieved also under this configuration. All the curves follow the same trend, besides the case with the smallest number of particles per cell, 10 ppc, that saturates after  $N_p=1024$ . For this specific case, where only about 5,000 particles per process are present, it is expected that the time spent for inter-process communications represents a relevant part of the total time spent to perform one time step.

chapter 4, instead, all the processors had exactly the same workload and, therefore, this issue was not present at all.

Another, more physical reason, apart from the just mentioned load balance issue, may be related to the fact that, in the present case, the DSMC area is concentrated in proximity of the walls, where the velocities are smaller, while in chapter 4, due to the different flow test setup, the DSMC area was present where the velocities were the largest. This reflects directly in the amount of time steps required to meet the convergence criterion.

Despite the non-perfect scaling, it should be emphasized that the hybrid model was able to provide an appreciable speed-up also for a very large simulation. In Table 6.1, the just mentioned results are collected.

Finally, as done for the LBM and the DSMC code, we performed a parallel scaling efficiency test also for the hybrid code. We ran the same flow set-up presented in section 6.4 using an increasing number of CPU cores. The results of such test are shown in Fig. 6.30. Also in this case, a good scaling property of the implemented

Method	CPUs	Comp. Time [h]	Scaling
<b>LBM - D3Q19</b>	256 (1600)	10 (1.9)	0.013 (0.016)
<b>DSMC</b>	1600	120	1
<b>Hybrid LBM-DSMC</b>	1600	29	0.242

**Table 6.1:** Collection of the information related to the computational cost for the three different numerical methods employed in this work. If the cost in terms of  $N_p \times h$  for the DSMC is normalized to 1, then the hybrid method costs 0.242 and the LBM 0.013. This last evaluation does not take into account the fact that the LBM simulation used 256 cores. If the information contained in Fig. 6.27 are used, then the data for 1600 cores can be extrapolated (see data in parenthesis for the LBM case). It is evident the advantage provided by the hybrid method with respect to the DSMC case, as well as that LBM is much faster. All the data refer to the same grid resolution (1600x52x1600).

code is obtained.

## 6.6 Conclusions

In this chapter, a comparative study employing three numerical methods based on the kinetic theory of gases, namely the Lattice Boltzmann Method, the Direct Simulation Monte Carlo approach and a hybrid LBM-DSMC method, applied to a flow in a complex geometry, is presented. Due to the common implementation in a single code infrastructure, the comparison of the results can be performed in a more rigorous and simpler way, as demonstrated, for example, by the fact that the same routines are used to define the scalar field representing the geometry of the flow domain.

For the particular, challenging, flow problem studied here, where both strong rarefaction and compressibility effects are present, it is recognized that the regularized LBM D3Q19 model is able to accurately reproduce the reference solution up to  $Kn=0.1$ . The application of the regularization procedure is fundamental in removing discrete artefacts due to excessive rarefaction and compressibility effects which cannot be accurately resolved with the employed lattice. The DSMC novel implementation specifically developed to treat 3D complex geometries shows a very good agreement with the reference DSMC axisymmetric solution over the whole flow domain. Finally, the application of the hybrid LBM-DSMC method allowed to sensibly reduce the computational cost, more than a four-fold reduction, while providing equally accurate results with respect to the case of the DSMC applied to the whole flow domain.

In the near future, it is planned to extend the range of applicability of the hybrid method both in terms of computational optimization and physical modeling. In

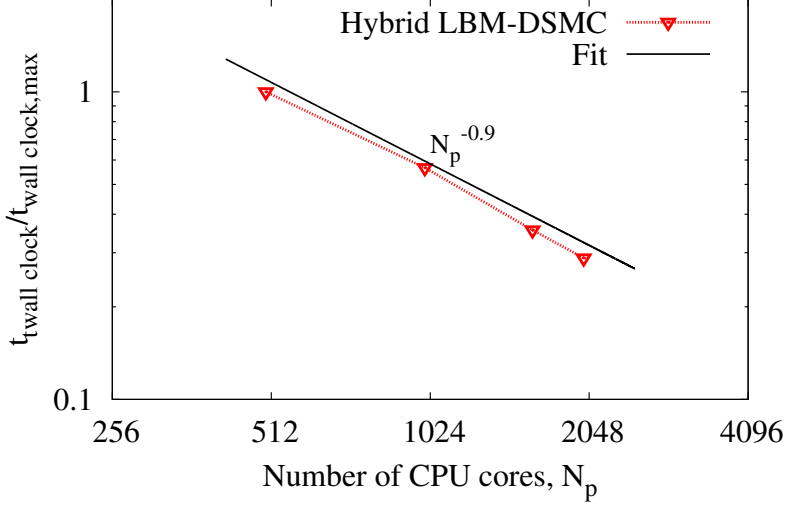


**Figure 6.30:** Strong scaling parallel efficiency for the hybrid code. The data refer to the simulation set-up presented in section 6.4 and are normalized with respect to the wall clock time needed to perform a single time step with  $N_p=512$  cores. The scaling coefficient is 0.9, similar to those already found for the LBM and DSMC solvers.

particular, an adaptive dynamic load-balancing can be beneficial in further reducing the computational cost, while the inclusion of thermal and compressibility effects into the LBM side of the method can enlarge the range of applicability of the present model towards, for example, high-Ma number flows.

## 6.A Conversion of units from LB to SI and vice versa

In chapter 2, we already presented the method to pass from lattice units to SI units. Here, we formalize the procedure.

For the problem investigated in this chapter, it is sufficient to take into account three basic physical dimensions: mass [M], length [L] and time [t]. Any physical quantity  $\phi$  is characterized by its dimension  $[\phi]$ , which, in turn, can be expressed as a product of the basic dimensions, i.e.  $[\phi] = M^\alpha L^\beta t^\gamma$ . To start with, the first step of the procedure is the selection of the characteristic scales for the basic physical dimensions. The most natural characteristic length, mass and time scales are the following:  $H$ , representing the channel height between the two disks,  $\rho_{g,in} H^3$ , where  $\rho_{g,in}$  is the gas density at inflow conditions,  $H/c_s$ , with  $c_s$  the speed of sound of the gas ( $H_2$  at the reference temperature of 295 K). Using these scales, any physical

quantity  $[\phi]$  can be made dimensionless via the following relation:

$$\phi^* = \frac{\phi}{(\rho_{g,in} H^3)^\alpha (H)^\beta (H/c_s)^\gamma} \quad (6.21)$$

where  $\phi^*$  now is dimensionless and the exponents  $\alpha$ ,  $\beta$  and  $\gamma$  are determined according to the dimensions of the physical quantity  $\phi$ .

We can now assign to the parameters used to define the characteristic scales their values in SI units:  $H=6$  mm,  $\rho_{g,in}=2.05 \cdot 10^{-5}$  kg/m<sup>3</sup>,  $c_s=1305.4$  m/s, and in LU:  $H = 24$ ,  $\rho_{g,in}=3$ ,  $c_s=1/\sqrt{3}$ . Note that the value of the density in LU is arbitrary while the value of  $H$  is chosen so to have enough resolution along the height of the expansion channel.

Finally, the values of  $H$ ,  $\rho_{g,in}$  and  $c_s$  in LU and SI units can be used to determine the scaling rules between LB and SI and vice versa.

## 6.B Implementation of slip boundary conditions in LBM

In section 6.3, we cited that the tangential momentum accommodation coefficient,  $\sigma_v$ , cannot be directly used within the LBM boundary condition represented by Eq. (6.9). This is due to the fact that an artificial excessive slip is produced by the discretized version of the diffuse boundary condition as demonstrated in [143]. This is also shown in Fig. 6.31, where the slip velocity for a force-driven laminar channel flow is plotted as a function of the parameter  $\sigma$  in Eq. (6.9) which represents the relative fraction of diffuse and specular reflection boundary condition ( $\sigma=1$ , fully diffuse;  $\sigma=0$  fully specular). The theoretical curve present in Fig. 6.31, derived in [143] for the LB equation in its standard formulation, i.e. without regularization, and for the channel flow case, is given by the relation:

$$U_s = \frac{u_s}{u_0} = 4 \frac{2-\sigma}{\sigma} \sqrt{\frac{6}{\pi}} \text{Kn} + \frac{32}{\pi} \text{Kn}^2 - \Delta^2, \quad (6.22)$$

where  $u_0 = aH^2/(8\nu)$  is the centerline velocity obtained in the continuum limit and  $u_s$  is the slip velocity. Here,  $a$  is the forcing magnitude on the fluid,  $H$  is the number of nodes along the channel height and  $\nu$  is the kinematic viscosity. From Eq. (6.22), the linear and quadratic dependence from the  $\text{Kn}=\lambda/H$  as well as the quadratic dependence from the the grid resolution,  $\Delta = 1/H$  are evident. As already mentioned, since we are using a D3Q19 lattice, we want to reproduce a second-order slip boundary condition for which the usual relation between the

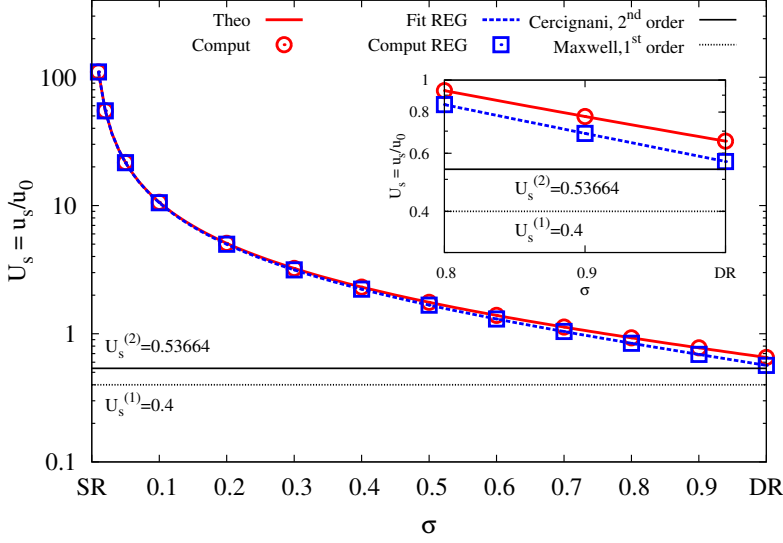


**Figure 6.31:** Force-driven channel flow with a height discretization equal to  $H=24$  nodes for  $Kn=0.1$ : the slip velocity normalized with the hydrodynamic limit ( $Kn \rightarrow 0$ ) of the centerline velocity as a function of the fraction of specular and diffuse reflection is compared when using the regularized LBM (blue square symbols) and the standard LBM (red circles). The blue symbol for  $\sigma = 1$ , indicated as *DR* on the x axis, shows that the found slip is close to the result of the 2<sup>nd</sup> order model from Cercignani, [182],  $U_s^{(2)}=0.53664$ , only when applying the regularization procedure. For such case, the difference is about 5%. The slip velocity, instead, is about 22% larger if the standard LBM is used. This means that, in general,  $\sigma \neq \sigma_v$ , that is the numerical and physical accommodation coefficients are not the same. As reference, the slip velocity obtained from the Maxwell 1<sup>st</sup> order model is also included. The red continuous line represents the theoretical values provided by the LBM (Theo), while the blue dashed line represents the fit of the data from regularized LBM simulations (Fit REG). As already demonstrated in section 2.3, the application of regularization is effective in reducing the excessive slip velocity.

slip velocity and the Kn number for a channel flow is provided by:

$$U_s = 4A_1Kn + 8A_2Kn^2. \quad (6.23)$$

Comparing Eq. (6.22) and Eq. (6.23), therefore, it is possible to derive the diffuse reflection fraction,  $\sigma$ , and consequently the specular reflection,  $1 - \sigma$ , needed to reproduce the intended slip velocity model characterized by the coefficients  $A_1$  and  $A_2$ :

$$\sigma = 2 \left[ 1 + \sqrt{\frac{\pi}{6}} \left( \frac{\Delta^2}{Kn} + A_1 + \left( 2A_2 - \frac{8}{\pi} \right) Kn \right) \right]^{-1}. \quad (6.24)$$



There is a vast literature about the determination of the coefficients  $A_1$  and  $A_2$  as a function of the  $\sigma_v$ , based both on theoretical considerations and experimental evidences. A thorough treatment of the subject is available in [112]. Here we choose to follow the analytical approach developed by Cercignani and co-workers in [184, 185], where a variational technique is applied to the Boltzmann equation based on the linearized collision operator. In particular, two different kinetic models of the collisional operator are compared: the Bhatnagar-Gross-Krook (BGK) model and the Cercignani-Lampis kernel for a hard-sphere gas (CL-HS).

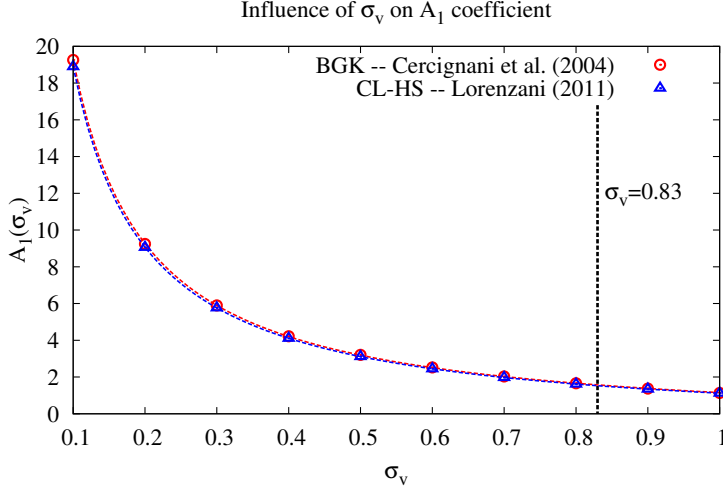
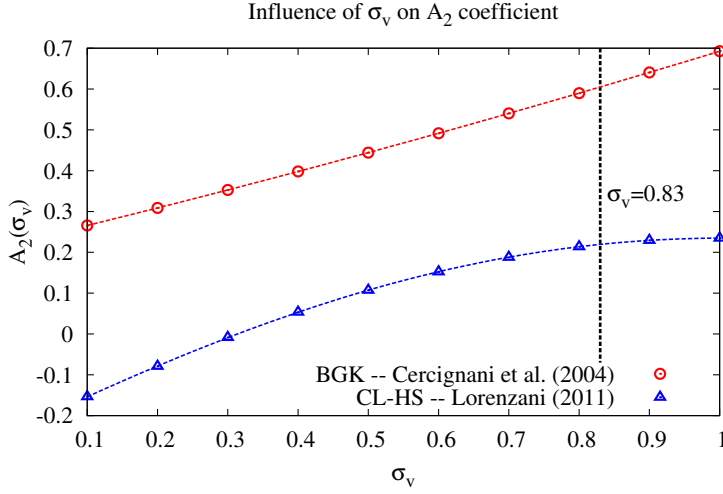
In Figs. 6.32a and 6.32b, the first- and second-order slip coefficients as a function of the accommodation coefficient  $\sigma_v$  obtained in [184] and [185] for the two collision kernels are plotted. While the different kernels do not significantly influence the first-order coefficient, the second-order coefficient is particularly affected by the chosen model.

For affinity with the LB method we use, which also adopts the BGK approximation for the collisional process, we employ the results of such model to calculate the two coefficients.

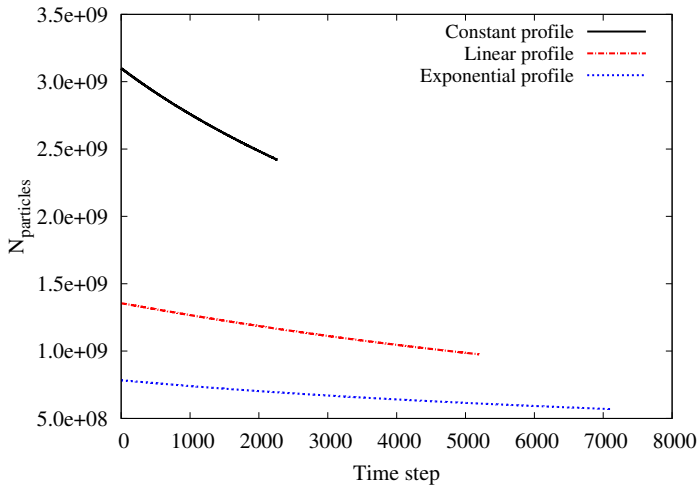
As underlined in [185], in order to take into account the Knudsen layer contribution to the flow rate for a Poiseuille flow, the second-order coefficient should be modified so that  $\tilde{A}_2 = A_2 + \xi$  and  $\xi \simeq 0.296$ . From the so-obtained coefficients, evaluated in correspondence of the accommodation coefficient  $\sigma_v$  proper of the gas-surface combination, the fraction  $\sigma$  of the diffuse reflection can be computed from the analytical relation of Eq. (6.24) when using the classical LBM or from the fit present in Fig. 6.31 (blue dashed line) when using the regularized LBM. Deriving an analytical relation also for the regularized LBM is subject of a future study.

## 6.C Set-up of initial conditions to speed-up the DSMC simulation

As mentioned in section 6.4, the proper definition of the initial pressure field is very important to reduce the time steps needed to extinguish the transient initial phase. Several small resolution simulations were conducted to investigate such aspect before running the fully resolved simulation. In Fig. 6.12, three possible initial profiles were shown: the case of a constant pressure, equal to the maximum pressure value, the case of a profile linearly changing along the radial distance, between the maximum and the outflow pressure and a profile exponentially changing with the radius. In Fig. 6.33, the number of particles evolved in the simulation for each of the tested initial pressure profiles is plotted: in the transient phase, a very large number of particles is removed, especially for the case of a constant pressure profile. The


 (a) First-order slip coefficient,  $A_1$  vs  $\sigma_v$ 

 (b) Second-order slip coefficient,  $A_2$  vs  $\sigma_v$ 

**Figure 6.32:** (a) First- and (b) second-order slip coefficients for the model of Eq. (6.23) as a function of the accommodation coefficient  $\sigma_v$ . Red symbols represent the analytical expressions in the case of BGK collisional operator, [184]. Blue symbols, instead, represent the analytical expressions in the case of CL-HS kernel, [185]. It is clear the small effect of the different kernels on the first-order coefficient,  $A_1$ , while a much larger effect is present in the case of the second-order coefficient,  $A_2$ . The vertical dashed line in (a) and (b) is drawn for  $\sigma_v = 0.83$ , which is the value experimentally found for the gas-surface combination of the geometry investigated in section 6.4. The intersections with the plotted curves for the BGK model provide the values of  $A_1 = 1.573$  and  $A_2 = 0.605$  and therefore, taking into account the Knudsen layer contribution,  $\xi \simeq 0.296$ ,  $\tilde{A}_2 = 0.901$ .



**Figure 6.33:** Evolution of the number of particles within the fluid domain for constant, linear and exponential initial pressure profiles in the early stage of the DSMC simulations. The application of an initial condition closer to the final one allows to speed-up the initial transient phase as a smaller number of particles has to be evolved. Note that these tests were performed in a grid with a smaller resolution with respect to the simulations of section 6.4:  $1000 \times 48 \times 1000 \cong 4.8 \cdot 10^7$  cells. Note also the orders of magnitude of the number of particles: hundreds or even billions of particles. The possibility to initialize the pressure field starting from vacuum conditions was not considered in order to avoid too frequent memory allocation operations.

simulations, moreover, ran for 2 hours using the same computational resources, and, while the case with an exponential profile ran for more than 7,000 time steps and the case with a linear profile performed 5,000 time steps, the constant initial profile performed only about 2,000 time steps. The exponential case, therefore performed 40% more time steps than the linear case and 350% more time steps than the constant case. Once the transient phase will be extinguished, the computational wall clock time per time step will be the same since the same final solution will be generated regardless of the initial condition, but the cumulated duration will be smaller for the exponential case. The full scale simulation, therefore, is initialized with an exponential pressure profile.

## 7 Concluding remarks and outlook

In the present thesis, we focused on questions related to the study of rarefied and non-equilibrium gas flows, a research field which still represents an open challenge from physics, mathematical modelling as well as computer science points of view. To address some of such questions, we proposed a new hybrid model combining two well established mesoscopic numerical methods, namely the Lattice Boltzmann Method and the Direct Simulation Monte Carlo. In this chapter, we first summarize the main results obtained by applying the developed hybrid model to study flows showing a large range of non-equilibrium and rarefaction effects. In addition, we underline the current limitations, essentially related to the isothermal assumption for the LBM side of the model, and we propose some directions to overcome such limitations.

### 7.1 Conclusions

In this thesis, we reported our findings related to the development and application of a new hybrid model to study flows characterized by a large range of rarefaction and non-equilibrium effects. The proposed hybrid model couples in a single tool two mesoscopic methods, the LBM and the DSMC, which can be interpreted as two different approaches to discretize the Boltzmann equation.

The most important results of this thesis are summarized here by answering the questions that were already posed in chapter 1.

- Can we understand what are the limitations for the LBM in describing flows at finite  $\text{Kn}$  as a function of the number of lattice discrete velocities? (chapters 2, 4)

The basic formulation of the LBM, the well-known D3Q19 model, aims to provide a flow description at the (isothermal) Navier-Stokes equations level. In this view, upon the application of proper wall boundary conditions, flows in the slip regime ( $\text{Kn} \leq 0.1$ ) may be accurately simulated. However, the LBM, due to its kinetic theory origins, is not limited only to such flows. In fact, as shown in chapter 2, it is possible to construct LB models which can deal with flows at larger  $\text{Kn}$ . This can be achieved by adopting higher-order lattices. In few words, adopting

the Grad's expansion in Hermite polynomials of the single particle distribution function and interpreting the lattice velocities as the abscissae of a Gauss-Hermite quadrature, it is possible to systematically derive hydrodynamic systems going beyond the Navier-Stokes equations representation. In chapter 4 we showed a comparison between the results obtained from the application of the D3Q19 and D3Q39 lattices with the DSMC for a Poiseuille channel flow at several values of the Kn number. The D3Q39 lattice, representing the next step beyond Navier-Stokes equations, is able to reproduce with a good accuracy the reference DSMC results up to  $\text{Kn}=0.25$ , and, therefore, to some extent within the transitional flow regime, thus confirming the theoretical predictions presented in chapter 2.

- Can we define a hybrid method which takes advantage of the peculiarities of the LBM and DSMC methods to simulate flows characterized by a large range of non-equilibrium effects? Is it possible to construct coupling algorithms between the LBM and the DSMC able to transfer also non-equilibrium information? (chapter 4)

chapter 4 is devoted to the consistent definition of the bi-directional LB2DSMC and DSMC2LB coupling schemes and to their validation. To establish them, we took advantage of the peculiarities of the LBM to construct schemes able to transfer non-equilibrium informations between the two methods. In fact, instead of adopting the Chapman-Enskog approach to represent the single particle probability distribution function, as routinely done for standard Navier-Stokes-DSMC hybrid methods (i.e. those not involving the LBM), we chose to use the Grad's formulation, which expresses the velocity pdf in a series in Hermite polynomials. As shown in chapter 4, the coefficients of such expansion can then be directly evaluated via the weighted summation of the discrete populations evolved in the LBM. The order at which the series is truncated, in turn closely related to the amount of non-equilibrium information which can be transferred between the LBM and the DSMC, is then determined by the chosen lattice, and, more precisely, by the degree of accuracy of the quadrature possessed by the lattice, as in depth shown in chapter 4. There, we also showed the results about the validation of the two schemes for a Poiseuille flow up to  $\text{Kn}=0.25$ . In particular for the LB2DSMC scheme we proved that the pdf of the microscopic velocity of the DSMC particles, as generated by sampling a pdf constructed using the LBM discrete distributions, closely reproduces the pdf of independent DSMC simulations. Analogously, for the DSMC2LB scheme, we showed that the discrete distributions, as provided by projecting the DSMC hydrodynamic variables onto the Hermite polynomials basis accessible to the chosen lattice, are in good agreement with the discrete distributions generated by independent LBM simulations for the same flow set-ups. Therefore, it can be concluded that the developed coupling schemes are capable to provide an

accurate way to pass information between the LBM and the DSMC including non-equilibrium contributions.

- Can we implement these algorithms in an efficient way in a single code infrastructure? (chapters 3, 4, 5, 6)

The coupling algorithms validated in chapter 4 are just one element of the hybrid model. In chapters 5, 6, we discussed the implementation of the coupling algorithms into the hybrid method based on a domain decomposition technique. While the LBM is applied to the whole flow domain, the DSMC is adopted only in those regions where non-equilibrium effects are stronger. In chapter 5, we applied such domain decomposition technique to a Couette flow so that the DSMC is employed in the flow domain only within the Knudsen layer, present in proximity of the walls. The main result of the test is that a large speed-up in the spent computational time to achieve the final solution is obtained, while preserving a good comparison with respect to a reference DSMC simulation. In fact, up to a sixfold reduction of the computational time cost is achieved. Such result is particularly significant because it could be obtained thanks to the integration within the same code infrastructure of the numerical codes as well as to the fact that the DSMC code has been specifically implemented to match the LBM algorithmic choices, in particular for what concerns the treatment of flows in complex geometries. Such treatment is discussed in chapter 3.

Moreover, in chapter 6, we applied the hybrid method to a three-dimensional flow of industrial interest and we further defined the criteria used to identify the flow domain areas where the non-equilibrium effects are stronger and that, therefore, should be assigned to the DSMC part of the model. Such criteria are based both on a global Kn number,  $Kn$ , defined according to a characteristic geometrical length scale, and on a local Kn number,  $Kn_l$ . Two formulations of  $Kn_l$  are investigated, finding that, for the nature of the problem at hand, the  $Kn_l$  based on the flow velocity magnitude gradient provides a better indication for the need to switch to the DSMC. Also for this problem, a large speed-up (more than a fourfold reduction in the wall clock time with respect to a full DSMC simulation for the same flow set-up) is achieved while preserving a good agreement with the reference DSMC results.

- Can we take advantage of the efficiency of the developed hybrid method to open up the possibility to investigate with high accuracy the physics of realistic flows within industrial applications? (chapters 3, 6)

One of the main reasons that pushes the research towards the definition of hybrid models is to provide more efficient alternatives to physically accurate but

computationally expensive numerical methods. In chapter 6, we showed that with the DSMC code implemented during the PhD work, we are able to perform accurate fully three-dimensional simulations which are orders of magnitude larger than what could be achieved by a popular DSMC code, *dsmcFoam*. In fact, due to limitations in the computational efficiency, with the latter code only the corresponding axisymmetric problem could be simulated. However, even if the efficiency needed to perform such large scale simulations is not easily accessible to many DSMC codes available to the scientific community, a single full DSMC simulation presented in chapter 6 costed about 200,000 computational hours. The investigated application, featuring a large range of non-equilibrium conditions, however, was particularly suitable to be studied with the hybrid method presented in this thesis. The application of the hybrid model, in fact, allowed to reduce by more than four times the computational cost and about 50,000 computational hours were needed to get a solution with a good accuracy with respect to the reference DSMC solution.

From a practical and industrial point of view, this means that in the same time frame during which a single DSMC simulation runs, four possible alternative designs may be studied if the hybrid model is used. It is therefore evident that the increase of the efficiency in the design process could be guaranteed by the adoption of the hybrid model.

## 7.2 Outlook

In this work, we presented a novel hybrid model which combines the accuracy of the DSMC method in dealing with flows characterized by large non-equilibrium and rarefaction effects, with the efficiency of the LBM when non-equilibrium effects can be dealt with perturbatively. As a newly develop method, however, extensions and improvements may be pursued in order to enlarge the range of applicability of the current implementation. In this view, what follows discusses some possible new directions.

**Extension to non-isothermal flows:** The present formulation of the hybrid model, due to the chosen LB model, is limited to isothermal flows. As shown in chapter 4, when adopting the Grad's formalism and the Gauss-Hermite quadrature technique, the molecular velocity,  $\xi$ , or, more precisely, the abscissae of the lattice quadrature,  $\xi_a$ , are measured in units of a characteristic velocity,  $c_s = \sqrt{RT}$ , which, indeed, is the speed of sound of the lattice gas. Allowing for the gas temperature to change, and therefore, also for the speed of sound to change, would reflect into a series of complications such as the fact that the grid nodes would not be equidistant

anymore. This, as it can be argued, would introduce algorithmic complexity for the LBM implementation. As reported in chapter 4, several methods recently appeared in literature in order to overcome this limitation, including the multispeed and the two distribution functions approach. In particular, the approach which considers the adoption of higher order lattices (multispeed approach) seems to be the suitable one to extend the current framework, as it is based on the same Grad's formalism.

**DSMC for low speed flows:** In several applications, the presence of a large range of rarefaction effects is associated with low speed flows. The standard DSMC formulation is not suitable for very low speed flows, as a large number of samples are needed to make emerge the macroscopic flow velocity from the thermal molecular speed. In such cases, the hybrid method we propose here may be adopted to speed up the simulation. However, in the case the two flow characteristics, low speed and rarefaction conditions, are present in the same areas of the flow domain, the hybrid method would be strongly slowed down by the DSMC requirements. In order to increase the efficiency of the DSMC method under such conditions, several approaches appeared in literature, being the low-variance method, [49, 50], and the Information Preservation method, [51], two promising options. Also this extension would allow to enlarge the range of applicability of the hybrid model.

**Extending the coupling algorithms to other numerical methods:** The proposed coupling algorithms needed to pass information from the LBM to the DSMC and vice versa are sufficiently general that they may be applied also to other combinations of numerical methods. In fact, the applications of the coupling schemes proposed here to the combination of a Molecular Dynamics code to the LBM has recently appeared, [186]. Another possible combination which could be considered would involve the coupling of the DSMC with a Moments Method (MM) model. In fact, also the latter method is based on the expansion of the single particle velocity distribution function into Hermite polynomials. Therefore, the only modification with respect to the LBM case would reside in the way the coefficients of the expansion are evaluated. While for the LBM those are calculated via the weighted summation of the discrete distributions, for the MM case, the coefficients should be calculated through the moments themselves.





# A Fluctuations on hydrodynamic moments: DSMC study

## A.1 Relations for fluctuations at equilibrium

General expressions for the evaluation of the macroscopic hydrodynamic variables and the associated statistical fluctuations in DSMC have been reported in several works, [1, 45, 187–190]. The understanding of such evaluations assumes particular importance for those situations where the number of statistical samples is limited. An example is provided by the evaluation of the temperature for simulations using temperature-dependent collisional model, [191], or the instantaneous evaluation of the average number of simulated particles used to determine the number of collisions to occur during a time step, [1]. Another example is the case of hybrid methods where the instantaneous macroscopic properties are required when the DSMC is couple to a continuum solver.

While all the main results shown in the present thesis refer to the solution of steady-state flows, in section 4.3, we presented the first results related to the case in which the instantaneous values of the DSMC hydrodynamic properties are used in the projection DSMC2LB step. In particular, we demonstrated that this coupling step is still accurate (and stable), see Fig. 4.12. Analogously, we were also interested in showing that the molecular velocities generated via the reconstruction LB2DSMC step is such that the measured hydrodynamic properties — calculated as averages of the molecular velocities of the particles present in a cell — and their distributions are physically accurate, e.g. the conserved moments distributions follow simple equilibrium statistical mechanics considerations, see Fig. 4.14. All the considerations explained there were based on the assumption that the present DSMC implementation correctly reproduces both the instantaneous and average evaluations of the macroscopic properties, as well as their distributions. In this Appendix, we will show few results to support such assumption.

We first take into consideration the expressions for evaluating the distributions of the instantaneous values of typical hydrodynamic properties. We then examine the related statistical error for the same quantities. All the data in this Appendix are taken from a force-driven Poiseuille simulation for which  $Kn=0.05$  and  $Ma=0.10$  (based on centerline velocity). The molecular information are collected in a cell

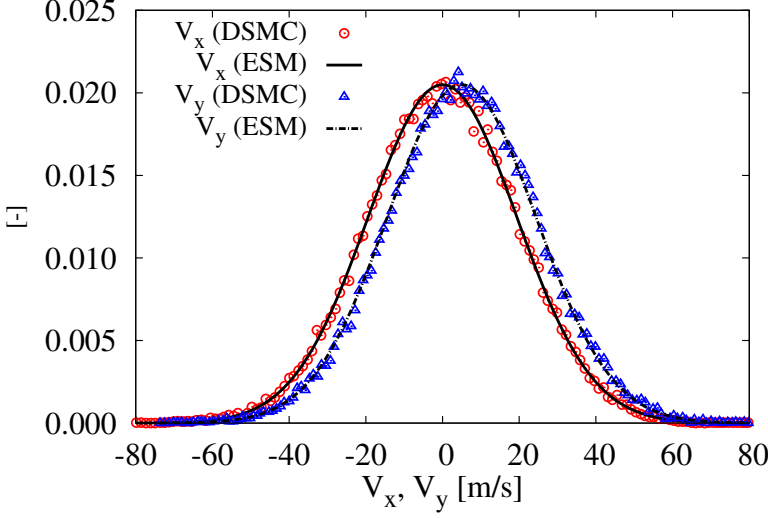


**Figure A.1:** Comparison between the distributions of the flow velocity components,  $V_x$  and  $V_y$ , as obtained by DSMC (symbols) and from Equilibrium Statistical Mechanics (ESM) (lines). The forcing on the fluid is along the (positive)  $y$ -direction as demonstrated by the shifted distribution for  $V_y$ .

in proximity of the wall after the flow reaches a steady state condition. In Fig. A.1, the distributions of the instantaneous flow velocity components  $V_x$  and  $V_y$  obtained from DSMC are compared with the theoretical prediction from equilibrium statistical mechanics (a normal distribution). The velocity components realizations are obtained as cumulative averages of the velocity of the particles,  $v_i$ , in a cell as:

$$V_i = \frac{\sum_{j=1}^{N_{\text{samples}}} \sum_{i=1}^{N(t_j)} v_i(t_j)}{\sum_{j=1}^{N_{\text{samples}}} N(t_j)}. \quad (\text{A.1})$$

For these variables, the standard deviation is given by:

$$\sigma_{V_i} = \sqrt{\frac{k_B \langle T \rangle}{m \langle N \rangle}}. \quad (\text{A.2})$$

As visible from Fig. A.1, both the standard deviation and the mean found from the DSMC simulation closely reproduce the expected values. In Fig. A.2, the distributions of the number of particles,  $N$ , in a cell and of the temperature,  $T$ ,

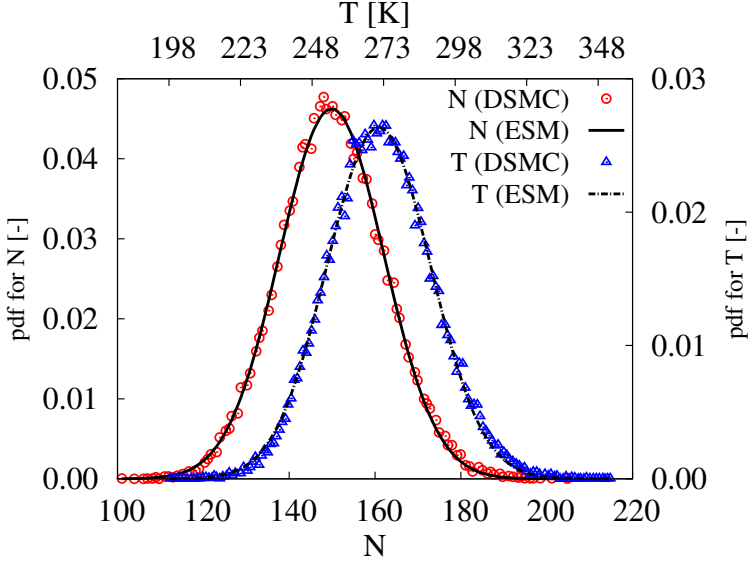


**Figure A.2:** Comparison between the distributions of the number of particles,  $N$ , and the temperature,  $T$ , as obtained by DSMC (symbols) and from equilibrium statistical mechanics (ESM, lines). Note that while the distribution for  $T$  is a normal distribution, the distribution for  $N$  is a Poisson one.

are shown. Once the distribution for  $N$  is known, then the distributions for the number density,  $n$ , and the mass density,  $\rho$ , can be readily found. In fact,

$$n = NF_N/\text{Vol}, \quad \rho = nm, \quad (\text{A.3})$$

where  $F_N$  is the number of real molecules, of mass  $m$ , represented by a single DSMC particle. Vol is the volume of a computational cell. The distribution of  $N$  obtained from the DSMC (red circles in Fig. A.2) is compared with the theoretical prediction (continuous black curve), which represents a Poisson distribution. In fact, as underlined in [45],  $N$  is a Poisson random variable. For the set-up of the test, both the numerical mean and the standard deviation of the distribution are in close agreement with the predictions:  $\langle N \rangle = 149.9$  vs the expected value of  $N_0 = 150$ ;  $\sigma_N = \sqrt{\langle N \rangle} = 12.24$  vs the expected value  $\sigma_N = \sqrt{\langle N_0 \rangle} = 12.25$ . The distribution for  $T$  obtained from DSMC (blue triangles in Fig. A.2) is also compared with the theoretical prediction (dashed black curve). It has to be noted that the evaluation of the temperature is strictly defined only for equilibrium flows and the equilibrium temperature of a flow,  $T$ , is calculated based on the thermal fluctuations of the particles velocity. When the sample size is sufficiently large,

and considering only the translational modes, the mean and standard deviation are given by:

$$T = \frac{m}{3k_B} (\langle V_x^2 + V_y^2 + V_z^2 \rangle - \langle V_x \rangle^2 - \langle V_y \rangle^2 - \langle V_z \rangle^2), \quad (\text{A.4})$$

$$\sigma_T = \sqrt{\frac{2\langle T \rangle}{3\langle N \rangle}}. \quad (\text{A.5})$$

In Eq. (A.4),  $\langle V_i \rangle$  are the average flow velocity components evaluated as cumulative average, [187]. These expressions become invalid when the sample size is limited, and for such case one has, [190]:

$$T = \frac{N_{\text{samples}}\langle N \rangle}{N_{\text{samples}}\langle N \rangle - 1} \frac{m}{3k_B} (\langle V_x^2 + V_y^2 + V_z^2 \rangle - \langle V_x \rangle^2 - \langle V_y \rangle^2 - \langle V_z \rangle^2) \quad (\text{A.6})$$

The distribution of the temperature realizations, then, follows a  $\chi^2$ -distribution in the form:

$$f(T) = \frac{3N_{\text{samples}}\langle N \rangle - 1}{\langle T \rangle} \frac{1}{2^{(3N_{\text{samples}}\langle N \rangle - 1)/2} \Gamma[(3N_{\text{samples}}\langle N \rangle - 1)/2]} \times \left( \frac{(3N_{\text{samples}}\langle N \rangle - 1)T}{\langle T \rangle} \right)^{(3N_{\text{samples}}\langle N \rangle - 1)/2} \exp \left( -\frac{(3N_{\text{samples}}\langle N \rangle - 3)T}{2\langle T \rangle} \right). \quad (\text{A.7})$$

The standard deviation, then, becomes:

$$\sigma_T = \sqrt{\frac{2\langle T \rangle}{3\langle N \rangle} - 1/N_{\text{samples}}}. \quad (\text{A.8})$$

The distribution of Eq. (A.7) approaches the corresponding normal distribution, with the same mean and variance when the sample size increases. In Fig. A.2, indeed, a normal distribution is used as the theoretical reference, finding a good agreement with the DSMC data (mean of the DSMC data equal to 272.8 vs the expected value of 273, and the standard deviation of the DSMC data equal to 18.3 vs the expected value of 18.2).

Finally, in Fig. A.3, the statistical errors for the temperature,  $E_T$ , the number of particles,  $E_N$ , and the flow  $y$  velocity component,  $E_{V_y}$ , as obtained from the DSMC simulation and the theoretical predictions are compared. In particular, one

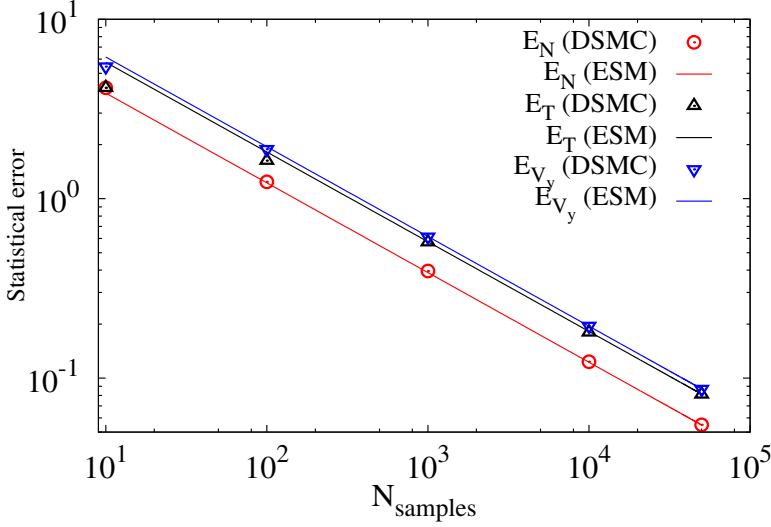


**Figure A.3:** Comparison between the statistical errors as obtained from the DSMC simulation and the theoretical predictions of Eq. (A.9) for the temperature,  $E_T$ , the number of particles,  $E_N$ , and the flow  $y$  velocity component,  $E_{V_y}$ .

has, [45]:

$$E_T = \sqrt{\frac{2\langle T \rangle}{3\langle N \rangle N_{\text{samples}}}}, \quad E_{V_y} = \sqrt{\frac{k_B \langle T \rangle}{m \langle N \rangle N_{\text{samples}}}}, \quad E_N = \sqrt{\frac{\langle N \rangle}{N_{\text{samples}}}}. \quad (\text{A.9})$$

The scaling of the statistical errors with the number of independent samples is well reproduced.

In principle, if the molecular information to evaluate the macroscopic properties are sampled at each time step, then the samples would be statistically dependent, and, as a consequence, there would be correlations among the flow properties. As underlined in [190], dependent samples show larger statistical errors than independent samples when the sample size is the same. In order to evaluate the time correlations among the flow properties, it is possible to use the correlation coefficient defined as:

$$\text{corr}(a, b) = \frac{\langle \delta a \delta b \rangle}{\sqrt{\langle \delta a^2 \rangle \langle \delta b^2 \rangle}}, \quad (\text{A.10})$$

where  $\delta a = a - \langle a \rangle$  and analogously for  $b$ .  $a$  and  $b$  represent two flow properties. For the present flow set-up, if the number of time steps between two consecutive

samples is 50, then, one has, e.g.:

$$\text{corr}(V_y, T) = -0.002, \quad \text{corr}(V_x, V_y) = -0.019. \quad (\text{A.11})$$

## **A.2 Conclusions**

Considering a force-driven Poiseuille flow, it was found that the present DSMC implementation is able to provide accurate results for the evaluation of the fluctuations and the statistical errors for the macroscopic flow properties, as classical equilibrium statistical mechanics relations are recovered. This result paves the way to the implementation of the hybrid method when the instantaneous evaluations of the hydrodynamic properties are needed, as shown in section 4.3.

# Bibliography

- [1] G. A. Bird, *Molecular gas dynamics and the direct simulation of gas flows*. Oxford: Clarendon University Press, 1994.
- [2] C. Cercignani, *The Boltzmann equation and its applications*. Berlin: Springer, 1988.
- [3] H. Struchtrup, *Macroscopic transport equations for rarefied gas flows: Approximation methods in kinetic theory*. Heidelberg: Springer-Verlag, 2005.
- [4] D. Frenkel and B. Smit, *Understanding molecular simulation: From algorithms to applications*. Cambridge: Academic Press, 2002.
- [5] L. Boltzmann, “Weitere studien über das wärmeleichgewicht unter gas-molekülen,” *Sitzungsberichte der Akademie der Wissenschaften, Wien*, vol. 66, pp. 275–370, 1872.
- [6] K. Huang, *Statistical mechanics*. New York: John Wiley & Sons, 1987.
- [7] J. E. Broadwell, “Study of rarefied shear flow by the discrete velocity method,” *J. Fluid Mech.*, vol. 19, pp. 401–414, 1964.
- [8] J. Y. Yang and J. C. Huang, “Rarefied flow computations using nonlinear model Boltzmann equations,” *J. Comput. Phys.*, vol. 120, pp. 323–339, 1995.
- [9] L. Mieussens, “Discrete-velocity models and numerical schemes for the Boltzmann-BGK equation in plane and axisymmetric geometries,” *J. Comput. Phys.*, vol. 162, pp. 429–466, 2000.
- [10] G. Dimarco and L. Pareschi, “Asymptotic preserving implicit-explicit Runge–Kutta methods for nonlinear kinetic equations,” *SIAM J. Numer. Anal.*, vol. 51, pp. 1064–1087, 2013.
- [11] M. Bennoune, M. Lemou, and L. Mieussens, “Uniformly stable numerical schemes for the Boltzmann equation preserving the compressible Navier–Stokes asymptotics,” *J. Comput. Phys.*, vol. 227, pp. 3781–3803, 2008.



- [12] S. Chapman, “On the law of distribution of molecular velocities, and on the theory of viscosity and thermal conduction, in a non-uniform simple monatomic gas,” *Phil. Trans. R. Soc. A*, vol. 216, pp. 279–348, 1916.
- [13] S. Chapman, “On the kinetic theory of a gas. Part II: a composite monatomic gas: diffusion, viscosity, and thermal conduction,” *Phil. Trans. R. Soc. A*, vol. 217, pp. 115–197, 1917.
- [14] D. Enskog, *Dissertation*. 1917.
- [15] D. Enskog, “The numerical calculation of phenomena in fairly dense gases,” *Arkiv Mat. Astr. Fys.*, vol. 16, 1921.
- [16] D. Burnett, “The distribution of molecular velocities and the mean motion in a non-uniform gas,” *Proc. Lond. Math. Soc.*, vol. 40, pp. 382–435, 1936.
- [17] H. S. Y. Zheng, “Burnett equations for the ellipsoidal statistical BGK model,” *Cont. Mech. Thermodyn.*, vol. 16, pp. 97–108, 2004.
- [18] M. S. Shavaliyev, “Super-Burnett equations for the ellipsoidal statistical BGK model,” *J. Appl. Maths. Mechs.*, vol. 57, pp. 573–576, 1993.
- [19] A. V. Bobylev, “The Chapman-Enskog and Grad methods for solving the Boltzmann equation,” *Sov. Phys. Dokl.*, vol. 27, pp. 29–31, 1982.
- [20] M. Torrilhon, J. D. Au, and H. Struchtrup, “Explicit fluxes and productions for large systems of the moment method based on extended thermodynamics,” *Cont. Mech. Thermodyn.*, vol. 15, pp. 97–111, 2003.
- [21] H. Grad, “On the kinetic theory of rarefied gases,” *Commun. Pure Appl. Math.*, vol. 2, pp. 331–407, 1949.
- [22] M. Torrilhon and H. Struchtrup, “Regularized 13-moment equations: shock structure calculations and comparison to Burnett models,” *J. Fluid Mech.*, vol. 513, pp. 171–198, 2004.
- [23] M. R. A. Abdelmalik and E. H. van Brummelen, “Moment closure approximations of the Boltzmann equation based on  $\phi$ -divergences,” *J. Stat. Phys.*, vol. 164, pp. 77–104, 2016.
- [24] S. Succi, *The Lattice Boltzmann Equation for fluid dynamics and beyond*. Oxford: Clarendon University Press, 2001.
- [25] S. Succi, *The Lattice Boltzmann Equation for complex states of flowing matter*. Oxford: Clarendon University Press, 2018.

- [26] E. S. Oran, C. K. Oh, and B. Z. Cybyk, “Direct Simulation Monte Carlo: recent advances and applications,” *Annu. Rev. Fluid Mech.*, vol. 30, pp. 403–441, 2004.
- [27] J. J. Monaghan, “Smoothed-particle hydrodynamics,” *Rep. Prog. Phys.*, vol. 68, pp. 1703–1759, 2005.
- [28] P. J. Hoogerbrugge and J. M. V. A. Koelman, “Simulating microscopic hydrodynamic phenomena with dissipative particle dynamics,” *Europhys. Lett.*, vol. 19, pp. 155–160, 1992.
- [29] A. Malevanets and R. Kapral, “Mesoscopic model for solvent dynamics,” *J. Chem. Phys.*, vol. 110, pp. 8605–8613, 1999.
- [30] L.-S. Luo, “Some recent results on discrete velocity models and ramifications for lattice Boltzmann equation,” *Comput. Phys. Commun.*, vol. 129, pp. 63–74, 2000.
- [31] X. Shan and H. Chen, “Lattice Boltzmann model for simulating flows with multiple phases and components,” *Phys. Rev. E*, vol. 47, pp. 1815–1819, 1993.
- [32] M. C. Sukop and D. Or, “Lattice Boltzmann method for modeling liquid-vapor interface configurations in porous media,” *Water Resour. Res.*, vol. 40, p. W01509, 2004.
- [33] R. Benzi and S. Succi, “Two-dimensional turbulence with the lattice Boltzmann equation,” *J. Phys. A: Math. Gen.*, vol. 23, pp. L1–L5, 1990.
- [34] R. Benzi, M. V. Struglia, and R. Tripiccone, “Extended self-similarity in numerical simulations of three-dimensional anisotropic turbulence,” *Phys. Rev. E*, vol. 53, pp. R5565–R5568, 1996.
- [35] P. Perlekar, R. Benzi, H. J. H. Clercx, D. R. Nelson, and F. Toschi, “Spinodal decomposition in homogeneous and isotropic turbulence,” *Phys. Rev. Lett.*, vol. 112, p. 014502, 2014.
- [36] F. Toschi and S. Succi, “Lattice Boltzmann method at finite Knudsen numbers,” *Europhys. Lett.*, vol. 69, pp. 549–555, 2005.
- [37] X. Shan, X.-F. Yuan, and H. Chen, “Kinetic theory representation of hydrodynamics: a way beyond the Navier-Stokes equation,” *J. Fluid Mech.*, vol. 550, pp. 413–441, 2006.

- [38] R. Zhang, Z. Shan, and H. Chen, “Efficient kinetic method for fluid simulation beyond the Navier-Stokes equation,” *Phys. Rev. E*, vol. 74, p. 046703, 2006.
- [39] S. Ansumali, I. V. Karlin, S. Arcidiacono, A. Abbas, and N. I. Pasianakis, “Hydrodynamics beyond Navier-Stokes: exact solution to the lattice Boltzmann method,” *Phys. Rev. Lett.*, vol. 95, p. 260605, 2007.
- [40] G. A. Bird, “The velocity distribution function within a shock wave,” *Journal of Fluid Mechanics*, vol. 30, pp. 479–487, 1967.
- [41] M. S. Ivanov and S. V. Rogasinsky, “Analysis of numerical techniques of the direct simulation Monte Carlo method in the rarefied gas dynamics,” *Sov. J. Numer. Anal. Math. Modelling*, vol. 2, pp. 453–465, 1988.
- [42] S. K. Stefanov, “On DSMC calculations of rarefied gas flows with small number of particles in cells,” *SIAM J. Sci. Comput.*, vol. 33, pp. 677–702, 2011.
- [43] D. Rader, M. Gallis, and J. Torczynski, “Direct Simulation Monte Carlo convergence behavior of the hard-sphere-gas thermal conductivity for Fourier heat flow,” *Phys. Fluids*, vol. 18, p. 077102, 2006.
- [44] A. L. Garcia, J. Bell, W. Crutchfield, and B. Alder, “Adaptive mesh and algorithm refinement using Direct Simulation Monte Carlo,” *J. Comput. Phys.*, vol. 154, pp. 134–155, 1999.
- [45] N. G. Hadjiconstantinou, A. L. Garcia, M. Z. Bazant, and G. He, “Statistical error in particle simulations of hydrodynamic phenomena,” *J. Comput. Phys.*, vol. 187, pp. 274–297, 2003.
- [46] L. Landau and E. Lifshitz, *Statistical Physics*. Oxford: Pergamon Press, 3rd ed., 1980.
- [47] C. Cercignani and M. Lampis, “Kinetic models for gas-surface interactions,” *Transport Theory and Statistical Physics*, vol. 1, pp. 101–114, 1971.
- [48] R. Lord, “Some extensions to the Cercignani-Lampis gas-surface scattering kernel,” *Phys. Fluids*, vol. 3, p. 706, 1991.
- [49] G. A. Radtke and N. G. Hadjiconstantinou, “Variance-reduced particle simulation of the Boltzmann transport equation in the relaxation-time approximation,” *Phys. Rev. E*, vol. 79, p. 056711, 2009.

- 
- [50] G. A. Radtke, N. G. Hadjiconstantinou, and W. Wagner, “Low-noise Monte Carlo simulation of the variable hard sphere gas,” *Phys. Fluids*, vol. 23, p. 030606, 2011.
- [51] C. Cai, I. Boyd, and J. Fan, “Direct simulation methods for low-speed microchannel flows,” *J. Thermophys. Heat Transfer*, vol. 14, pp. 368–378, 2000.
- [52] W. Wagner, “A convergence proof for Bird’s direct simulation Monte Carlo method for the Boltzmann equation,” *J. Stat. Phys.*, vol. 66, pp. 1011–1044, 1992.
- [53] X. He and L.-S. Luo, “Theory of the lattice Boltzmann method: From the Boltzmann equation to the lattice Boltzmann equation,” *Phys. Rev. E*, vol. 56, p. 6811, 1997.
- [54] X. Shan and X. He, “Discretization of the velocity space in the solution of the Boltzmann equation,” *Phys. Rev. Lett.*, vol. 80, pp. 65–68, 1998.
- [55] I. V. Karlin, A. Ferrante, and H. C. Öttinger, “Perfect entropy functions of the Lattice Boltzmann method,” *Europhys. Lett.*, vol. 47, pp. 182–188, 1999.
- [56] S. S. Chikatamarla, S. Ansumali, and I. V. Karlin, “Entropic lattice Boltzmann models for hydrodynamics in three dimensions,” *Phys. Rev. Lett.*, vol. 97, p. 010201, 2006.
- [57] I. V. Karlin, F. Bösch, and S. S. Chikatamarla, “Gibbs’ principle for the lattice-kinetic theory of fluid dynamics,” *Phys. Rev. E*, vol. 90, p. 031302(R), 2014.
- [58] P. L. Bhatnagar, E. P. Gross, and M. Krook, “A model for collision processes in gases. i. small amplitude processes in charged and neutral one-component systems,” *Phys. Rev.*, vol. 94, pp. 511–525, 1954.
- [59] P. Lallemand and L. S. Luo, “Theory of the lattice Boltzmann method: Dispersion, dissipation, isotropy, Galilean invariance, and stability,” *Phys. Rev. E*, vol. 61, p. 6546, 2000.
- [60] D. D’Humières, I. Ginzburg, M. K. M., P. Lallemand, and L. S. Luo, “Multiple-relaxation-time lattice Boltzmann models in three dimensions,” *Philos. Trans. A Math. Phys. Eng. Sci.*, vol. 360, pp. 437–451, 2002.
- [61] X. He, S. Chen, and G. D. Doolen, “A novel thermal model for the lattice Boltzmann method in incompressible limit,” *J. Comput. Phys.*, vol. 146, pp. 282–300, 1998.

- [62] J. D. Sterling and S. Chen, “Stability analysis of Lattice Boltzmann Methods,” *J. Comput. Phys.*, vol. 123, pp. 196–206, 1996.
- [63] S. Ansumali and I. V. Karlin, “Kinetic boundary conditions in the lattice Boltzmann method,” *Phys. Rev. E*, vol. 66, p. 026311, 2002.
- [64] P. J. Davis and P. Rabinowitz, *Methods of numerical integration*. New York: Academic Press, 1975.
- [65] P. Perlekar, L. Biferale, M. Sbragaglia, S. Srivastava, and F. Toschi, “Droplet size distribution in homogeneous isotropic turbulence,” *Phys. Fluids*, vol. 24, p. 065101, 2012.
- [66] L. Biferale, P. Perlekar, M. Sbragaglia, and F. Toschi, “Convection in multiphase fluid flows using lattice boltzmann methods,” *Phys. Rev. Lett.*, vol. 108, p. 104502, 2012.
- [67] A. Gupta, H. J. H. Clercx, and F. Toschi, “Simulation of finite-size particles in turbulent flows using the Lattice Boltzmann Method,” *Comm. Comput. Phys.*, vol. 23, pp. 665–684, 2018.
- [68] M. A. Gallis, J. R. Torczynski, D. J. Rader, M. Tij, and A. Santos, “Normal solutions of the Boltzmann equation for highly nonequilibrium Fourier flow and Couette flow,” *Phys. Fluids*, vol. 18, p. 017104, 2006.
- [69] N. Hadjiconstantinou, “The limits of Navier-Stokes theory and kinetic extensions for describing small-scale gaseous hydrodynamics,” *Phys. Fluids*, vol. 18, p. 111301, 2006.
- [70] C. Bardos, R. E. Caflisch, and B. Nicolaenko, “The Milne and Kramers problems for the Boltzmann equation of a hard sphere gas,” *Commun. Pure Appl. Math.*, vol. 39, pp. 323–352, 1986.
- [71] C. Cercignani, *Rarefied gas dynamics*. Cambridge: Cambridge University Press, 2000.
- [72] Y. Sone, *Kinetic theory and fluid dynamics*. Boston: Birkhauser, 2002.
- [73] C. E. Siewert, “The linearized Boltzmann equation: concise and accurate solutions to basic flow problems,” *Z. Angew. Math. Phys.*, vol. 54, pp. 273–303, 2003.
- [74] X. Gu and D. Emerson, “A computational strategy for the regularized 13 moment equations with enhanced wall-boundary conditions,” *J. Comp. Phys.*, vol. 225, pp. 263–283, 2007.

- 
- [75] S. Mizzi, R. W. Barber, D. R. Emerson, J. M. Reese, and S. K. Stefanov, "A phenomenological and extended continuum approach for modelling non-equilibrium flows," *Continuum Mech. Thermodyn.*, vol. 19, pp. 273–283, 2007.
- [76] H. Struchtrup and M. Torrilhon, " $H$  theorem, regularization, and boundary conditions for linearized 13 moment equations," *Phys. Rev. Lett.*, vol. 99, p. 014502, 2007.
- [77] M. Torrilhon and H. Struchtrup, "Boundary conditions for regularized 13-moment-equations for micro-channel-flows," *J. Comp. Phys.*, vol. 227, pp. 1982–2011, 2008.
- [78] C. R. Lilley and J. E. Sader, "Velocity gradient singularity and structure of the velocity profile in the Knudsen layer according to the Boltzmann equation," *Phys. Rev. E*, vol. 76, p. 026315, 2007.
- [79] C. R. Lilley and J. E. Sader, "Velocity profile in the Knudsen layer according to the Boltzmann equation," *Proc. R. Soc. A*, vol. 464, pp. 2015–2035, 2008.
- [80] K. Koura and H. Matsumoto, "Variable soft sphere molecular model for inverse-power-law or Lennard-Jones potential," *Phys. Fluids A*, vol. 3, pp. 2459–2465, 1991.
- [81] D. Willis, "Comparison of kinetic theory analyses of linearized Couette flow," *Phys. Fluids*, vol. 5, pp. 127–135, 1962.
- [82] S. K. Loyalka and K. Hickey, "Velocity slip and defect: Hard sphere gas," *Phys. Fluids A*, vol. 1, pp. 612–614, 1989.
- [83] S. Chapman and T. G. Cowling, *The mathematical theory of non-uniform gases: an account of the kinetic theory of viscosity, thermal conduction and diffusion in gases*. Cambridge: Cambridge University Press, 3rd ed., 1970.
- [84] C. Cercignani, "A variational principle for boundary value problems in kinetic theory," *J. Stat. Phys.*, vol. 1, pp. 297–311, 1969.
- [85] B. P., P. J. H., and B. A., "A unified engineering model for steady and quasi-steady shear driven gas micro flows," *Microscale Thermophys. Eng.*, vol. 7, pp. 291–315, 2003.
- [86] M. N. Kogan, *Rarefied Gas Dynamics*. New York: Plenum Press, 1969.

- [87] T. Veijola and M. Turowski, “Compact damping models for laterally moving microstructures with gas-rarefaction effects,” *Microelectromech. Sys.*, vol. 10, pp. 263–273, 2001.
- [88] U. Ghia, K. Ghia, and C. Shin, “High-Re solutions for incompressible flow using the Navier-Stokes equations and a multigrid method,” *J. Comput. Phys.*, vol. 48, pp. 387–411, 1982.
- [89] P. N. Shankar and M. D. Deshpande, “Fluid mechanics in the driven cavity,” *Annual Review of Fluid Mechanics*, vol. 32, no. 1, pp. 93–136, 2000.
- [90] S. Naris and D. Valougeorgis, “The driven cavity flow over the whole range of the Knudsen number,” *Phys. Fluids*, vol. 17, p. 097106, 2005.
- [91] Z. Guo, K. Xu, and R. Wang, “Discrete unified gas kinetic scheme for all Knudsen number flows: Low-speed isothermal case,” *Phys. Rev. E*, vol. 88, p. 033305, 2013.
- [92] J. Benzi, X.-J. Gu, and D. R. Emerson, “Investigation of heat and mass transfer in a lid-driven cavity under nonequilibrium flow conditions,” *Numer. Heat Tr. B.-Fund.*, vol. 58, pp. 287–303, 2010.
- [93] H. Struchtrup and M. Torrilhon, “Regularization of Grad’s 13 moment equations: Derivation and linear analysis,” *Phys. Fluids*, vol. 15, pp. 2668–2680, 2003.
- [94] H. Struchtrup, “Scaling and expansion of moment equations in kinetic theory,” *J. Stat. Phys.*, vol. 125, pp. 569–591, 2006.
- [95] A. Rana, M. Torrilhon, and H. Struchtrup, “A robust numerical method for the R13 equations of rarefied gas dynamics: Application to lid driven cavity,” *J. Comput. Phys.*, vol. 236, pp. 169–186, 2013.
- [96] J. Benzi, X.-J. Gu, and D. R. Emerson, “Effects of incomplete surface accommodation on non-equilibrium heat transfer in cavity flow: A parallel DSMC study,” *Comput. & Fluids*, vol. 45, pp. 197–201, 2011.
- [97] E. Farbar and I. Boyd, “Subsonic flow boundary conditions for the direct simulation Monte Carlo method,” *Comput. & Fluids*, vol. 102, pp. 99–110, 2014.
- [98] M. Ikegawa and J. Kobayashi, “Development of a rarefield gas flow simulator using the direct-simulation monte carlo method: 2-d flow analysis with the

- pressure conditions given at the upstream and downstream boundaries,” *JSME Int. J. Ser.*, vol. 2, pp. 463–467, 1990.
- [99] J.-S. Wu and K.-C. Tseng, “Analysis of micro-scale gas flows with pressure boundaries using direct simulation monte carlo method,” *Comput. & Fluids*, vol. 30, pp. 711–735, 2001.
- [100] R. Nance, D. Hash, and H. Hassan, “Role of boundary conditions in Monte Carlo simulations of MEMS devices,” *J. Thermophys. Heat Transf.*, vol. 12, pp. 447–449, 1998.
- [101] M. Wang and Z. Li, “Simulations for gas flows in microgeometries using the direct simulation monte carlo method,” *Int. J. Heat Fluid Flow*, vol. 25, pp. 975–985, 2004.
- [102] Y. Fang and W. W. Liou, “Computations of the flow and heat transfer in microdevices using DSMC with implicit boundary conditions,” *J. Heat Transf.*, vol. 124, pp. 338–345, 2002.
- [103] W. Liou and Y. Fang, “Implicit boundary conditions for direct simulation Monte Carlo method in MEMS flow predictions,” *Comput. Model. Eng. Sci.*, vol. 1, pp. 119–128, 2000.
- [104] D. Whitfield, “Three-dimensional unsteady Euler equations solution using flux vector splitting,” in *17th Fluid Dynamics, Plasma Dynamics, and Lasers Conference*, American Institute of Aeronautics and Astronautics, 1984.
- [105] N. A. Gatsonis, R. E. Chamberlin, and S. N. Averkin, “An unstructured direct simulation Monte Carlo methodology with kinetic-moment inflow and outflow boundary conditions,” *J. Comput. Physics*, vol. 233, pp. 148–174, 2013.
- [106] M. W. Tysanner and A. L. Garcia, “Non-equilibrium behaviour of equilibrium reservoirs in molecular simulations,” *Int. J. Numer. Meth. Fluids*, vol. 48, pp. 1337–1349, 2005.
- [107] E. B. Arkilic, M. A. Schmidt, and K. S. Breuer, “Gaseous slip flow in long microchannels,” *J. Micromech. Sys.*, vol. 6, pp. 167–178, 1997.
- [108] T. Reis and P. J. Dellar, “Lattice Boltzmann simulations of pressure-driven flows in microchannels using Navier-Maxwell slip boundary conditions,” *Phys. Fluids*, vol. 24, p. 112001, 2012.



- [109] G. Di Staso, H. J. H. Clercx, S. Succi, and F. Toschi, “DSMC-LBM mapping scheme for rarefied and non-rarefied gas flows,” *J. Comput. Sci.*, vol. 17, pp. 357–369, 2016.
- [110] C.-M. Ho and Y.-C. Tai, “Micro-electro-mechanical-systems (MEMS) and fluid flows,” *Annu. Rev. Fluid Mech.*, vol. 30, pp. 579–612, 1998.
- [111] J. M. Reese, M. A. Gallis, and D. A. Lockerby, “New directions in fluid dynamics: non-equilibrium aerodynamic and microsystem flows,” *Phil. Trans. R. Soc. Lond. A*, vol. 361, pp. 2967–2988, 2003.
- [112] G. Karniadakis, A. Beskok, and N. Aluru, *Microflows and Nanoflows. Fundamentals and Simulation*. New York: Springer-Verlag, 2005.
- [113] I. D. Boyd, G. Chen, and G. V. Candler, “Predicting failure of the continuum fluid equations in transitional hypersonic flows,” *Phys. Fluids*, vol. 7, p. 210, 1995.
- [114] M. M. Mansour, F. Baras, and A. Garcia, “On the validity of hydrodynamics in plane Poiseuille flows,” *Physica A*, vol. 240, pp. 255–267, 1997.
- [115] W.-M. Zhang, G. Meng, and Z. Wei, “A review on slip models for gas microflows,” *Microfluid. Nanofluid.*, vol. 13, pp. 845–882, 2012.
- [116] R. Roveda, D. B. Goldstein, and P. L. Varghese, “Hybrid Euler/particle approach for continuum/rarefied flows,” *J. Spacecraft Rockets*, vol. 35, pp. 258–265, 1998.
- [117] H. S. Wijesinghe, R. D. Hornung, A. L. Garcia, and N. G. Hadjiconstantinou, “Three-dimensional hybrid continuum-atomistic simulations for multiscale hydrodynamics,” *J. Fluids Eng.*, vol. 126, pp. 768–777, 2004.
- [118] J.-S. Wu, Y.-Y. Lian, G. Cheng, R. P. Koomullil, and K.-C. Tseng, “Development and verification of a coupled DSMC-NS scheme using unstructured mesh,” *J. Comput. Phys.*, vol. 219, pp. 579–607, 2006.
- [119] T. E. Schwatzentruber, L. C. Scalabrin, and I. D. Boyd, “A modular particle continuum numerical method for hypersonic non-equilibrium gas flows,” *J. Comput. Phys.*, vol. 225, pp. 1159–1174, 2007.
- [120] D. A. Kessler, E. S. Oran, and C. R. Kaplan, “Towards the development of a multiscale, multiphysics method for the simulation of rarefied gas flows,” *J. Fluid Mech.*, vol. 661, pp. 262–293, 2010.

- 
- [121] S. Pantazis and H. Rusche, “A hybrid continuum-particle solver for unsteady rarefied gas flows,” *Vacuum*, vol. 109, pp. 275–283, 2014.
- [122] K. Farber, P. Farber, J. Grabel, S. Krick, J. Reitz, and P. Ueberholz, “Development and validation of a coupled Navier-Stokes/DSMC simulation for rarefied gas flow in the production process for OLEDs,” *Appl. Math. Comput.*, vol. 272, pp. 648–656, 2016.
- [123] J.-F. Bourgat, P. L. Tallec, and M. Tidriri, “Coupling Boltzmann and Navier-Stokes equations by friction,” *J. Comput. Phys.*, vol. 127, pp. 227–245, 1996.
- [124] P. L. Tallec and F. Mallinger, “Coupling Boltzmann and Navier-Stokes equations by half-fluxes,” *J. Comput. Phys.*, vol. 136, pp. 51–67, 1997.
- [125] A. L. Garcia and B. J. Alder, “Generation of the Chapman-Enskog distribution,” *J. Comput. Phys.*, vol. 140, pp. 66–70, 1998.
- [126] H. A. Al-Mohssen, N. G. Hadjiconstantinou, and I. G. Kevrekidis, “Acceleration methods for coarse-grained numerical solution of the Boltzmann equation,” *J. Fluids Eng.*, vol. 129, pp. 908–912, 2007.
- [127] P. Degond, J.-G. Liu, and L. Mieussens, “Macroscopic fluid models with localized kinetic upscaling effects,” *Multiscale Model. Simul.*, vol. 53, pp. 940–979, 2006.
- [128] S. Succi, “Mesoscopic modeling of slip motion at fluid-solid interfaces with heterogeneous catalysis,” *Phys. Rev. Lett.*, vol. 89, p. 064502, 2002.
- [129] M. Sbragaglia and S. Succi, “Analytical calculation of slip flow in lattice Boltzmann models with kinetic boundary conditions,” *Phys. Fluids*, vol. 17, p. 093602, 2005.
- [130] M. Sbragaglia and S. Succi, “A note on the lattice Boltzmann method beyond the Chapman-Enskog limits,” *Europhys. Lett.*, vol. 73, pp. 370–376, 2006.
- [131] X.-D. Niu, S.-A. Hyodo, T. Mune-kata, and K. Suga, “Kinetic lattice Boltzmann method for microscale gas flows: Issues on boundary condition, relaxation time, and regularization,” *Phys. Rev. E*, vol. 76, p. 036711, 2007.
- [132] G.-H. Tang, Y.-H. Zhang, and D. Emerson, “Lattice Boltzmann models for nonequilibrium gas flows,” *Phys. Rev. E*, vol. 77, p. 046701, 2008.
- [133] J. Meng and Y. Zhang, “Accuracy analysis of high-order lattice Boltzmann models for rarefied gas flows,” *J. Comput. Phys.*, vol. 230, pp. 835–849, 2011.

- [134] J. Meng and Y. Zhang, “Gauss-Hermite quadratures and accuracy of lattice Boltzmann models for nonequilibrium gas flows,” *Phys. Rev. E*, vol. 83, p. 036704, 2011.
- [135] T. Reis and P. Dellar, “Lattice Boltzmann simulations of pressure-driven flows in microchannels using Navier-Maxwell slip boundary conditions,” *Phys. Fluids*, vol. 24, p. 112001, 2012.
- [136] X. Liu and Z. Guo, “A lattice Boltzmann study of gas flows in a long micro-channel,” *Comput. Math. Appl.*, vol. 65, pp. 186–193, 2013.
- [137] S. Tao and Z. Guo, “Boundary condition for lattice Boltzmann modeling of microscale gas flows with curved walls in the slip regime,” *Phys. Rev. E*, vol. 91, p. 043305, 2015.
- [138] J. Zhang, “Lattice Boltzmann method for microfluidics: models and applications,” *Microfluid. Nanofluid.*, vol. 10, pp. 1–28, 2011.
- [139] F. Verhaeghe, L.-S. Luo, and B. Blanpain, “Lattice Boltzmann modeling of microchannel flow in slip flow regime,” *J. Comput. Phys.*, vol. 228, pp. 147–157, 2009.
- [140] Z. Guo, J. Qin, and C. Zheng, “Generalized second-order slip boundary condition for nonequilibrium gas flows,” *Phys. Rev. E*, vol. 89, p. 013201, 2014.
- [141] Z. Chai, Z. Guo, L. Zheng, and B. Shi, “Lattice Boltzmann simulation of surface roughness effect on gaseous flow in a microchannel,” *J. Appl. Phys.*, vol. 104, p. 014902, 2008.
- [142] A. Montessori, M. L. Rocca, G. Falcucci, and S. Succi, “Regularized lattice BGK versus highly accurate spectral methods for cavity flow simulations,” *Int. J. Mod. Phys. C*, vol. 25, p. 1441003, 2014.
- [143] Z. Guo, C. Zheng, B. Shi, and T. S. Zhao, “Thermal lattice Boltzmann equation for low Mach number flows: Decoupling model,” *Phys. Rev. E*, vol. 75, p. 036704, 2007.
- [144] J. Meng, Y. Zhang, N. G. Hadjiconstantinou, G. A. Radtke, and X. Shan, “Lattice ellipsoidal statistical BGK model for thermal non-equilibrium flows,” *J. Fluid Mech.*, vol. 718, pp. 347–370, 2013.

- 
- [145] P. Lallemand and L.-S. Luo, "Theory of the lattice Boltzmann method: Acoustic and thermal properties in two and three dimensions," *Phys. Rev. E*, vol. 68, p. 036706, 2003.
- [146] G. H. Tang, W. Q. Tao, and Y. L. He, "Lattice Boltzmann method for gaseous microflows using kinetic theory boundary conditions," *Phys. Fluids*, vol. 17, p. 058101, 2005.
- [147] G. H. Tang, Y. H. Zhang, X. J. Gu, and D. R. Emerson, "Lattice Boltzmann modelling Knudsen layer effect in non-equilibrium flows," *Europhys. Lett.*, vol. 83, p. 40008, 2008.
- [148] X. Shan, "General solution of lattices for cartesian lattice Bhatnagar-Gross-Krook models," *Phys. Rev. E*, vol. 81, p. 036702, 2010.
- [149] T. Ohwada, Y. Sone, and K. Aoki, "Numerical analysis of the Poiseuille and thermal transpiration flows between two parallel plates on the basis of the Boltzmann equation for hard-sphere molecules," *Phys. Fluids A*, vol. 1, no. 12, pp. 2042–2049, 1989.
- [150] G. Di Staso, H. J. H. Clercx, S. Succi, and F. Toschi, "Lattice Boltzmann accelerated direct simulation Monte Carlo for dilute gas flow simulations," *Phil. Trans. R. Soc. A*, vol. 374, p. 20160226, 2016.
- [151] M. K. Borg, D. A. Lockerby, and J. M. Reese, "Fluid simulations with atomistic resolution: a hybrid multiscale method with field-wise coupling," *J. Comput. Phys.*, vol. 255, pp. 149–165, 2013.
- [152] G. Lu, E. B. Tadmor, and E. Kaxiras, "From electrons to finite elements: A concurrent multiscale approach for metals," *Phys. Rev. B*, vol. 73, p. 024108, 2006.
- [153] A. K. Nair, D. H. Warner, and R. G. Hennig, "Coupled quantum-continuum analysis of crack tip processes in aluminum," *J. Mech. Phys. Solids*, vol. 59, pp. 2476–2487, 2011.
- [154] H. Talebi, M. Silani, and T. Rabczuk, "Concurrent multiscale modeling of three dimensional crack and dislocation propagation," *Adv. Eng. Softw.*, vol. 80, pp. 82–92, 2015.
- [155] B. Rotenberg, I. Pagonabarraga, and D. Frenkel, "Coarse-grained simulations of charge, current and flow in heterogeneous media," *Faraday Discuss.*, vol. 144, pp. 223–243, 2010.

- [156] R. Potestio, S. Fritsch, P. Español, R. Delgado-Buscalioni, K. Kremer, R. Everaers, and D. Donadio, “Hamiltonian adaptive resolution simulation for molecular liquids,” *Phys. Rev. Lett.*, vol. 110, p. 108301, 2013.
- [157] P. Español, R. Delgado-Buscalioni, R. Everaers, R. Potestio, D. Donadio, and K. Kremer, “Statistical mechanics of Hamiltonian adaptive resolution simulations,” *J. Chem. Phys.*, vol. 142, p. 064115, 2015.
- [158] U. Alekseeva, R. G. Winkler, and G. Sutmann, “Hydrodynamics in adaptive resolution particle simulations: Multiparticle collision dynamics,” *J. Comput. Phys.*, vol. 314, pp. 14–34, 2016.
- [159] S. Schmieschek, D. K. N. Sinz, F. Keller, U. Nienke, and J. Harting, “Mesoscopic simulation of diffusive contaminant spreading in gas flows at low pressure,” *ArXiv e-prints*, 2015.
- [160] N. G. Hadjiconstantinou, “Hybrid atomistic-continuum formulations and the moving contact-line problem,” *J. Comput. Phys.*, vol. 154, pp. 245–265, 1999.
- [161] T. Werder, J. H. Walther, and P. Koumoutsakos, “Hybrid atomistic-continuum method for the simulation of dense fluid flows,” *J. Comput. Phys.*, vol. 205, pp. 373–390, 2005.
- [162] S. P. Thampi, I. Pagonabarraga, and R. Adhikari, “Lattice-Boltzmann-Langevin simulations of binary mixtures,” *Phys. Rev. E*, vol. 84, p. 046709, 2011.
- [163] R. Delgado-Buscalioni and G. D. Fabritiis, “Embedding molecular dynamics within fluctuating hydrodynamics in multiscale simulations of liquids,” *Phys. Rev. E*, vol. 76, p. 036709, 2007.
- [164] S. Succi, “Lattice Boltzmann 2038,” *Europhys. Lett.*, vol. 109, p. 50001, 2015.
- [165] A. Montessori, P. Prestininzi, M. L. Rocca, and S. Succi, “Lattice Boltzmann approach for complex nonequilibrium flows,” *Phys. Rev. E*, vol. 92, p. 043308, 2015.
- [166] F. J. Higuera and S. Succi, “Simulating the flow around a circular cylinder with a lattice Boltzmann equation,” *Europhys. Lett.*, vol. 8, pp. 517–521, 1989.
- [167] F. J. Higuera, S. Succi, and R. Benzi, “Lattice gas dynamics with enhanced collisions,” *Europhys. Lett.*, vol. 9, pp. 345–349, 1989.

- 
- [168] R. Delgado-Buscalioni, E. G. Flekkøy, and P. V. Coveney, “Fluctuations and continuity in particle-continuum hybrid simulations of unsteady flows based on flux-exchange,” *Europhys. Lett.*, vol. 69, p. 959, 2005.
- [169] M. Tij and A. Santos, “Combined heat and momentum transport in a dilute gas,” *Phys. Fluids*, vol. 7, pp. 2858–2866, 1995.
- [170] V. Garzó and A. Santos, *Kinetic theory of gases in shear flows: nonlinear transport*. Dordrecht: Kluwer Academic, 2003.
- [171] J. J. Brey, A. Santos, and J. W. Dufty, “Heat and momentum transport far from equilibrium,” *Phys. Rev. A*, vol. 36, pp. 2842–2849, 1987.
- [172] C. S. Kim, J. W. Dufty, A. Santos, and J. J. Brey, “Analysis of nonlinear transport in Couette flow,” *Phys. Rev. A*, vol. 40, pp. 7165–7174, 1989.
- [173] G. Di Staso, S. Srivastava, E. Arlemark, H. J. H. Clercx, and F. Toschi, “Hybrid lattice Boltzmann-direct simulation Monte Carlo approach for flows in three-dimensional geometries,” *Comput. & Fluids*, vol. 172, pp. 492–509, 2018.
- [174] F. J. Uribe and A. L. Garcia, “Burnett description for plane Poiseuille flow,” *Phys. Rev. E*, vol. 60, pp. 4063–4078, 1999.
- [175] K. K. Mattila, P. C. Philippi, and L. A. H. Jr., “High-order regularization in lattice-Boltzmann equations,” *Phys. Fluids*, vol. 29, p. 046103, 2017.
- [176] N. Frapolli, S. S. Chikatamarla, and I. V. Karlin, “Entropic lattice Boltzmann model for gas dynamics: Theory, boundary conditions, and implementation,” *Phys. Rev. E*, vol. 93, p. 063302, 2016.
- [177] B. Chun and A. J. C. Ladd, “Interpolated boundary condition for lattice Boltzmann simulations of flows in narrow gaps,” *Phys. Rev. E*, vol. 75, p. 066705, 2007.
- [178] Z.-G. Feng and E. E. Michaelides, “The immersed boundary-lattice Boltzmann method for solving fluid-particles interaction problems,” *J. Comput. Phys.*, vol. 195, pp. 602–608, 2004.
- [179] S. Kuchlin and P. Jenny, “Parallel Fokker-Planck-DSMC algorithm for rarefied gas flow simulation in complex domains at all Knudsen numbers,” *J. Comput. Phys.*, vol. 328, pp. 258–277, 2017.

- [180] S. Zabelok, R. Arslanbekov, and V. Kolobov, “Adaptive kinetic-fluid solvers for heterogeneous computing architectures,” *J. Comput. Phys.*, vol. 303, pp. 455–469, 2015.
- [181] T. J. Scanlon, E. Roohi, C. White, M. Darbandi, and J. M. Reese, “An open source, parallel DSMC code for rarefied gas flows in arbitrary geometries,” *Comput. & Fluids*, vol. 39, pp. 2078–2089, 2010.
- [182] C. Cercignani, *Mathematical methods in kinetic theory*. New York: Plenum, 1990.
- [183] D. A. Lockerby, J. M. Reese, and H. Struchtrup, “Switching criteria for hybrid rarefied gas flow solvers,” *Proc. R. Soc. A*, vol. 465, pp. 1581–1598, 2009.
- [184] C. Cercignani, M. Lampis, and S. Lorenzani, “Variational approach to gas flows in microchannels,” *Phys. Fluids*, vol. 16, p. 3426, 2004.
- [185] S. Lorenzani, “Higher order slip according to the linearized Boltzmann equation with general boundary conditions,” *Phil. Trans. R. Soc. A*, vol. 369, pp. 2228–2236, 2011.
- [186] Z.-X. Tong, M.-J. Li, X. Chen, and Y.-L. He, “Direct coupling between molecular dynamics and lattice Boltzmann method based on velocity distribution functions for steady-state isothermal flow,” *Int. J. Heat Mass Transfer*, vol. 115, pp. 544–555, 2017.
- [187] M. W. Tysanner and A. L. Garcia, “Measurement bias of fluid velocity in molecular simulations,” *J. Comput. Phys.*, vol. 196, pp. 173–183, 2004.
- [188] A. L. Garcia, “Nonequilibrium fluctuations studied by a rarefied-gas simulation,” *Phys. Rev. A*, vol. 34, pp. 1454–1457, Aug 1986.
- [189] G. Chen and I. D. Boyd, “Statistical error analysis for the Direct Simulation Monte Carlo technique,” *J. Comput. Phys.*, vol. 126, pp. 434–448, 1996.
- [190] Q. Sun and I. D. Boyd, “Evaluation of macroscopic properties in the direct simulation monte carlo method,” *J. Thermophys. Heat Transfer*, vol. 19, pp. 329–335, 2005.
- [191] I. D. Boyd, “Analysis of vibration-dissociation-recombination processes behind strong shock waves of nitrogen,” *Phys. Fluids A*, vol. 4, pp. 178–185, 1992.

# List of publications

## Refereed journal articles

- G. Di Staso, H. J. H. Clercx, S. Succi, and F. Toschi, "DSMC-LBM mapping scheme for rarefied and non-rarefied gas flows", *J. Comput. Sci.*, vol. 17, pp. 357-369, 2016.
- G. Di Staso, H. J. H. Clercx, S. Succi, and F. Toschi, "Lattice Boltzmann accelerated direct simulation Monte Carlo for dilute gas flow simulations", *Phil. Trans. R. Soc. A*, vol. 374, pp. 20160226, 2016.
- G. Di Staso, S. Srivastava, E. Arlemark, H. J. H. Clercx, and F. Toschi, "Hybrid lattice Boltzmann-direct simulation Monte Carlo approach for flows in three-dimensional geometries," *Comput. & Fluids*, vol. 172, pp. 492-509, 2018.

## Publications in preparation

- G. Di Staso, H. J. H. Clercx, and F. Toschi, "Simulation of finite-size particles motion in rarefied gases with a hybrid lattice Boltzmann-direct simulation Monte Carlo method".

## Refereed conference proceedings

- G. Di Staso, S. Srivastava, E. Arlemark, H.J.H. Clercx, and F. Toschi, "Hybrid lattice Boltzmann-Direct Simulation Monte Carlo approach for non-equilibrium flows in complex geometries", *Proceedings of the 5th European Conference on Microfluidics -  $\mu$ Flu18 and 3rd European Conference on Non-Equilibrium Gas Flows - NEGF18, Strasbourg, France, February, 28 - March, 2, 2018*.

## Non-refereed conference proceedings

- G. Di Staso, H. J. H. Clercx, S. Succi, and F. Toschi, "Hybrid DSMC-LBM scheme for rarefied and continuum gas flows", *Proceedings of the 2nd*



*European Conference on Non-equilibrium Gas Flows - NEGF15, Eindhoven, The Netherlands, December, 9-11, 2015.*

### List of presentations (selection)

- G. Di Staso, H. J. H. Clercx, and F. Toschi, "Hybrid DSMC-LBM scheme for force-driven flows", *67th APS Annual Meeting - Division of Fluid Dynamics*, San Francisco, USA, November, 23, 2014.
- G. Di Staso, H. J. H. Clercx, S. Succi, and F. Toschi, "Hybrid DSMC-LBM scheme for rarefied and non-rarefied gas flows", *24th International Conference on Discrete Simulation of Fluid Dynamics - DSFD 2015*, Edinburgh, UK, July, 15, 2015.
- G. Di Staso, H. J. H. Clercx, S. Succi, and F. Toschi, "DSMC-LBM hybrid scheme for rarefied and non-rarefied flows", *68th APS Annual Meeting - Division of Fluid Dynamics*, Boston, USA, November, 23, 2015.
- G. Di Staso, H. J. H. Clercx, S. Succi, and F. Toschi, "Hybrid DSMC-LBM scheme for rarefied and continuum gas flows", *2nd European Conference on Non-equilibrium Gas Flows - NEGF15*, Eindhoven, The Netherlands, December, 9, 2015.
- G. Di Staso, H. J. H. Clercx, S. Succi, and F. Toschi, "Hybrid Monte Carlo and lattice Boltzmann equation model for rarefied and non-rarefied gas flows", *Solvay Workshop — Bridging the gaps at the PBC interface, Multiscale modelling in Physics, Chemistry and Biology*, Université Libre de Bruxelles, Bruxelles, Belgium, April, 21, 2016.
- G. Di Staso, H. J. H. Clercx, S. Succi, and F. Toschi, "DSMC and hybrid DSMC-LBM for non-equilibrium flows", *Workshop Lattice Boltzmann 2016*, University of Rome Tor Vergata, Rome, Italy, June, 9, 2016 (Invited speaker).
- G. Di Staso, H. J. H. Clercx, S. Succi, and F. Toschi, "LBM-DSMC hybrid method for complex out-of-equilibrium flows", *Flowing Matter 2017*, Workshop COST-Action MP1305 "Flowing matter", Porto, Portugal, January, 26, 2017.
- G. Di Staso, S. Srivastava, E. Arlemark, H.J.H. Clercx, and F. Toschi, "Hybrid lattice Boltzmann-Direct Simulation Monte Carlo approach for non-equilibrium flows in complex geometries", *3rd European Conference on Non-Equilibrium Gas Flows - NEGF18*, Strasbourg, France, March, 1, 2018.

# Summary

## Hybrid discretizations of the Boltzmann equation for the dilute gas flow regime

This PhD thesis deals with the development and validation of a hybrid model coupling the Lattice Boltzmann Method (LBM) with the Direct Simulation Monte Carlo (DSMC) to study gas flows characterized by variable rarefaction and non-equilibrium effects. This kind of flows represents an open research challenge from the physics, mathematical modeling and computer science points of view. From the physics point of view, in fact, several peculiar phenomena, not encountered under continuum flow conditions, appear when rarefied conditions are present. The velocity slip and temperature jump at a solid surface are just two of the most common ones.

The modeling of such flows, moreover, requires a different approach with respect to the continuum flow case since the classical Navier-Stokes equations are not valid anymore. A more fundamental method, based on the Boltzmann equation (BE), is therefore required. However, the direct numerical simulation of the BE is a very expensive task from the computational point of view. Alternative approaches have to be sought.

It is in this view that we developed a hybrid model that couples two mesoscopic numerical methods, the LBM and the DSMC, in order to accurately and efficiently simulate such type of flows.

In this thesis, we introduced the basics of the two methods, the LBM and the DSMC, underlining their common kinetic theory roots and the reasons why they represent ideal candidates for such hybrid model. The implementation and validation of the DSMC code developed during the PhD project was briefly described. Such implementation was driven by the constraint that a full compatibility with the treatment of flows in complex geometries, especially in relation to the application of the boundary conditions as done in the LBM, had to be preserved. The performed validations showed very good results for some classical rarefied gas flow tests (Knudsen layer formation in proximity of a solid surface, shear stress evaluation for several rarefaction conditions, cavity flow under rarefaction conditions, pressure-driven channel flow in slip flow regime).

We then introduced the coupling algorithms needed to exchange information on

the flow between the LBM and the DSMC. Such algorithms are based on the Grad's formalism to represent the single particle velocity distribution function via a series expansion in Hermite polynomials and on the Gauss-Hermite quadrature technique to evaluate the coefficients of the expansion. The validation performed on the coupling schemes showed that the proposed algorithms provide an accurate transfer also of non-equilibrium contributions up to  $Kn=0.25$  for a D3Q39 lattice and to  $Kn=0.10$  for a D3Q19 lattice. The coupling schemes were then integrated within a single code infrastructure and were applied to a Couette flow after the domain was assigned to the LBM or DSMC solver based on a domain decomposition technique. Employing the DSMC only within the Knudsen layer, located in proximity of the solid walls, allowed to obtain up to a sixfold reduction of the required computational time with respect to a DSMC simulation over the whole domain, while still preserving a good solution. The same hybrid model was then applied to a more realistic three-dimensional flow of industrial interest. Such flow posed challenges both from the modelling and the computational points of view, thus representing a good validation test benchmark for the proposed hybrid model. In fact, several characteristic length and time scales, i.e. a large range of rarefaction and non-equilibrium conditions, were present. Moreover, the flow characteristics, in particular the level of pressure within the flow domain, were such that a very large scale simulation, involving hundreds of millions of cells and, therefore, billions of particles, was needed. The domain decomposition was based on the evaluation of a local Knudsen number in turn defined according to the local gradient of the flow velocity magnitude. We showed that the application of the hybrid method allowed to obtain an accurate solution when compared with a DSMC simulation performed over the whole domain at a fraction of the required computational cost (more than a fourfold computational time reduction). Finally, we discussed about the limitations of the current hybrid method implementation, principally related to the isothermal assumption on the LBM side of the model, and we delineated ways on how to overcome such limitations. Perspectives to extend the proposed coupling schemes to numerical methods different from the LBM and the DSMC were also suggested.

# Acknowledgements

This booklet is the final result of my PhD project. During the last five years, I have devoted myself to the completion of this project. As for any other PhD, also in my case, without the help, guidance and encouragement of many people this work would not have been possible. I take now the opportunity to express my gratitude to them for the support they were able to provide me.

First of all, I would like to thank my supervisors, Prof. Herman Clercx and Prof. Federico Toschi for giving me the possibility to do my PhD on such an interesting and challenging topic. I am indebted with you for your guidance, encouragement and trust in me. Besides the scientific guidance, you also provided me a clear example of full dedication to work which was and is inspiring me in my daily activities.

I am also thankful to Dr. Sauro Succi, whose collaboration was fundamental at the beginning of my PhD project.

I wish to express my gratitude to my defense committee members: Prof. Alejandro Garcia, Prof. Gerrit Kroesen, Prof. Jens Harting, Prof. Paul van der Schoot, Prof. Harald van Brummelen, who have been so kind to review my thesis.

I would like to thank STW and the industrial partner ASML for funding this project research. In particular, my thanks go to Dr. Sudhir Srivastava and Dr. Erik Arlemark at ASML for the fruitful discussions and their collaboration.

A special thank to the WDY group secretaresse, Marjan Rodenburg, for her efforts for arranging all the burocratic formalities. She has always been very helpful:

*Torna presto!*

I would also like to thank my friends and colleagues at WDY group. They made the last five years delightful. In particular, my gratitude goes to my (ex-)officemates: Dennis (thanks for your three-year long patience shown when so many people daily entered our office to ask me questions, arguably disturbing you), Riccardo, Marlies, Kim and Abhineet who made the work fun. I would like to thank also all the other friends and colleagues at the Cascade building: Chung-min, Vitor, Steven, Altug, Ozge, Hadi, Francesca, Josje, Pranav, Alessandro, Wolfram, Neehar, Dario, Michel, Cosimo, Bijan, Jonathan, Pinaki, Abheeti, Sten, Xiao, Anders, Haijing, Dennis, Ivo, Matteo (Lulli and Madonia), Samuel, Felix, Andrei, GertJan, Leon, Rudie, Willem, Bas, Maarten, and many more I might have missed to mention. I really enjoyed and will always remember all the extra-work activities we did together.

I cannot finish without expressing my gratitude to my family. I am thankful to my parents, for giving me full independence to take my own decisions and, afterwards, to support me in the difficult times. I am also thankful to my brother, Nicola, who has provided me an example to devotion to study since we were kids. I dedicate to the three of you this thesis.

Finally, this work completes a fundamental part of my professional career. But a new phase has already started which, I hope, and strongly believe, will be full of exciting moments and successes.

Federico, Herman, thank you for having placed so much trust in me.

Gianluca Di Staso  
Eindhoven, September 2018

# Curriculum Vitae

Gianluca Di Staso was born on 23-06-1983 in Foggia, Italy. After having completed his high school education at the Liceo Classico Dante Alighieri in Ravenna, Italy, he studied Aerospace Engineering at the Università degli Studi di Bologna, Italy. In 2006, he graduated with a Bachelor of Engineering on the "Application of the momentum theorem to the measurement of the drag vehicle". From 2006 to 2009, he studied Astronautical Engineering at the Università di Roma Sapienza, Italy. In 2010 he graduated with a Master of Science on the "Application of CNT nanofluids for on-board electronic device cooling". From 2010 to 2013, he joined as development engineer an SME company in Rome (Ingegneria Sistemi Impianti Servizi) working on two FP7 EU funded collaborative projects in the field of nanotechnologies (NanoHex project) and space propulsion technologies (DiPoP project). From November 2013 he started a PhD project at the Turbulentie en Werveldynamica (WDY) group at the Eindhoven University of Technology in Eindhoven, The Netherlands, the results of which are presented in this dissertation.